Finite Element Simulation and Mechanical Characterization of Composite Insulators

Anurag Bansal
B. Tech. (Metallurgical Engineering)
Institute of Technology, Banaras Hindu University
Varanasi, India, 1991

A dissertation submitted to the faculty of the
Oregon Graduate Institute of Science & Technology
in partial fulfillment of the
requirements for the degree
Doctor of Philosophy
in
Materials Science and Engineering

January, 1996

The dissertation "Finite Element Simulation and Mechanical Characterization of Composite Insulators" by Anurag Bansal has been examined and approved by the following Examination Committee:

Dr. M.S. Kumosa
Dissertation Advisor
Associate Professor, Dept. of Electrical Engineering and Applied Physics

Dr. D.G. Atteridge
Professor, Dept. of Materials Science and Engineering

Dr. L. L. Meekisho
Assistant Professor, Dept. of Materials Science and Engineering

Dr. J. F. Holmes
Professor, Dept. of Electrical Engineering and Applied Physics

To my parents........

for their sacrifices towards my education

Acknowledgments

First and foremost, I wish to thank my dissertation advisor, Dr. Maciej Kumosa, for his ideas, generous support, and encouragement, during the course of this research. The many technical discussions which I had with him have tremendously broadened my knowledge of the mechanics of composite materials. I sincerely appreciate his effort and technical input towards the completion of this work.

I also wish to express sincere appreciation to the members of my dissertation committee, Drs. D.G. Atteridge, L. L. Meekisho, and J. F. Holmes, for their critical review of this dissertation. In particular, I am grateful to Dr. Meekisho for his personal guidance and useful technical suggestions. I would also like to take this opportunity to thank the OGI faculty and staff for their help and support. I thank Mr. Rick Neimann for his help in the non-destructive evaluation.

This research was funded by the Bonneville Power Administration (Dept. of Energy), the Electric Power Research Institute, and the National Science Foundation. My thanks are due to Mr. Dan Nichols, Mr. Calvin Ek, and Mr. Leon Kempner, for their technical support.

Finally, I wish to thank my friends who have helped me on numerous occasions, and have made my stay at OGI a very pleasant and memorable one. In particular, I would like to mention Bala, Venky, Shiliang, Priya, Ujwal, Shafqat, Javed, Rajesh, and Andreas, for their help. Last, but certainly not the least, I wish to thank Neena for her moral support, encouragement, and for being by my side through the best and worst of times.

Table of Contents

List of Tables

List of Figures

Page

ABSTRACT

Finite Element Simulation and Mechanical Characterization of Composite Insulators

Anurag Bansal
Supervising Professor: Dr. M. Kumosa

Composite Insulators are required to fulfill long-term structural roles in power transmission and substation applications. These insulators consist of a glass reinforced polymer (GRP) composite rod, with two metal end-fittings either mechanically crimped or adhesively bonded to the ends of the rod during assembly. In comparison with their porcelain counterparts, composite insulators offer significant advantages such as a high mechanical strength-to-weight ratio, improved damage tolerance, flexibility, and ease of installation. However, since they are a relatively new product, their design is still in an evolutionary stage, and their structural integrity and expected life to failure is a subject of great interest to both utilities and manufacturers.

The objective of this study was to evaluate the short-term structural integrity of composite insulators subjected to externally applied multi-axial loads, in conjunction with the residual radial compression applied to the GRP rod during crimping. In order to achieve this goal, comprehensive axisymmetric- and three-dimensional finite element models have been developed in this study. The models assumed either a perfectly bonded interface, or an imperfect interface between the GRP rod and metal end-fittings. The internal stresses in the GRP rod of 115 kV substation insulators, caused by radial compression applied during crimping, and seven different cases of expected multi-axial loads were analyzed. In addition, destructive and non-destructive tests were performed on five substation insulators in order to determine their mechanical strengths under three different modes of external loading, and to measure the extent of radial compression applied to the insulators during crimping. Furthermore, the finite element models were used to perform a parametric study of the influence of design variables such as the radius of the GRP rod, the magnitude and shape of radial compression applied during crimping, and the coefficient of friction at the GRP-metal interface, on the axial loading capacity and the internal stresses in the GRP rod of both substation and suspension insulators. In addition, a methodology employing the biaxial Iosipescu fixture was suggested for measuring the biaxial failure strength, in particular, the resistance to axial splitting (or debonding), of unidirectional composites used in insulators.

Results obtained from this study indicate that the magnitude and shape of the radial compression profile of the GRP rod, and the mechanical performance under external loads, can be significantly different among insulators intended for the same application. The perfect interface models were inappropriate for computing the maximum internal stresses, since they assume a linear mechanical behavior and predict singular stresses at the GRP-metal interface corner. On the other hand, the imperfect interface models could accurately predict the structural non-linearity of insulators, and were in good agreement with experimental results obtained under three different modes of external loading. From the parametric design analysis, the effects of several variables were evaluated, and semi-empirical relationships were derived to extrapolate the numerical data within a well defined range of the design variables. It was shown that the biaxial Iosipescu test is a reliable technique for measuring the resistance of unidirectional composites to intralaminar splitting under biaxial loading conditions.

Chapter 1

Introduction

Electrical insulators are required to fulfill long-term structural roles in power transmission and substation applications. The primary objective of these insulators is to provide mechanical support to a high-voltage overhead line by transferring the conductor load to a tower, while providing electrical insulation between the tower and conductor. Due to the prohibitive costs involved in line maintenance, utilities desire that insulators fulfill this objective continuously for a period of at least fifty years. These insulators have traditionally been manufactured from toughened porcelain or tempered glass. In fact, in most countries, porcelain or glass insulators are still in service.

The history of polymeric insulators began in the 1940s when organic materials were used to manufacture high voltage indoor electrical insulators from epoxy resins. [1] These insulators were made feasible for outdoor use in the 1950s with the discovery that alumina trihydrate fillers can improve the tracking and erosion resistance of the polymer material. In the late 1960s and early 1970s, manufacturers in Germany, England, France, Italy, and the United States started introducing a glass fiber reinforced composite rod to serve as the principal load bearing component of insulators, leading to the first generation of composite transmission line insulators.[1,2] Since then, composite insulators have rapidly replaced the traditional ceramic insulators in outdoor transmission and distribution lines, as well as substations. A study published in 1991 has reported that composite insulators have already captured 20% of the transmission line market in the United States, and the market share is expected to increase rapidly.[1] In comparison with their brittle ceramic counterparts, composite insulators offer significant advantages such as a high mechanical strength-to-weight ratio, improved damage tolerance, flexibility, impact resistance, and ease of installation.[3] However, since these insulators are a relatively new product, their design is still in an evolutionary stage. Furthermore, due to insufficient field experience, their structural integrity and expected life is a subject of great interest to both utilities and manufacturers.[3-5]

1.1. INSULATOR DESIGN

Composite insulators rely on a unidirectional glass reinforced polymer (GRP) composite rod as the principal load bearing component. The rods are manufactured by pultrusion, and the constituents are either polyester, modified vinyl-ester, or epoxy resins, reinforced with E-glass or ECR-glass fibers. The fibers are axially aligned and constitute 60 to 70 percent of the rod by volume. The ends of the GRP-rod are supported by two metal end-fittings made of either aluminum, forged steel, or galvanized cast iron. The primary function of the end-fittings is to provide a mechanical link and to transfer loads from the high-voltage conductor to the GRP rod (at the line-end), and from the GRP rod to the tower (at the tower-end). The end-fittings for suspension insulators traditionally had the epoxy cone design, wherein the ends of the rod were chemically bonded to epoxy resins injected in a cone-shaped metal shell (see fig. 1.1 a). However, due to a lower cost of production, insulator manufacturers have recently shifted to the crimped end-fitting design (see fig. 1.1 b). In the crimped design, the end-fittings are radially compressed on to the ends of the GRP rod until the onset of plastic deformation in the end-fittings. Unlike the epoxy-cone design, the bond achieved between the rod and crimped end-fittings is purely mechanical in nature. [6]

The GRP-rod is covered by a rubber sheath with several disk-shaped weathersheds. This layer is made of either ethylene-propylene (EP), ethylene-propylene diene monomer (EPDM), or silcone rubber compounds. The primary function of the rubber sheath is to protect the composite rod from moisture ingress and electrical leakage currents. The weathersheds are used to provide a longer leakage path between the high-voltage conductor and transmission-line tower to prevent electrical failures of insulators (also known as flashover). Since the GRP composite is susceptible to stress-corrosion cracking due to moisture ingress and internal partial discharge, the physical and chemical properties of the rubber layer have been the subject of several investigations. [2] Under service conditions, the rubber layer is required to exhibit good hydrophobicity, good tracking or corona-cutting resistance, and superior wear resistance. For insulators to be used in very high voltage applications (up to to 735 kV), the number of weathersheds and the overall length of the insulator is increased in order to maintain a sufficiently large leakage distance. In some insulators, the interface between the rubber sheath and GRP rod is chemically bonded with an epoxy resin, while in others it is coated with silicone grease without any adhesive bonding.

1.2. LOADING CRITERIA

Based upon their intended applications, composite insulators can be categorized as suspension, substation, and line-post insulators. Figures 1.2 (a) and (b) show suspension insulators loaded in overhead transmission lines in the I-string and V-string configurations, respectively. A typical line-post composite insulator is shown in figure 1.3. Figure 1.4 (a) shows the traditional porcelain substation insulators loaded in service, and figure 1.4 (b) shows a typical 115 kV substation composite insulator. The following sections describe the applications and loading conditions for these insulators.

(a) Suspension Insulators :

Suspension insulators are used in overhead transmission lines with line voltages in the range of 69 kV to 735 kV. During service, they are most frequently loaded in the I-string configuration (see figure 1.2 a) such that the dominant loading mode is axial tension. In some areas where the line-loads are expected to be higher due to wind-gusts, suspension insulators may be loaded in the V-string configuration (see figure 1.2 b). This configuration employs two insulators instead of one, thereby reducing the axial tensile load experienced by each insulator. The V-string configuration is however less popular due to the higher overall cost of the transmission line. The mechanical rating of commercially available suspension insulators can range from 40 kN to 600 kN. While the design of the insulators remains the same, the radius of the GRP rod is used to manipulate the maximum permissible load to be applied in service. At present, insulators rated at 40 to 60 kN typically have a rod radius of 8 mm, while insulators rated at 60 to 111 kN have a rod radius of 11 mm. Furthermore, the number of weathersheds and the overall length of the insulator is used to manipulate the specific leakage distance, and therefore the applicable line voltage. Suspension insulators used in 345 kV lines are typically longer, and have more weathersheds, than insulators in 69 kV lines.

(b) Line-Post Insulators :

The design of line-post insulators is similar to that of suspension insulators. The radius of the GRP-rod is approximately 20mm. During service, these insulators are loaded horizontally on transmission and distribution line poles, with the other end supporting the high-voltage conductor. The dominant loading mode is bending for these insulators (see figure 1.3).

(c) Substation Insulators :

These insulators are used in electrical substations. The 115 kV substation insulators are approximately 1140 mm in length, with a rod radius of approximately 31 mm. The crimped end-fittings in these insulators have a flat base which acts like a flange. During service, two or three substation insulators may be axially stacked on top of each other to serve as a support pillar (see figure 1.4 a). The top-most insulator carries the high-voltage conductor, the lower-most insulator is supported to the ground, and the intermediate insulator(s) serve as pillars to transfer the load from the conductor to the ground.

In addition to the most dominant loading modes expected for the insulators (*i.e.,* axial tension for suspension insulators, bending for line-post insulators, and axial compression for substation insulators), there are usually several other sources of static and cyclic loading during service. All of the above insulators are subjected to torsional forces either during normal service conditions, or during line maintenance and installation. Furthermore, natural causes such as ice-deposition during winters, extreme winds, and earth-quakes are factors that are taken into account. The overall loading conditions for all of the above insulators are therefore multi-axial in nature.

Composite suspension insulators represent 2 to 5 percent of the cost of a transmission line. During service, mechanical failure of a single insulator may instantly increase the load on adjacent insulators, thereby creating a possibility for a series of cascading failures along several miles of a transmission line. This situation can be further aggravated by the fact that composite insulators have been known to loose their strength with time.[7] Due to these concerns, the design of transmission lines is governed by stringent loading criteria in order to minimize the chances of insulator failures. In fact, the design philosophy of some utilities is to prefer failure of transmission line towers prior to insulator failure. There are two approaches currently being used in line design.

(i) **Working Load Design**

The working load design (WLD) is a reliability based approach which employs empirical methods to determine normal working loads, and probabilistic methods to evaluate the chances of insulator failure.[8] In this approach, safety factors ranging from 1.5 to 4.0 are used to separate the normal working loads from the strength of an insulator. These factors are determined from the bare-wire loads, and possible deviations in the average strength of an insulator. The main objective of the WLD approach is to prevent failure at design loads, without considering occasional overloads caused by wing gusts or seismic activity. This method is most frequently recommended by safety codes such as the National Electric Safety Code (NESC).

(ii) **Ultimate Load Design**

Unlike the WLD, the ultimate load design (ULD) is based upon actual failure loads of an insulator, instead of probabilistic predictions. The method considers extreme overloads which are likely to be encountered once in 25 to 50 years. A major advantage of the ULD is that it permits utility engineers to design for failure (*e.g.*, tower versus insulator) by providing a lower stress reduction factor to one component than to another.[8]

In practice, it is found that neither of the above approaches are sufficient alone. Furthermore, in order to apply either the WLD or the ULD and thereby limit the anticipated loads experienced by an insulator in service, prior knowledge of several parameters is necessary. The following parameters are determined by several considerations relevant to the performance of insulators.

(i) *Bare Wire Load:* This is the load of a conductor assuming no ice deposition or wind loading. A suspension insulator must support 1.5 times this load continuously throughout its life of approximately fifty years. In addition, some utilities expect that an insulator should support five times this load for at least one minute without failure.

(ii) *Rigging or Stringing Load:* This load is larger than the bare wire load, and is encountered during line maintenance. For instance, if one insulator is unloaded for inspection, the vertical loads would increase 1.5 times on the adjacent insulators. Furthermore, since human safety is involved, safety factors between 1.5 to 4.0 are attached to the stringing loads.

(iii) *Fatigue Loads:* These loads occur due to wind and aeolian vibrations in the conductor and tower.

(iv) *Maximum Ice and Wind Load:* This load is calculated from wind gusts ranging from 50 to 100 mph, and radial ice deposition on the conductor ranging from 24 to 45 mm in thickness. Design engineers require that an insulator should be capable of supporting this load continuously for one week without failure, at any time during its expected life.

In addition to the above parameters, dynamic load amplifications caused by seismic activity are frequently taken into consideration. To account for variations in insulator strengths, and the reduction in insulator strength with time, most utilities presently use stress reduction factors of ≈ 0.5 for axial tensile or compressive loads, and ≈ 0.4 for cantilever (bending) loads.[8]

1.3. INSULATOR RATINGS

Insulator ratings describe the maximum load that should be applied to an insulator in service. Rating tests are performed by either insulator manufacturers or utilities. These tests can be categorized as design tests, sample tests, and routine tests. Design tests are performed when design or material changes are introduced by a manufacturer, sample tests are performed on one insulator produced from each lot of a manufacturing schedule, and routine tests (or proof tests) are performed on each insulator. The methods to be used in rating insulators have been standardized by organizations such as the American National Standards Institute (ANSI), the International Electrotechnical Commission (IEC), the Institute of Electrical and Electronics Engineers (IEEE), and the Canadian Electrical Association (CEA). However, most of these standards require tests to be performed under static axial tensile loads only, while in service, composite insulators are subjected to multi-axial loads which include axial tension/compression, bending, and torsion. Furthermore, the loads applied in service are frequently cyclic in nature.

Since polymer matrix composites materials are microscopically heterogeneous materials, the strengths of composite insulators exhibit significant deviations. Therefore, utilities rely on statistical methods to evaluate the possibility of failures below the specified mechanical rating. This approach assumes that the standard deviations ($\bar{\sigma}$) of the strengths of insulators follow a Gaussian distribution about the mean strength ($\bar{x}$) obtained from several tests. Figure 1.5 shows a probability density function obtained from this assumption. The area under any section of the curve represents the probability of a composite insulator failing at a load above or below that range of standard deviations ($\bar{\sigma}$) from the mean strength ($\bar{x}$). The total area under the curve is 1.0. The probability of insulator failures in the range $\bar{x} \pm 1\,\bar{\sigma}$ is 68%, while the probability of failures in the range $\bar{x} \pm 3\,\bar{\sigma}$ is almost 100 %. Using this approach, in conjunction with experimental data provided by manufacturers, utility engineers can assess the reliability of a transmission line. For example, if sample tests show that n insulators in a batch of N are under the mean strength ($\bar{x}$) rated at $\bar{x} - 2\,\bar{\sigma}$, then the probability of failure of a transmission line with M insulators can be obtained as follows:

$$\text{Probability of an insulator failing below } \bar{x} = \frac{n}{N}$$

$$\text{Probability of an insulator not failing below } \bar{x} = 1 - \frac{n}{N}$$

$$\text{Probability that any insulator on the line will not fail} = \left(1 - \frac{n}{N}\right)^{M}$$

$$\text{Therefore, probability of transmission line failure} = 1 - \left(1 - \frac{n}{N}\right)^{M}$$

The mechanical rating of composite insulators consists of three components, namely; specified mechanical load tests, time-load tests, and routine tests.

1.3.1. Specified Mechanical Load Tests

The specified mechanical load (SML) test is a sample test performed on one insulator from each lot of a manufacturing schedule. At present, the SML rating is an ambiguous term since most manufacturers follow different methods to define the SML.

The standard procedure described by ANSI C29.11 [9] dictates that in order for a load to be termed as the SML load, an insulator should be able to withstand 75% of this load for 90 seconds without failure, and on further loading to 100% of the load, the insulator should fail instantly. [9] The main disadvantage associated with the ANSI definition of SML is that it does not specify the number of insulators to be tested, thereby ruling out a probabilistic analysis of failure. Furthermore, instead of the onset of intralaminar splitting in the composite rod, the term "failure" in the ANSI tests is usually considered as the macroscopic separation of the insulator into two or more pieces.

The IEC standard [10] definition of the SML rating is essentially the same. However, it does specify the number of insulators to be tested. For instance, in a manufacturing lot ranging from 300 to 2000 insulators, IEC recommends that SML tests be performed on at least 4 insulators. While this standard is more widely used, it does not require the manufacturers to report the mean strength $(\bar{x})$ and the standard deviations $(\bar{\sigma})$ associated with the SML tests.

There are several inadequacies which render the SML rating as an insufficient index to characterize the in-service capabilities of an insulator. Some of the problems associated with the SML rating are :

- Instead of testing complete insulator units with the end-fittings attached, some manufacturers report SML ratings obtained from the bare GRP rod. Since failure of the interface between the rod and end-fittings has been widely reported as a mode of failure,[6] results obtained from bare GRP rods may be misleading.
- Some manufacturers report the SML as the mean failure load $(\bar{x})$, while others include their own safety factors by reporting the SML as the mean failure load minus two or three standard deviations.
- The SML tests can characterize only short-term strengths of insulators. Unlike their porcelain counterparts, composite insulators have been known to loose their strength with time.[7, 11]

- The SML tests rate the performance of an insulator only in axial tension. In service, suspension insulators are also subjected to bending and torsional loads in both static and cyclic conditions. Furthermore, it appears that substation insulators are also rated by SML tests (performed under axial tension), whereas during service they are subjected mainly to axial compressive loads.

1.3.2. Load-Time Tests

Composite suspension insulators can fail at 50% of their SML rating if the load persists for several years, and 10% of their SML rating if the GRP rod is exposed to acid-rain and electrical partial discharge.[12, 13] The strength of the GRP rod has been reported to degrade linearly as a function of the logarithm of time.[7, 11] In order to provide an indication of the long-term strengths of insulators, manufacturers perform load-time tests on the GRP rod. Since the strength of an insulator after 50 years is of interest to utilities, the load-time tests are usually performed to determine the strength after 96 hours, and the data is extrapolated to 50 years by assuming a linear reduction in strength with the logarithm of time (see figure 1.6).

The ANSI C29.11 standard[9] requires three insulators to be continuously loaded at 60% of their SML rating for a period of 96 hours. If there are no failures, then the results can be interpreted as an 87.5% probability that the strengths of all insulators will exceed 60% of the SML after 96 hours. The IEC specification[10] of the load-time characteristics is essentially the same, with the exception that it requires the three insulators to be loaded at 70% of the SML for 96 hours. The rationale for this specification is that if the insulator strength versus log. time behavior is assumed to be linear, then the IEC specification ensures that the slope of the straight line is less than 8% of the SML.

Figure 1.6 shows that if the strength of the insulator is 60% of the SML after 96 hours (4 days), then by extrapolation, it is determined that the strength at the end of 50 years will be 40% of the SML. Therefore, most utilities design transmission lines such that the typical working load of an insulator is less than 40% of the SML, and the worst case of load amplification (*e.g.*, due to wind gusts, ice deposition, and seismic activity) will never exceed 60% of the SML rating. In spite of these precautions, composite insulators have been reported to fail in service. Some of the main problems associated with the load-time tests are :

- The tests are frequently performed on bare GRP rods, without the attached end-fittings. Since failure of the end-fittings and the rod-metal interfaces are likely to be time dependent phenomena, the test results can be misleading.
- The tests are performed under pure uniaxial tension, without considering the effects of axial compression (for substation insulators), bending (especially for line-post insulators), and torsion.
- The slope of the load-time line can be significantly larger in the presence of cyclic loads, corrosive environments, and internal partial discharge.

1.3.3. Proof or RTL Tests

Proof or routine test load (RTL) tests are performed on every insulator manufactured. The present practice is to apply an axial tensile load equivalent to 50% of the SML for a period of three seconds. This is simply a quality assurance test and does not provide any indication of the long-term performance of an insulator. In fact, the RTL test does not guarantee that an insulator can withstand the same load of 50% of SML again. In some cases, when RTL tests are repeated, insulators have been reported to fail at a load below 50% of the SML rating.[8]

1.4. FAILURE MODES

In the previous section, it was seen that there are several inadequacies in the methods presently being used to rate the mechanical performance of insulators. In the past decade, utilities have reported several "brittle failures" in composite suspension insulators. These failures, in conjunction with the lack of sufficient field experience, have significantly retarded the growth of the composite insulator market. In this section, some of the possible failure modes for composite insulators are described. It should be mentioned that electrical failures resulting in flashover of the insulators have also been widely reported. However, only mechanical failure modes will be described.

(i) Stress-Corrosion Cracking

The so-called *"brittle fracture"* mechanism of composite suspension insulators has been extensively studied by Kumosa and Qiu.[12, 13] These failures were reported to occur in suspension insulators based on the epoxy-cone design of end-fittings, at mechanical loads as low as 10% of the SML rating of the insulators. Kumosa et al. [12] reproduced the fracture surface morphology of the field-failed insulators in laboratory GRP specimens subjected to acidic environments, electrical discharge, and low tensile loads. Based on these studies, it was concluded that the brittle fracture process is essentially a stress-corrosion cracking (SCC) mechanism caused by moisture (or acid rain) ingress into the end-fittings.[12, 13] In this process, stress-corrosion cracks propagate perpendicular to the fibers by causing individual fiber failures. Since the crack-growth rate is extremely slow with very low mechanical loads involved, the fracture surface of the SCC failed GRP-rod is very smooth. Eventually, the remaining cross-sectional area of the GRP rod becomes too small, and results in brittle fracture with a brush-like fracture surface.

(ii) Intralaminar Failure of GRP rod

As mentioned earlier, composite suspension, line-post, and substation insulators can be subjected to bending and torsional loads during service. According to the beam theory of linear elastic bodies,[14] if the composite rod is subjected to bending loads, then one edge of the rod will experience axial tensile stresses, the opposite edge will experience axial compressive stresses, and the central axis of the rod will experience intralaminar shear stresses. If the external bending loads are excessive, then intralaminar shear failure of the rod can occur, resulting in axial splits within the rod. These splits will be very difficult to detect, and further loading of the insulator can result in brittle fracture.

Similarly, under torsional loads, the shear stresses will be maximum on the surface of the rod. [14] Under excessive torsional loading, intralaminar axial splits will develop on the external surface of the rod.

(iii) Crimping Damage

In the crimped end-fittings presently being use, large magnitudes of radial compression are applied to the rod via the end-fittings. In some cases wherein the SML rating of the insulator is required to be very large, and the radius of the GRP-rod is not sufficiently large, the crimping process can generate intralaminar compressive damage in the rod. This damage will exist in the form of multiple cracks in the compressed GRP-rod. When loaded in service, insulators with this type of internal damage might encounter failure either due to end-fitting slippage, propagation of the micro-cracks, or electrical discharge within the micro-cracks.[15, 16]

(iv) End-fitting Slippage

As mentioned above, excessive radial compression during crimping can result in internal damage to the GRP rod. On the other hand, if the radial compression applied during crimping is not sufficiently large, then the axial tensile or compressive forces applied during service can result in internal sliding of the rod withing the end-fittings. In suspension insulators, this type of failure at the GRP-metal interface can result in complete separation of the end-fittings from the rod. This situation is further aggravated by the fact that composite insulators are expected to be in service for a long period of time (≈ 50 years).

1.5. OBJECTIVE OF THIS STUDY

This study addresses the possibility of short-term mechanical failures of composite insulators. The goal of this study is to evaluate the maximum load bearing capacity of insulators subjected to a wide variety of multi-axial loads, and to evaluate the present design of crimped end-fittings in composite insulators.

In order to achieve this goal, comprehensive two- and three dimensional finite element analyses have been performed for composite insulators subjected to several cases of multi-axial loading conditions which are likely to be encountered in service, in conjunction with the residual compressive stresses generated due to crimping. Destructive mechanical tests have been performed to verify the finite element models under different modes of loading.

To evaluate the design of crimped end-fittings, compression profiles have been determined experimentally, and simulated using finite element models. Several design variables have been considered in order to optimize the internal stresses and axial loading capacity of composite insulators.

Since the GRP composite rod of insulators is subjected to a wide range of multi-axial loads during service, the intralaminar failure and fracture properties of unidirectional polymer matrix composite materials have been studied under a wide range of multi-axial loading conditions. These studies are based on experimental data and finite element simulations of the biaxial Iosipescu test method.

1.6. OUTLINE

Chapter 2 presents a detailed description of the analytical and experimental techniques employed in subsequent parts of this study. The experimental characterization of composite insulators is described in chapter 3. This includes non-destructive ultrasonic evaluation of the radial compression applied to the GRP rods, and the destructive mechanical tests performed on five substation insulators under axial compression, bending, and torsional loads. The axisymmetric and three-dimensional finite element models, the multi-axial loading conditions, and the experimental verification of the models is presented in chapter 4. Chapter 5 focuses on the application of the biaxial Iosipescu test method for characterizing the intralaminar failure and fracture properties of unidirectional composite materials, including the GRP composite used in insulator rods. An overall discussion of the computed internal stresses in the GRP rods is presented in chapter 6. Based upon the computed stresses and the experimental characterizations performed in chapters 3 and 5, the possible failure modes of insulators have also been outlined. In addition, a systematic parametric study is presented which evaluates the effects of the radius of the GRP rod, the magnitude of radial compression applied to an insulator rod during crimping, the shape of the radial compression profile, and the frictional properties of the GRP-metal interface, on the axial load bearing capacity and internal stresses of the GRP rods of insulators.

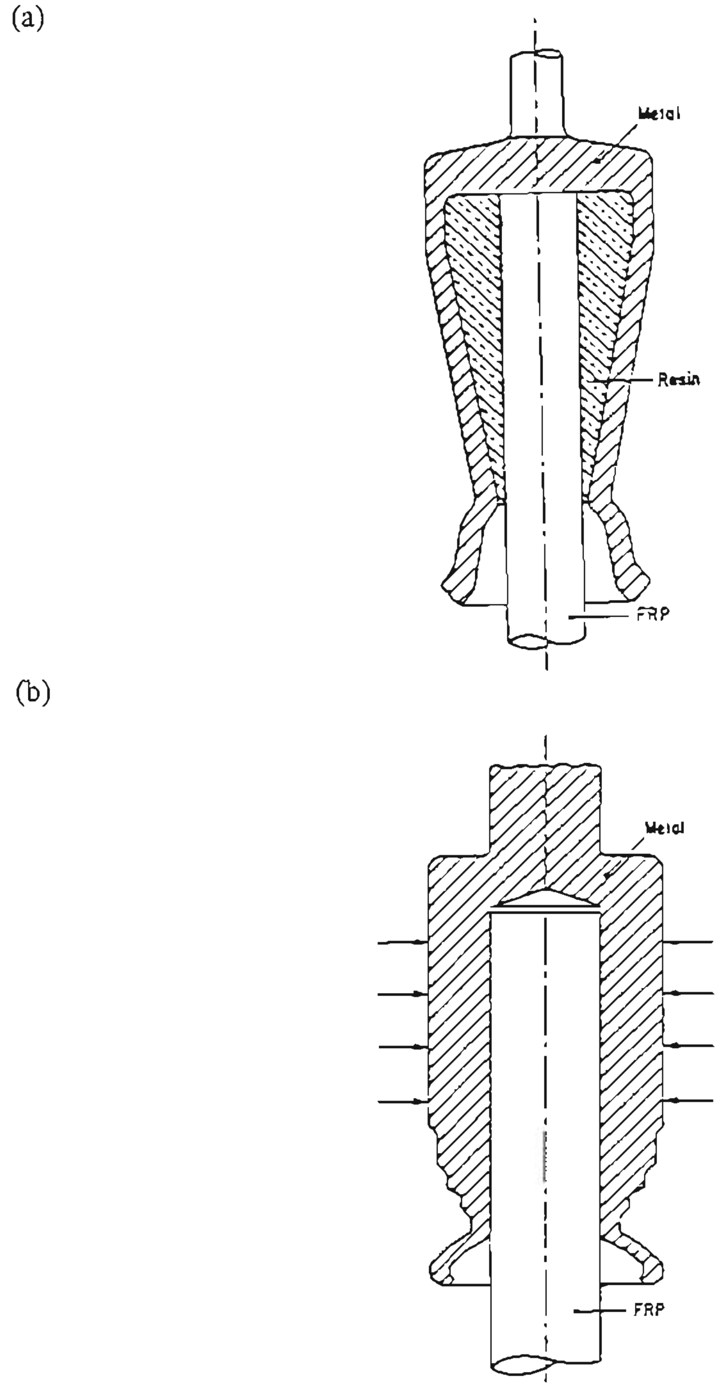

Figure 1.1 : End-fitting designs in composite suspension insulators;
(a) Epoxy cone design, and (b) Crimped design.

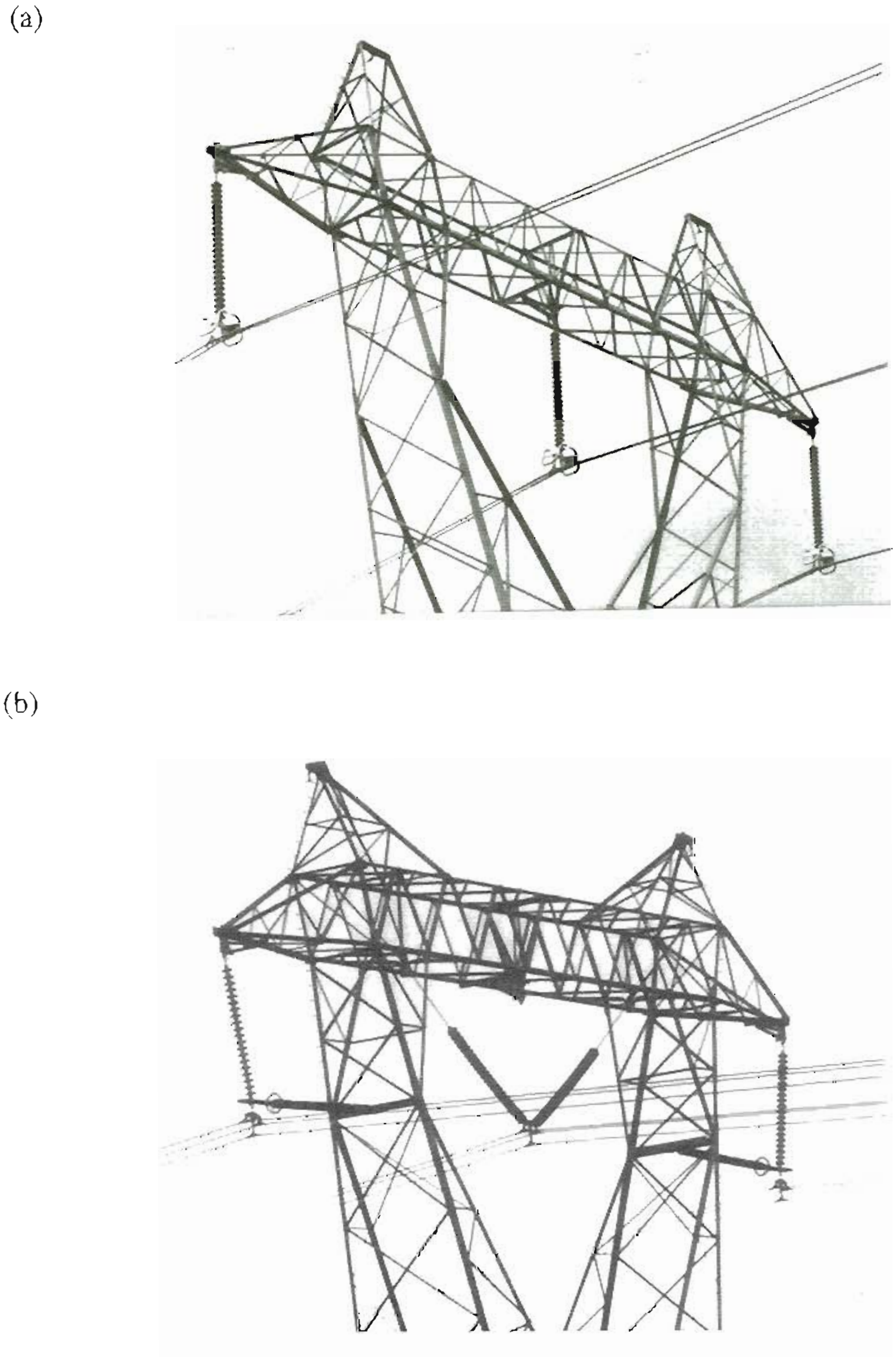

Figure 1.2 : Loading configurations of suspension insulators:
(a) I-string configuration, and (b) V-string configuration.

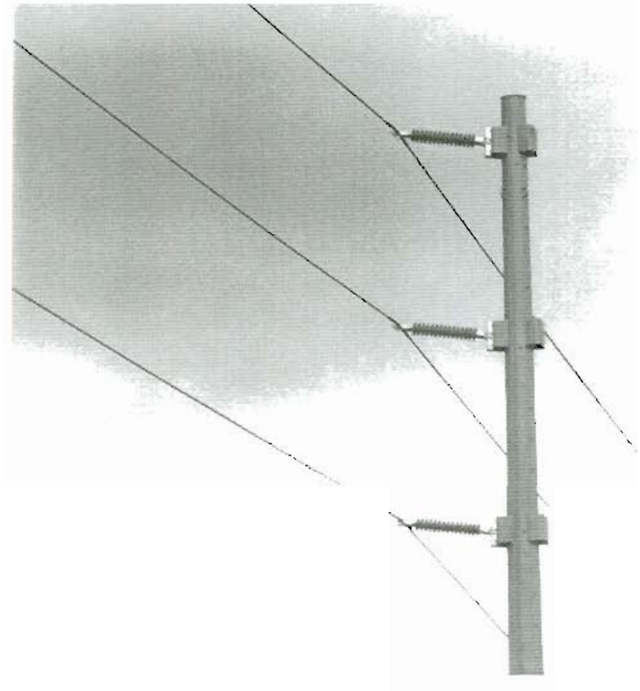

Figure 1.3 : Line-post composite insulator loaded in service.

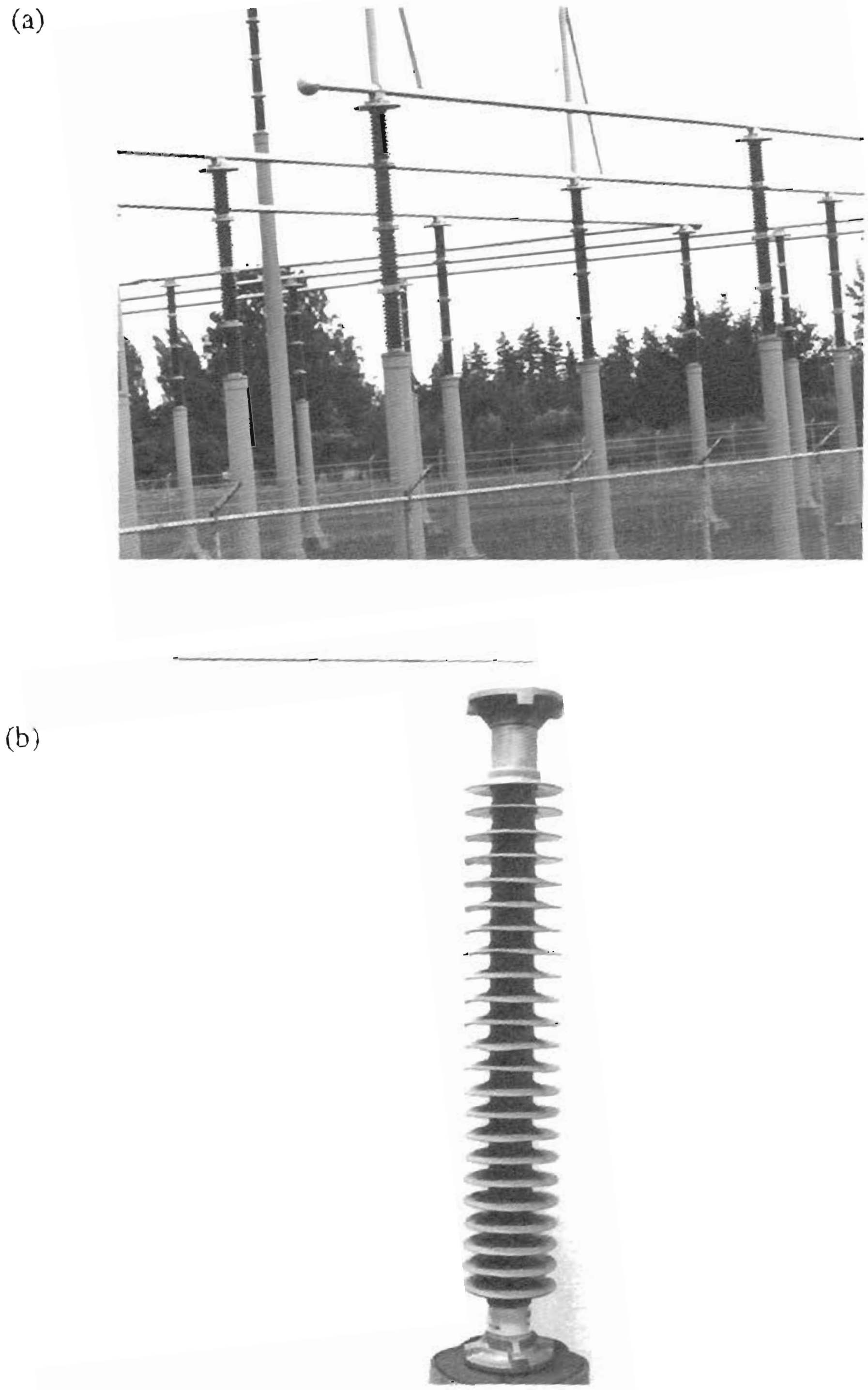

Figure 1.4 : Substation insulators: (a) Porcelain insulators in service, and (b) Typical 115 kV composite substation insulator.

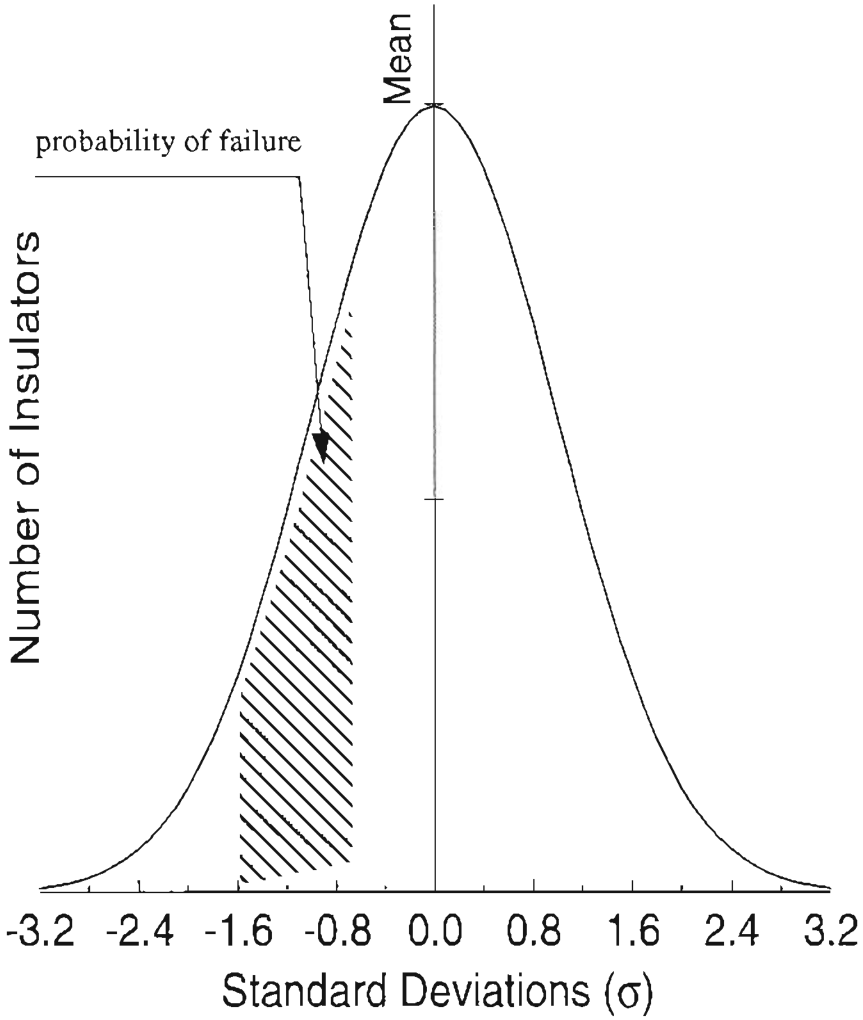

Figure 1.5 : Gaussian probability density function for insulator failures.

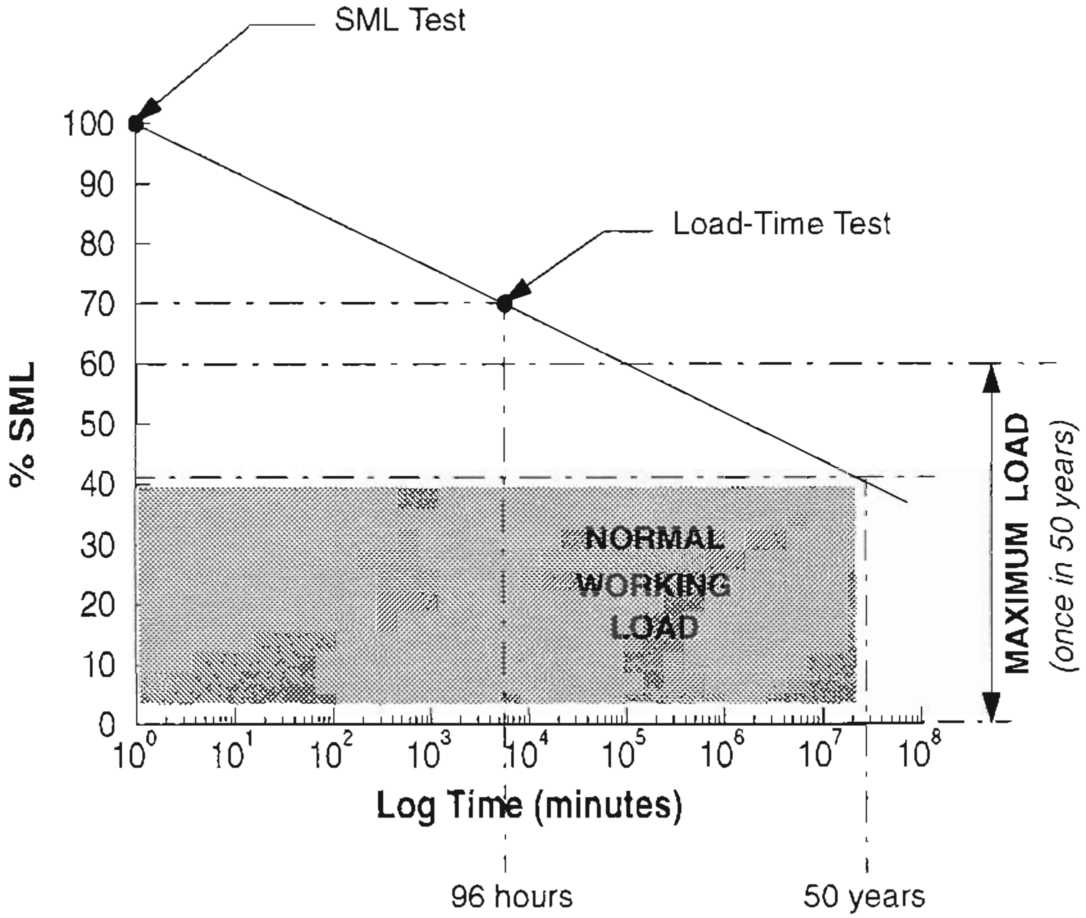

Figure 1.6 : Load-time characteristics of composite insulators relative to their SML rating.

Chapter 2

Background Information

This chapter describes the background, theory, and procedures for all the experimental and analytical techniques employed in subsequent chapters of this study. Since composite insulators rely on a unidirectional E-glass/epoxy composite rod as the primary structural component, a brief description of polymer matrix composites has been given, along with some presently available theories for estimating the elastic moduli and strengths of these materials. Since the GRP rod of the insulators is subjected to multi-axial loads during service, the biaxial Iosipescu test has been described as a means to experimentally measure the intralaminar failure strength of the GRP material. In addition, the application of the principles of linear fracture mechanics to unidirectional composites, and the currently available methods for evaluating the crack-tip fracture parameters are presented. According to the theory of linear elasticity, the stresses at the interface corner between the GRP rod and metal end-fittings may be singular in nature. Therefore, numerical techniques are described to evaluate the presence of singular stress fields. Finally, analytical and numerical methods are presented for the solution of general contact problems such as the mechanical contact between the GRP rod and end-fittings of composite insulators.

2.1. POLYMER MATRIX COMPOSITES

Polymer matrix composite (PMC) materials are a synergetic combination of a high stiffness reinforcing material with a ductile matrix, which leads to a high specific strength and stiffness in comparison with the unreinforced monolithic material. In the past two decades, the emphasis on light-weight structural materials has lead to a dramatic rise in the use of polymer matrix composite materials in the industry, particularly for aerospace, automobile, sporting goods, and electrical transmission applications. The impetus on the growth of structural PMCs has been complemented by the development of high-modulus and -strength fibers (*e.g.* graphite, glass, aramid, boron) which may be used to reinforce either thermosetting or thermoplastic resins. Thermosetting resins (*e.g.* epoxy, polyester, polyamides, phenolic) have a cross-linked molecular structure for high-temperature stability and strength. On the other hand, thermoplastic resins (*e.g.* polypropylene, nylon, polysulphone, polycarbonate, and polyether-ether-ketone) consist of monomer units which result in a high ductility and large creep relaxations at room temperature. Depending upon their geometry, fiber reinforced composite structures consist of either flat laminates, or are filament wound (for cylindrical structures *e.g.*, tubes, shafts, and pipes). Flat laminates consist of layers of laminae stacked in a predetermined sequence to achieve optimum properties and performance in service. The fibers within each lamina may be unidirectionally aligned, woven, or randomly distributed in two or three dimensions.[17, 18]

Due to the heterogeneity of their microstructure, polymer matrix composites are highly susceptible to premature failures by the initiation and propagation of intralaminar and interlaminar crack-like flaws. Intralaminar flaws exist within a lamina in the form of multiple microscopic debondings and matrix cracks. On the other hand, interlaminar flaws occur as delaminations along the free surface between adjacent laminae. In both cases, the micro-flaws can generate macroscopic splits under relatively low loads, resulting in a drastic reduction in the stiffness and strength of the material. Final catastrophic fracture of the composite structure occurs by the unstable growth of these splits under the combined influence of transverse tensile (mode I), in-plane shear (mode II), and anti-plane shear (mode III) stresses. Figure 2.1 shows the three fundamental modes of crack extension in composite laminae.

2.1.1. Constitutive Relations

In the generalized form, Hooke's law can be expressed as [17]

$$\sigma_i = \sum_{j=1}^{6} C_{ij}\varepsilon_j \quad (i, j = 1, 2, ...6) \tag{2-1}$$

where, σ_i are the stress components, ε_j are the strain components, and C_{ij} denotes the stiffness matrix. It can be shown that $C_{ij} = C_{ji}$.[17] In thin plates where a plane stress condition can be assumed (*i.e.*, $\sigma_3 = \tau_{23} = \tau_{31}$), equation 2-1 can be simplified to

$$\begin{bmatrix} \varepsilon_1 \\ \varepsilon_2 \\ \gamma_{12} \end{bmatrix} = \begin{bmatrix} a_{11} & a_{12} & a_{16} \\ a_{12} & a_{22} & a_{26} \\ a_{16} & a_{26} & a_{66} \end{bmatrix} \begin{bmatrix} \sigma_1 \\ \sigma_2 \\ \tau_{12} \end{bmatrix} \tag{2-2}$$

For unidirectional composite laminae, due to the orthotropy (or transverse isotropy) the compliance matrix $[A_{ij}]$ requires only four material constants (E_{11}, E_{22}, ν_{12}, and G_{12}) with[17, 19]

$$\begin{gathered} a_{11} = 1/E_{11};\ a_{22} = 1/E_{22};\ a_{12} = -\nu_{12}/E_{11} = -\nu_{21}/E_{22}; \\ a_{66} = 1/G_{12};\ \text{and}\ a_{16} = a_{26} = 0 \end{gathered} \tag{2-3}$$

It is customary to denote the direction parallel to the fibers as the 11 - direction, while the directions 22 and 33 are perpendicular to the fibers (*i.e.*, $E_{11} > E_{22}$).

For isotropic materials, determination of the matrix A_{ij} requires only three constants (E, ν, and G), and only two of these are independent with

$$a_{11} = a_{22} = 1/E; \; a_{12} = -\nu/E; \qquad (2\text{-}4)$$
$$a_{66} = 2\,(a_{11} - a_{12}) = 1/G; \text{ and } a_{16} = a_{26} = 0$$

for plane stress conditions.[17, 19]

2.1.2. Stiffness of Unidirectional Laminae

This section presents some simplistic analytical models that may be used to predict the elastic properties of unidirectional fiber reinforced composite laminae. These methods estimate the composite properties from the elastic properties of the constituent fibers and the matrix, the volume fraction (V_f) of fibers, and in some cases, the packing geometry of fibers.

(a) Rule of Mixtures:

The rule of mixtures assumes a perfect bond between fibers and the resin matrix. This assumption implies that the fibers and the matrix undergo the same amount of strain in the longitudinal direction (11-direction parallel to fibers), and they encounter the same stress in the transverse direction (22-direction perpendicular to fibers). The composite elastic moduli are given by

$$E_{11} = E_f\,V_f + E_m\,(1-V_f) \qquad (2\text{-}5a)$$

$$E_{22} = \frac{E_f\,E_m}{E_f\,(1-V_f) + E_m\,V_f} \qquad (2\text{-}5b)$$

and

$$\nu_{12} = \nu_f\,V_f + \nu_m\,(1-V_f) \qquad (2\text{-}5c)$$

where, E and ν are elastic properties of the constituents with subscripts f and m referring to the fiber and matrix respectively, and V_f is the volume fraction of fibers in the composite material.[17, 19]

(b) Halpin-Tsai Equations:

This method is more complex than the simple relationships of the rule of mixtures. In reference 19 a modified version of the Halpin-Tsai equations is given as

$$M = \frac{M_m (1 + \xi \eta V_f)}{(1 - \psi \eta V_f)} \tag{2-6a}$$

where,

$$\eta = \frac{(M_f/M_m) - 1}{(M_f/M_m) + \xi} \tag{2-6b}$$

M represents E_{22}, G_{12}, and ν_{23} for the composite, and M_f and M_m represent the corresponding elastic property of the fibers and matrix, respectively. ξ is an empirical parameter that depends on the extent of fiber reinforcement, packing geometry, and loading conditions, and ψ is a parameter that accounts for the maximum packing possible. The following expression is used to determine the value of ψ: [19]

$$\psi = 1 + \left[\frac{1 - V_{f,max}}{(V_{f,max})^2} \right] V_f \tag{2-6c}$$

where, $V_{f,max}$ is the theoretically maximum possible volume fraction of fibers. For a parallel hexagonal packing of fibers, $V_{f,max}$ is estimated to be 0.907. [19] Note that equation (2-6a) will be equivalent to the original Halpin-Tsai equation when ψ is taken as unity.

The main difficulty in using equations (2-6 a,b) is the appropriate choice of the value of ξ. Hull [17] suggests that a value of $\xi = 0.2$ will lead to accurate results in fibrous glass/polyester composites with a fiber volume fraction (V_f) of 50%. Whereas, both Krishnamachari [19] and Jones [20] state that $\xi = 2$ is a good choice for the estimation of E_{22} (assuming circular fibers in a square array), while for the estimation of G_{12} of composites with a fiber volume fraction greater than 50%, the parameter ξ may be determined from: [20]

$$\xi = 1 + 40\,(V_f)^{10} \tag{2-6d}$$

2.1.3. Strength of Unidirectional Laminae

Since the 1960s, several failure theories have been developed in the form of simple mathematical functions of the stresses and strengths. In order to accurately predict the strength of a composite structure, these mathematical functions must represent the onset of failures under all stress conditions. Most failure theories applied to polymer matrix composites (PMCs) are extensions of those developed for homogeneous isotropic materials.

Under multi-axial loads, the failure criteria are represented by a surface in six-dimensional space (*i.e.*, 3 normal- and 3 shear-strength axes). Azzi and Tsai[21] have proposed a generic failure theory which is applicable to unidirectional laminae, as well as laminates once the strengths of the individual laminae have been established. Tsai and Wu[22] subsequently developed a tensor-polynomial criterion which accounts for positive and negative stress components. For transversely isotropic thin shells loaded in plane-stress, the failure theory is represented by an ellipsoidal surface in three dimensional space by [21, 22]

$$\left[\frac{\sigma_{xx}}{\sigma^f_{xx}}\right]^2 - \left[\frac{\sigma_{xx}\,\sigma_{yy}}{(\sigma^f_{xx})^2}\right] + \left[\frac{\sigma_{yy}}{\sigma^f_{yy}}\right]^2 + \left[\frac{\tau_{xy}}{\tau^f_{xy}}\right]^2 = 1 \tag{2-7a}$$

where, σ^f_{xx} is the longitudinal tensile strength of the unidirectional composite, σ^f_{yy} is the transverse tensile strength, and τ^f_{xy} is the shear strength in the 1–2 plane. Note that for highly orthotropic laminae with $\sigma^f_{xx} >> \sigma^f_{yy}$, equation (2-7) reduces to an ellipse in two dimensional space.[17]

$$\left[\frac{\sigma_{yy}}{\sigma^f_{yy}}\right]^2 + \left[\frac{\tau_{xy}}{\tau^f_{xy}}\right]^2 = 1 \tag{2-7b}$$

This criterion will henceforth be referred to as the Tsai-Hill criterion. Owen et al.[23] and Found[24] have reviewed and extensively verified the existing failure criteria.

2.2. BIAXIAL TESTS FOR UNIDIRECTIONAL PMCs

In most engineering applications, unidirectional PMCs are subjected to multi-axial loads. Therefore, the need to obtain mechanical properties and failure envelopes under multi-axial stress conditions is evident. In the domain of biaxial stress states, the case of pure shear is the most difficult to generate. As a result, most of the presently available biaxial test methods are modifications of an existing shear test.

The application of a pure, uniform shear-stress state to unidirectional composite materials poses considerable difficulty due to the coupling between shear and normal loads at off-axis angles. Currently existing shear-test methods which may be applicable to unidirectional composites include[25]

(i) The torsion test of hoop-wound tubes,[23, 25-27]

(ii) The 10^0 Off-axis tension test,[28] and

(iii) The Iosipescu test.[29]

Other less popular shear test methods include the picture-frame test, the rail-shear test, [30] the ±45^0 Off-axis test, [28] the cross-beam sandwich test, and the slotted-tension test. However, most of these methods suffer from certain disadvantages ranging from a non-uniform shear stress distribution in the specimen gauge section, to difficulty and expense of specimen fabrication. [31] The rail-shear specimens have large shear-stress concentrations at the free edges. [30] The 10^0 Off-axis specimens suffer from end-constraint effects and out-of-plane bending. [28, 32] The torsion test of hoop-wound tubes is a reliable method, however, it requires cylindrical hoop-wound specimens and a complex testing rig. In an extensive evaluation of the existing shear-test methods, Lee and Munro 31 employed a decision analysis technique and rated the Iosipescu, and ±45^0 tests, to be most suitable for the in-plane shear characterization of unidirectional composites. Figure 2.2 schematically illustrates the specimen geometries and loading conditions of some of these tests.

Commonly used biaxial tests which are applicable to unidirectional composite materials include the off-axis tension test, [28] the cruciform test, the Arcan test, [33-35] the combined axial, radial, and torsional loading of thin-walled hoop-wound tubes, [23, 25] and the compact tension-shear test. [36]

Most of these methods suffer from the same limitations as their pure-shear counterparts. The off-axis tests are simple to conduct, but end-constraint effects, out-of-plane bending, and fiber misalignments can give inaccurate results. Arcan specimens have a complex geometry, and premature failure often occurs at the specimen-adherend interface. The cruciform and hoop-wound tubes are capable of generating reliable results, but specimen fabrication and testing are expensive. Furthermore, the filament winding technique required for fabrication of hoop-wound tubes could alter the material behavior in comparison with flat laminae.

An ideal shear or biaxial test for composite materials should employ small, easily fabricated specimens. It should impose a uniform stress field in the gauge-section, and should be applicable to unidirectional laminae, cross-ply or woven laminates, and sheet-molding compounds (SMCs). The Iosipescu shear test appears to meet most of these requirements. The method was originally proposed in 1967 for measuring shear properties of (isotropic) metals. [29] Adams and Walrath [37-41] have subsequently designed a modified fixture for shear testing of composite materials. Since then, a number of other investigators have used the method for testing a wide variety of materials ranging from unidirectionally reinforced fibrous composites, wood, and SMCs. [32, 42-52] Finite element methods have been employed to analyze the specimen with respect to the notch-angle, [39, 53-55] the notch-radius, [39, 56] and loading-conditions [39, 51, 52] Notably, Sukumar and Kumosa [53, 54] have employed the Finite Element Iterative Method to evaluate the notch-tip asymptotic singular fields as a function of the notch angle and orthotropy ratio. Ho and co-workers [52] performed non-linear analysis of the Iosipescu specimen by considering frictional sliding at the specimen-fixture interface, and a non-linear material behavior. Specimen fabrication techniques and test procedures have been optimized by Lee and Munro [48] in order to minimize experimental errors. In addition, Adams et al. [38] and Ifju[57] have independently developed modified shear-strain gauges for directly measuring the average shear strains in the specimen gauge-section.

Based on the Iosipescu test, a number of modified versions have also evolved. The antisymmetric four point bend test [58] employs similar specimens with a modified loading scheme, and has often been compared with the Iosipescu test. [42, 43, 46]

The Iosipescu shear test essentially consists of a double edge-notched beam specimen with two counteracting force couples applied such that the net bending moment at the specimen midlength is zero, and an almost pure uniform shear stress field is expected in the mid-section of the specimen (see figure 2.3). [29] Although the test method is currently most popular for shear characterization of composites, some drawbacks have been identified:

(i) Linear elastic finite element analyses performed by a number of researchers[39, 51, 56, 59] have shown that the stress distribution in the gauge-section of highly orthotropic specimens is not uniform. The shear stress distribution is dependent on the orthotropy ratio (E_{11}/E_{22}), fiber orientation, notch geometry, and loading boundary conditions. [59] Unidirectional composite specimens with fibers oriented along the specimen length (0^o specimens) have the maximum shear stresses at the notch tips and minimum shear stresses at the specimen center, while specimens with fibers oriented parallel to the notch-root axis (90^o specimens) have the maximum shear stress at the center and minimum shear stress at the notch tips. It is therefore necessary to apply correction factors to the measured shear modulus in order to account for the non-uniformity of stresses. [32] Sukumar and Kumosa[53, 54] employed the Finite Element Iterative Method (FEIM) to demonstrate that the stresses at the tip of a perfectly sharp notch in 0^o Iosipescu specimens are actually singular in nature. However, non-linear finite element analyses [52] indicate that at sufficiently large loads, the shear strains become concentrated at the notch tips, while the stresses are more or less uniform along the entire gauge length.

(ii) Unidirectional composite specimens with fibers aligned parallel to the notch-root axis (90^o specimens) have been shown to encounter premature failures away from the gauge-section. [44, 56] The 90^o specimens therefore indicate a significantly lower shear

strength in comparison with the 0^o specimens. Barnes et al. [44] have shown that this behavior results from the fact that 0^o Iosipescu shear specimens also have a significant component of transverse tensile stresses (σ_{xx}) in addition to the in-plane shear stresses (τ_{xy}) along the notch-root axis.

(iii) Out-of-plane twisting of the specimen can lead to inaccurate results. [48]

2.2.1. Biaxial Iosipescu Test

The biaxial Iosipescu test (BIT) fixture was developed at the University of Cambridge by Broughton, Kumosa, and Hull. [25,27] The fixture design is based upon the original Iosipescu shear test [29] and the Arcan in-plane stress method. [33] Figure 2.4 shows the universally adaptable fixture which is a modified version of the fixture originally designed at Cambridge. [25,27] It is capable of testing Iosipescu specimens in either pure shear or a combination of shear and transverse tensile or compressive stresses under either static or cyclic loads. Shear tests are performed under externally applied compressive loads P_0 normal to the longitudinal axis of the specimen like in the traditional test. For in-plane biaxial tests, the specimen is rotated in either a clockwise or counter-clockwise direction such that the compressive load P_α is applied at various angles α to the normal (see figure 2.5). Clockwise rotation of the specimen leads to a combination of shear and transverse tensile stresses along the notch-root axis, while counter-clockwise rotation leads to a combination of shear and transverse compressive stresses. As a convention, the loading angle α is taken to be negative for clockwise rotations (shear & tension) and positive for counter-clockwise rotations (shear & compression). From simple force and moment balance equations, the force couples P_1 and P_2 can be evaluated as [55, 56]

$$P_1 = \frac{P_\alpha}{\left[1 - \dfrac{b - h\tan\alpha}{a + h\tan\alpha}\right]} \quad \text{and} \quad P_2 = \frac{P_\alpha}{\left[\dfrac{a + h\tan\alpha}{b - h\tan\alpha} - 1\right]} \tag{2-8}$$

where P_α is the externally applied compressive load, h is the specimen width, a is the distance between outer load components P_2, b is the distance between inner load components P_1, and α is the loading angle. Additional details of the fixture can be found in the author's recent publications.[56, 60]

Broughton employed the BIT fixture for testing (isotropic) polycarbonate and unidirectional carbon/epoxy and carbon/PEEK specimens under various load orientations. [25] The failure modes observed in the biaxial tests were reported to be identical to the failures observed earlier in the traditional Iosipescu shear tests. Brittle isotropic materials fail by crack initiation at the notch tips, and propagation along the plane of the principal tensile stress (45^o for the shear test). 0^o specimens have been known to fail due to development of axial cracks nucleating at the notch tips, and propagating along the long axis of the specimen away from the nearest loading position. The axial splitting phenomenon was first reported by Adams et al., [38] who suggested that the development of axial cracks was, in fact, an effective way of relieving stress concentrations at the notch roots. Kumosa and Hull [59] and Sukumar and Kumosa [61] performed numerical analyses of the propagation of axial cracks in the 0^o specimens. They showed that the splits nucleate due to shear stress concentrations close to the notch tip and propagate under mixed modes (I and II), with mode I playing the dominant role for short crack lengths. Furthermore, it was shown that the 0^o specimens are more prone to failure under combined shear and tension, than under shear-compression loadings. Unidirectional composite specimens with 90^0 fibers invariably fail along the notch-root axis.

2.3. FRACTURE MECHANICS OF UNIDIRECTIONAL PMCs

Fracture mechanics is the study of failure phenomena of materials by stable or unstable crack extension. The theory of linear elastic fracture mechanics (LEFM) depends on crack tip parameters such as the stress intensity factors (SIFs) denoted by K_i, the strain energy release rates (SERRs) denoted by G_i, and the path independent J-integral [62] to predict the "equilibrium" of cracks at the onset of extension. Williams [63] has developed the stress and displacement solutions in the vicinity of a crack tip in isotropic bodies, wherein the stress intensity factors (K_i) can be used to describe the details of the near field variables. The crack-tip strain energy release rate (G_i) is however more commonly endorsed in fracture tests since it is a physically well defined quantity that can be measured experimentally. Irwin[64] has computed the elastic strain-energy release rates (G_i) associated with the three fundamental modes (i = I, II, III, see figure 2.1) of crack extension and related them to the stress intensity factors (K_i). For isotropic bodies

$$G_I = \frac{K_I^2}{\kappa E}, \quad \text{and} \quad G_{II} = \frac{K_{II}^2}{\kappa E} \tag{2-9}$$

where $\kappa = 1$ for plane stress, and $\kappa = 1/(1-\nu^2)$ for plane stress. Corresponding relations have been developed by Sih, Paris, and Irwin [64] for homogeneous orthotropic materials with cracks along the principal material directions

$$G_I = K_I^2 \left[\frac{a_{11} a_{22}}{2}\right]^{1/2} \left[\left[\frac{a_{22}}{a_{11}}\right]^{1/2} + \frac{2a_{12} + a_{66}}{2a_{11}}\right]^{1/2} \tag{2-10a}$$

and

$$G_{II} = K_{II}^2 \left[\frac{a_{11}}{\sqrt{2}}\right] \left[\left[\frac{a_{22}}{a_{11}}\right]^{1/2} + \frac{2a_{12} + a_{66}}{2a_{11}}\right]^{1/2} \tag{2-10b}$$

The principles of LEFM are based on the following assumptions which hold for homogeneous isotropic materials: [65]

(a) Crack extension is always self-similar.

(b) Crack-face displacements can be separated into three fundamental modes (I, II, and III) as shown in figure 2.1.

(c) The crack-tip stress distribution is independent of material properties, and exhibits a singularity of the order $r^{-1/2}$.

(d) Application of purely symmetric stresses results in pure mode I displacements. The same can be stated for mode II and III displacements.

Since unidirectional PMCs appear as macroscopically orthotropic and microscopically heterogeneous materials, great care is needed in extending LEFM to the fracture analysis of composites. [64-66] The elastic stress distribution in the vicinity of a crack tip for rectilinearly anisotropic bodies have been shown to exhibit a stress singularity of the order $r^{-1/2}$ by Sih et al.[64] However, unlike the isotropic case, these stresses are a function of the crack orientation (with respect to principal material directions) and material properties, and both crack-opening and -sliding displacements occur under pure mode I type loads. Furthermore, an arbitrarily inclined crack in unidirectional composites will always propagate along the fiber direction. These deviations limit the general application of LEFM to cracked anisotropic structures. However, Parhizgar and co-workers [65] have shown that in the special case of a crack aligned parallel to the fibers in a unidirectional composite material, the aligned fibers ensure macroscopically self-similar crack extension since the fracture toughness is lowest in this direction. In addition, the stresses are independent of the principal material directions, and the equations of Sih et al.[64] indicate that the crack-face displacements are not mixed-mode in nature under a single fundamental mode of loading. It has therefore been concluded that LEFM is applicable to unidirectional PMCs for the special case of cracks along the fiber direction. [64-66] From a practical standpoint, this particular case holds greatest relevance since unidirectional PMCs are highly susceptible to intralaminar flaws created either during manufacturing or in service.

2.3.1. Evaluation of Fracture Parameters

Currently available techniques for extracting fracture parameters (G_i) and (K_i) in unidirectional PMCs can be broadly classified into three categories.

2.3.1.1. Analytical Methods

Closed-form analytical expressions are the most preferred approach for crack-tip fracture parameter measurement. For instance, the beam-theory solutions proposed by J. G. Williams [67-69] can predict crack-tip strain energy release rates (G) in cracked orthotropic beams. The approach has frequently been applied to popular mode I, mode II, and mixed-mode problems. For instance, Williams [67-69] has applied the method to cracked double cantilever beam (DCB) specimens, Sukumar and Kumosa [61] used the approach for evaluating G values in biaxially loaded 0^o Iosipescu specimens with axial splits, and Gillespie et al.[70] applied the beam solutions to mode II end-notched flexure (ENF) specimens. However, most existing analytical solutions tend to make highly simplistic assumptions and are not easily available for orthotropic materials, complex domains, and combined loads.

2.3.1.2. Experimental Compliance Calibration

The compliance calibration method is the most widely used experimental technique for determining the total energy release rate (G). By definition

$$G = \frac{P^2}{2B}\left[\frac{dC}{da}\right] \tag{2-11}$$

where, P is the external load applied to a specimen, B is the thickness of the cracked gauge-section, C is the load-point compliance of the specimen, and a is the crack length. The test procedure involves mechanical loading of specimens with a growing crack to determine the compliance as a function of the crack length. The critical energy release rate (G_c) is subsequently determined from equation (2-11). Slepetz and Carlson [71] have used this method for measuring the mode I fracture toughness of S-glass/epoxy and graphite/epoxy compact tension specimens. Williams and Birch [72] have used compliance calibration for evaluating mixed-mode fracture properties ($K_{I,II}$) in wood specimens. In some studies, the finite element method has also been employed to determine the compliance numerically.[70,71,73] The main disadvantage of the compliance calibration method is that it is highly prone to experimental errors caused by fiber bridging between the crack faces [71] and large deformation of the specimen. Furthermore, equation (2-11) cannot be used to partition the energy release rates into mode I and mode II components.

2.3.1.3. Finite Element Methods

In the past two decades, the finite element method has become an important tool in fracture mechanics. Although numerical results are usually more difficult to interpret, the method imposes fewer limitations on the complexity of the problem (regarding boundary conditions, specimen geometry, and anisotropy). Various direct and indirect numerical schemes employing distorted singular crack-tip elements (*e.g.* isoparametric elements with mid-side nodes moved to the quarter position), [74, 75] or conventional non-singular elements have been proposed for extracting the fracture parameters. [76-84] Direct methods are used to extract SIFs by extrapolation of a displacement or stress parameter to the crack tip, [76] while indirect methods are used to compute energy parameters like strain energy release rates (G_i),[77-82, 85, 86] J-integrals, [62] which can be related to the stress intensity factor. In the following subsections, the principles and important equations of the displacement correlation, displacement extrapolation, and virtual crack closure techniques have been outlined.

2.3.1.3.1. Displacement Correlation Method

With reference to figure 2.6, using singular isoparametric elements with mid-side nodes moved to the quarter position, [74, 75] displacements along the crack face (ABC) are given by

$$u_y = (4u_{By} - u_{Cy})\sqrt{r/L} + (-4u_{By} + 2u_{Cy})(r/L) \qquad \textit{(for pure mode I)} \qquad \text{(2-12a)}$$

and

$$u_x = (4u_{Bx} - u_{Cx})\sqrt{r/L} + (-4u_{Bx} + 2u_{Cx})(r/L) \qquad \textit{(for pure mode II)} \qquad \text{(2-12b)}$$

Shih et al.[83] have computed SIFs $K_{I,II}$ by correlating the $\sqrt{r}$ term of equations (2-12 a,b) with the crack-field displacement solution along the crack face ($\theta = \pi$) given by Williams [63] for isotropic bodies. Saouma & Sikiotis [87] and Boone et al. [88] have subsequently extended this correlation approach to two- and three dimensional orthotropic fracture analysis. The displacement eigenfunction expansions for cracked orthotropic structures have been given by Sih, Paris, and Irwin.[64] If we consider cracks parallel to a principal material direction, on correlating the $\sqrt{r}$ term of the expansion with equations (2-12 a,b), the equations for the mode I and II stress intensity factors are obtained as[55, 59, 61, 87, 88]

$$K_I = \sqrt{\frac{\pi}{2}} \frac{\mu_1 \mu_2}{a_{22} (\mu_1 + \mu_2)} \left[\frac{4u_{By} - u_{Cy}}{\sqrt{L}} \right] \qquad (2\text{-}13a)$$

and

$$K_{II} = \sqrt{\frac{\pi}{2}} \frac{1}{a_{11} (\mu_1 + \mu_2)} \left[\frac{4u_{Bx} - u_{Cx}}{\sqrt{L}} \right] \qquad (2\text{-}13b)$$

where μ_1 and μ_2 are imaginary roots of the characteristic equation,[64] and always occur in conjugate pairs as μ_1, $\bar{\mu}_1$, μ_2, and $\bar{\mu}_2$:

$$a_{11} \mu^4 - 2 a_{16} \mu^3 + (2a_{12} + a_{66}) \mu^2 - 2 a_{26} \mu + a_{22} = 0 \qquad (2\text{-}14)$$

a_{ij} are the anisotropic compliances which can be calculated from the elastic properties of the orthotropic material (refer Section 2.1.1). In equation (2-13 a,b), $u_{By,x}$ and $u_{Cy,x}$ are the relative opening and sliding displacements at nodes B and C with respect to the crack tip node (see figure 2.6).

2.3.1.3.2. Displacement Extrapolation Method

Chan et al.[76] have suggested the method of displacement/stress extrapolation which is conceptually similar to the displacement correlation scheme. Quarter-point elements [74, 75] are preferred at the crack tip. Crack-opening and -sliding displacements are extracted for nodes along the crack face ($\theta = \pi$, found to yield most accurate results by Chan et al.[76]). These displacements are scaled by a factor of $r^{-/2}$, and a linear regression analysis is performed from the crack-tip element corner node to a distance (r), beyond which the crack-face displacement solutions are invalid. The best fit straight line, extrapolated to the crack tip (r=0), yields the displacement parameters u_y^* and u_x^* associated with the crack-opening and -sliding profiles respectively. Finally, by substituting the terms $4u_{By} - u_{Cy}/\sqrt{L}$ and $4u_{Bx} - u_{Cx}/\sqrt{L}$ in equations (2-13 a,b) by u_y^* and u_x^* respectively, $K_{I,II}$ and thereafter energy release rates $G_{I,II}$ can be computed.

2.3.1.3.3. *Virtual Crack Closure Method*

The Virtual Crack Closure (VCC) scheme is based upon Irwin's contention that the work required to open a crack by an infinitesimal length is equal to the work required to close the crack back to its original length.[64] Referring to the notation in figure 2.7 for a crack extending from a length of a to $a + \Delta a$, the crack opening (or closure) work, and subsequently the crack tip energy release rates were obtained in the integral form as [64]

$$G_I(a) = \lim_{\Delta a \to 0} \frac{1}{2\Delta a} \int_{x=0}^{x=\Delta a} \sigma_y(r=x,\ \theta=0,\ a)\ u_y(r=\Delta a - x,\ \theta=\pi,\ a+\Delta a)\ dx, \qquad \text{(2-15a)}$$

and

$$G_{II}(a) = \lim_{\Delta a \to 0} \frac{1}{2\Delta a} \int_{x=0}^{x=\Delta a} \tau_{xy}(r=x,\ \theta=0,\ a)\ u_x(r=\Delta a - x,\ \theta=\pi, a+\Delta a)\ dx, \qquad \text{(2-15b)}$$

where, σ_y and τ_{xy} are the normal and shear stresses ahead of the tip of the original crack, and $u_{y,x}$ are relative opening and sliding displacements behind the tip of the extended crack.

Rybicki and Kanninen [80] proposed a finite element idealization of equations (2-15 a,b) employing 4-noded quadrilateral elements. Subsequently, the approach has been extended to higher order singular and non-singular elements. [73, 81, 82, 84, 85, 89-91] According to O'Brien [91] using ordinary non-singular linear strain elements at the crack tip (refer figures 2.8 a,b), the equations (2-15 a,b) may be represented as

$$G_I(a) = \frac{1}{2L\,t}\left[F_{y,i}(a)\,\Delta u_{y,j-2}\,(a+\Delta a) + F_{y,i+1}(a)\,\Delta u_{y,j-1}\,(a+\Delta a)\right] \qquad (2\text{-}16a)$$

and

$$G_{II}(a) = \frac{1}{2L\,t}\left[F_{x,i}(a)\,\Delta u_{x,j-2}\,(a+\Delta a) + F_{x,i+1}(a)\,\Delta u_{x,j-1}\,(a+\Delta a)\right] \qquad (2\text{-}16b)$$

where, $F_{x,y}$ represent the nodal reaction forces, i, j represent the node locations as indicated in figures 2.8 (a,b), and t is the thickness of the specimen. This method, henceforth referred to as the VCC-2c method, requires two calculations to be performed for crack lengths a and $a+\Delta a$ in order to extract energy release rates $G_{I,II}(a)$.

In order to avoid the disadvantage of two finite element computations, the following formulae proposed for the non-singular linear strain element discretization (refer figure 2.8 a) require a single analysis to extract the G-values:[81, 82, 85, 89, 90]

$$G_I(a) = \lim_{\Delta a \to 0} \frac{1}{2L\,t}\left[F_{y,i}(a)\,\Delta u_{y,i-2}\,(a) + F_{y,i+1}(a)\,\Delta u_{y,i-1}\,(a)\right] \qquad (2\text{-}17a)$$

and

$$G_{II}(a) = \lim_{\Delta a \to 0} \frac{1}{2Lt}\left[F_{x,i}(a)\,\Delta u_{x,i-2}\,(a) + F_{x,i+1}(a)\,\Delta u_{x,i-1}\,(a)\right] \qquad (2\text{-}17b)$$

This scheme is henceforth referred to as the modified crack closure integral (MCCI), or the VCC-1c method. It should be noted that as opposed to the VCC-2c scheme (equations 2-16), the above formulation is exact only for infinitesimal crack extensions (*i.e.*, lim $\Delta a \to 0$). In the case of conventional constant strain elements, the above equations are simplified to [82]

$$G_I(a) = \lim_{\Delta a \to 0} \frac{1}{2L\,t}\left[F_{y,i}(a)\,\Delta u_{y,i-1}\,(a),\right] \qquad (2\text{-}18a)$$

and

$$G_{II}(a) = \lim_{\Delta a \to 0} \frac{1}{2Lt}\left[F_{x,i}(a)\,\Delta u_{x,i-1}\,(a)\right] \qquad (2\text{-}18b)$$

In comparison with other indirect methods, [62, 77-79] the VCC methods are particularly attractive since they permit calculation of individual mode partitions G_I and G_{II} in mixed-mode problems. Furthermore, excessive mesh refinement and the use of singular crack-tip elements is not required to obtain accurate results.

2.3.2. Mixed-mode Fracture Criteria

For a given intralaminar defect in a unidirectional composite, crack extension may be accomplished in pure mode I (opening), mode II (shearing), mode III (tearing), and mixed-mode conditions. It is therefore necessary to develop fracture criteria and test methods for measuring the critical fracture parameters which describe the single and mixed-mode fracture behavior. The mixed-mode fracture criteria are developed in the form of mathematical functions of the stress intensity factors and fractures toughnesses under a combination of the fundamental modes of loading.

A number of generic mixed-mode fracture criteria have been proposed to describe the influence of loading modes (I and II) on the intralaminar and interlaminar fracture of composites. Wu performed mixed-mode fracture experiments on balsa-wood and glass/epoxy composites to determine an empirical criterion of the form [66]

$$\left[\frac{K_I}{K_{Ic}}\right] + \left[\frac{K_{II}}{K_{IIc}}\right]^2 = 1 \tag{2-19}$$

This criterion was later verified by McKinney[92] from tests conducted on unidirectional graphite/epoxy composites. Jurf et al.[93] and Russell et al. [94] were however in agreement on the criterion

$$\left[\frac{K_I}{K_{Ic}}\right]^2 + \left[\frac{K_{II}}{K_{IIc}}\right]^2 = 1 \tag{2-20}$$

The most general mixed-mode fracture criterion was proposed by Hahn. [95] This criterion was derived from the energy balance principle which states that fracture occurs when the crack tip energy release rate reaches a critical value *(i.e.,* $G_{total} = G_c$). If macroscopic self-similar crack extension is assured, and the conditions for application of LEFM hold, then G_{total} can be calculated from the elasticity theory. Microscopically, however, the critical fracture energy G_c depends very much on the localized morphology of fracture, which in turn depends critically on the mode of loading (K_I and K_{II}). [96] The following criterion describing the dependence of G_c on K_I and K_{II} was obtained by Hahn [95]

$$g\left[\frac{K_I}{K_{Ic}}\right]^2 + (1-g)\left[\frac{K_I}{K_{Ic}}\right] + \left[\frac{K_{II}}{K_{IIc}}\right]^2 = 1 \tag{2-21}$$

where, $g = G_{Ic}/G_{IIc}$. Note that if the fracture energy is independent of the loading mode, *i.e.,* $G_{Ic} = G_{IIc}$, then equation (2-21) reduces to equation (2-20). Whereas, if $G_{Ic} \ll G_{IIc}$, then equation (2-21) reduces to equation (2-19).

2.4. ANALYSIS OF SINGULAR STRESSES

Within the framework of linear elastic fracture mechanics (LEFM), several studies have demonstrated that the stress field in the vicinity of abrupt geometric discontinuities (*e.g.*, cracks, sharp notches, re-entrant corners) and abrupt material discontinuities (*e.g.*, bimaterial interface corners of perfectly bonded dissimilar elastic bodies) could be singular in nature. [97-99] The following sections briefly outline three approaches for evaluating singular stress fields.

2.4.1. Airy Stress Function Approach

Williams proposed the Airy stress function solution for the stress singularities in the vicinity of a sharp notch embedded in an isotropic body under extension.[97] Hein and Erdogan,[100] Bogy and Wang,[98, 99] and more recently Ding et al.[101, 102] have employed the Airy stress function formulation to obtain closed-form analytical solutions for the interface corner singularity in isotropic-isotropic bimaterial wedge corners.

The approach consists of selecting an Airy stress function (ψ) which satisfies the biharmonic equation in polar coordinates[97]

$$\nabla^4 \psi = 0 \tag{2-22}$$

where,

$$\nabla^2 = \frac{\partial^2}{\partial r^2} + \frac{1}{r}\frac{\partial}{\partial r} + \frac{1}{r^2}\frac{\partial^2}{\partial \theta^2}$$

The stresses can be written in terms of the Airy stress function by the relations given by

$$\sigma_r = \frac{1}{r^2}\frac{\partial^2 \psi}{\partial \theta^2} + \frac{1}{r}\frac{\partial \psi}{\partial r} \tag{2-23a}$$

$$\sigma_\theta = \frac{\partial^2 \psi}{\partial r^2} \tag{2-23b}$$

and

$$\tau_{r\theta} = \frac{1}{r}\frac{\partial^2 \psi}{\partial r \, \partial \theta} + \frac{1}{r^2}\frac{\partial \psi}{\partial \theta} \tag{2-23c}$$

Using these equations in conjunction with the appropriate boundary conditions, solutions for isotropic sharp notches,[53, 97] and isotropic-isotropic bimaterial wedge corners[98-102] are available in the literature. Unfortunately, such closed-form solutions are not easily available for orthotropic notches subjected to mixed-mode loads, and isotropic-orthotropic bimaterial wedge problems. Therefore, numerical solutions using the Finite Element Method, and the Finite Element Iterative Method must be sought.

2.4.2. Finite Element Method

Raju and Crews [103] have used the conventional finite element method (FEM) to evaluate singularities at the free edge in cross-ply composite laminates. Ding and Kumosa [101] have employed the method to analyze adhesive interface corners. The stress along a radial line from the origin of the singularity ($r = 0$) can be expressed as [97]

$$\sigma_{ij} = A_1\, r^{-\lambda} + O(r^{-\lambda+1}) \qquad (2\text{-}24)$$

where, r is the radial distance from the singularity, A_1 is a constant, λ is the power of the singular field, and $O(r^{-\lambda+1})$ represents terms of the order $r^{-\lambda+1}$ and higher. In the vicinity of the singular zone, the higher order terms may be neglected and equation (2-24) may be expressed as [103]

$$\log \sigma_{ij} = (-\lambda) \log r + \log A_1 \qquad (2\text{-}25)$$

hence, a $\log \sigma_{ij}$ versus $\log r$ plot is obtained from the finite element analysis in order to compute the singular power (λ). This method is, however, highly mesh sensitive. It requires a very dense mesh near the expected origin of the singularity, and can give only approximate values for the power of the singular field. [101]

2.4.3. Finite Element Iterative Method

The Finite Element Iterative Method (FEIM) was developed by R. S. Barsoum [104-108] to evaluate asymptotic singular stress fields in elastic media, by making use of general purpose finite element codes. This approach has been adopted by researchers to analyze singular stress fields arising in cracks and sharp notches,[53,55] bimaterial interface corners,[101,102] and interfacial cracks,[106] in both isotropic and anisotropic elastic media. Barsoum and Chen[108] have also extended the approach to three dimensional interface surface cracks. Reference 105 discusses the theoretical basis and convergence of the FEIM procedure.

The following steps are involved in the iterative solution procedure:

(i) A fan shaped mesh is constructed around the origin of the singularity as shown in figure 2.9. Since the power of the singular field (λ) is not known *a priori*, ordinary eight-noded quadrilateral and six-noded triangular isoparametric elements are used. The mesh is made incrementally dense near the origin of the singularity, with several rings of elements in the radial (r) direction, and several rays in the tangential (θ) direction.

(ii) Displacement vectors $Ux_i^{(0)}$ and $Uy_i^{(0)}$ are prescribed at nodes along the outer ring (R_{out}) for the initial iteration. Recent studies have shown that the value of the singular power is independent of the far-field boundary conditions $Ux_i^{(0)}$ and $Uy_i^{(0)}$.[55] Therefore, the displacement vectors may be arbitrary, provided that they simulate the appropriate mode of loading (*i.e.*, pure mode I, pure mode II, or mixed-mode).

(iii) A finite element analysis is performed. For a particular ray (θ), the singular power is obtained by a linear regression analysis of the relationship

$$\sigma_{ij} = K\, r^{-\lambda}\, f_{ij}(\theta) \tag{2-26}$$

plotted on a log-log scale. Most studies consider the von-Mises equivalent stress for the analysis,[53,55,101,102] and the value of λ is computed independently from each ray of the fan-shaped mesh.

(iv) In order to eliminate rigid body displacements, the displacement obtained at the origin of singularity ($U_o^{(0)}$) is subtracted from the displacement vector obtained at the inner ring (R_{in}). For the next iteration, this displacement vector is prescribed at the outer ring (R_{out}) after scaling it up according to

$$U_{R,out}^{(1)} = \Lambda^{(0)} \cdot (U_{R,in}^{(0)} - U_o^{(0)}) \tag{2-27}$$

where, $\Lambda^{(0)}$ is a scalar multiplier for normalizing the inner-ring displacements. Barsoum has suggested that the scalar multiplier be evaluated as[104]

$$\Lambda^{(0)} = \left[\frac{R_{out}}{R_{in}}\right]^{1-\lambda^{(0)}} \tag{2-28}$$

(v) The steps (iii) and (iv) are repeated several times until the value of λ, along all rays in the fan-shaped mesh, converge in accordance with a predefined criterion. Usually, the convergence is set in the range[53,101]

$$\left|\frac{\lambda_i^{(m+1)} - \lambda_i^{(m)}}{\lambda_i^{(m+1)}}\right| \leq 10^{-5} \ \ to \ \ 10^{-4} \tag{2-29}$$

where, m indicates the iteration number, and i indicates the ray number (i = 1, 2, ...25 in figure 2.9).

A more detailed description of the theory of the FEIM and its application can be found elsewhere.[55,101,102,105]

2.5. GENERAL CONTACT ANALYSIS

The term *contact analysis* refers to analytical or numerical solutions for the size and geometry of the area of contact, the stresses, and the displacements involved when two or more deformable bodies contact each other under the influence of external tractions. This section outlines some of the analytical and numerical methods available for such analyses.

2.5.1. Analytical Solutions

The most widely used analytical solutions for contact of elastic bodies is based on the solution of Hertz given by Timoshenko et al.[14] and Johnson. [109] The solution is applicable for contact of non-conforming spherical elastic bodies. The essential assumptions of the analysis are that the area of contact is either circular or elliptical, with an effective radius (R) which is much smaller in comparison with the radii of the contacting bodies. Furthermore, the analysis assumes frictionless contact.

Figure 2.10 shows two spheres of radii (R_1 and R_2) much larger than the radius (a) of the circular contact patch created under a normal traction of P. The Hertz theory predicts the size of the contact patch as [14, 109]

$$a = \left[\frac{3PR}{4\bar{E}}\right]^{1/3} \tag{2-30}$$

where,

$$\frac{1}{\bar{E}} = \frac{(1-\nu_1^2)}{E_1} + \frac{(1-\nu_2^2)}{E_2}$$

and

$$\frac{1}{R} = \frac{1}{R_1} + \frac{1}{R_2}$$

The maximum contact pressure (p_o) is given by

$$p_o = \frac{3P}{2\pi a^2} = \left[\frac{6P\bar{E}^2}{\pi^3 R^2}\right]^{1/3} \tag{2-31}$$

Another approach is based on the potential functions of Boussinesq and Cerruti given by Love.[110] This solution can be used to determine stresses and displacements in an elastic half-space bounded by a plane surface, with or without tangential tractions caused by friction at the plane surface. The main disadvantage of the Boussinesq and Cerruti methods is that it requires the surface normal and tangential tractions, and the precise area of the contact patch to be known *a priori*. Furthermore, it assumes that the surface of contact is completely planar.

In summary, it appears that the analytical solutions presently available in the literature may not be applicable to *general contact* problems, where the shape and size of the contact area, and the tractions acting at the contact interface are not known in advance. In addition, most of the existing analytical solutions are not applicable to the analysis of anisotropic elastic bodies with interface friction, and without any restrictions on the shape and size of the contact area. For such cases, numerical solutions can be obtained by using the Finite Element Method.

2.5.2. Finite Element Method

The degrees of freedom of ordinary constant strain or linear strain elements used in finite element analysis can only be constrained explicitly in the model. Much of the difficulty in applying the Finite Element Method to general contact problems stems from the fact that the precise nodes of contact are not known *a priori*, thereby requiring special numerical algorithms to prevent geometric incompatibilities such as the interpenetration of one body into another. In the past two decades, several numerical algorithms have been proposed to solve such problems.[111-118] Wilson et al.,[111] proposed the method of differential displacements for frictionless contact problems, while Chan et al.,[112, 113] and Bathe and Chaudhary[116] proposed the most general iterative solution procedure for contact problems with consideration of Coulomb friction.

The general contact analysis in the ANSYS finite element code[119] is structurally nonlinear, and therefore requires an iterative solution procedure based either on the full- or partial Newton-Raphson method. The nonlinearity stems from the fact that the algorithm assumes no prior knowledge of the area of contact, and the local contact conditions (*i.e.*, sticking, sliding, or open gap conditions). The capabilities of the general surface to surface contact elements (CONTAC48 and CONTAC49) available in ANSYS include static or dynamic analyses, frictional or frictionless contact, and flexible-flexible or rigid-flexible contact problems with large permissible sliding between the contacting bodies. The procedure requires one body to be defined as the target body (preferably stationary) and the other body to be defined as the contact body (preferably moving towards the target surface).

With reference to figure 2.11, precise kinematic tracking of the contact node K (on the surface of the contact body) is required to establish the contact conditions with respect to a segment IJ (on the target surface). Over each iteration, the normal gap (g) and the tangential projection (s^*) is computed. If $g > 0$, then an open-gap condition is assumed and the contact surface is set traction free. On the other hand, $g \leq 0$ implies an interpenetration of the contacting surfaces. Since this is a violation of geometric compatibility, normal contact forces f_n are developed at the node K, with equal and opposite contact forces acting on the segment IJ. This force f_n will simply minimize the interpenetration to an acceptable numerical value. Using a penalty method, [119] the contact forces are prescribed as:

$$f_n = \begin{cases} K_n\, g & \text{if } g \le 0 \quad (\textit{contact penetration}) \\ 0 & \text{if } g > 0 \quad (\textit{open gap}) \end{cases} \tag{2-32}$$

where, K_n is a user-defined normal stiffness of the contact elements. In addition, tangential forces (f_s) are prescribed, in accordance with Coulombs law of friction, to simulate frictional forces which oppose the relative tangential displacement between the contact node (K) and the target segment (IJ). Figures 2.12 (a,b) show the two models for determining f_s. The *Elastic Coulomb Friction* model considers both sticking and sliding conditions, and the tangential forces are given by

$$f_s = \begin{cases} 0 & (\textit{for frictionless contact}) \\ K_t\, u_s^{\{e\}} < -\mu_s f_n & (\textit{for sticking contact}) \\ -\mu_d f_n & (\textit{for sliding contact}) \end{cases} \tag{2-33}$$

where, μ_s and μ_d denote the coefficients of static- and dynamic- friction respectively, K_t is the tangential contact stiffness, and $u_s^{\{e\}}$ is the elastic component of the relative tangential displacement between the contacting bodies. Note that the sticking region is reversible (and is therefore sometimes referred to as the elastic contact region), while the sliding region is not (also referred to as the inelastic contact region). The need for an iterative solution procedure is apparent from equations (2-32) and (2-33) since the algorithm assumes no prior knowledge of the status of the contact nodes, their direction of relative motion, and the frictional resistance encountered. The other approach is the *Rigid Coulomb Friction* model, wherein the two surfaces are assumed to be always in sliding contact. The tangential contact forces in this model are simply defined as

$$f_s = \mu_d f_n \tag{2-34}$$

as shown in figure 2.12 (b).

One of the main difficulties in applying the above method lies in selecting the appropriate values for the normal contact stiffness (K_n) and the tangential contact stiffness (K_t). From equations (2-32) and (2-33), it is evident that the larger the value of K_n, the more accurate the solution will be since the interpenetration (g) will be smaller. However, a very large value normally leads to convergence difficulties and an ill-conditioned stiffness matrix which may result in large round-off errors. Similarly, if K_t is very large, convergence difficulties may be caused by a very small sticking zone.

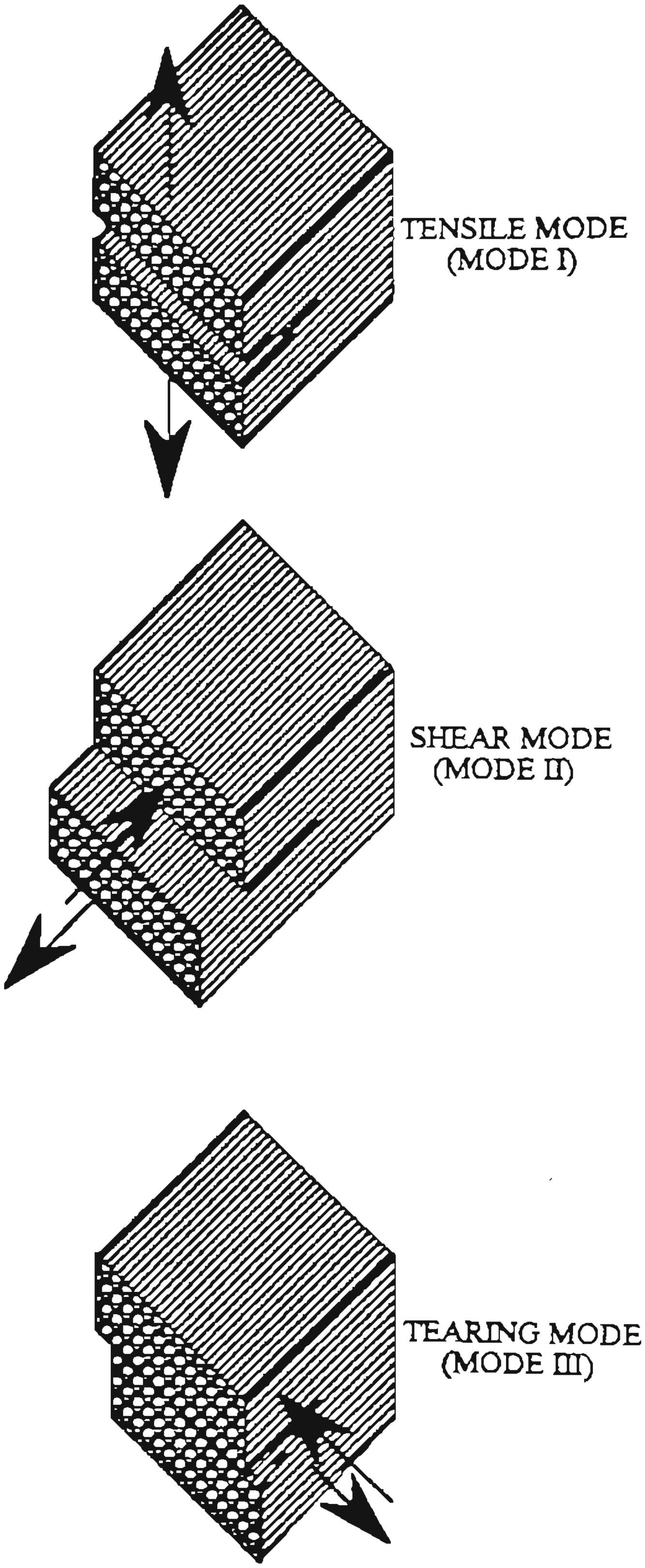

Figure 2.1 : Three fundamental modes of crack extension.

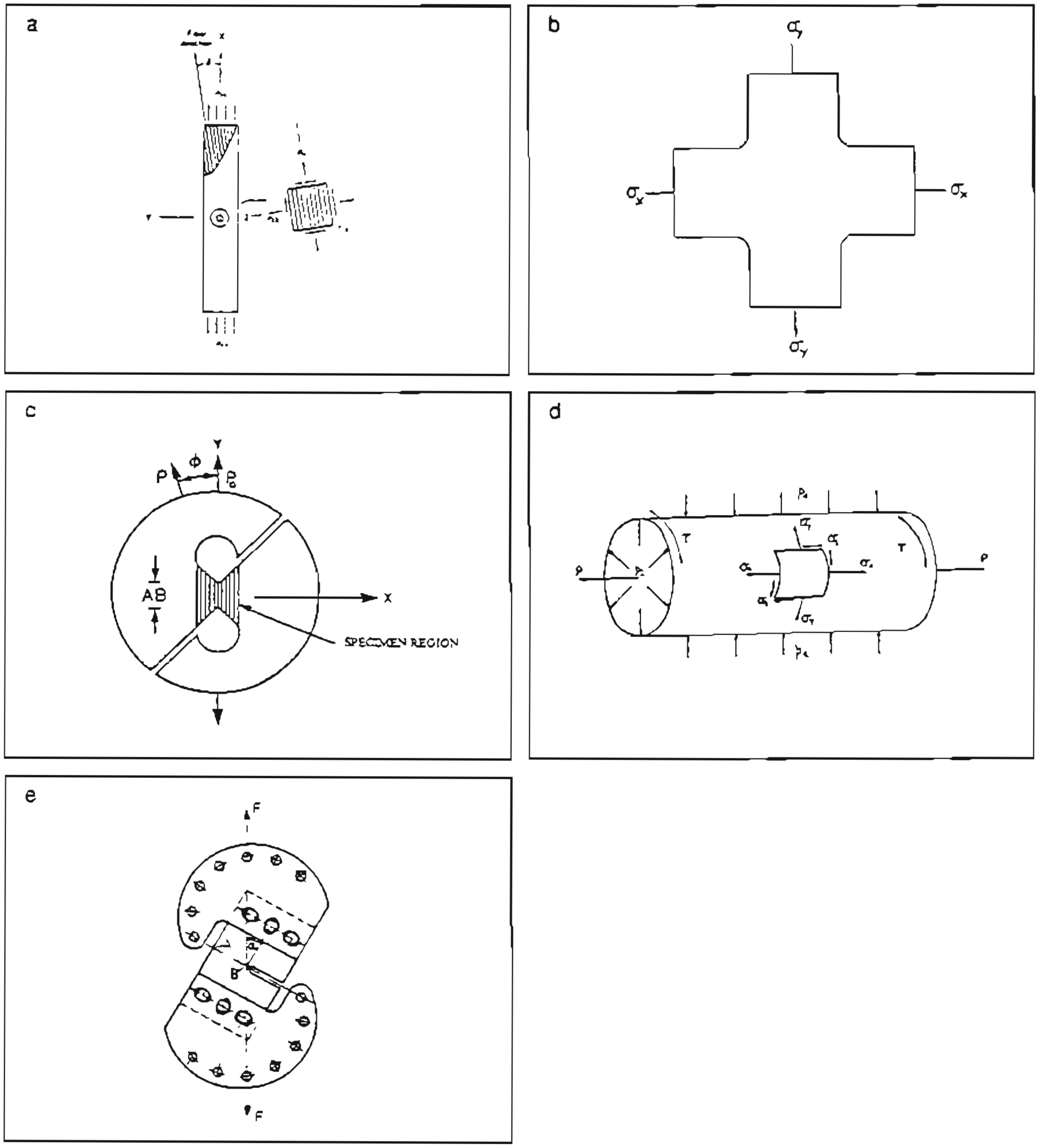

Figure 2.2 : Shear and biaxial tests; (a) Off-axis tension, (b) Cruciform, (c) Arcan, (d) Hoop-wound tubes, and (e) Compact tension-shear.

(a) Force Diagram

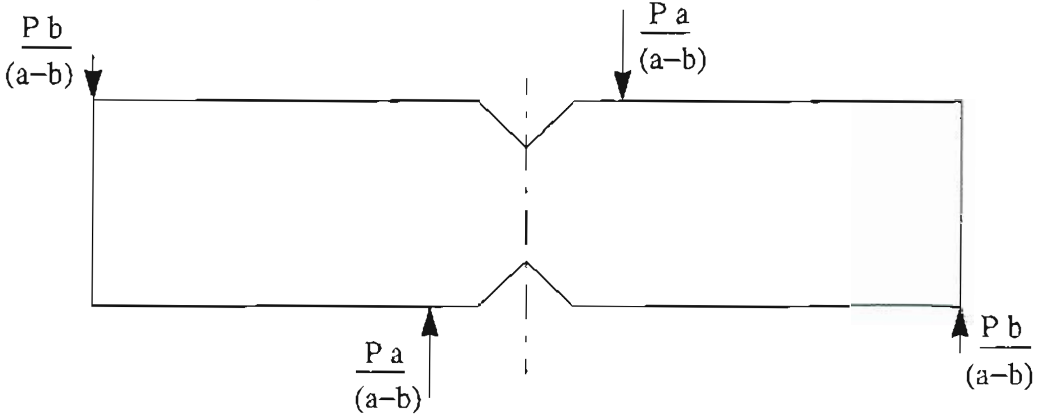

(b) Shear Diagram

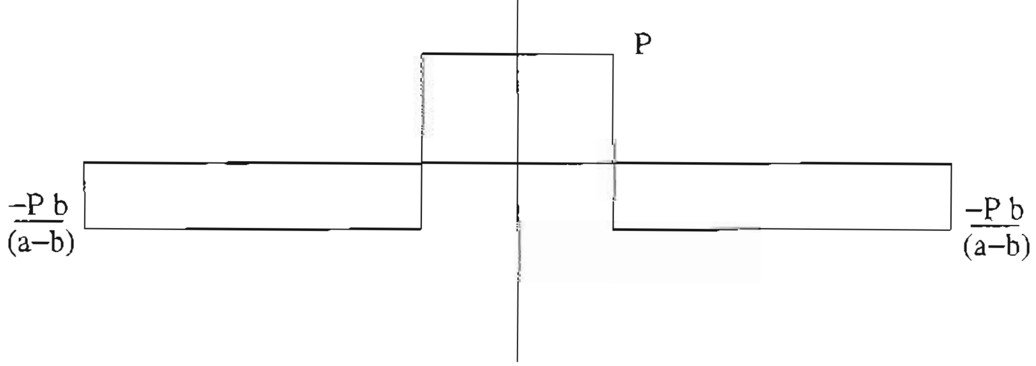

(c) Moment Diagram

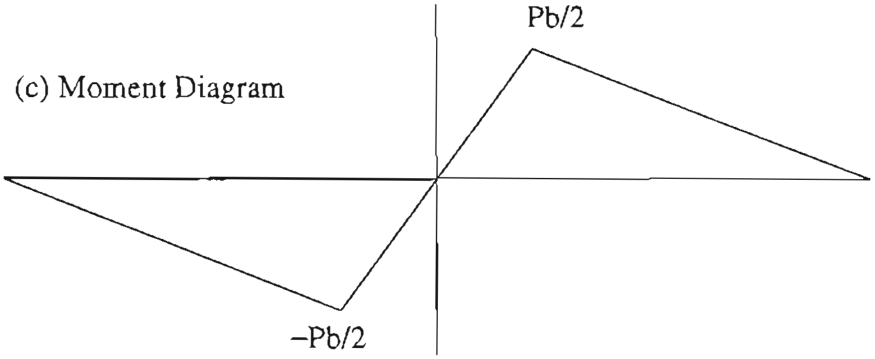

Figure 2.3 : Iosipescu shear test; (a) Force Diagram, (b) Shear diagram, and (c) Moment diagram.

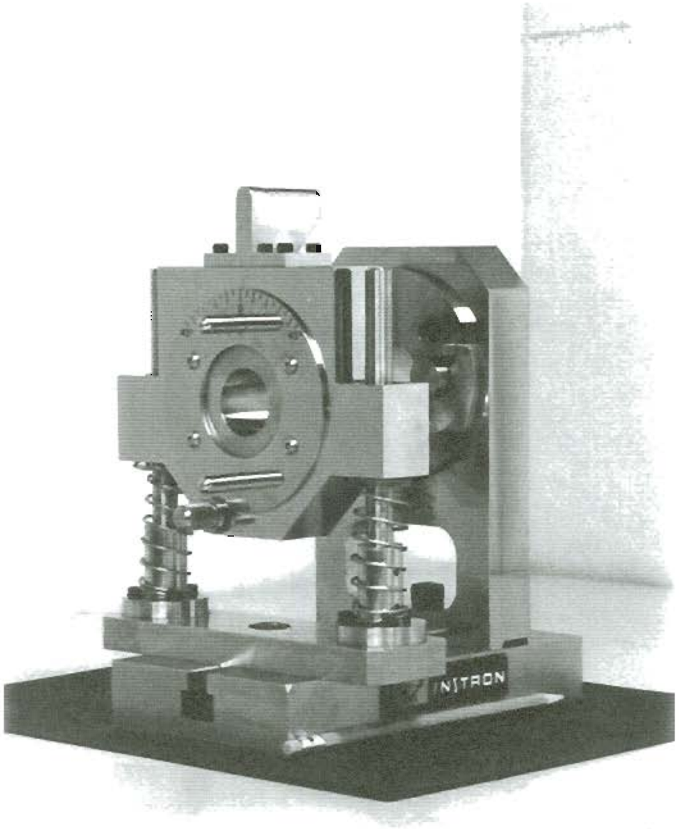

Figure 2.4 : Biaxial Iosipescu test fixture.

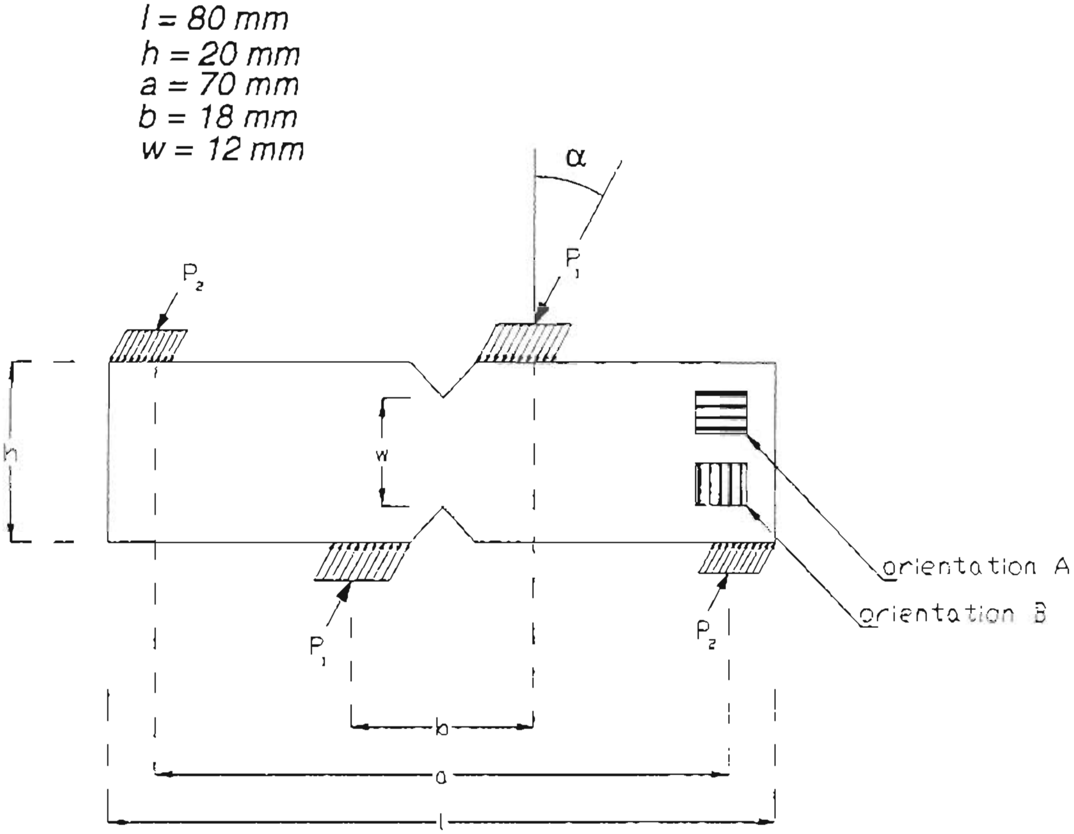

Figure 2.5 : In-plane biaxial loading of Iosipescu specimen.

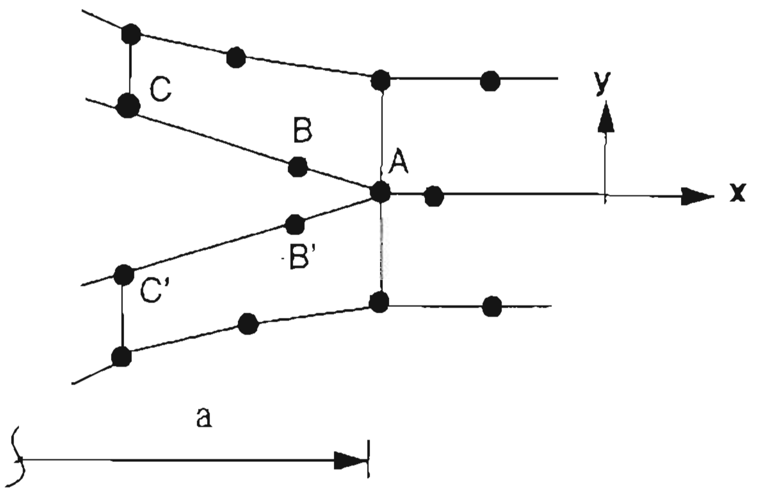

Figure 2.6 : Singular isoparametric elements at the crack-tip with nodal lettering convention.

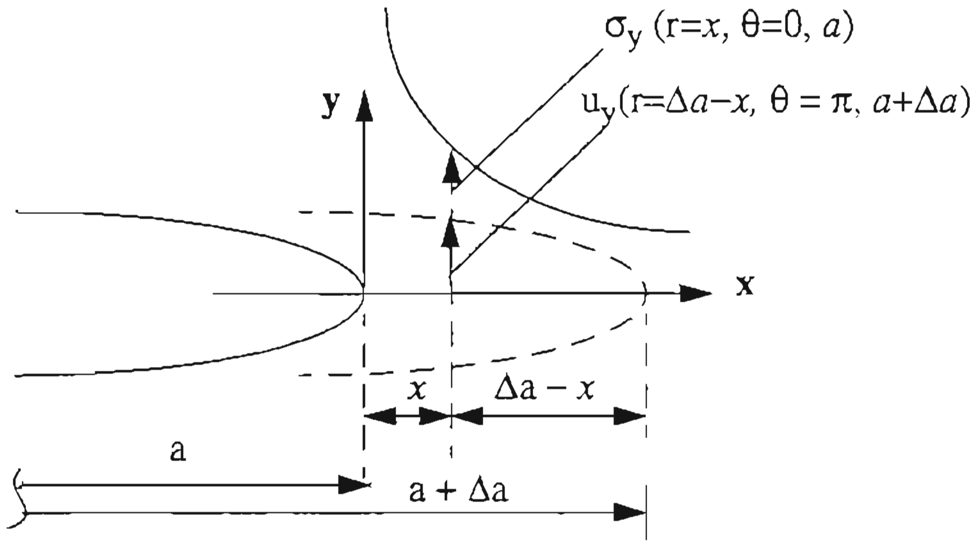

Figure 2.7 : Virtual crack closure integral method

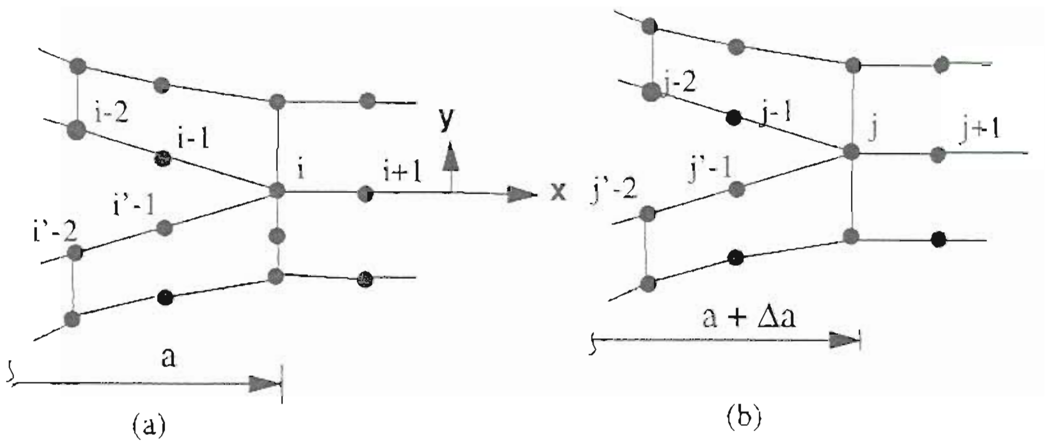

Figure 2.8 : Virtual crack closure method with isoparametric elements:
(a) Original crack, and (b) After extension.

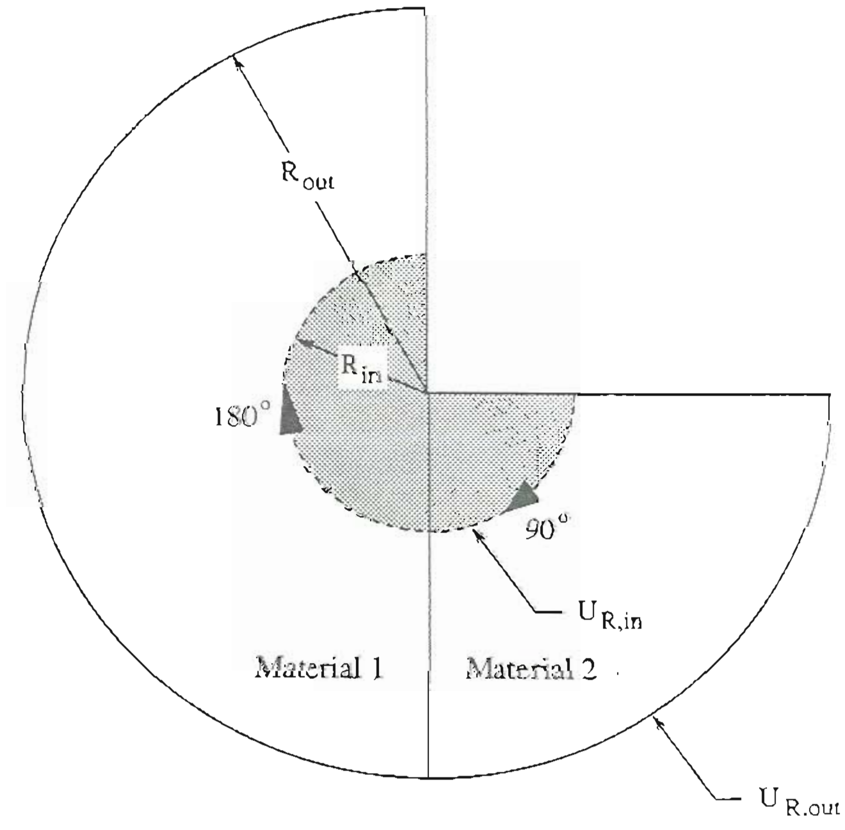

Figure 2.9 : Schematic of the Finite Element Iterative Method

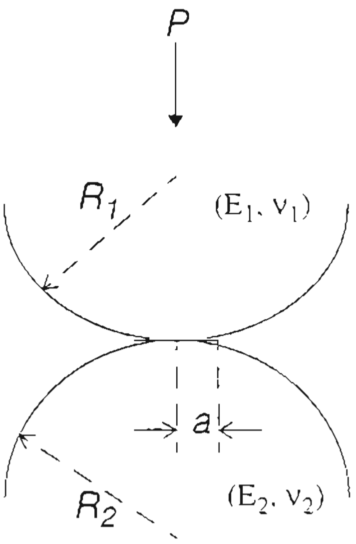

Figure 2.10 : Hertz analysis for elastic spheres in contact.

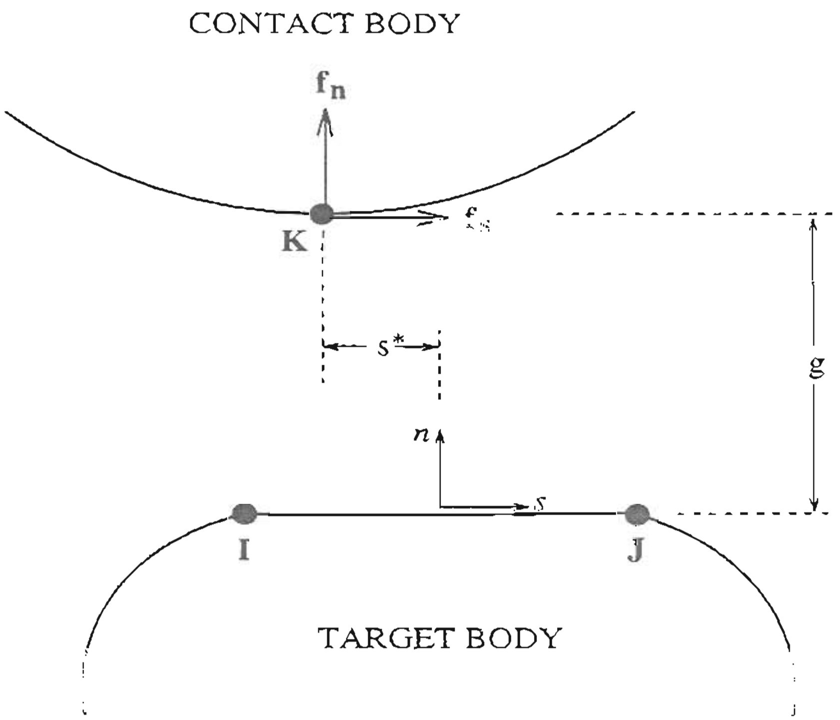

Figure 2.11 : Kinematic tracking of contact node with respect to target.

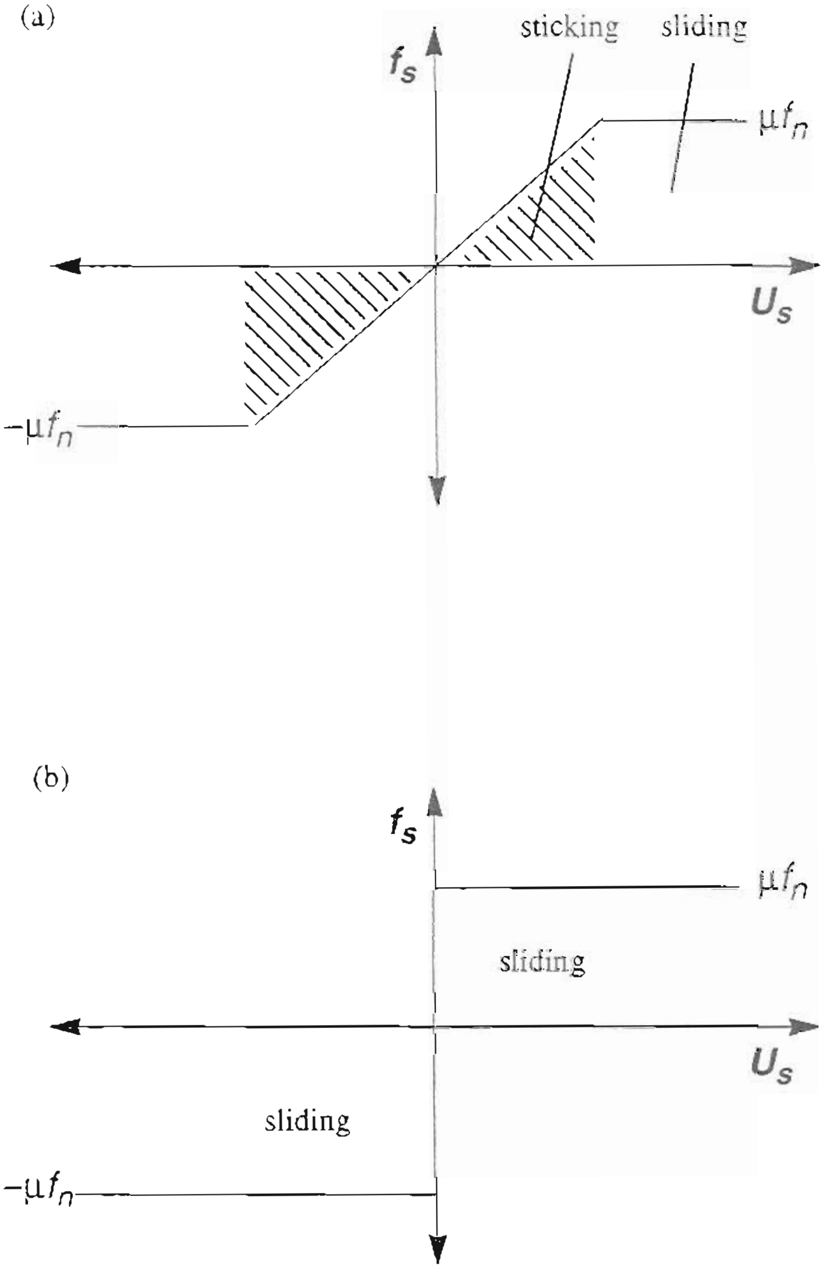

Figure 2.12 : Frictional contact models; (a) Elastic Coulomb friction, and (b) Rigid Coulomb friction.

Chapter 3

Characterization of Composite Insulators

3.1. INTRODUCTION

As mentioned in chapter 1, the composite (GRP) rods of insulators with the crimped end-fitting design are subjected to both, residual stresses generated during assembly and stresses caused by external loading of the insulator during service. The internal residual stresses are generated during the crimping process, where bonding between the GRP rod and metal end-fittings is achieved by radially compressing the end-fittings on to the rod. The magnitude of radial compression that must be applied to an insulator such that it may be able to withstand the service loads is a subject of great interest to design engineers. Clearly, excessive radial compression applied to the GRP-rod during crimping can lead to radial stresses large enough to initiate intralaminar debondings and fiber failures in the GRP-rod. On the other hand, a low value of radial compression during crimping, coupled with large axial loads applied during service, can cause internal sliding failures in the crimped end-fitting design. In the past, field failures of crimped suspension insulators have been blamed on both of these mechanisms. In an earlier study, Maza and co-workers [6] performed destructive axial tensile tests on suspension insulators with crimped end-fittings. They reported that at a low temperature of -25^oC, the insulator failed due to sliding of the rod from the end-fitting, while at room temperature and elevated temperatures of 45^oC, longitudinal tensile failure of the rod occurred by intralaminar splitting.[6] It is therefore important to be able to control the levels of radial compression applied to insulators during assembly. This information may then be correlated with the extent of internal compressive damage generated in the GRP rods of insulators subjected to excessive crimping, and the axial strength of crimped end-fittings.

In this chapter, five 115 kV substation insulators from five different manufacturers have been characterized with respect to the extent of internal radial deformation of the GRP rod, the extent of internal damage of the rods compressed during crimping, and the axial strength of the insulator ends. These five insulators are henceforth referred to as insulators A, B, C, D, and E.

3.2. RADIAL COMPRESSION DURING CRIMPING

3.2.1. Ultrasonic Pulse-echo Tests

In this section, a new ultrasonic technique has been described to measure the magnitude of radial compressive displacements applied to the GRP-rods of all five insulators during crimping. This technique is capable of determining the magnitude and shape of the radial compression function with an accuracy of ± 0.1 mm, provided that the GRP-metal interface is smooth with no interfacial voids.

The ends of all insulators (A, B, C, D, and E) were sectioned off as shown in figure 3.1, the rubber weathersheds were removed, and the external surfaces of the end-fittings were machined smooth in order to impart a uniform radius. The machining was performed by clamping the GRP rod, thereby ensuring that the axes of the rod and end-fitting were concentric. The machined external surface was subsequently discretized into 24 lines along the circumference (θ), and 10 lines in the axial direction (z). This resulted in a measurement grid of 240 equi-spaced points on the surface of the end-fitting. Horizontal linearity was established by sweep calibration on three steps of different thicknesses machined on the base of the end-fittings. A Panametrics 26DL PLUS digital thickness meter with an internal data logger was used in conjunction with a 10 MHz (model no. D793, 5.08mm diameter) dual element transducer. The interface depth (x) was measured with an accuracy of ±0.1 *mm*, and the internal radius of the compressed GRP-rod was determined as :

$$r_{in} = r_{ef} - x \tag{3-1a}$$

where r_{ef} is the measured external radius of the end-fitting. From the outer radius of the uncompressed GRP-rod (r_{out}), the extent of radial compression (U_r) of the GRP-rod was determined as :

$$U_r = r_{out} - r_{in} \tag{3-1b}$$

Figure 3.2 schematically illustrates the measurement procedure.

The three dimensional radial compression profiles $U_r(\theta, z)$ of insulators A, B, C, D, and E are presented in figures 3.3 (a to e). It is evident that the compression profiles are highly dependent on the design of individual end-fittings, and the technique of crimping employed by the manufacturers. The following sub-sections describe the observations.

(a) INSULATOR A :

From figure 3.3 (a), it is evident that at any particular angle (θ) along the circumference, the magnitude of radial compression in insulator A is more or less uniform, with the maximum compression occurring at the midlength of the end-fitting (between z_1 and z_2). Furthermore, at any particular length in the axial direction (z), the compression profile has six distinct and equi-spaced maxima and minima separated by 30^o along the circumference. It should be mentioned that the external surface of the aluminum end-fittings of this insulator exhibited well defined flats prior to the machining. These flats were most likely created due to plastic deformation of the aluminum during crimping. The wave-like compression profile, and the flats on the end-fitting surface, strongly suggest that a hexagonal die was used to crimp the end-fittings on to the GRP rod.

(b) INSULATOR B :

Figure 3.3 (b) shows the three-dimensional radial compression profile of insulator B. During machining of the external end-fitting surface, the sectioned insulator end was inadvertently clamped from the end-fitting flange, instead of the GRP rod end. This resulted in a mismatch between the axes of rotation of the end-fitting and the GRP-rod. Therefore, radial compression measurements (which assume that the axes are coincident) would lead to erroneous results. To solve this problem, the data in figure 3.3 (b) is presented in terms of the diametric compression (divided by two) along twelve equi-spaced lines in the tangential (θ) direction. It can be seen that the compression profile of insulator B is more uniform in nature than for insulator A.

(c) INSULATOR C :

The end-fitting of insulator C was much longer than the other insulators, and was therefore discretized into 16 lines in the axial direction (z). Unlike insulator A, the radial compression profile of this insulator (see figure 3.3 c) shows four maxima and four minima, separated by 90^o along the circumference. This indicates that a square dye may have been used during the crimping process.

(d) INSULATOR D :

The compression profile of insulator D (figure 3.3 d) indicates that most of the internal surface of the GRP-rod had a negative radial compression. This seems erroneous because the internal radius of the GRP-rod (r_{in} in equation 3-1b) should never be greater than the external radius (r_{out}) if any mechanical bonding is to be achieved. However, since ultrasonic waves are reflected back by an abrupt change in the density of the medium, a void between the internal surface of the end-fitting and the external surface of the GRP-rod could cause r_{in} to appear to be greater than r_{out}. To verify these results, ultrasonic measurements were performed on another end-fitting of insulator D, and similar results were obtained. This effect will be further examined in a later section of this chapter.

(e) INSULATOR E :

The radial compression in insulator E was found to be highly uniform, and significantly lower in magnitude than in insulators A, B, and C. The magnitude of radial compression was found to vary between 0 mm to 0.18 mm (see figure 3.3 e).

3.2.2. Analytical Model for Radial Compression

From the ultrasonic compression data, it is evident that the radial compression along the surface can be highly non-uniform in some insulators. This non-uniformity occurs in both the axial (z) and tangential (θ) directions in insulators A and C. In order to have a better understanding of the compression profiles, and also to simulate these profiles in a finite element model, there is a need for generic mathematical functions which can closely simulate both the shape and magnitude of the compression profiles observed in figures

3.3 (a to e). This section presents the definition of some of the key parameters, and the generic form of the mathematical functions, that have been used in the finite element models described in the next chapter. In order to simplify the analysis from three dimensions to two dimensions, the axial and tangential non-uniformities of the compression profiles have been treated separately. In other words, we shall assume that an axially non-uniform compression profile will be uniform in the tangential direction, and vice-versa.

If the three-dimensional radial compression profile $U_r(\theta, z)$ of an insulator is known, then the **total magnitude** of radial compression (M_T) can be defined as the surface integral

$$M_T = \int_{z_1}^{z_2} \int_{0}^{2\pi} U_r(\theta, z) \,.\, d\theta \,.\, dz \tag{3-2a}$$

where, the locations z_1 and z_2 are indicated in figure 3.2. The **average magnitude** (**M**) will now be defined as

$$M = \frac{M_T}{2\pi\,(z_2 - z_1)} \tag{3-2b}$$

Using this approach, the average magnitudes of radial compression (M) are presented in table 3.1 for insulators A, B, C, D, and E.

(a) Axially Non-uniform Compression

If a radial compression profile is non-uniform only in the z-direction and uniform in the θ-direction, then the problem is axisymmetric. Therefore, in the axisymmetric finite element models developed in the next chapter, radial compression due to crimping is prescribed according to a two-dimensional 5^{th} order polynomial defined as

$$-U_r = P_o(z) = C_0 + C_1 z + C_2 z^2 + C_3 z^3 + C_4 z^4 + C_5 z^5 \qquad (3\text{-}3a)$$

where, the coefficients C_0, C_1.....C_5 can be easily determined by non-linear regression of the axial radial compression data of any of the insulators (figures 3.3). From the regressed radial compression function $P_o(z)$, the average magnitude (M) of radial compression will become

$$M = \frac{\int_{z_1}^{z_2} P_o(z)\,.\,dz}{(z_2 - z_1)} \qquad (3\text{-}3b)$$

From equations (3-3 a,b), it is evident that the average magnitude of applied radial compression (M) can be changed in the axisymmetric models if the coefficients C_0, C_1,....C_5 are multiplied by a constant factor. The shape of the compression profile will however remain the same. This will facilitate the simulation of axially non-uniform compression profiles with different values of M, while maintaining the same shape.

Similar to the polynomial P_o(z), we can define general 5^{th} order polynomials of the form

$$P_j(z) = b\,C_0 + a\left[C_1 z + C_2 z^2 + ...C_5 z^5\right] \quad (j = 1, 2, \cdots) \qquad (3\text{-}4a)$$

where a and b are unknown constants defining the shape of the polynomial. In order to maintain the same measured average magnitude of radial compression (M), we can impose the condition

$$\frac{\int_{z_1}^{z_2} P_j(z)\,.\,dz}{(z_2 - z_1)} = \frac{\int_{z_1}^{z_2} P_o(z)\,.\,dz}{(z_2 - z_1)} = M \quad (j = 1, 2, \cdots) \qquad (3\text{-}4b)$$

Using equations (3-4 a,b), we can now simulate several shapes of radial compression along the axial direction, while keeping the same average magnitude (M). This is done by calculating the values of b at some assumed values of a. Note that if $a = 1$, then from equation (3-4b) we find that $b = 1$, and the polynomial $P_j(z)$ becomes the same as $P_o(z)$.

For the analysis of insulator A for instance, figure 3.4 shows the experimentally determined average radial compression data in the axial direction. Using equations (3-2 a,b), the average magnitude M_A was calculated to be 0.176318 mm (see table 3.1). A fifth order non-linear regression analysis was subsequently performed to determine the coefficients C_0, C_1,....C_5 of the actual experimentally measured polynomial $P_A(z)$. Figure 3.5 shows the original $P_A(z)$ and three new polynomials; $P_2(z)$ at a = 0.25, $P_3(z)$ at a = 0, and $P_4(z)$ at a = -1, which have the same magnitude (M_A = 0.176318 mm) and different shapes.

(b) Tangentially Non-uniform Compression

In figures 3.3 (a to e), it was seen that insulator A had six well defined peaks of maxima and minima along the tangential direction (θ), insulator C had four peaks, and insulator E had a uniform compression profile. This wave-like non-uniform compression profile can be simulated in the form of a sinusoidal wave function by assuming that the compression is uniform along the axial (z) direction. In a three dimensional finite element model, the radial compression due to crimping can be applied as

$$U_r = -A \left| \sin\left[\frac{n\,\theta}{2}\right] \right| \quad (0 \le \theta \le 2\pi) \tag{3-5}$$

where, A is the **amplitude of radial compression** defining the maxima of the wave-like compression profile, n defines the **number of peaks** of the compression function, and θ defines a point on the end-fitting surface from 0 to 2π in radians. Figures 3.6 (a,b) show the radial compression profiles that would be simulated by equation (3-5) by keeping the same amplitude (A) and changing the number of peaks (figure 3.6 a), and by keeping the same number of peaks (n) and changing the amplitudes (A). This wave function will be used in the finite element models described later in this study. From our previous definition (equations 3-2 a,b), we find that the average magnitude of the tangentially non-uniform radial compression will be given by

$$M = \frac{2A}{\pi} \tag{3-6}$$

It is interesting to note that by using the sinusoidal wave-function, the average magnitude (M) is linearly dependent on the amplitude (A), and completely independent of the number of peaks (n). This implies that we can simulate crimping profiles where M and A are held as constant parameters, while the number of peaks are allowed to change. For insulator A, which has an average magnitude (M_A) of 0.176318 mm, if we assume that the radial compression profile can be represented by equation (3-5), then from equation (3-6) the amplitude of radial compression A_A is 0.277 mm.

3.3. ROD PUSH-OUT TESTS

During service, composite substation and suspension insulators are subjected to axial compressive and tensile loads, respectively. As mentioned in chapter 1, the present design practice is to ensure that the maximum axial load should never exceed 60 percent of the specified mechanical load (SML) rating of an insulator throughout its expected life of 50 years. However, the fact that the SML rating tests are frequently performed on bare insulator rods (without the attached end-fittings) makes them quite questionable. The bonding between the GRP-rod and metal end-fittings is purely due to residual compressive stresses, with no adhesive at the interface. Therefore, if the mechanical bonding of the rod and end-fittings is weak, under sufficiently large axial loads, the insulators may encounter failure due to internal sliding of the GRP rod within the end-fittings. On the other hand, if the crimped joints are strong, the GRP rod can encounter intralaminar compressive damage accumulation leading to failure. In this section, destructive "push-out" tests have been performed on the end-fittings of insulators A, B, C, D, and E under externally applied axial compression. The purpose of these tests was :

(i) to establish the mode of failure and maximum loading capacity of the insulators under externally applied axial compression,

(ii) to verify the finite element models developed in a later part of this study, and

(iii) to evaluate the frictional properties of the GRP-metal interface in conjunction with finite element models.

3.3.1. Procedure

In order to perform the push-out tests, one end of each insulator had to be sectioned off (as shown in figure 3.1), and the flange (base of the end-fitting) was also sectioned off such that the two ends of the GRP rod were now exposed, while the central region was still encased by the end-fitting due to the residual radial compression. The sectioned assembly was mounted on a hollow cylindrical fixture made of steel, whose internal wall diameter was 5 mm larger than the diameter of the GRP rod. The fixture was loaded on an Instron universal testing machine with a load capacity of 450 kN, and an axial compressive load was applied on the GRP rod at a displacement rate of 0.254

mm/second. During the test, acoustic emission (AE) was monitored from the surface of the GRP rod in order to monitor the onset of sliding, or the accumulation of internal damage in the rod. A piezoelectric transducer (AC 375L) with a resonant frequency of 375 kHz, and a sensitivity better than -70dB referred to $1V\,(\mu bar)^{-1}$, was attached to the the surface of the GRP rod and connected to the AET 5500 system mainframe via a preamplifier with a fixed gain of 60dB.[120] The complete experimental set up is schematically illustrated in figure 3.7.

3.3.2. Results

Figure 3.8 shows the experimental load versus displacement curve and acoustic emission obtained from insulator A. It is evident that the structural response was fairly linear initially. At a load of approximately 310 kN, a well defined kink (accompanied by large AE signals) was observed on the load-displacement curve. This kink marked to the onset of internal sliding of the rod within the end-fitting. The load subsequently exhibited significant non-linearity, and after reaching a maximum of 387 kN, free sliding of the rod was detected. This caused a steady drop in the load with large axial displacements. After unloading the sectioned insulator end, the GRP rod was found to have emerged from the base of the end-fitting shell by about 12 mm, and no visible damage was detected on the surface of the rod.

Experimental load-displacement curves for insulators B, C, D, and E, are presented in figure 3.9. All the other insulators exhibited the same mode of failure. Although, insulator C showed a significant load drop after the onset of internal sliding. It is interesting to note that insulators D and E produced a wave-like response in the non-linear (sliding) regime. This phenomenon will be discussed in the next section. The following important inferences can be made from the push-out test results:

(a) Substation insulators subjected to excessive axial compression will encounter failure due to internal sliding of the GRP rod within the metal end-fittings. In all five insulator ends examined in this study, there was an 8 to 10 mm long gap between the inner base of the end-fitting flange and the end of the GRP rod. This implies that under excessive axial compression, the GRP rods can experience a total of 16 to 20 mm of internal sliding at both ends.

(b) This type of failure of the GRP-metal interface seems to occur at loads well below the load required to cause longitudinal compressive failures of the GRP composite.

(c) Based upon the estimated in-service loads given for 115 kV substation insulators in service, [121] it can be stated that the load at the onset of interfacial sliding is significantly larger than the estimated maximum axial compressive load applied to substation insulators. The worst case of axial compression is expected to be 1.34 kN, which results in factors of safety of 231, 108, 206, 84 and 48, for insulators A, B, C, D, and E respectively.

Table 3.1 lists the measured loads at the onset of sliding (P_f) for all insulators. It seems evident that the insulators with large magnitudes of radial compression (M) are less susceptible to interfacial sliding at the GRP-metal interface.

3.4. BENDING TESTS

Apart from axial loads, composite insulators (especially line-post type) are subjected to cantilever bending loads in service. In this section, insulators A, C, and D were subjected to horizontal bending loads. These tests were performed by C. Ek at the Bonneville Power Administration, [122] and are being presented in this section in order to verify some of the numerical predictions of this study. The main objective of these tests was to determine the mode of failure and the ultimate strength of the insulators in bending, and also to verify the finite element models presented in the next chapter of this study.

3.4.1. Procedure

The lower end-fitting of the insulators was constrained to the ground by bolts. One edge of the upper end-fitting was subjected to horizontal bending loads by a steel cable connected to a hydraulic machine via a load cell. The opposite edge of the upper end-fitting was attached to a displacement transducer. Figure 3.10 (a) shows one of the insulators loaded in bending. The composite substation insulators (A, C, and D) have a rated capacity of 8 kN (1800 lbs) under bending. Therefore, the first stage of tests involved proof testing, wherein the insulators were slowly loaded to 8 kN and held for five minutes before unloading. Four acoustic emission sensors were attached to the lower end-fitting in order to determine the onset of internal sliding or intralaminar failures in the GRP rod. In the next stage, the insulators were loaded to ultimate failure.

3.4.2. Results

In all three insulators, the load versus displacement response was fairly linear upto failure. During the proof tests, the acoustic emission signals did not indicate any accumulation of damage in the insulators. Furthermore, the mechanical behavior of the three insulators A, C, and D, was very similar as indicated by the slopes of the load-displacement curves, the loads at ultimate failure (P_{bend}), and the maximum horizontal displacements at the onset of failure (U_{bend}). Table 3.2 lists the maximum loads and displacements for the three insulators. Clearly, the composite insulators could undergo very large deformations ($\approx$ 0.3 meters, also see figure 3.10 a) prior to failure. The flexibility of porcelain insulators will certainly be much lower in comparison.

Failure of all three insulators occurred close to the interface corner of the lower end-fitting and the GRP rod. This was expected since the maximum stress concentrations under bending is expected to occur near the interface corner of the lower end-fitting and the GRP rod. Figure 3.10 (b) shows the fracture surface of the GRP-rod. The morphology of the surface is clearly consistent with the predictions of the theory of elasticity.[14] The brush-like fracture surface with extensive fiber pull-out on one half of the rod's cross-section (towards the loading direction) demonstrates a longitudinal tensile mode of failure, [17] while the flat crushed features on the other half demonstrate compressive failure. The central region of the surface, separating the tensile and compressive parts, encountered intralaminar shear failure as evidenced by a wedge inclined at 45^o with respect to the rest of the fracture surface.

3.5. TORSION TESTS

The torsional performance of composite substation insulators insulators will be important for switchgear applications. This section presents the results of destructive torsion tests performed by C. Ek, at the Bonneville Power Administration, [122] on insulator brands A, B, C, D, and E.

3.5.1. Procedure

Figure 3.11 shows the experimental setup for the torsion tests. Torsional loads were applied to both ends of the insulator by means of end plates which served as lever arms. The load was applied by a steel cable attached to a hydraulic machine via a load cell. Similar to the bending tests, one arm of each end plate was attached to a displacement transducer. By applying equal torsion to each end, the effects of axial loading and cantilever loading were negligible. The applied torsional load, the end rotation, and acoustic emission of the insulator were monitored during the test.

The torsional load was applied at a fixed displacement rate in four steps as follows:

(i) Preload insulator to 556 N and hold.

(ii) Monotonic load to 2372 Nm and hold for a few seconds.

(iii) Monotonic load to 3616 Nm and hold for a few seconds.

(iv) Monotonic load to 3954 Nm, hold for a few seconds and unload.

3.5.2. Results

During the tests, large acoustic emission signals, accompanied with a drop in the applied load and a sudden increase in the rotational displacements, were used to identify the onset of either intralaminar shear failure of the GRP rod, or internal sliding of the rod within the end-fittings. Figure 3.12 (a) shows the torsional load versus rotational displacement response of insulator A. The mechanical response of insulators B, C, and D was almost identical. These insulators failed at torsional loads in the range of 3000 to 3700 Nm ($\simeq$ 32,000 lb.in), with rotational displacements of about 50^o (see table 3.3). The failure was not catastrophic, and was most probably caused by the initiation of intralaminar splits in the GRP rod which generated large acoustic emission signals. In contrast to these insulators, the failure load for insulator E was significantly lower. Figure 3.12 (b) shows the torsional load versus displacement diagram for insulator E. This insulator failed due to internal sliding of the rod at a load of 903 Nm (8000 lb.in), as indicated by the sharp drop in the applied load followed by large rotational displacements (upto 140°).

Referring back to the ultrasonic radial compression data presented in section 3.2, the observed torsional failure modes can be explained. The average magnitudes of radial compression (*M*) for insulators A, B, and C, were significantly larger than for insulator E. Clearly, this resulted in insulator E being much more susceptible to internal sliding. The above results demonstrate that if the average magnitude of radial compression applied during crimping is sufficiently large, then failure under torsional loads will occur by the initiation of intralaminar splits in the GRP composite. On the other hand, if the value of *M* is very low (as in insulator E) and the coefficient of friction (μ) in the tangential direction is also low, then the GRP rod will encounter internal sliding prior to intralaminar failure.

3.6. OPTICAL MICROSCOPY

In this section, the end-fittings the five substation insulators were further sectioned to perform optical microscopic examinations of the GRP-rod and the GRP-metal interface. It is important to mention that these end-fittings had been subjected to the rod push-out tests reported in the previous section.

3.6.1. Procedure

The end-fittings were sectioned along two planes. The first section was along the midlength of the end-fitting perpendicular to the axial direction (*i.e.*, between z_1 and z_2). This exposed the plane of the GRP rod along which the extent of radial compression was expected to be maximum. The second section was parallel to the axial direction through the central axis of the GRP rod. Figure 3.13 shows the two sectioning planes which resulted in four semi-cylindrical pieces of the end-fitting. An optical stereo microscope was used to characterize the quality of the GRP-metal interface in one semi-cylindrical specimen with the GRP rod still attached to the end-fitting. From another semi-cylindrical specimen, the GRP composite was carefully separated from the end-fitting. The internal surface of the end-fitting was observed, and the GRP specimen was polished to 800 grit using silicon carbide emery paper. Note that the polishing was done until all the external asperities (created during sectioning) were removed. Microscopic examinations were performed to detect any internal damage in the GRP-rod extracted from all five insulators.

3.6.2. Results

The following subsections describe the observed characteristics.

(a) Insulator A

The internal surface of the end-fitting was very smooth, indicating a low coefficient of friction. There were no voids detected at the interface, and the overall mechanical bonding appeared to be good. Figure 3.14 (a) shows an axial view of the GRP-metal interface at a magnification of 10x. The polished GRP rod specimen however had a network of circumferential cracks spanning approximately 90^o of the circumference along the plane where the radial compression was maximum (midlength of z_1 and z_2). Figure 3.14 (b) shows an axial view of these cracks at a magnification of 75x.

(b) Insulator B

The internal surface of the end-fitting was very smooth, and the quality of interfacial bonding appeared to be good, with no voids between the GRP-rod and end-fitting. Figure 3.15 (a) shows an axial view of the GRP-metal interface at a magnification of 15 x. The GRP-rod was mostly free from internal damage. Although, looking at the central region of the GRP-rod, an array of very small microscopic cracks were found along the central axis of the rod (see figure 3.15 b). These cracks could have been generated during the manufacturing of the GRP rod.

(c) Insulator C

The internal surface of the end-fitting was very smooth. The quality of interfacial bonding was once again very good, with no evidence of voids (see figure 3.16 a). The GRP-rod however showed strong evidence of internal cracking. Looking at the midplane (midlength of z_1 and z_2) from the axial direction, two cracks were detected. One crack started from the circumference and traversed to the center (labeled as crack P in figure 3.16 b), while the other crack was smaller in size and was located at the center of the circular cross-section (crack Q in figure 3.16 c).

(d) Insulator D

The internal surface of the end-fitting consisted of a series of large u-shaped grooves. Looking at the interface from the axial direction, a large void was found between the GRP rod and end-fitting. This void was most probably seen because the lateral sectioning plane happened to coincide with a valley of the u-shaped grooves (see figure 3.17 a). However, looking from front, the geometry of these grooves becomes clearly apparent (see figure 3.17 b). It is important to note that the u-shaped grooves were so wide that the effective area of contact between the end-fitting and the GRP rod seems to have reduced significantly. Similar to insulator A, the circumference of the GRP rod exhibited a network of microscopic cracks. These cracks were smaller in size, and the total damaged area was more localized (spanning approximately 20^o) in comparison with the extent of damage found in insulator A (figure 3.18 a). Furthermore, the entire external surface of the GRP rod showed lines of circumferential damage created by the peaks of the grooved surface of the end-fitting. This was expected since a smooth end-fitting surface would transfer the radial crimping stresses more uniformly to the GRP rod than a a grooved surface, where the peaks act like notches embedded in the rod and cause large stress concentrations. Figure 3.18 (b) shows that the peaks on the grooved surface of the end-fitting got embedded in the composite, resulting in fiber fractures and resin cracking.

(e) Insulator E

The quality of interfacial bonding between the rod and end-fitting was good. No voids were observed at the interface (see figure 3.19). Similar to insulator D, the internal surface of the end-fitting was grooved. However, these grooves were much finer than the coarse grooves seen in insulator D. There was no evidence of any internal damage in the GRP-rod.

Figure 3.20 schematically illustrates the the size and location of internal defects found in the GRP rods from all five insulators. Since these specimens had been subjected to the push-out tests described earlier, the actual cause of some of the defects remains uncertain. The network of circumferential microcracks observed in insulators A and D, and the straight cracks in insulator C, could have been created either during the crimping process, or during the push-out tests. Certainly, the damage zones observed on the surface of the GRP rod of insulator D were created during the crimping process.

The quality of interfacial bonding, and the roughness of the internal surface of the end-fitting, can be used to explain some of the previous experimental observations. In section 3.2, it was seen that the radial compression data for insulator D indicated predominantly negative compression values. This is because we had assumed that the GRP rod was in perfect contact with the end-fitting surface. However, the u-shaped grooved end-fitting surface of insulator D significantly reduces the effective area of contact, with a series of large voids at the interface. During radial compression measurements, the ultrasonic transducer actually measured the depth (x in equation 3-1 a) of the metal-void interface, thus making the internal rod radius (r_{in}) to appear to be greater than the external radius of the uncompressed part of the GRP rod (r_{out}). This problem did not arise in insulator E because the grooves of the end-fitting surface were extremely fine, and proper rod-metal contact had been achieved during crimping.

In section 3.3, the rod push-out test results exhibited a wave-like response for insulators D and E in the non-linear (*i.e.,* sliding) regime, while the curves were smooth for insulators A, B, and C. Furthermore, the fact that the "wave-lengths" were much larger in insulator D than in insulator E, can be explained by the internal surface morphology of the end-fittings. The onset of sliding occurs at a critical load (P_f) which marks the transition from linear to non-linear response. Now, if the internal surface of the end-fitting is grooved, then the peaks of the grooved surface offer resistance to unrestricted sliding of the GRP rod. Therefore, a small load increment (ΔP) is required to overcome the resistance due to the peaks. When sliding commences again, the external load gets relaxed back to (P_f) until the next peak of the grooved surface is encountered. This process will lead to the wave-like mechanical response observed in figure 3.9. It is evident that the so called wave-length will be directly proportional to the coarseness of the grooved surface of the end-fittings.

Table 3.1 : Ultrasonic radial compression and rod push-out test results for the five substation insulators.

INSULATOR	M (mm)	P_f (kN)
A	0.176318	310.0
B	0.234103†	145.0
C	0.107347	277.0
D	0.005609†	112.0
E	0.030533	64.5

†Incorrect value

Table 3.2 : Bending test results for insulators A, C, and D.[122]

INSULATOR	Max. Load P_{bend} (kN)	Max. Displ. U_{bend} (mm)
A	18.68	297.2
C	18.73	312.4
D	16.39	281.9

Table 3.3 : Torsion test results for the five substation insulators.[122]

INSULATOR	Max. Torque (Nm)	Rotation (degrees)	Probable Failure Mode
A	3672	46°	Intralaminar Damage
B	3050	46°	Intralaminar Damage
C	3615	52°	Intralaminar Damage
D	3559	57°	Intralaminar Damage
E	903	7°	Internal Sliding

Figure 3.1 : Sectioned insulator end for radial compression measurement.

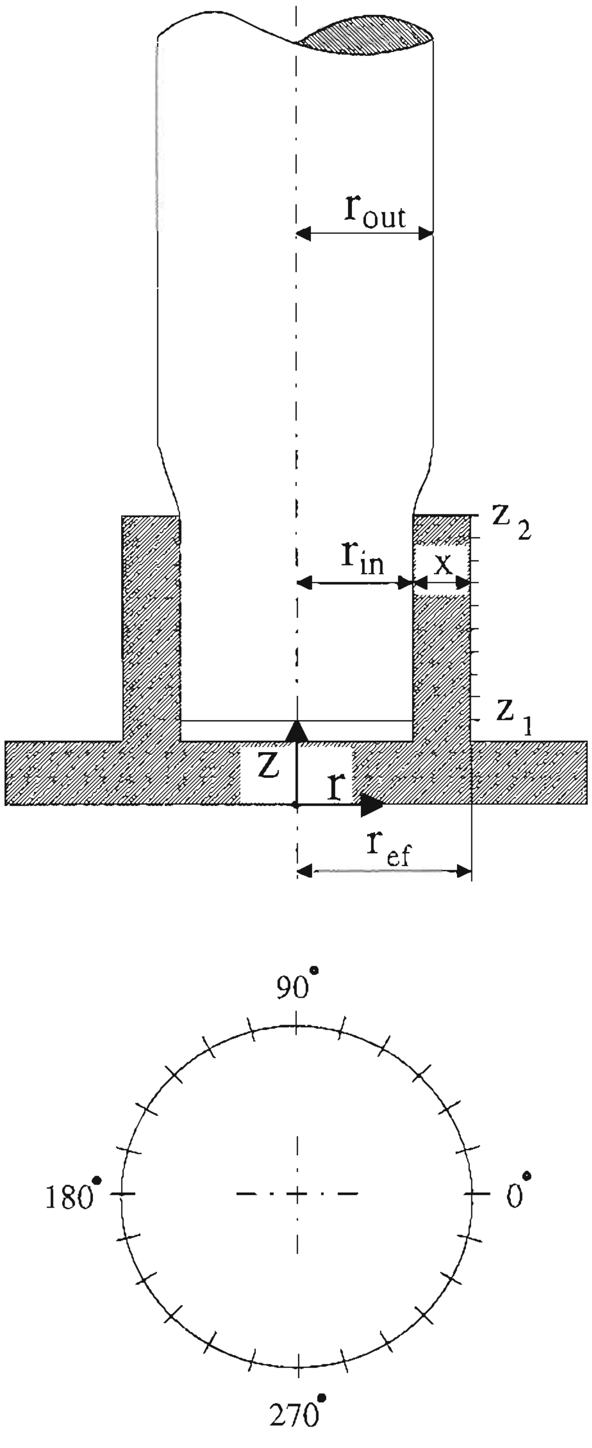

Figure 3.2 : Schematic of ultrasonic pulse-echo measurement technique.

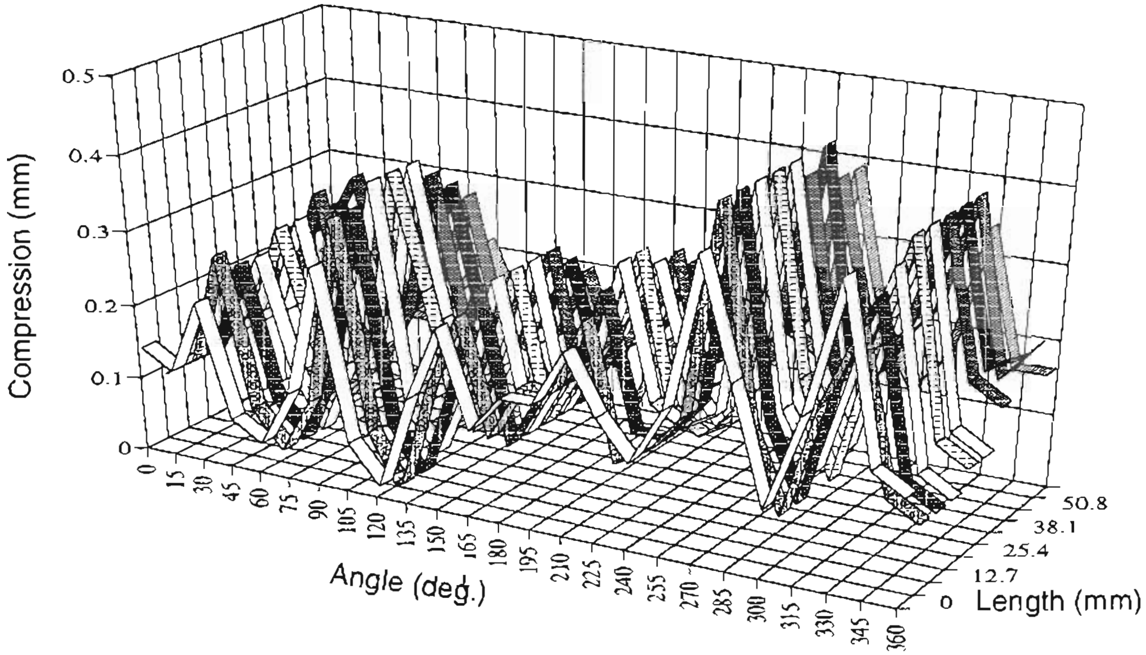

Figure 3.3 (a) : Three dimensional radial compression profile for insulator A.

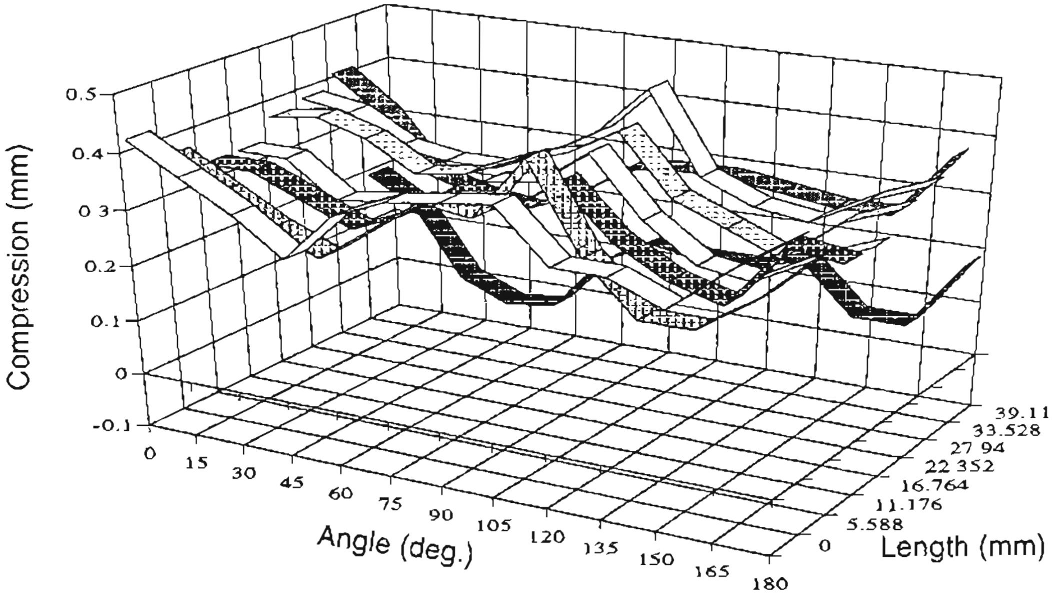

Figure 3.3 (b) : Three dimensional radial compression profile for insulator B.

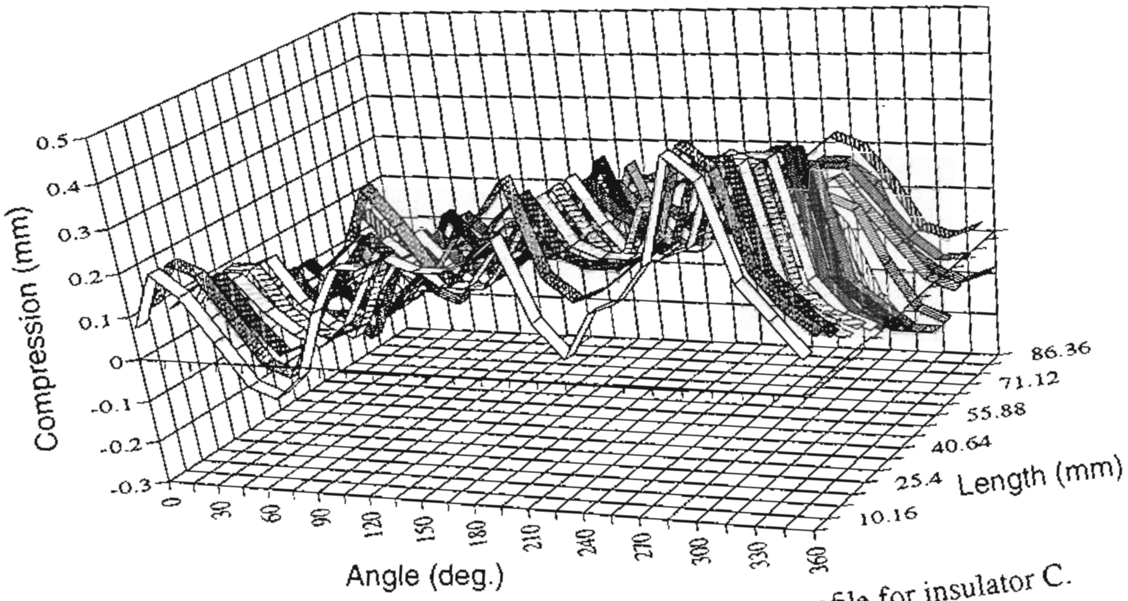

Figure 3.3 (c) : Three dimensional radial compression profile for insulator C.

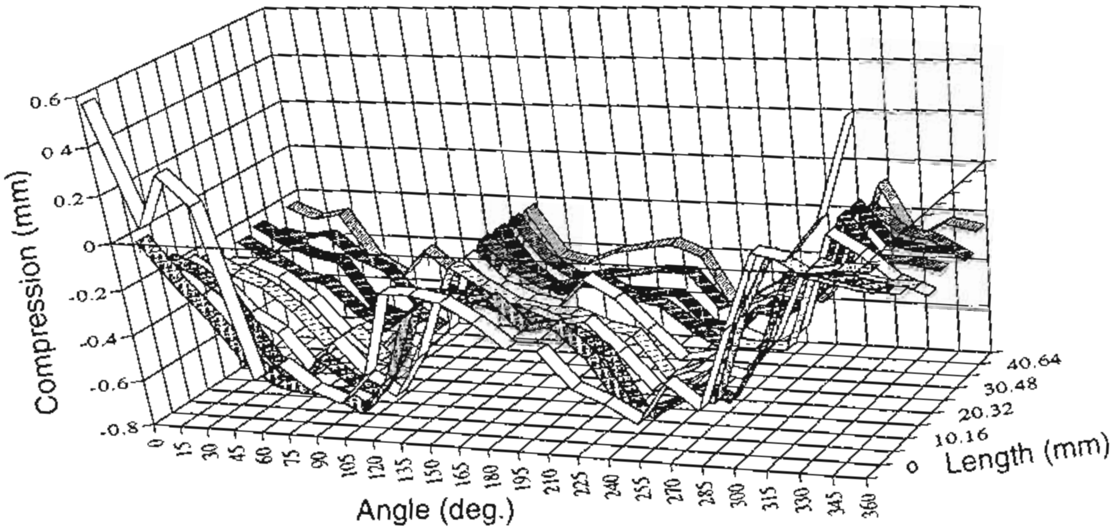

Figure 3.3 (d) : Three dimensional radial compression profile for insulator D.

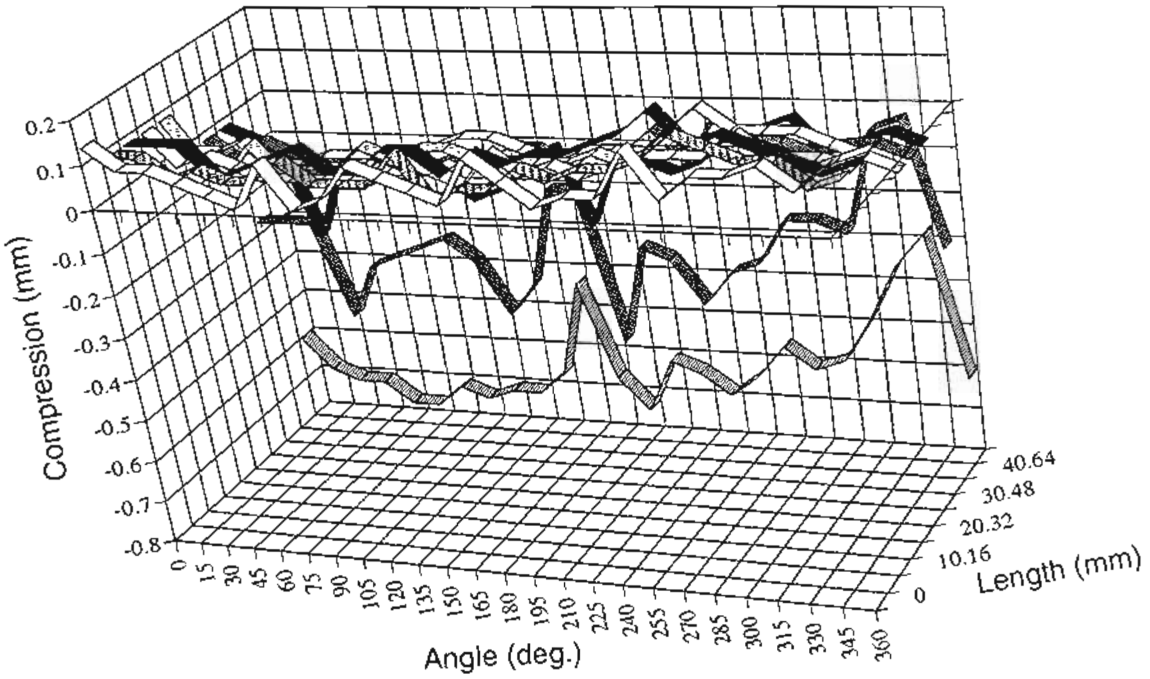

Figure 3.3 (e) : Three dimensional radial compression profile for insulator E.

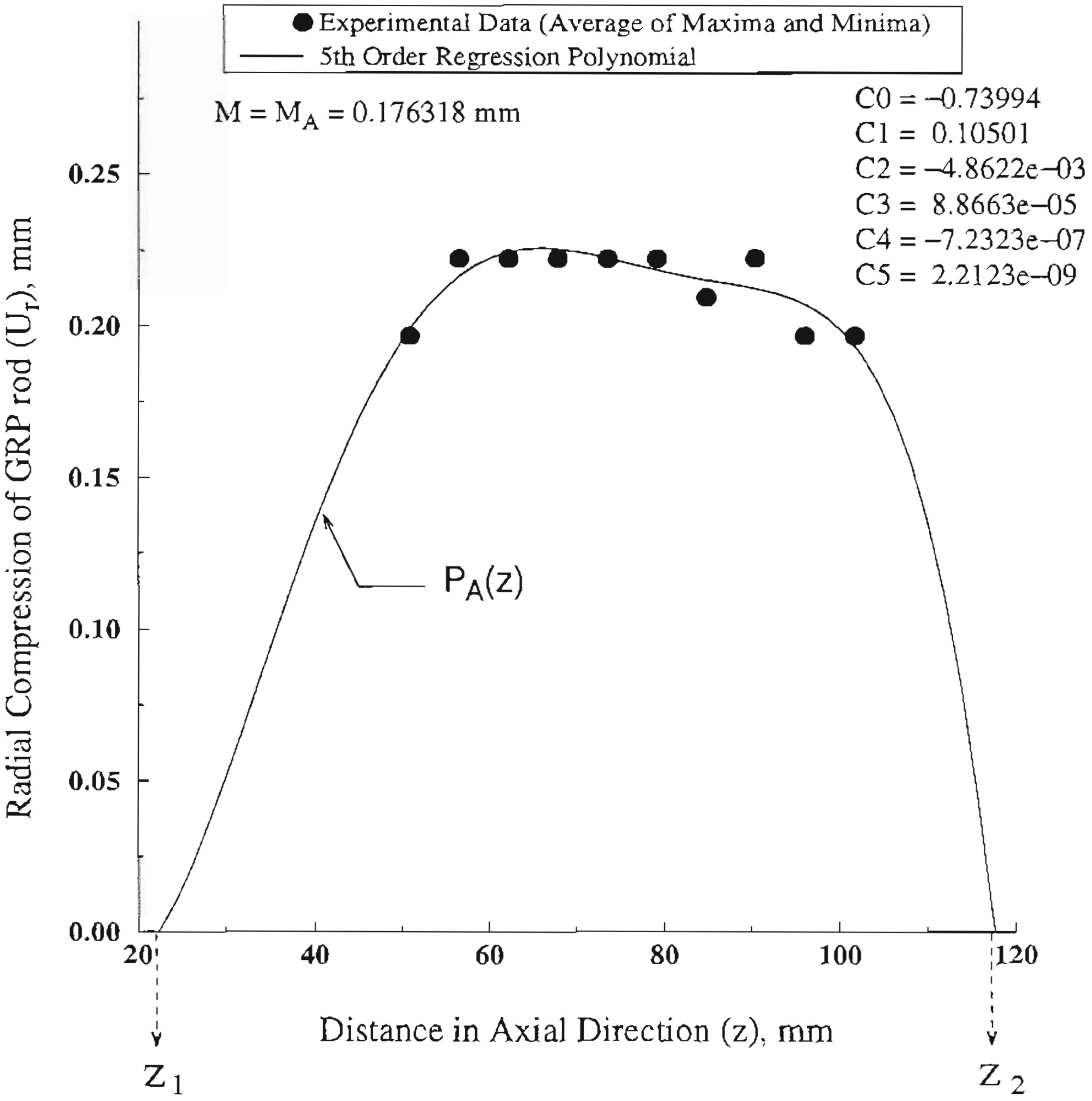

Figure 3.4 : Regression polynomial $P_A(z)$ for axially non-uniform compression in insulator A.

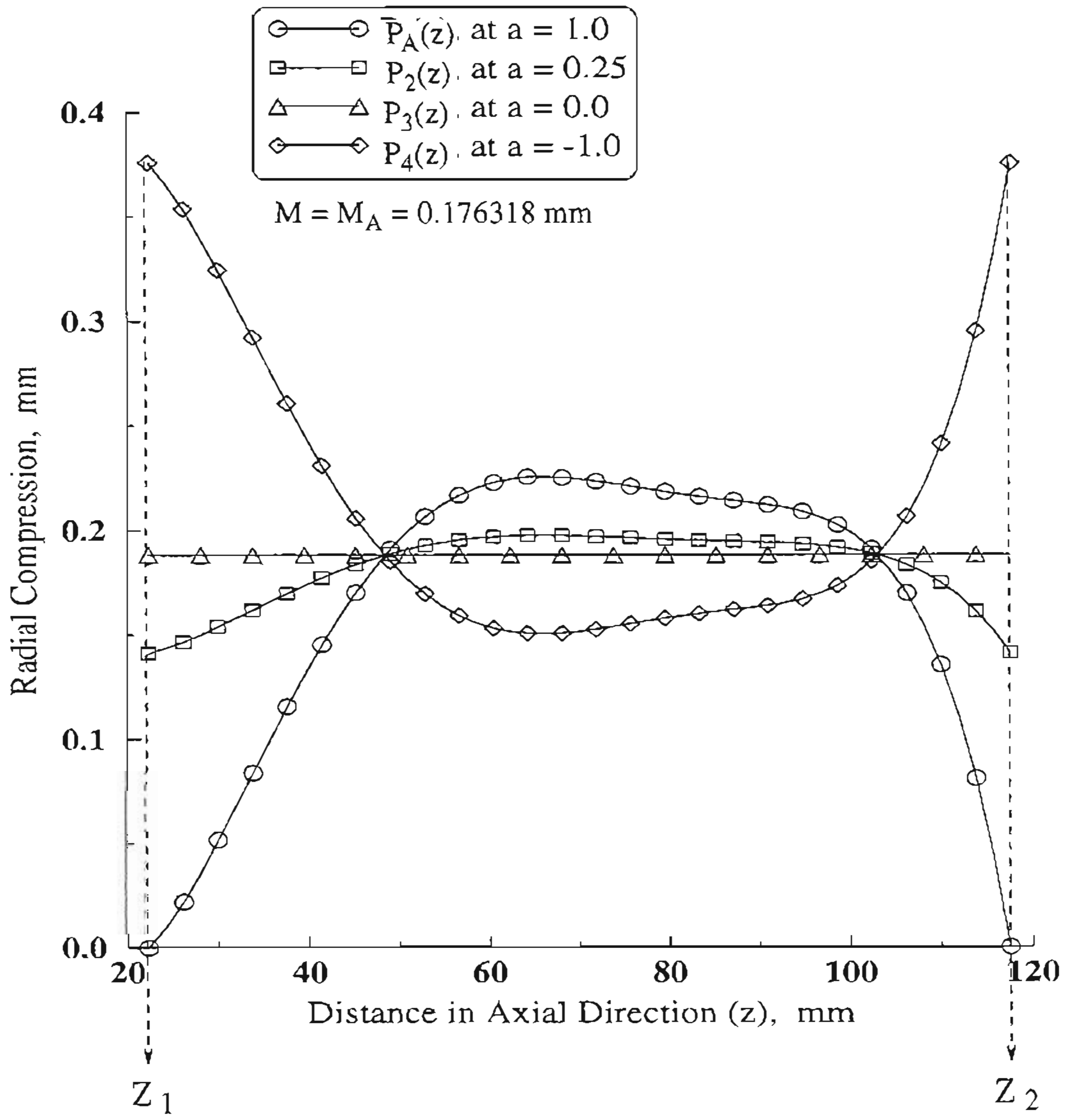

Figure 3.5 : Polynomials with different shapes and average magnitude of insulator A.

)

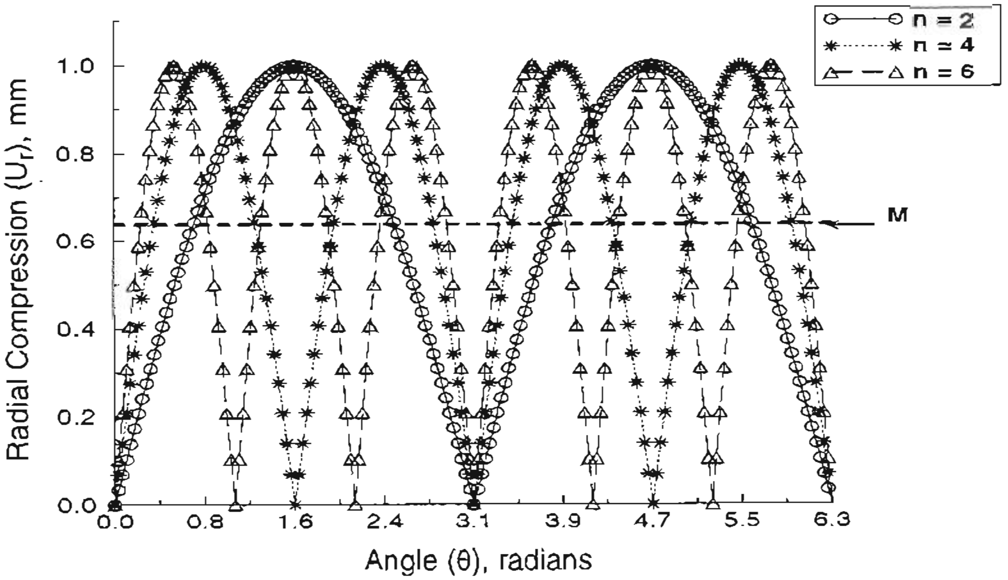

(a)

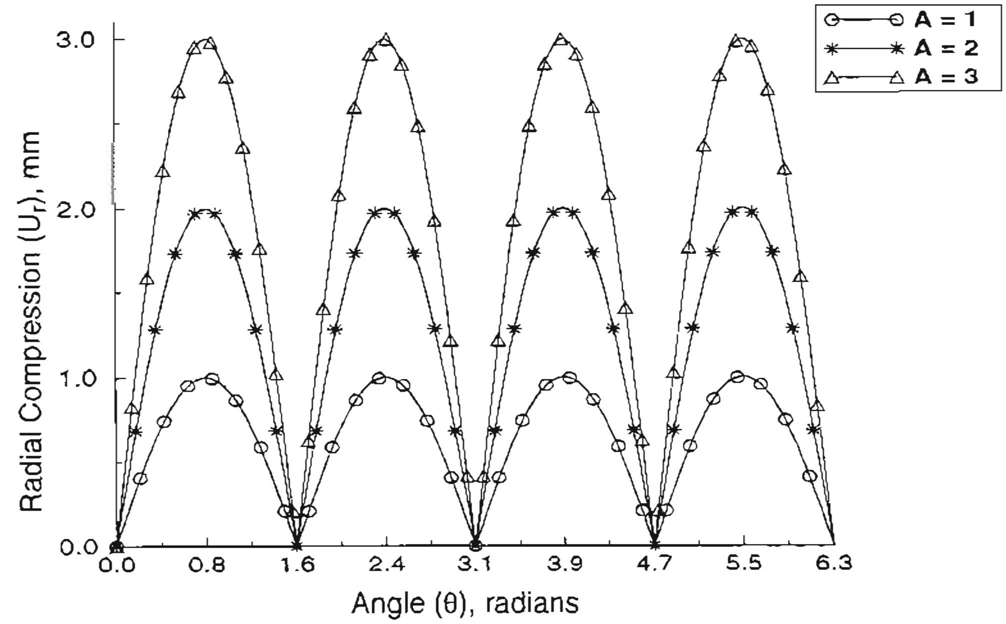

(b)

Figure 3.6 : Tangentially non-uniform radial compression; (a) A = 1 and n = 2, 4, and 6, and (b) n = 4 and A = 1, 2, and 3.

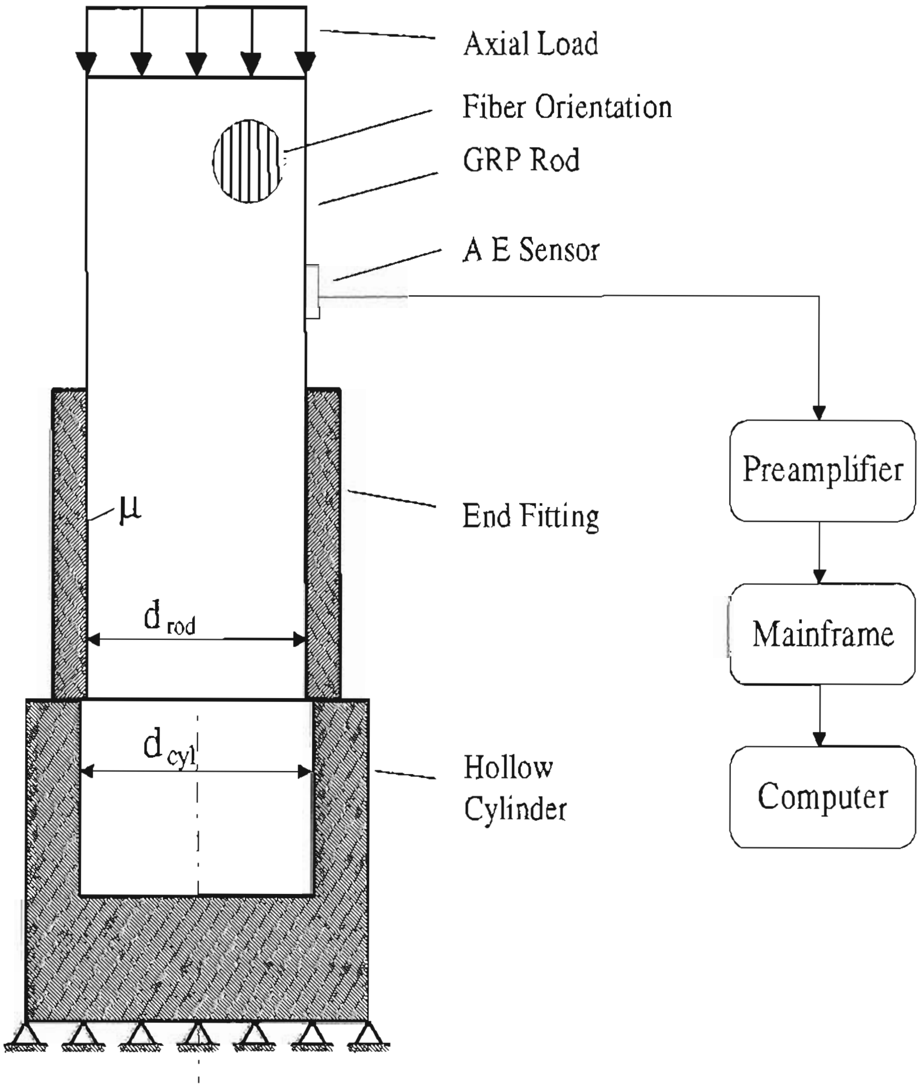

Figure 3.7 : Experimental setup for rod push-out tests.

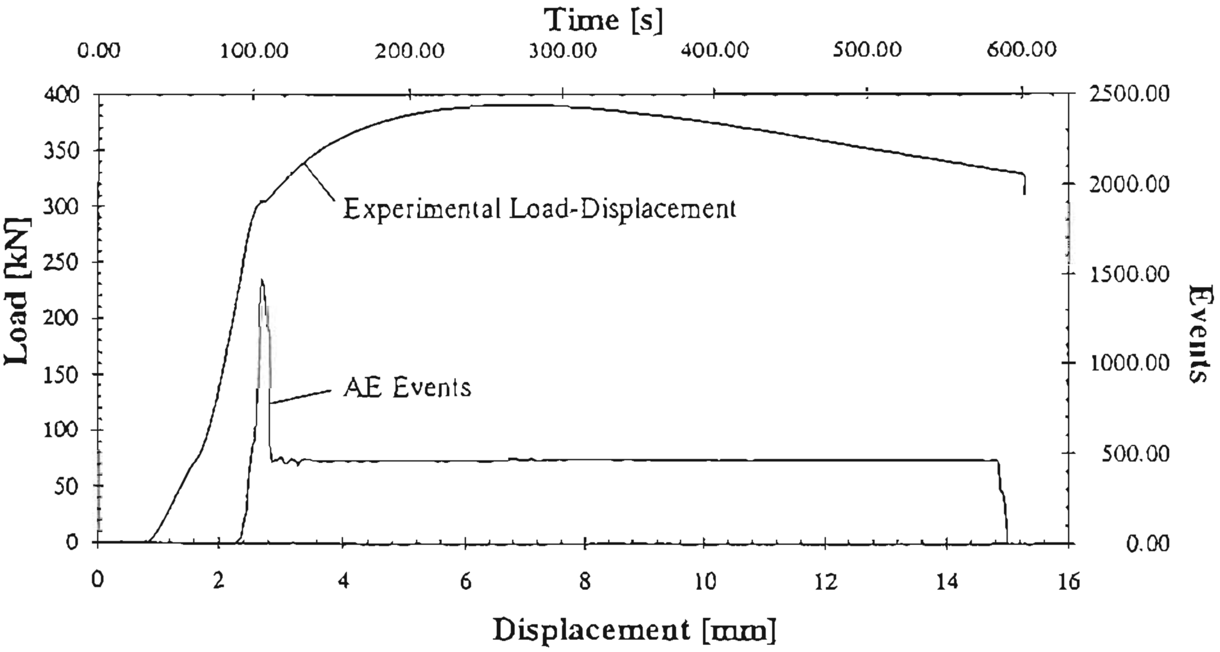

Figure 3.8 : Load-displacement and acoustic emission from push-out test of insulator A.

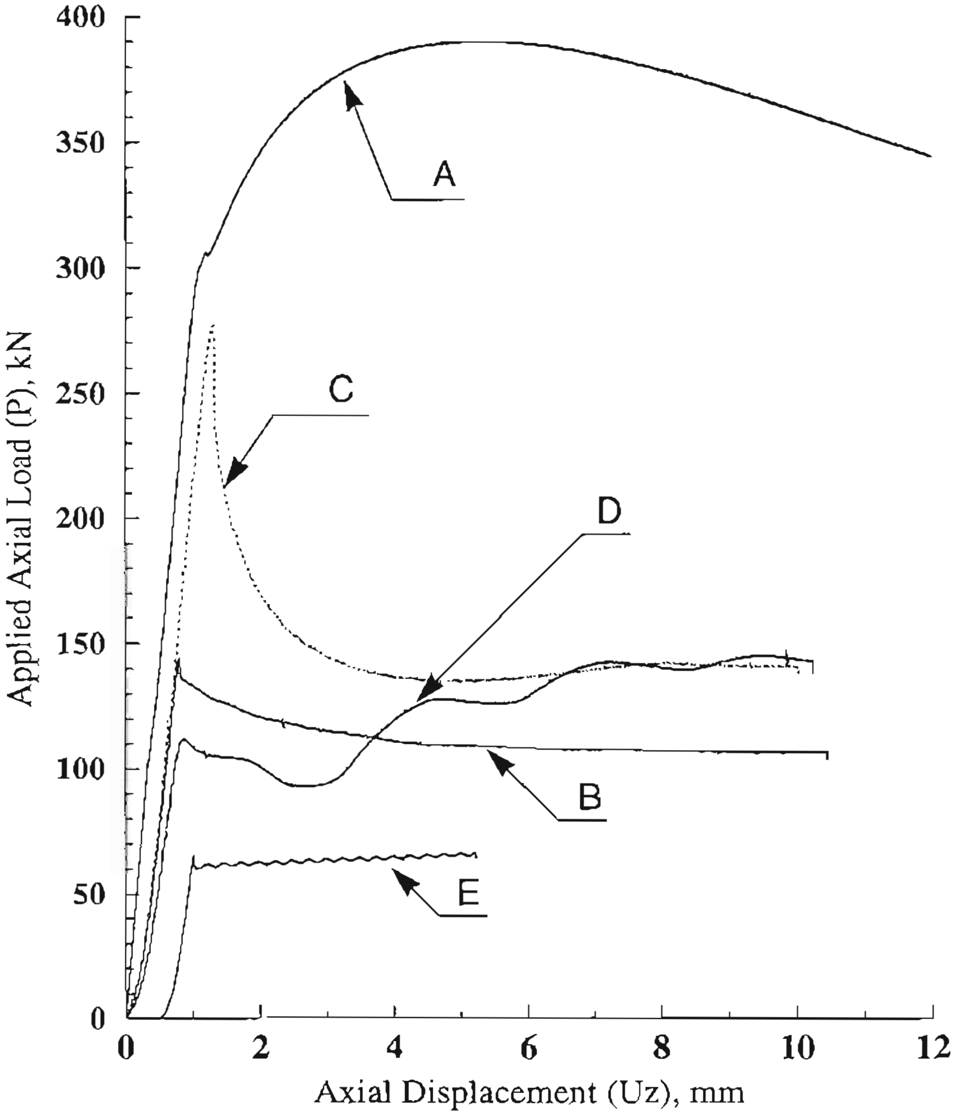

Figure 3.9 : Rod push-out test results for all insulators.

(a)

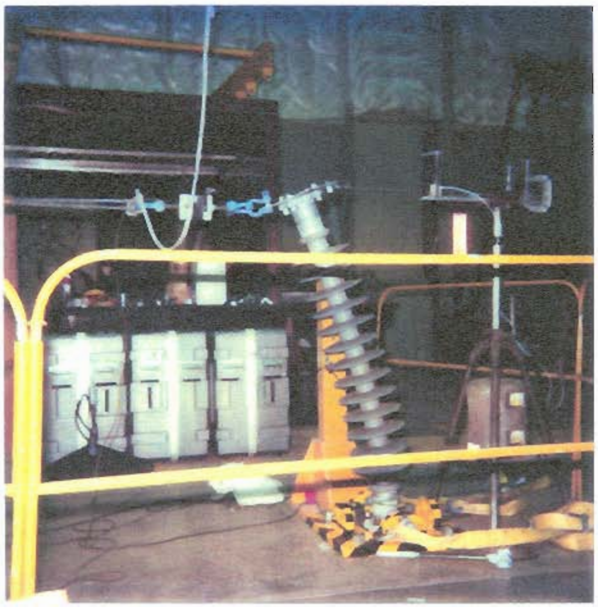

(b)

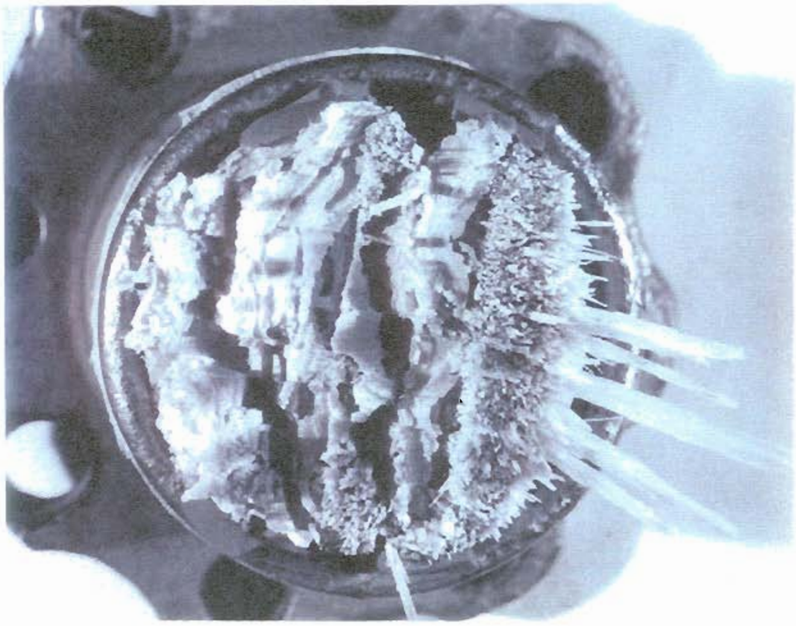

Figure 3.10 : Bending tests of composite substation insulators;

(a) An insulator being loaded, and

(b) Fracture surface of GRP rod.

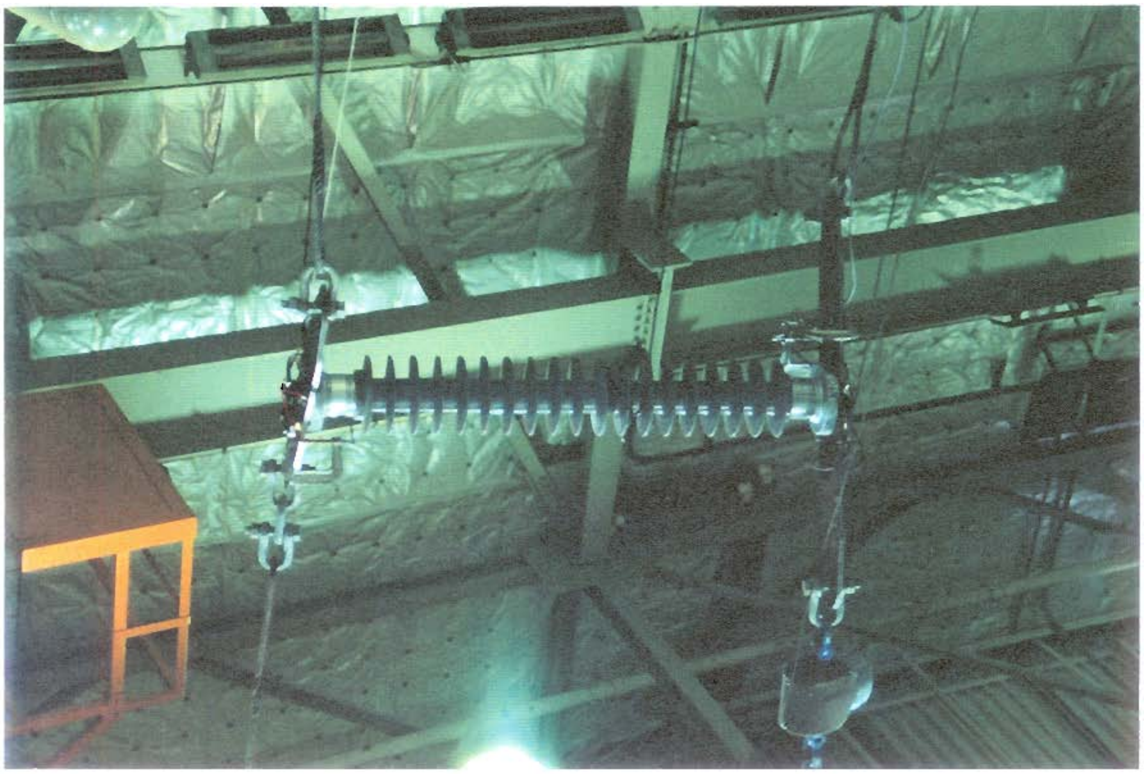

Figure 3.11 : Torsional loading of a composite substation insulator.

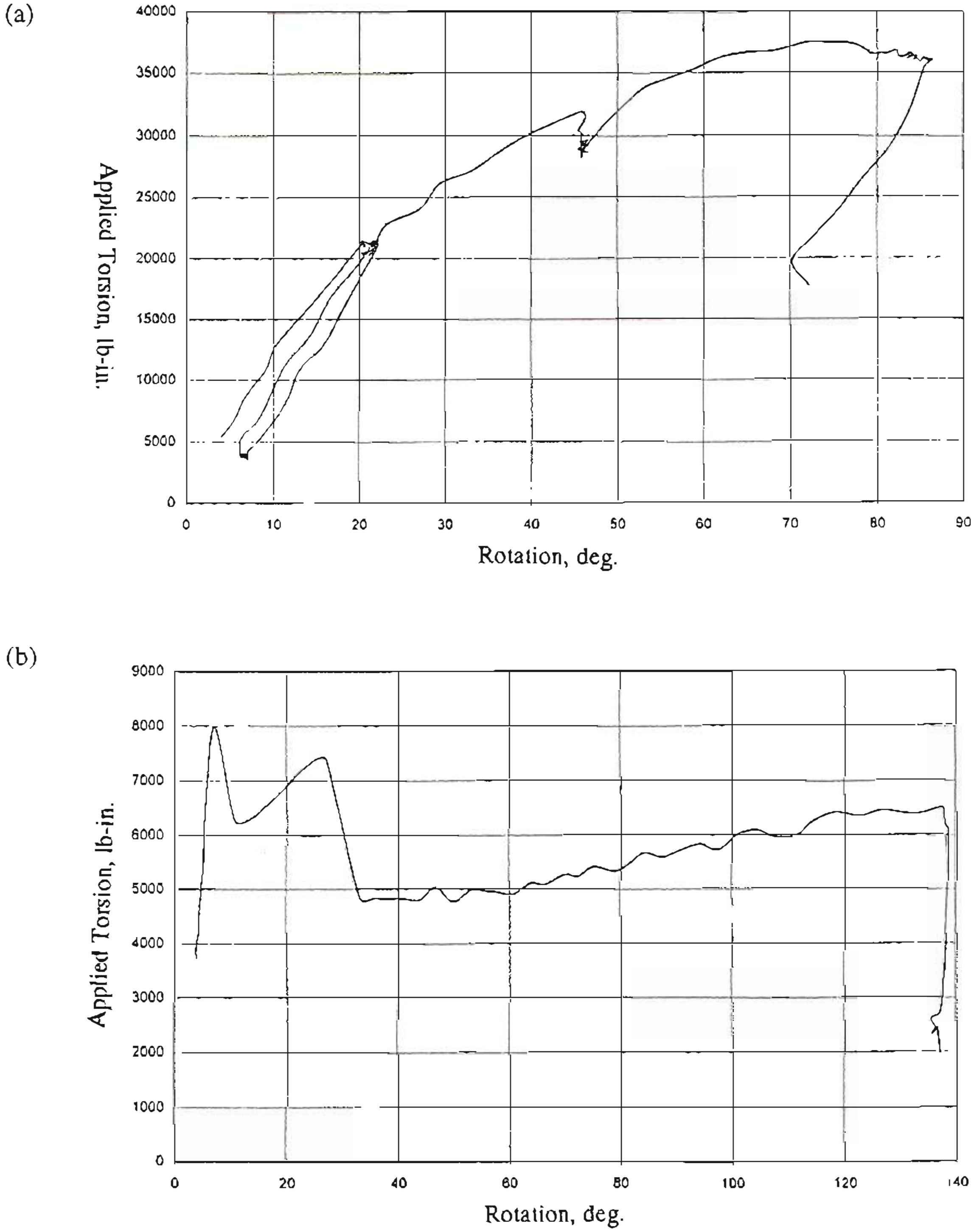

Figure 3.12 : Torsional load versus rotational displacement;
(a) For insulator A, and (b) For insulator E.

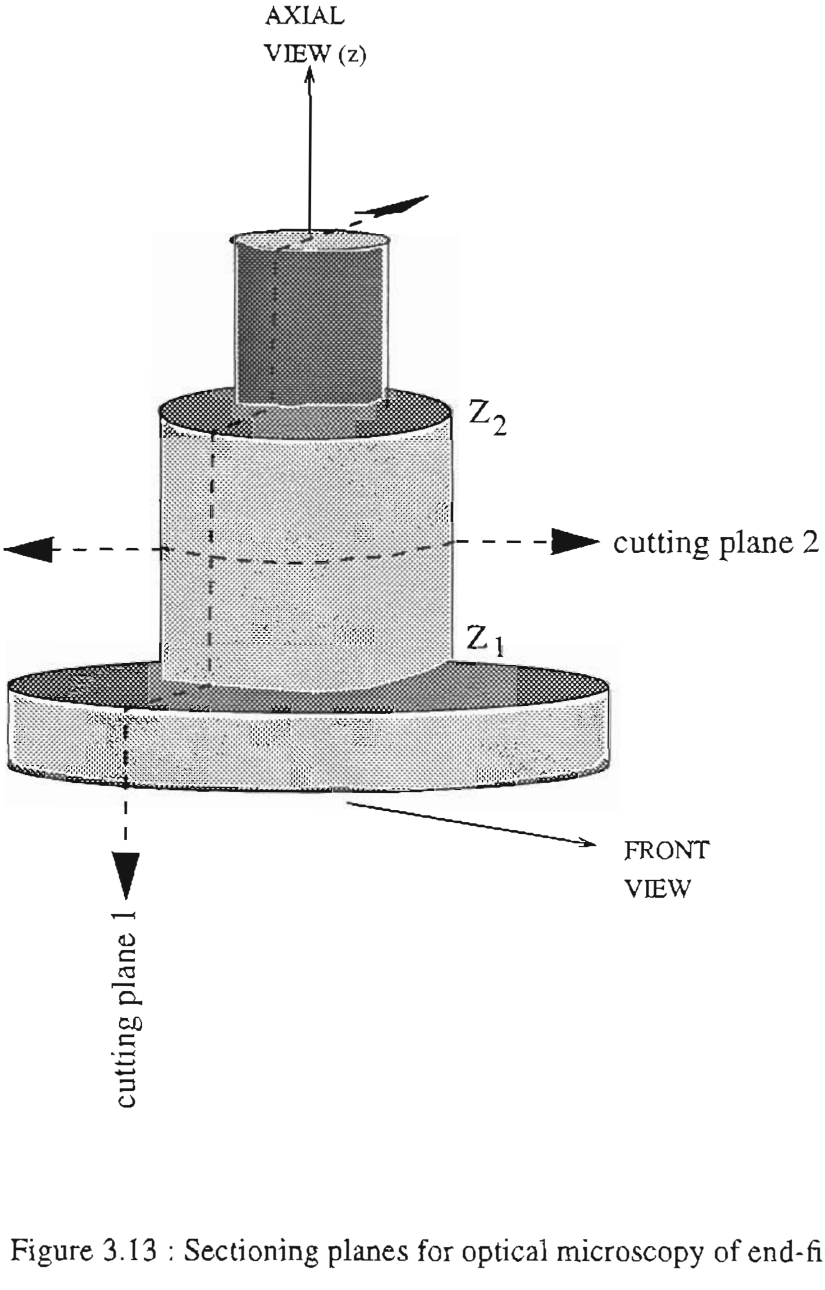

Figure 3.13 : Sectioning planes for optical microscopy of end-fittings.

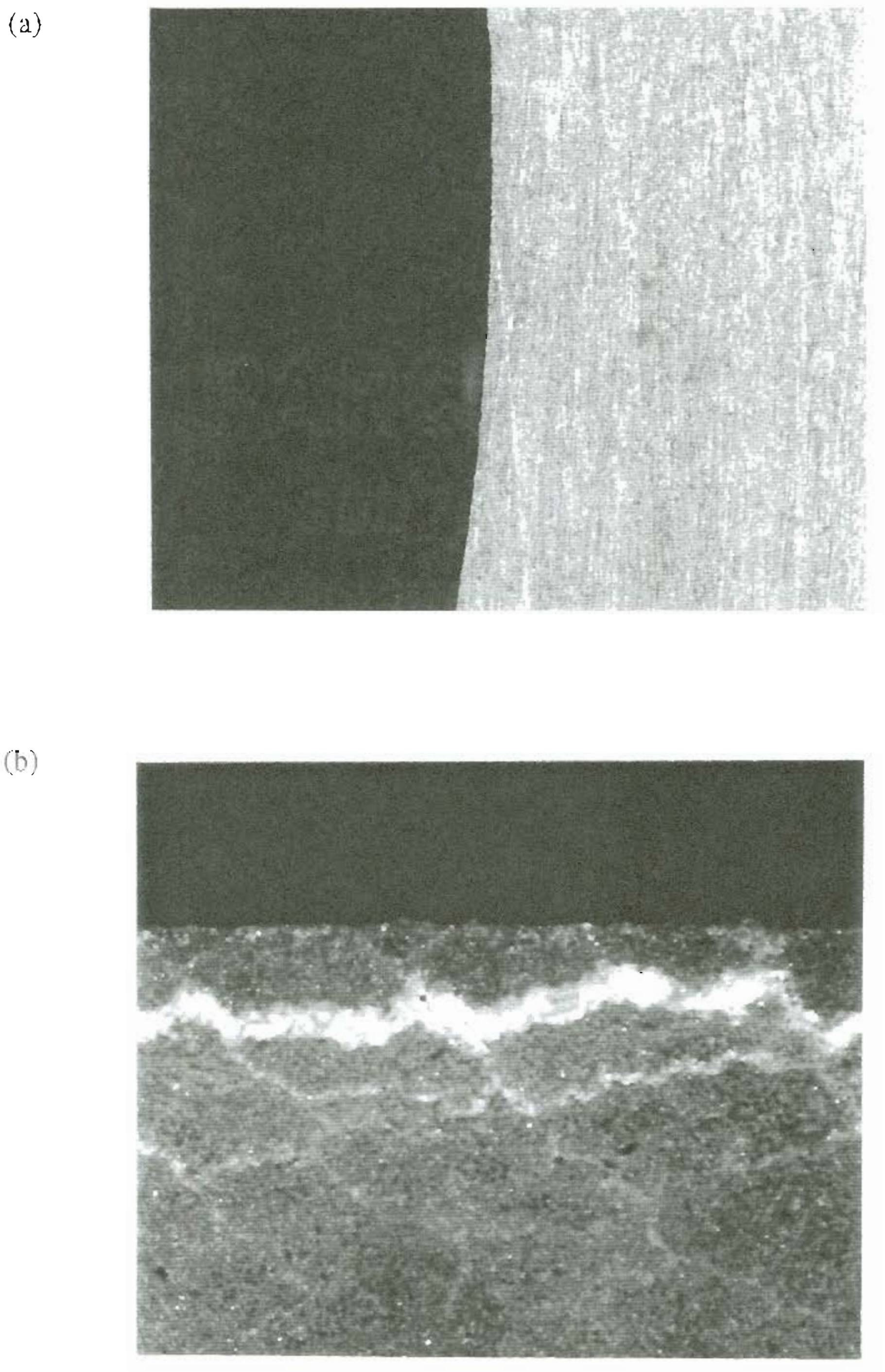

Figure 3.14 : Observations of Insulator A;
(a) Axial view of GRP-metal interface (10 x),
and (b) Network of circumferential micro-cracks in GRP-rod (75 x).

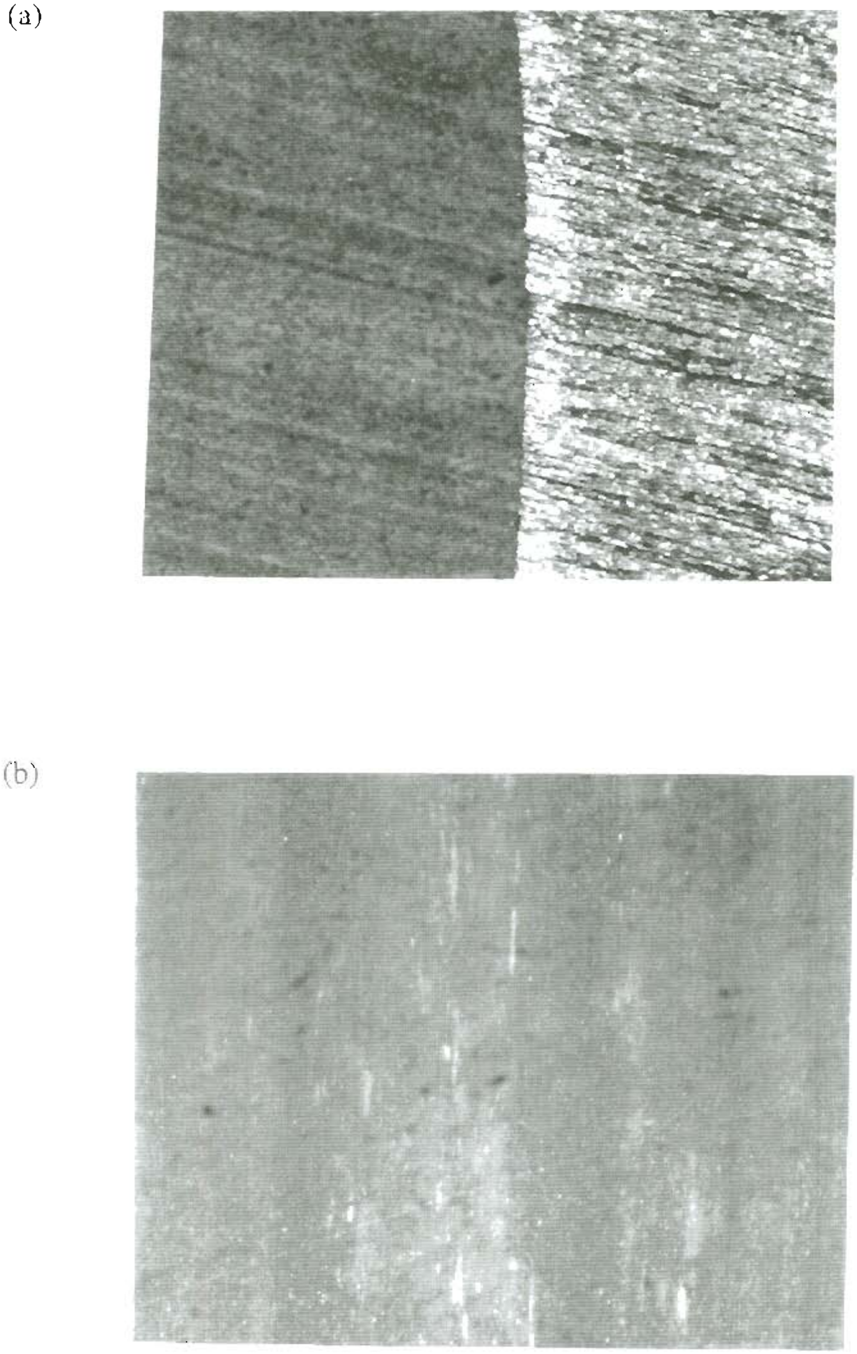

Figure 3.15 : Observations of Insulator B:
(a) Axial view of GRP-metal interface (15 x),
and (b) Micro-cracks at the center of the GRP-rod (20 x).

(a)

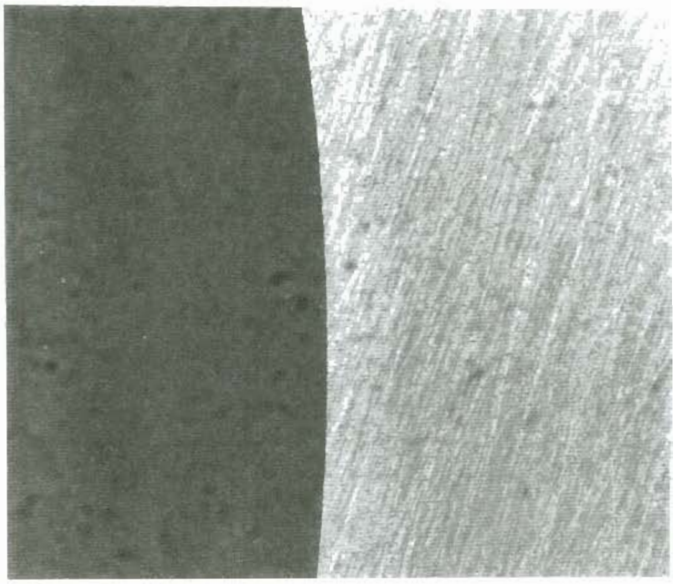

(b)

(c)

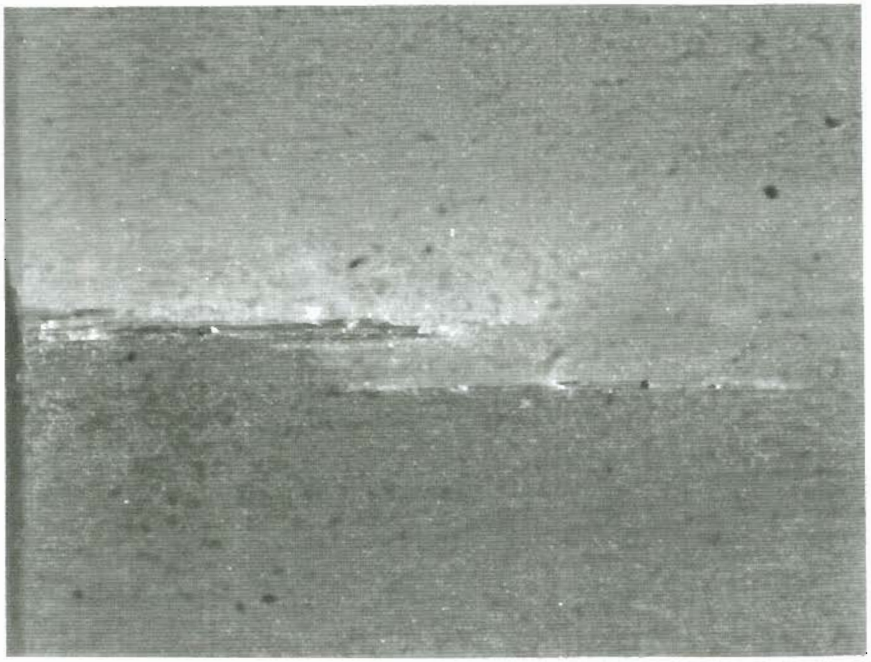

Figure 3.16 : Observations of Insulator C:

(a) Axial view of GRP-metal interface (10 x),

(b) Axial view of crack P from circumference towards center (60 x),

and (c) Front view of crack Q (60 x).

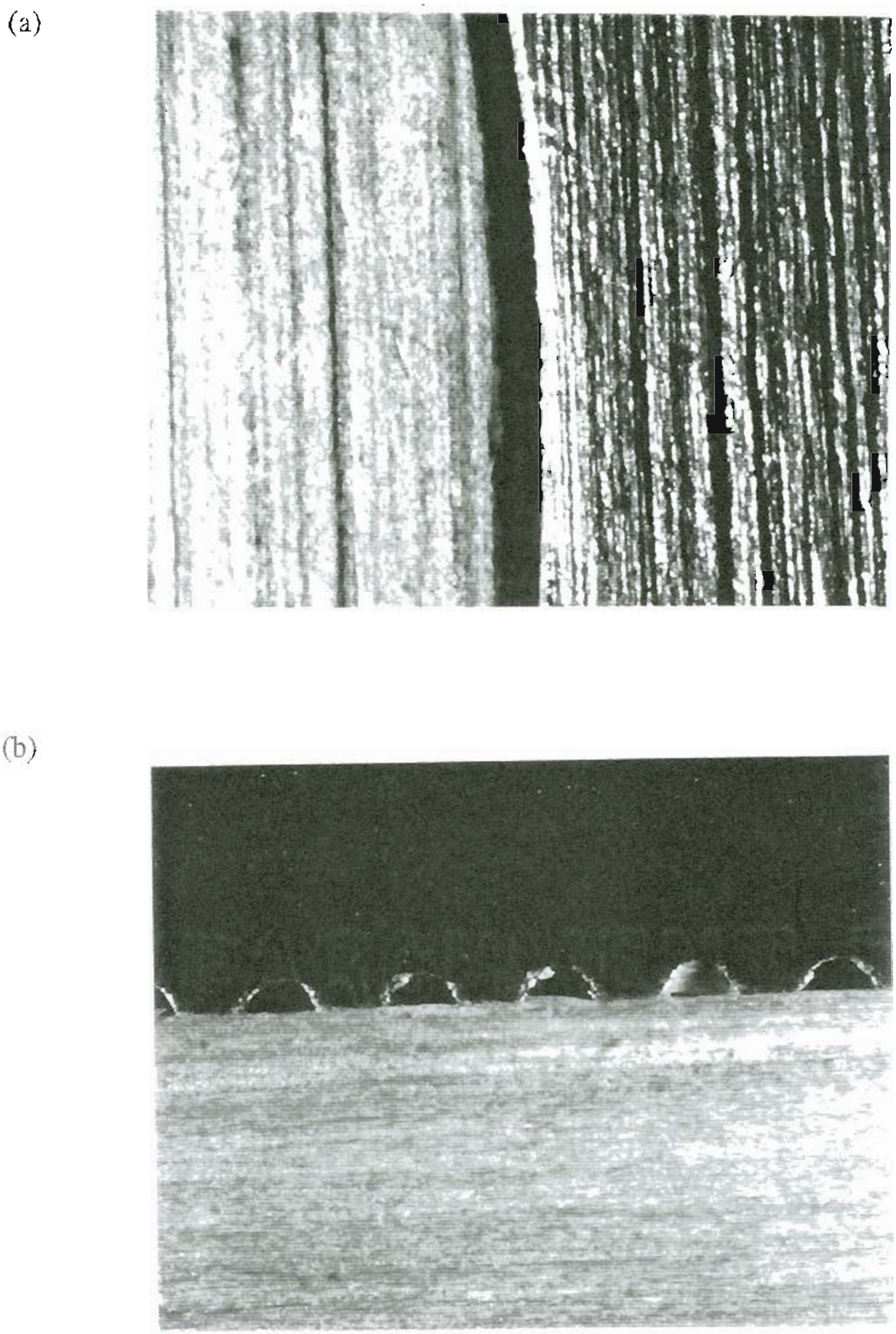

Figure 3.17 : Observations of Insulator D:
(a) Axial view of GRP-metal interface shows large separation (10 x),
and (b) Front view of GRP-metal interface shows u-shaped grooves (7.5 x).

(a)

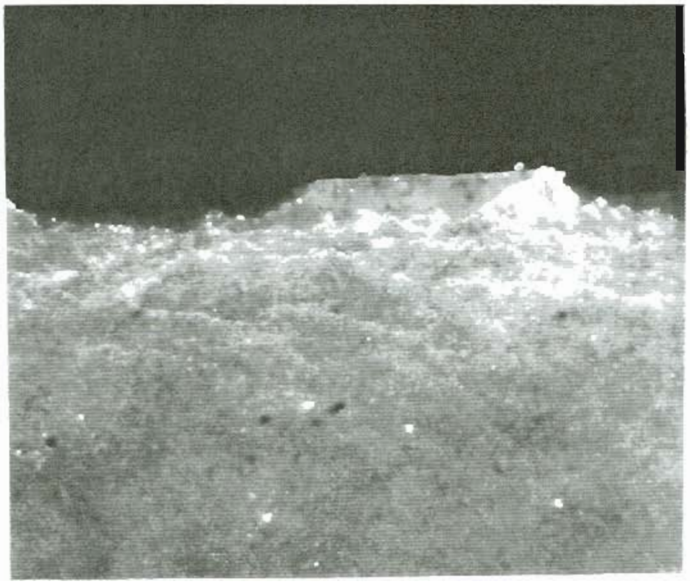

(b)

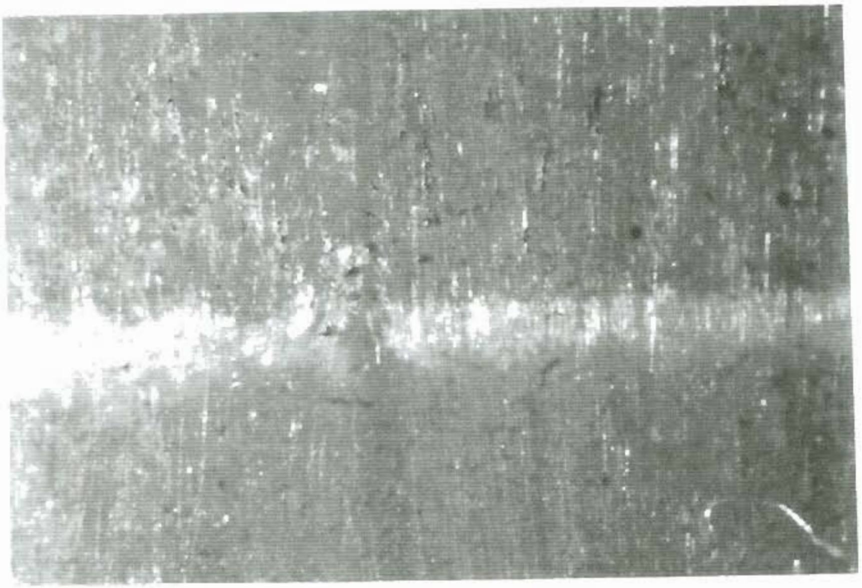

Figure 3.18 : Observations of Insulator D;

(a) Network of circumferential micro-cracks near GRP-metal interface (75 x), and (b) External surface of the GRP-rod shows damage zones (45 x).

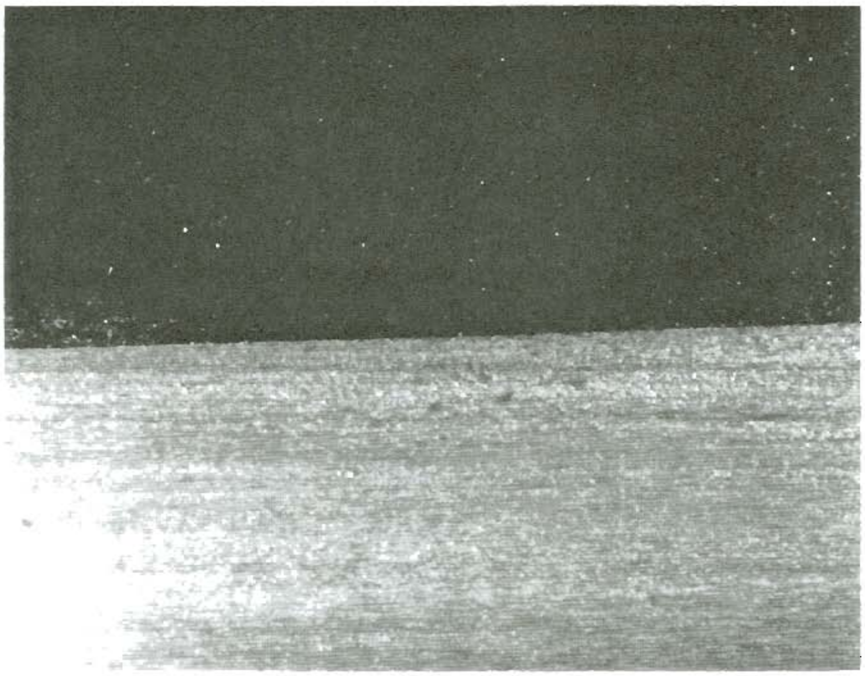

Figure 3.19 : Axial view of GRP-metal interface in insulator E (7.5 x).

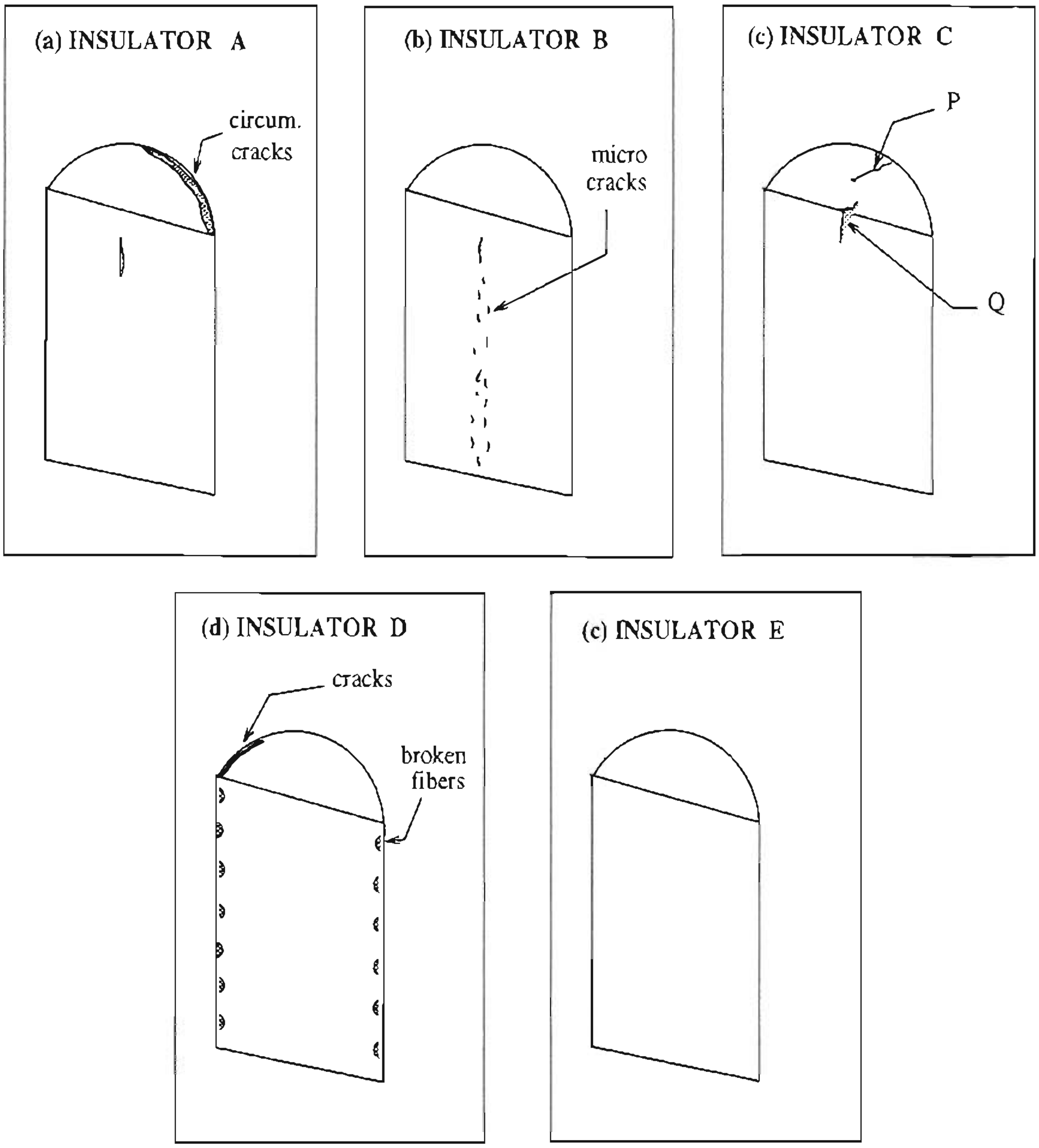

Figure 3.20 : Schematic of observed damage in GRP rods of all insulators.

Chapter 4

Finite Element Analysis of Composite Insulators

4.1. INTRODUCTION

Depending upon the type of application, composite insulators can be subjected to a wide variety of multi-axial loading conditions. As mentioned in chapter 1, suspension insulators are predominantly subjected to axial tension, with significant contributions from horizontal bending loads (caused by ice deposition and wind gusts) and torsional loads (see figure 1.2). Line post insulators are predominantly loaded in bending (see figure 1.3), and substation insulators are subjected to axial compression with very strong contributions of bending (figure 1.4).[121] In addition to the external multi-axial loads applied during service, the composite GRP rod is subjected to radial compression during the crimping process. In this chapter, detailed two- and three dimensional finite element models have been developed for analyzing the internal stresses and overall deformations of composite substation insulators subjected to several cases of multi-axial loads in service. In chapter 3, it was seen that the mechanical behavior of insulators A and E were significantly different under axial compression (section 3.3) and torsional loads (section 3.5). This was caused mainly due to the fact that their radial compression profiles were very different. The average magnitude of radial compression of insulator A (M_A = 0.176318 mm) was significantly larger than the average magnitude of radial compression of insulator E (M_E = 0.030533 mm). Therefore, in this chapter, particular attention has been given to insulators A and E for the finite element analysis. In chapter 6, these finite element models will be modified to simulate composite suspension insulators. Figure 4.1 shows the dimensions and loading components of a typical 115 kV substation insulator loaded in service.

In order to develop an accurate finite element model, the elastic properties of the GRP rod and metal end-fittings were required. In chapter 2 (section 2.1.1), the rule of mixtures and Halpin-Tsai equations were presented as a convenient analytical approach for estimating the elastic properties of unidirectional composite laminae. [17, 19, 20] These equations were therefore used to evaluate the complete set of elastic properties of the GRP material (see Appendix C). However, since these analytical tools are highly simplistic in nature, and since they cannot be used to estimate the strength properties, mechanical tests were required. In reference 121 the real elastic and strength properties were obtained by performing experiments on GRP composite specimens extracted from the GRP rod of insulator A. Tensile coupons were used to determine the longitudinal (E_{11}), and transverse Youngs moduli (E_{22} or E_{33}), and the Poisson's ratio (ν_{12}) in accordance with ASTM D 3039 - 76. The shear modulus (G_{12}) and the intralaminar shear strength (τ_{12}^{f}) were determined from the Iosipescu shear test.[121] The analytically estimated and experimentally measured elastic properties of the GRP composite of insulator A are compared in Appendix C. Clearly, there was considerable disagreement between the two approaches. For the finite element models developed in this chapter, the experimentally measured set of properties were used.

The finite element analyses of crimped joints, wherein interfacial bonding is purely due to mechanical compression, can be highly sensitive to the interface characteristics assumed in the model. The analyses have therefore been performed by assuming both, a perfectly bonded interface, and an imperfect interface, between the GRP rod and the end-fitting. The perfectly bonded interface is modeled as an abrupt material discontinuity which requires continuity of displacements across the interface. The imperfect interface, on the other hand, is a general contact problem with Coulomb friction and permissible internal sliding of the GRP rod within the end-fittings. All computations have been performed on an IBM RS 6000 workstation using the ANSYS finite element software (versions 5.0 and 5.1).[119]

4.2. AXISYMMETRIC ANALYSIS

In this section, axisymmetric finite element models are developed for analyzing substation insulators subjected to axisymmetric radial compression profiles (*i.e.,* only axially non-uniform radial compression), and only axial loads acting externally.

4.2.1. Perfect Interface Model

The perfectly bonded GRP-metal interface was modeled by nodal connectivity to ensure continuity of displacements across the interface. Figure 4.2 (a) shows the axisymmetric finite element mesh of one half of the insulator with the appropriate boundary conditions. The mesh consists of 1726 eight-noded isoparametric quadrilateral- and collapsed triangular elements with axisymmetric properties. Since the maximum stresses are expected to occur close to the lower end-fitting, the fillet radius (ρ) at the GRP-metal interface corner could have a significant influence on the computed stress concentration factors.[56] The perfect interface analyses were therefore performed for several edge-radii (ρ) ranging from 0 (perfectly sharp corner) to 3.5 mm (round corner). The elements close to the edge corner were 10% of the size of finite elements in other non-critical locations (see figures 4.2 a,b).

The base of the axisymmetric mesh was constrained against translation in the radial (r) and axial (z) directions, and the central axis of the rod was constrained in the radial direction. A state of uniform axial compression was applied from the mid-plane in the form of nodal displacements ($U_z = -1mm$). In addition, radial compression due to crimping was prescribed in the form of compressive radial displacements on the surface (z_1 - z_2) of the end-fitting. Since the analysis is axisymmetric, the tangential non-uniformity caused by the wave-like radial compression of insulator A could not be simulated (see figure 3.3 a). Only the axial non-uniformity was simulated by applying the fifth-order polynomial ($P_A(z)$) as described in section 3.2.2.

Figure 4.3 (a) shows the von-Mises equivalent stress (σ_{eqv}) along the path ABC perpendicular to the GRP-metal interface. It is obvious that the stresses are highly concentrated at the interface corner (point B), and bounded elsewhere in the GRP-rod. As would be expected, the magnitude of stress concentration is highly dependent on the fillet radius (ρ). Figure 4.3 (b) shows the magnitude of the maximum equivalent stress at the interface corner as a function of the fillet radius (ρ). The stresses are clearly highest for a perfectly sharp corner ($\rho = 0$), and progressively decrease as the corner radius is increased. Furthermore, for the case of a perfectly sharp corner, a mesh sensitivity analysis was performed to evaluate the influence of the degree of mesh refinement on the stress concentration factors. Figure 4.3 (b) clearly demonstrates that the calculated stresses increase asymptotically with a decreasing size of finite elements (ξ) at the interface corner. This trend indicates that the numerically obtained stresses at the interface corner may be misleading since the exact solutions, conforming to the theory of linear elasticity, will be approached only when the size of finite elements is made infinitesimally small ($\xi \rightarrow 0$). From figures 4.3 (a,b) it seems very likely that the actual stress field at the interface corner is either singular, or severely concentrated. In the next section, the finite element iterative method (FEIM) is used to evaluate the presence of the singular field.

4.2.2. Finite Element Iterative Analysis

Within the framework of linear elastic fracture mechanics (LEFM), several studies have demonstrated that the stress field at the interface corner of two perfectly bonded dissimilar elastic bodies could be singular in nature. [98-102] Since closed-form analytical solutions based on William's Airy stress function approach [97] are not presently available for isotropic-orthotropic material combinations, the finite element iterative method (FEIM) [104-108, 123] was used to solve the eigenvalue problem at a perfectly bonded GRP-Aluminum interface corner.

The FEIM algorithm was implemented by using the ANSYS parametric design language (APDL) [119] in order to compute the power of the corner singularity. Due to the highly localized domain of the singular zone, a generalized plane-strain condition was assumed for the linear-elastic analysis.

Figure 4.4 shows the fan shaped mesh constructed around the GRP-Al interface corner. The GRP rod was modeled as a homogeneous orthotropic medium which spans a wedge angle of 180^o. The isotropic aluminum end-fitting spanned an angle of 90^o. Ordinary eight-noded quadrilateral and six-noded triangular isoparametric elements were used. Considering the interface corner as the local origin of a polar coordinate system, the mesh shown in figure 4.4 consists of 69 rings of elements in the radial (r) direction, and 25 rays of nodes in the tangential (θ) direction. The radii of these rings followed an r^2 refinement. The outer-most ring had a radius (R_{out}) of 100. For the initial iteration, displacements $Ux_i^{(0)}$ and $Uy_i^{(0)}$ were prescribed at nodes along the outer ring (R_{out}).

Since the value of the singular power is independent of the magnitude of the far-field boundary conditions,[53] for a node (i) located at (r, θ), where $r = R_{out}$ and θ varies from 0 to 270°, we prescribed

$$Ux_i^{(0)} = 0.01\cos\theta \tag{4-1a}$$

and

$$Uy_i^{(0)} = 0.01\sin\theta \tag{4-1b}$$

This ensured a mixed-mode situation at the interface corner due to the combined presence of symmetric (mode I) and skew-symmetric (mode II) displacements. The iterative solution procedure was subsequently implemented as outlined in chapter 2 (section 2.4.3). Convergence was achieved when the value of the singular power (λ), along all 25 rays shown in figure 4.4, converged according to

$$\left|\frac{\lambda_i^{(m+1)} - \lambda_i^{(m)}}{\lambda_i^{(m+1)}}\right| \leq 10^{-5} \tag{4-2}$$

where, m indicates the iteration number, and i indicates the ray number (i = 1, 2, ...25).

The analysis was performed to evaluate value of λ as a function of the fiber volume fraction (V_f) of the E-glass/epoxy composite material. This was done by providing the value of V_f as an input parameter to calculate the elastic properties E_{11}, E_{22}, G_{12}, and ν_{12}. Considering the unidirectional composite as a homogeneous orthotropic material, the rule of mixtures and Halpin-Tsai equations [17, 19, 20] were used for V_f values in the range 1% to 99 %. The calculated elastic properties were subsequently supplied as input parameters to the generalized FEIM macro (created using APDL) which calculated the singular power.

In order to validate the FEIM algorithm for the GRP-aluminum interface corner, the singular power was first computed for the aluminum-aluminum material combination.

This case corresponds to a notch in isotropic media with a vertex angle of 270^o, which has been solved analytically by Williams.[97] Results presented in table 4.1 indicate that the numerical solution is in excellent agreement with the analytical solution. Two additional calculations were performed where the ratio of elastic moduli of the two isotropic materials ($E^{(1)}/E^{(2)}$) were 0.1 and 5. This case has been solved analytically by Hein and Erdogan.[100] Table 4.1 shows that these results were also in good agreement with the analytical solutions for an isotropic-isotropic bimaterial wedge. It can therefore be concluded that singulars powers (λ) computed for the isotropic-orthotropic material combinations will also be accurate.

Figure 4.5 shows the computed values of λ as a function of the volume fraction of E-glass fibers for our case of a perfectly bonded GRP-Al interface corner. The stresses are clearly singular in nature. The power of the singular field is only slightly lower than the classical square-root singularity, and seems to increase with the fiber volume-fraction, at least within the domain of structural composites (V_f = 40 to 80 %). For a GRP composite with a fiber volume fraction of 62 % (used in substation insulators), the computed value of λ was 0.4924.

The number of iterations required to achieve convergence was found to decrease with increasing fiber volume fractions (V_f) of the GRP-material. At $V_f = 99\%$, convergence was achieved in 10 iterations, whereas, at $V_f = 1\%$, up to 102 iterations were required for convergence. This was probably due to the stringent convergence criterion defined in equation (4-2). However, at the point of convergence, the singular powers obtained from all 25 rays were identical to the fourth decimal place.

From these results, it is clear that the assumption of perfect bonding (*i.e.*, continuity of displacements and no relative sliding) will lead to singular stress fields at the perfectly sharp interface corner. Even if the edge corner is assigned a finite fillet radius (ρ), on a micro scale, this condition will be equivalent to an interface crack which has been shown to exhibit a singular field at the crack tip. [106, 108] Further discussion of the singular behavior and the shape of the singularity dominated region is beyond the scope of this work.

4.2.3. Imperfect Interface Model

An imperfectly bonded interface will be simulated if the rod and end-fitting are treated as separate entities which exhibit discontinuous stresses and displacements across the interface, and, at sufficiently high loads, are capable of undergoing large relative sliding with frictional resistance. In this section, these conditions are satisfied by employing general axisymmetric point-to-surface contact elements at the bimaterial interface.

Unlike the linearized perfect interface solutions presented in section 4.2.1, a general contact analysis is significantly more expensive since the problem is structurally nonlinear and requires an iterative solution procedure. The nonlinearity stems from the fact that we assume no prior information about the local contact conditions *(ie, sticking, sliding, or open-gap).* Such solutions are frequently sought in the analysis of assembled components joined together by pure mechanical compression,[113, 116] where the classical Hertz solutions [14, 109] are not necessarily applicable.

Figure 4.6 (a) shows the modified axisymmetric finite element mesh of the composite substation insulator. The interface between the GRP rod and metal end-fitting was meshed with general surface-to-surface contact elements (CONTAC48 in ANSYS 5.0). A detailed description of the general contact algorithm was given in chapter 2 (section 2.5.2). Since the two bodies (*i.e.*, GRP rod and end-fitting) are expected to be in constant contact, and since they both have the same radius of curvature, the relative definition of the contact and target bodies was not very clear. Therefore, symmetric contact conditions were applied,[119] wherein one set of contact elements were generated by considering the GRP rod as the contact body and the metal end-fitting as the target body, and another set of elements by reversing the definition of the contact and target bodies. It should also be mentioned that the general contact elements could not be used with the eight-noded isoparametric elements employed in the perfect interface model. Therefore, the GRP rod and end-fitting had to be re-meshed with four-noded constant strain quadrilateral elements. Furthermore, since both sticking and sliding contact conditions must be considered, the elastic Coulomb friction model was adopted for the analysis. The mesh shown in figure 4.6 (a) consists of 78 contact elements and 240 four-noded quadrilateral elements.

The central axis of the rod was once again constrained in the radial direction, and the base of the end-fitting was constrained in all directions. The axially non-uniform radial compression function of insulator A ($P_A(z)$) was prescribed on the surface $z_1 - z_2$ of the end-fitting. A full Newton-Raphson iteration scheme was employed to obtain solutions with axial compression prescribed as displacements in 12 load-steps :

$$U_z = 0, -0.1, -0.5, -1.0, -1.5, -2, -3, -4, -6, -8, -11, \text{and } -15 \text{ mm.}$$

The first load-step ($U_z = 0$) corresponds to the case of pure radial compression applied to the insulator during the crimping process, whereas subsequent load-steps simulate the residual radial compression in conjunction with quasi-statically incremented axial compression applied during service. For the present analysis, the coefficient of static friction was assumed to be equal to the coefficient of dynamic friction (*i.e.*, $\mu_s = \mu_d$). This assumption is reasonable because during service, the onset of relative sliding between the GRP rod and the metal end-fitting will constitute failure of the substation insulator. Our main interest, therefore, lies in computing the internal stress distribution within the elastic (sticking) contact regime. Subsequent kinematics of sliding governed by the value of μ_d are relatively unimportant.

The non-linear problem was solved for several values of μ in the range 0.2 to 1.0. For the case of $\mu = 0.3$, figure 4.6 (b) shows a zoomed-in view of the original finite element mesh superimposed with the deformed structure after the 10^{th} load-step ($U_z = -8\ mm$). It is clear that the rod has experienced significant sliding into the end-fitting socket. The extent of relative sliding for all 12 load-steps (U_z = 0 to -15 mm) is graphically illustrated in figure 4.7. For all values of μ considered, sliding is minimal up to approximately 2 mm of applied axial displacement. Depending upon the friction coefficient, as the applied axial displacement is further increased, the extent of relative sliding will increase quite rapidly. Figure 4.8 shows the von-Mises equivalent stress distribution along the path ABC perpendicular to the GRP-Al interface for three load-steps. In contrast with the perfect interface solutions presented in section 4.2.1 (compare with figure 4.3), it is immediately apparent that the stresses are finite and discontinuous at the GRP-Al interface corner (point B). Figure 4.9 shows the individual stress components along the plane PQR (mid-plane of z_1 and z_2) where the extent of radial compression is expected to be highest. The non-linearity of the problem is evident since the internal stresses do not increase linearly as the applied axial displacement (U_z) is increased from -1 mm (in the linear sticking regime) to -8 mm (in the non-linear sliding regime). All the normal stresses (σ_r, σ_θ, and σ_z) are compressive in the GRP rod, and the magnitude of the radial (σ_r) and tangential stress (σ_θ) is almost identical in the rod.

4.2.4. Discussion

From the results presented so far, it is clear that the computed stress distribution strongly depends on the interface characteristics assumed in the finite element models. The perfect interface model shows large stress concentrations in the vicinity of the GRP-Al interface corner, with the magnitude of stress concentration rapidly decreasing with increasing fillet radii (ρ). However, from figure 4.3(b) it is apparent that the actual magnitudes of the corner stresses tend to increase exponentially with a decrease in the size of elements (ξ) employed in the finite element mesh close to the GRP-Al interface corner. Using the finite element iterative approach, it is found that the results obtained from a perfect interface model are misleading since the linear elastic solutions of a perfectly bonded GRP-Al interface result in a singularity at the interface corner.

The imperfect interface model employed general axisymmetric surface-to-surface contact elements to simulate relative motion, discontinuous stresses and displacements, and Coulomb friction at the interface. The non-linear problem required an iterative solution procedure for several load-steps with progressively increasing axial compressive displacement (U_z). Unlike the perfect interface solutions, the stresses at the GRP-Al interface corner were found to be bounded for all load steps considered. This is because relative sliding is initiated as soon as the applied axial load locally exceeds the limiting frictional force ($-\mu_s f_n$) defined by Coulombs law (section 2.5.2). The interfacial contact stresses are consequently relaxed, and the development of a singular zone is prevented at the interface corner. Table 4.2 summarizes the principal differences arising between the perfect interface and the imperfect interface models.

4.3. THREE DIMENSIONAL ANALYSIS

4.3.1. Introduction

In section 4.2, axisymmetric finite element analyses were performed for substation insulators subjected to externally applied axial compression, in conjunction with axially non-uniform internal radial compression. Since these insulators are subjected to combined multi-axial loads during service, three-dimensional finite element models will be required to analyze the multi-axial load cases. Seven different cases of multi-axial static loading were provided by the Bonneville Power Administration. [121]

(i) *Fault Current Forces:*

This condition represents the normal working load of a vertically mounted 115 kV substation insulator.

(ii) *Extreme Fault Current Forces:*

This represents the occasional overloading of an insulator without considering environmental factors.

(iii) *Extreme Wind Forces:*

This condition represents the normal working load of an insulator under extreme wind conditions (*e.g.*, hurricanes etc.). The forces have been estimated by assuming a wind speed of 160 km/hour, with a gust factor of 1.2.

(iv) *Wind with Glaze Ice:*

Extremely low temperatures cause a layer of ice to be deposited on the conductor, resulting in a higher static axial load on the insulator. The forces for this condition were estimated by considering 90 km/hour winds, with radial deposition of a 25.4 mm thick layer of glaze ice. The density of glaze ice is 910 kg/m^3.

(v) *Wind with Rime Ice:*

This condition represents a relatively less severe environment than case (iv). The wind speed is assumed to be 64 km/hour, with a 5 mm thick radial layer of rime ice which has a density of 240 kg/m^3.

(vi) *Seismic Condition:*

Substation insulators are required to be in service for approximately 50 years. This condition simulates the dynamic load amplification caused by earth-quakes. The forces were estimated by considering a downward thrust, resulting in an acceleration due to gravity of 3.92 $m/second^2$ (0.4 g), with 5 percent damping.

(vii) *Switch Torsional Force:*

At present, composite substation insulators are not being used in switch-gear applications since their torsional strength is uncertain. This condition was required to evaluate the possibility of switch-gear applications. A torque of 2480 Nm is the estimated load required to rupture a thin layer of ice deposited at one end of the insulator.

The above multi-axial load cases are combinations of uniaxial loads which include; axial compression (F_A), bending forces (F_B), insulator weight (F_C), wind forces (F_D), and torsional loads (M_T). Figure 4.10 (a) schematically illustrates the location and direction of these forces, and table 4.3 lists their individual values for all load cases. It may be noted that forces F_A, F_B, and M_T are active on the flange of the upper end-fitting, F_D acts along the entire length of the insulator, and F_C acts at the center of gravity. The following sub-sections describe the three-dimensional models developed in this study.

4.3.2. Global Insulator Model

A three dimensional global finite element mesh of composite substation insulators was constructed with the dimensions indicated in figure 4.1. The mesh shown in figure 4.10 (b) consists of 1200 eight-noded constant strain hexahedral elements. Since this model is significantly more computer intensive than the axisymmetric models described in section 4.2, the following assumptions were made:

(a) The GRP rod is perfectly bonded to the end-fitting (*i.e.,* continuous stresses/displacements, and no relative sliding).

(b) The GRP rod is a homogeneous orthotropic structure with higher stiffness (E_{11}) in the axial (z) direction, and equal stiffnesses ($E_{22} = E_{33}$) in the x- and y-directions perpendicular to the axis of the rod.

(c) The interface corner between the GRP rod and end-fitting is perfectly sharp ($\rho = 0$).

(d) The rubber weathersheds covering the GRP rod, and the bolt holes in the flanges of the end-fittings, have a negligible contribution on the overall deformation and stress distribution of insulators.

(e) All loads applied to the insulator are static in nature.

Similar to the axisymmetric models, the flange of the lower end-fitting was constrained against translation in the radial (r), tangential (θ), and axial (z) directions. The axial compressive load (F_A) was applied as a uniform external pressure acting into the surface of the upper end-fitting. The bending load (F_B) was prescribed along the +y direction. The value of F_B was divided by the number of nodes on the top-most surface of the upper end-fitting, and uniformly applied to all nodes on the surface. The insulator weight (F_C) had to be applied such that the top-most part of the insulator was unstressed, with the axial load increasing linearly in the downward direction. The lower-most end of the insulator should experience the complete weight (F_C) of the insulator. Clearly, this type of distribution cannot be obtained by prescribing a vertical point force (F_C) at the center of gravity. Therefore, an indirect approach had to be employed. A hypothetical density of the GRP rod was determined as

$$Density = \frac{F_C}{g \ x \ volume \ of \ GRP \ rod} \tag{4-3}$$

This value of density was specified as a material property for the GRP rod, and an acceleration due to gravity ($g = 9.8 \ m/s^2$) was applied to the model in the upward ($+z$) direction. This resulted in nodal reaction forces which simulated the linear distribution of axial forces caused by the weight of the insulator. It should however be noted that this approach assumes that the entire weight of the insulator is due to the GRP rod, and the end-fittings are weightless. The wind forces (F_D) could act in any direction along the xy-plane. However, the worst case would be simulated by applying F_D in the +y direction, thereby complementing the applied bending forces (F_B). The total force due to F_D was uniformly applied in the +y direction on a surface of the GRP rod, which spanned the entire exposed length of the rod and subtended an angle of 60^o towards the central axis of the rod. The torsional load (M_T) was applied along the circumference of the top surface of the end-fitting. This was accomplished by applying tangential forces (F_T) to all twelve nodes along the circumference given by

$$M_T = 12\, F_T\, x\, r \tag{4-4}$$

where, r is the radius of the end-fitting flange.

It should be noted that in addition to the external loads applied during service (table 4.3), internal radial compression due to crimping had to be simulated. For the axisymmetric analysis described in section 4.2, an average radial compression polynomial $P_A(z)$ was used since the tangential non-uniformity of the radial compression profile of insulator A could not be simulated. However, in the present three-dimensional model, the applied radial compression profile was both axially and tangentially non-uniform. The wave-like profile of insulator A (see figure 3.3 a) was simulated by alternately applying the averaged displacement functions of the maxima ($P_{A,\max}(z)$) and the minima ($P_{A,\min}(z)$), separated by 30^o along the circumference of the end-fitting. This generated the "wave-like" profile of insulator A, with six maxima and six minima. Furthermore, the polynomials $P_{A,\max}(z)$ and $P_{A,\min}(z)$ were selected such that the average magnitude of radial compression applied to the GRP rod in the model was equal to the experimentally determined value for insulator A (M_A = 0.176318). Unfortunately, these radial displacements could only be applied to the external surface of the lower end-fitting. This is because displacements are the primary degrees of freedom in the finite element model. Therefore, radial displacements $U_r(\theta, z)$ applied to the upper end-fitting would act as constraints against further deformation of the insulator caused by the external loads. However, the fact that radial compression due to crimping was applied only to the lower end-fitting should have a negligible effect on the overall displacement of the insulator model, and the internal stresses (near the lower end-fitting). The global three-dimensional model was solved for all seven cases of multi-axial loading conditions. From the boundary conditions applied, it is evident that the maximum displacements are expected to occur at the upper end of the insulator, while the maximum stresses will occur near the lower end which is constrained.

4.3.3. Non-linear Sub-model of End-fitting

The global insulator model described in the previous section was linear, since it assumed that the GRP rod is perfectly bonded to the end-fitting (*i.e.,* no relative sliding). In addition, it assumed that the interface corner between the rod and end-fittings is perfectly sharp ($\rho = 0$). As demonstrated in section 4.2, these assumptions will lead to inaccurate stress results in the vicinity of the GRP-Al interface corners, since the true stresses predicted by the theory of linear elasticity are singular in nature. Therefore, the global three-dimensional model can only be used to compute the overall deformation of an insulator under various loading conditions. In order to obtain the accurate stress distribution near the end-fittings, a three-dimensional structurally non-linear model, with an imperfect interface between the rod and end-fittings, will be required. In this section, a three-dimensional non-linear sub-model was developed with an imperfect interface. The sub-model was created in order to avoid the computational expense of a full non-linear insulator model. Only the region close to the lower end-fitting was considered since the maximum internal stresses are expected to occur near this end. Furthermore, the mesh was refined (in comparison with the global model) in the tangential direction.

The sub-modeling scheme is based upon Saint Venant's principle [14] which states that if an actual distribution of forces or displacements applied to a structure is replaced by a statically equivalent system, then the distribution of internal stresses or strains is altered only near the region of load application. Figures 4.11 (a,b) show the finite element mesh of the submodel, which consists of 816 conventional eight-noded hexahedral elements with 288 three-dimensional surface-to-surface contact elements (CONTAC49 in ANSYS 5.0[119]) at the interface. These elements are the three-dimensional counterpart of the contact elements used in section 4.2.3. They can be used to simulate Coulomb friction and internal sliding of the GRP rod in the axial (z) as well as tangential (θ) directions. For the present analysis of the seven multi-axial load cases, the coefficient of friction (μ) was assumed to be 0.3. The following step-wise procedure was employed for all loading conditions.[119]

Step 1 : For each load case, the *linear* global insulator model was created, external forces and constraints were applied, and the model was solved.

Step 2 : The finite element mesh of the *non−linear* submodel was created with three-dimensional general surface-to-surface contact elements at the GRP-Al interface.

Step 3 : The top surface of the GRP rod in the sub-model was defined as the "cut-boundary". This was done by writing the node numbers on the surface, and their locations (r, θ, z), to a file called *submodel.node*.

Step 4 : The database of the global insulator model was resumed, and the file *submodel.node* was read. Based upon the nodal locations stored in this file, the displacement solutions of the global model (u_r, u_θ, u_z) were obtained at each location and saved in a file called *global.cbdo*. Note that the nodal locations in *submodel.node* did not have to coincide with nodes in the global model since the displacement solutions can be obtained at any location from the element shape functions.

Step 5 : The database for the sub-model was resumed. The base of the end-fitting was constrained in all directions, and radial displacements due to crimping (6 maxima and 6 minima of insulator A) were prescribed on the external surface of the end-fitting. The file *global.cbdo* was read in order to apply the displacements from the global model, along the cut-boundary plane, as displacement boundary conditions to the sub-model. The sub-model was subsequently solved to obtain internal stresses near the lower end-fitting.

Figure 4.12 schematically illustrates the transfer of displacements from the global model to the sub-model. Since the sub-model is non-linear, the iterative solution procedure adopted was the same as for the axisymmetric imperfect interface model (section 4.2.3). For each loading condition approximately 12 to 15 iterations were required for convergence.

4.4. VERIFICATION OF MODELS

In this section, an attempt is made to verify the axisymmetric and three-dimensional finite element models with experimental results obtained under axial compression, bending, and torsional loads.

4.4.1. Under Axial Compression

In section 4.2, the axially non-uniform average radial compression polynomial $P_A(z)$ was applied to the end-fitting of the axisymmetric models in conjunction with axial loads. Figure 4.13 (a) compares the experimental rod push-out test result of insulator A with the load-displacement curves computed from the axisymmetric perfect- and imperfect interface models. The assumption of a perfect interface is clearly inappropriate since the true response is structurally non-linear due to sliding of the GRP rod within the end-fitting. Furthermore, the slope of the linear response from the perfect interface model is found to depend on the fillet radius (ρ) employed in the finite element mesh. The imperfect interface model, on the other hand, is capable of simulating the contact non-linearity. At a friction coefficient of $\mu = 0.3$, the computed load-displacement curve is found to be in excellent agreement with experimental results. It may be noted that the coefficient of static friction between the GRP rod and the internal surface of the Al end-fitting was experimentally estimated to be 0.32.

In section 4.3.3, a three-dimensional sub-model was developed with an imperfect interface. In this case, radial compression was applied in the form of six maxima ($P_{A,max}(z)$) and six minima ($P_{A,min}(z)$) to simulate the axially and tangentially non-uniform profile of insulator A. In order to verify this three-dimensional simulation, axial compression was applied to the sub-model in twelve load-steps. Figure 4.13 (a) shows that the load-displacement response of the three-dimensional imperfect interface model is also in good agreement with the rod push-out test results for insulator A.

The same approach was now applied to insulator E. In chapter 3, it was seen that insulator E has the lowest radial compression (M_E = 0.030533 mm), and consequently the lowest axial load at the onset of sliding (P_f = 64.5 kN). Since the radial compression profile was almost completely uniform, a uniform radial compression was applied to the axisymmetric imperfect interface model with an average magnitude of M_E. Figure 4.13 (b) shows the experimental rod push-out test results of insulator E with load-displacement curves calculated at μ = 0.3, 0.7, 0.75, and 0.8. It is apparent that at a coefficient of friction of 0.75, the experimental and computed results are in good agreement. Since the magnitude of radial compression was very low, if the GRP-metal interface had a friction coefficient of $\mu = 0.3$ (as in insulator A), then failure due to internal sliding would have occurred at only 10 kN. In other words, the high frictional resistance in insulator E was primarily responsible for sustaining an axial load of 63 kN prior to internal sliding. Such a large value of μ seems reasonable since the internal surface of the end-fitting was found to be grooved in chapter 3 (section 3.6).

From these results, it can be concluded that the structural non-linearity of insulators, and the axial loads at the onset of internal sliding (P_f), can be accurately computed by using either the axisymmetric or three-dimensional imperfect interface models, provided that the average magnitude of radial compression (M) and the coefficient of friction (μ) assumed in the model are accurate.

4.4.2. Under Bending Loads

In chapter 3 (section 3.4), mechanical tests were described for insulators A, C, and D loaded in bending.[122] In order to verify the *linear* three-dimensional global insulator model, the model was solved under a pure bending load (F_B), with all other forces (F_A, F_C, F_D, and M_T) set to zero (see figure 4.14 a). Figure 4.14 (b) shows that the computed load-displacement response is in excellent agreement with the experimental results of insulators A, C, and D up to a load of 8 kN. It can therefore be concluded that the global three-dimensional insulator model (with a perfect interface) can be used to accurately determine the overall displacements of an insulator for all other cases of multi-axial loading conditions.

4.4.3. Under Torsional Loads

In order to verify the three-dimensional global and sub-models under torsion, the models were solved under a pure torsional load (M_T), with all other forces (F_A, F_B, F_C, and F_D) set to zero. The maximum torsional rotation (in degrees) was obtained from the global insulator model, and the maximum shear stress ($\tau_{\theta z}$) was obtained from the non-linear sub-model.

For an *isotropic* cylindrical rod of length l and radius r subjected to pure torsional loads, the angular displacement (u_θ) and the maximum shear stress ($\tau_{\theta z}$) can be obtained from the theory of elasticity by[14]

$$u_\theta = \left[\frac{M_T \, l}{\frac{\pi}{2} r^4 \, G} \right] \tag{4-5a}$$

and

$$\tau_{\theta z} = \left[\frac{M_T}{\frac{\pi}{2} r^3} \right] \tag{4-5b}$$

where M_T is the applied torsional load in Nm, and G is the shear modulus of the cylindrical rod. Although these equations are valid only for a simple isotropic rod with no radial compression induced by end-fittings, they may be used to approximately determine the torsional behavior of composite insulators. Equations (4-5) are expected to be applicable because the GRP composite rod is transversely isotropic (in the (r, θ) plane). Considering the typical dimensions of the GRP rod in substation insulators (l = 1.143 m, r = 0.0316 m and $G = G_{23} = 3.897 \times 10^9 \ N/m^2$), figure 4.15 shows that the numerical results agree fairly well with the linear elastic solutions for an isotropic rod. Both the shear stress and rotational displacement agree from the two approaches. In addition, upon converting the units, it can be seen that up to a torsional load of 2480 Nm, the rotations shown in figure 4.15 are in agreement with the experimental results obtained in chapter 3 (section 3.5) for insulator A.

4.5. RESULTS AND DISCUSSION

From the results presented thus far, it is clear that a perfect interface model is inappropriate for determining the maximum stresses in composite insulators, since these stresses are theoretically singular if the GRP-metal interface is assumed to be perfectly bonded. Furthermore, a perfect interface model predicts a linear structural response. On the other hand, both the axisymmetric model and the three-dimensional sub-model are found to be capable of simulating the structural non-linearity of insulators, caused by internal sliding of the rod within the end-fitting. The maximum axial load (P_f) at the onset of internal sliding can be accurately determined, provided that the magnitude of radial compression and the coefficient of friction assumed in the model are accurate.

This section presents the internal stresses and overall deformations obtained from the three-dimensional analysis of insulator A. The results are presented for pure crimping forces (with no external loads), and the seven multi-axial load cases described in section 4.3.1. The internal stresses have been determined from the sub-model with an imperfect interface, while the overall displacement results have been computed from the global insulator model with a perfect interface. Furthermore, since failure of the metal end-fittings due to stress concentrations are highly unlikely and have never been reported in the literature (except due to fatigue), only the stresses within the GRP rod are described in this section. The maximum deformation of the insulator, and the location of the nodes encountering these displacements are presented in table 4.4. Table 4.5 lists the maximum and minimum values of the six stress components under all loading conditions. In the following sub-sections, the computed stress components will frequently be compared to the failure strengths of the E-glass/epoxy composite which are given in appendix C. It should be noted that all the stress and displacement components conform to a cylindrical coordinate system (r, θ, z) with the origin at the geometric center of the GRP rod.

4.5.1. Crimping Forces

This load case includes the effects of radial compression caused by crimping only. Figures 4.16 (a, b, c, and d) show the iso-stress contours for the normal stresses σ_r (radial), σ_θ (tangential), σ_z (axial), and the shear stress $\tau_{r\theta}$ respectively. It is evident that the crimping applied to insulator A will cause large compressive radial and tangential stresses in the GRP rod close to the interface. In chapter 3 (section 3.6), optical microscopy of the GRP rod of insulator A showed internal micro-cracks near the GRP-Al interface. However, since these cracks were observed after the rod had been subjected to the push-out tests, their cause remained uncertain.

Since the axial stress (σ_z) in the rod within the end-fitting is mostly tensile in nature, and since the magnitude of σ_z is very low in comparison with the axial tensile strength (σ^f_{11}), the stress state in the GRP rod is biaxial compression. The magnitude of σ_r (-176 MPa) is clearly larger than the transverse compressive strength of the composite ($\sigma^f_{22,C}$ = -140 MPa). However, this strength value found in the literature, [17] was obtained by subjecting hoop-wound glass/epoxy composite tubes to axial compressive stresses. The transverse compressive strength of -140 MPa is therefore applicable only under *uniaxial compression*. Since the stress state of the GRP rod within the end-fitting is *biaxial compression*, with very large radial and tangential compressive stresses, the strength of the composite is expected to be higher than the strength uniaxial transverse compression. This is because unidirectional composite materials fail in a shear mode under uniaxial transverse compression. [17] Under biaxial compression, the material will be constrained in both the radial and tangential directions, thereby resulting in a higher resistance to failure. At this point, the biaxial compressive strength of the GRP material is not known, and needs to be determined in future study. Despite the fact that the radial stresses (σ_r) caused by crimping are as large as -176 MPa, it is not certain if these stresses are large enough to generate compressive damage in the GRP rods of insulator A.

4.5.2. Fault-Current Forces

This load case involves mainly bending forces, with some contribution from axial compression. The iso-stress contours of the normal stresses σ_r and σ_θ, and also the three shear stress components, were found to be almost completely identical to the case of pure crimping presented above (refer table 4.5). However, due to the bending force (F_B), the values of axial stress (σ_z) were tensile along one edge of the rod and compressive at the opposite edge (refer table 4.5). While the maximum and minimum values of σ_z occurred in the GRP rod outside the end-fitting, their magnitudes were small in comparison with the axial tensile and compressive strengths of the composite.

4.5.3. Extreme Fault-Current Forces

This load case is the most severe as far as bending forces are concerned ($F_B = 9990$ N). Once again, the stress contours of σ_r, σ_θ, and $\tau_{r\theta}$, were found to be identical to the case of pure crimping. Due to the severe bending, the axial stress σ_z outside the end-fitting region was tensile at one edge (429 MPa) and compressive at the other (-384 MPa) as shown in figure 4.17 (a). These stresses are below the axial tensile and compressive strength of the composite. The bending also caused large shear stresses τ_{rz} and $\tau_{\theta z}$ at the center of the rod (figure 4.17 b). These stresses are quite close to the intralaminar shear strength (τ_{12}^{f}) of 60 MPa. Furthermore, the biaxial residual compressive stresses (σ_r and σ_θ) induced due to crimping, are quite large. The bending also causes a total deflection of 152 mm (see table 4.4). This load case may therefore require some caution. However, since it represents the extreme load on an insulator (expected only once in a few years), it appears that the insulator will withstand the load.

4.5.4. Extreme Wind Forces

The stress components σ_r and σ_θ were once again identical to the case of pure crimping forces. The axial stress (σ_z) and shear stress components were lower than the case of extreme fault current forces (described above). Therefore, with the exception of the residual biaxial compressive stresses generated during crimping, the external load caused by wind gusts will not initiate failure.

4.5.5. Wind With Glaze Ice

The total axial compression (F_A) of 1740 N makes this loading case the most severe in axial compression. However, since the GRP-rod is reinforced in the axial direction, the axial stresses were found to be quite low in comparison with the expected axial compressive strength of the GRP rod (see figure 4.18). The stresses caused by crimping, σ_r and σ_θ, were still the same. All shear stress components were within safe limits.

4.5.6. Wind with Rime Ice

This case of external loading did not seem to have any influence on the internal stress distribution. All stress components in the GRP rod were similar to those generated during crimping.

4.5.7. Seismic Forces

For this condition, crimping was still the dominant factor. All stress components, except σ_z, were identical to the case of pure crimping. Due to the small bending forces, the axial stress in the rod outside the end-fitting region (σ_z) was tensile at one edge, and compressive at the other. The magnitudes of all stress components, except the biaxial compressive stresses due to crimping, were well below the strength values of the composite.

4.5.8. Switch Torsional Force

For this loading case, in addition to the crimping forces, a torsional load of 2480 Nm was prescribed on the upper end-fitting. The maximum tangential displacement given in table 4.4 translates to a rotational displacement of 23.8^o. In spite of the severe torsional twisting of the rod (figure 4.19 a), all normal stresses σ_r, σ_θ, and σ_z, were identical to the case of pure crimping forces. The shear components $\tau_{r\theta}$ and τ_{rz} were also found to be identical to pure crimping. However, figure 4.19 (b) shows that the shear stress $\tau_{\theta z}$ is very significantly affected outside the end-fitting. The value of $\tau_{\theta z}$ is very low at the center of the rod outside the end-fitting, and rapidly increases to approximately 48 MPa at the surface. It may be noted that the shear strength of the GRP material in the transverse plane ($\tau^f{}_{23}$) is not available. Usually it is approximately 10% lower than the shear strength in the 1-2 and 1-3 planes (τ^f_{12} = 60 MPa in table C.1). Torsional loads of 2480 Nm can therefore lead to the initiation of intralaminar splits on the surface of the rod. This situation is further aggravated by the fact that the large shear stresses occur outside the end-fitting. Therefore, if these splits nucleate, they will be located outside the end-fitting, and their propagation will be very likely when external bending loads are applied to the insulator.

There is another note of caution. For the present analysis of insulator A, the average magnitude of radial crimping (*M*) was very high, and the GRP-metal interface has a coefficient of friction (μ) of 0.3. In insulator E, the value of *M* is much lower, and the coefficient of friction at the GRP-metal interface may be in the same range (or smaller) in the tangential direction. This is because the circumferentially aligned grooves on the internal surface of the end-fitting can only enhance the friction coefficient in the axial direction (μ = 0.75 in axial direction, refer figure 4.13 b). In the tangential direction, the value of μ may be similar to that of a smooth end-fitting surface (*i.e.,* 0.3 or less). This low value of μ, coupled with a low magnitude of radial compression (M_E = 0.0305 mm), could lead to interfacial sliding if torsional loads as large as 2480 Nm are active. In order to demonstrate this effect, the sub-modeling procedure was repeated for insulator E. Under a torsional load of 2480 Nm, figures 4.20 show the partial sliding of the rod within the end-fitting for three values of the coefficient of friction. If the value of μ is 0.3 in the tangential direction, then 33% of the interface encounters sliding. This in turn tends to relax the surface shear stresses to 42.5 MPa. If the value of μ is 0.2 then 39% of the interface will slide, and the maximum shear stress reduces to 41.3 MPa. Figure 4.20 (c) shows the extreme case where the entire interface encounters sliding if the value of μ is 0.1, and the maximum shear stress is reduced to 39 MPa. Therefore, there will be two possible modes of failure under switch torsional forces :

(i) If the average magnitude of radial compression applied during crimping is large (as in insulator A), large shear stresses may nucleate intralaminar splits on the surface of the rod outside the end-fitting. These splits can propagate to cause brittle fracture of the insulator.

(b) If the magnitude of crimping is low and the coefficient of friction in the tangential direction is also low (as in insulator E), then the shear stresses will be relaxed, but failure can occur due to sliding of the rod in the end-fitting.

In summary, is clear that the biaxial compressive stresses (σ_r and σ_θ) caused by crimping are very large in insulator A. The maximum radial compressive stress in the GRP rod, generated by crimping, tends to exceed the uniaxial transverse compressive strength of the material given in the literature.[17] However, it is expected that the actual strength of the material under a state of biaxial compression will be higher. Therefore, the stresses generated by crimping of insulator A may, or may not, be large enough to damage the GRP rod. Furthermore, under most of the multi-axial load cases analyzed above, the stress contours are very similar. This implies that the internal stress field in the GRP rod remains dominated by the residual stresses generated during the crimping process. Since the average magnitudes of radial compression measured in other insulators (C, D, and E) are significantly lower, it appears that the biaxial compressive stresses in these insulators will be lower than in insulator A.

While most of the multi-axial load cases are safe, the cases of extreme fault current forces and switch torsional forces can be identified as the ones which are closest to the ultimate strength of the insulator. Under extreme fault current forces, the center of the

GRP rod inside the lower end-fitting experiences shear stresses which are close to the critical shear stress required to initiate intralaminar splitting in the rod. Under switch torsional forces, there can be two independent modes of failure depending upon the magnitude of radial compression applied during crimping. If the value of M is large, the surface of the GRP rod will develop shear stresses which are close to the shear strength of the composite material. On the other hand, if the values of both M and μ are low, the GRP rod can encounter partial sliding within the end-fittings.

Table 4.1 : Comparison of numerical (FEIM) and analytical solutions for isotropic-isotropic bimaterial wedges.

$\frac{E^{(1)}}{E^{(2)}}$	$\nu^{(1)} = \nu^{(2)}$	Singular Power (λ) FEIM solution	 Analytical solution
0.1	0.20	0.2872	0.29*
1.0	0.31	0.4549	0.4555†
5.0	0.20	0.4961	0.5*

* From Hein and Erdogan,[100] † From Williams[97]

Table 4.2 : Comparison of perfect and imperfect interface models.

Perfect Interface	Imperfect Interface
• Nodal connectivity at interface	• Nodes at interface connected by point-to-surface contact elements
• Analysis is linear	• Analysis is non-linear
• Stresses and displacements are continuous across interface	• Stress and displacements are discontinuous across interface
• Singular stresses at interface corner	• Finite stresses at interface corner

Table 4.3 : Multi-axial loading components for composite substation insulators.

CASE No.	LOADING CONDITION	F_A (N)	F_B (N)	F_C (N)	F_D (N)	M_T (Nm)
1	Fault Current Forces	445	2500	200	0	0
2	Extreme Fault Current Forces	445	9990	200	0	0
3	Extreme Wind Forces	445	1735	200	400	0
4	Wind with Glaze Ice	1340	580	400	110	0
5	Wind with Rime Ice	1020	400	310	67	0
6	Seismic Forces	445	710	200	200	0
7	Switch Torsional Force	0	0	0	0	2480

Table 4.4 : Maximum displacements and their locations under multi-axial load cases.

	RADIAL		TANGENTIAL		AXIAL	
LOADING-CONDITION	$(U_r)_{max}$ (mm)	Location (r, θ, z) (mm, deg, mm)	$(U_\theta)_{max}$ (mm)	Location (r, θ, z) (mm, deg, mm)	$(U_z)_{max}$ (mm)	Location (r, θ, z) (mm, deg, mm)
Crimping Forces	-0.4506	(47.5,120,507.8)	-0.0055	(19.7,30,494.6)	0.557	(31.6,60,535.3)
Fault-Current	-38.040	(63.5,90,571.5)	-38.040	(15.8,0,571.5)	4.541	(79.4,90,571.5)
Extreme-Fault	-152.01	(63.5,90,571.5)	-152.01	(15.8,0,571.5)	17.408	(79.4,90,571.5)
Extreme-Wind	28.097	(63.5,-90,571.5)	-28.097	(15.8,0,571.5)	3.393	(79.4,90,571.5)
Wind w/ Glaze-ice	-9.292	(63.5,90,571.5)	-9.292	(15.8,0,571.5)	1.288	(79.4,90,571.5)
Wind w/ Rime-ice	-6.371	(63.5,90,571.5)	-6.371	(15.8,0,571.5)	0.961	(79.4,90,571.5)
Seismic Forces	11.652	(63.5,-90,571.5)	-11.652	(15.8,0,571.5)	1.549	(79.4,90,571.5)
Switch Torsion	7.9×10^{-4}	(31.6,-60,453.8)	33.026	(79.4,180,571.5)	2.1×10^{-3}	(31.6,60,427.1)

Table 4.5 : Maximum and minimum stresses in GRP rod of insulator A (in MPa) under multi-axial load cases.

	σ_r		σ_θ		σ_z		$\tau_{r\theta}$		τ_{rz}		$\tau_{\theta z}$	
LOAD CASE	Max. Tens.	Max. Compr.	Max. Tens.	Max. Compr.	Max. Tens.	Max. Compr.	Max.	Min.	Max.	Min.	Max.	Min.
Crimping Forces	82.3	-176.5	23.6	-113.6	65.4	-160.3	36.5	-36.5	13.5	-30.4	11.9	-11.9
Fault Current	83.3	-183.3	22.7	-114.7	126.5†	-156.7	39.5	-34.1	17.0	-33.1	13.5	-13.5
Extreme-Fault	95.8	-210.9	30.7	-134.1	429.8†	−384.2†	47.4	-37.1	40.2	-40.6	43.0	-41.8
Extreme Wind	82.2	-180.4	22.7	-114.3	107.1†	-153.1	38.8	-34.2	16.9	-32.3	13.1	-13.2
Wind w/ Gl. ice	81.2	-174.6	23.8	-113.7	70.4†	-158.0	37.2	-35.3	14.7	-30.5	12.4	-12.4
Wind w/ Rm. ice	81.2	-174.4	23.3	-113.7	67.4†	-158.1	37.1	-36.0	14.3	-30.5	12.2	-12.2
Seismic Forces	80.9	-175.3	23.7	-113.8	74.7†	-157.1	37.5	-35.0	15.0	-30.7	12.5	-12.5
Switch Torsion	88.2	-179.6	32.3	-116.6	65.2	-171.0	36.3	-36.0	12.8	-29.3	47.9†	−11.8†

†Located outside the end-fitting

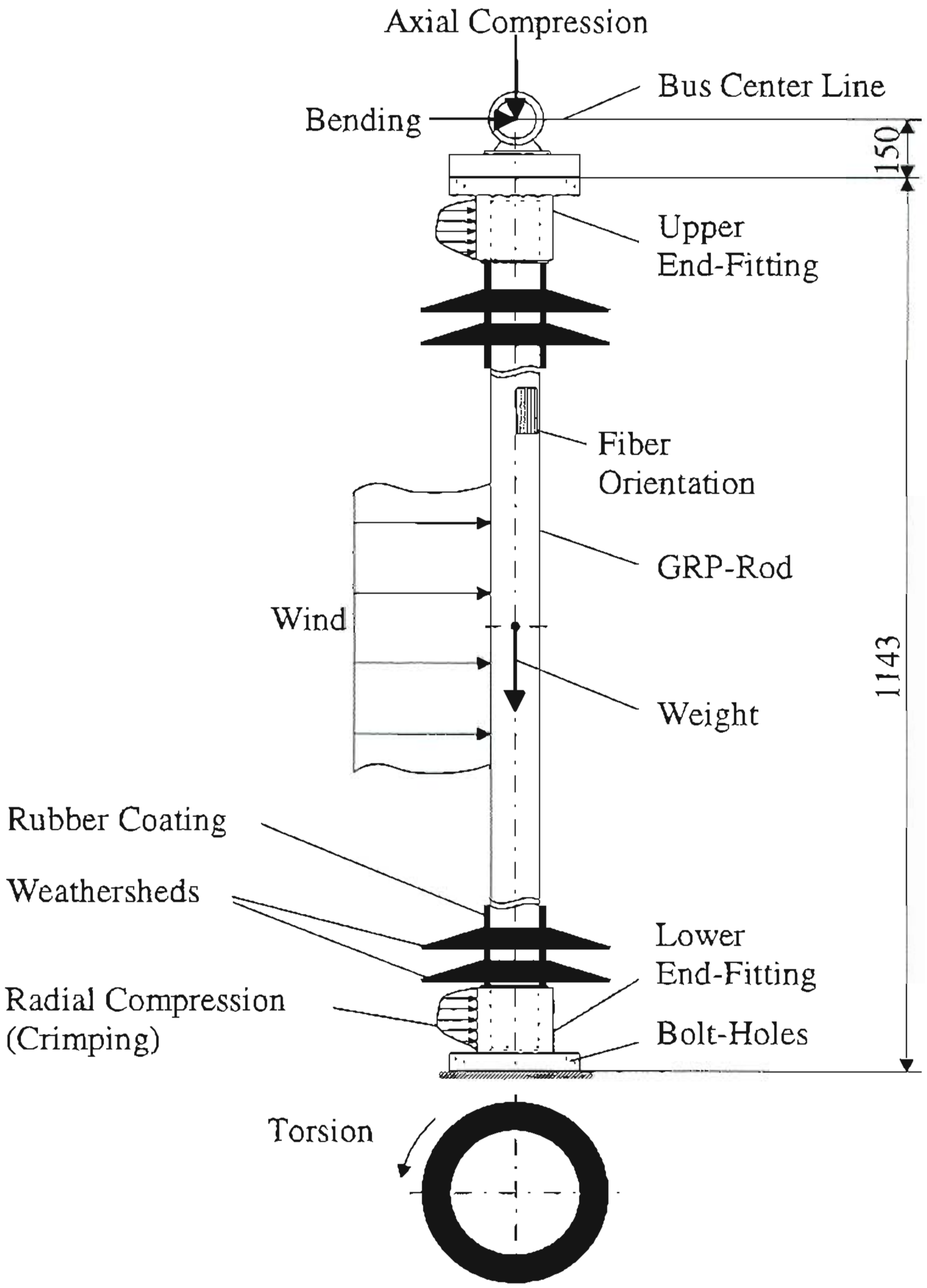

Figure 4.1 : A Typical 115 kV composite substation insulator with service loads (dimensions in mm).

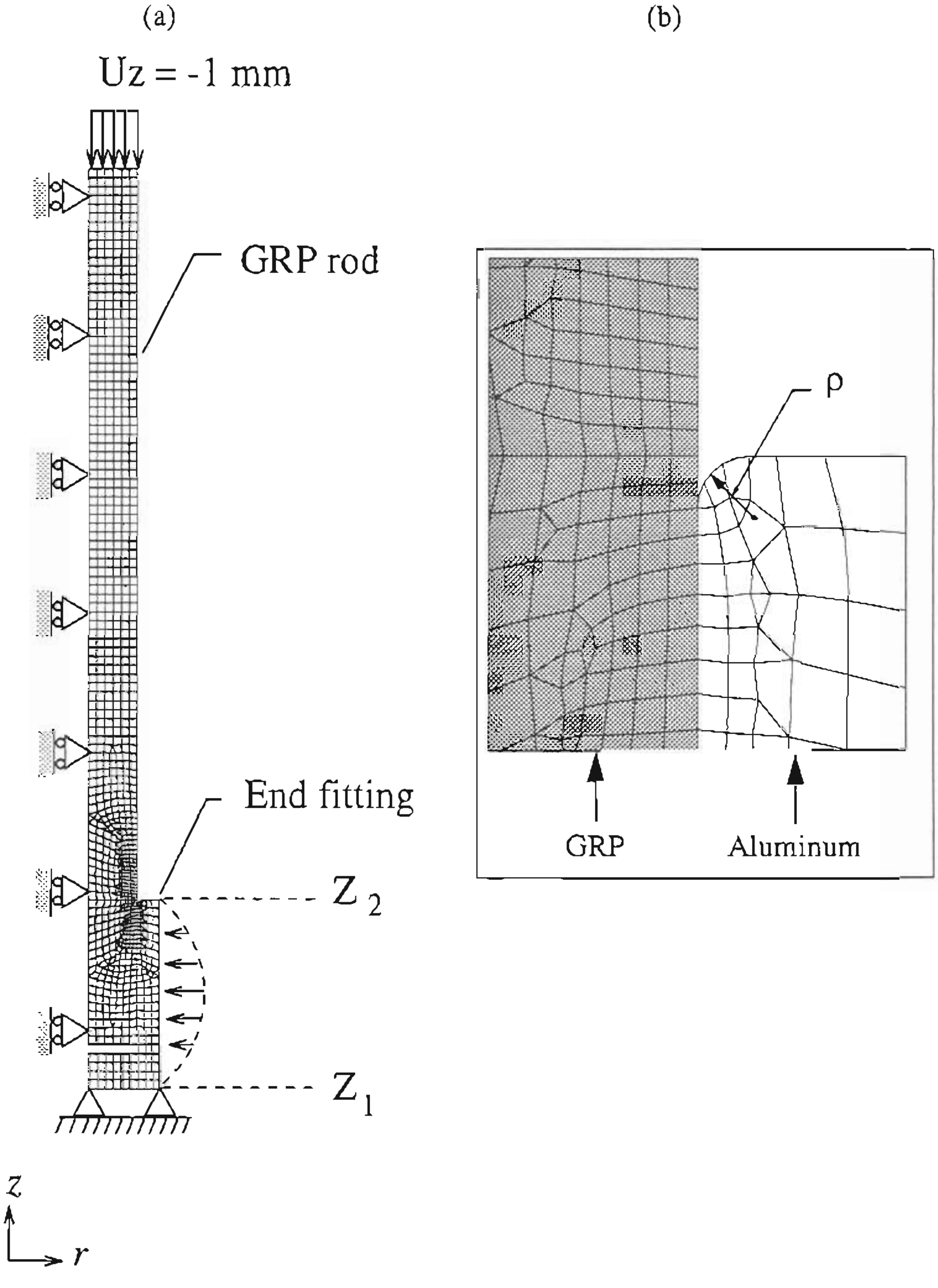

Figure 4.2 : Axisymmetric finite element mesh with perfect interface; (a) Full mesh, and (b) Zoomed-in view showing fillet radius (ρ).

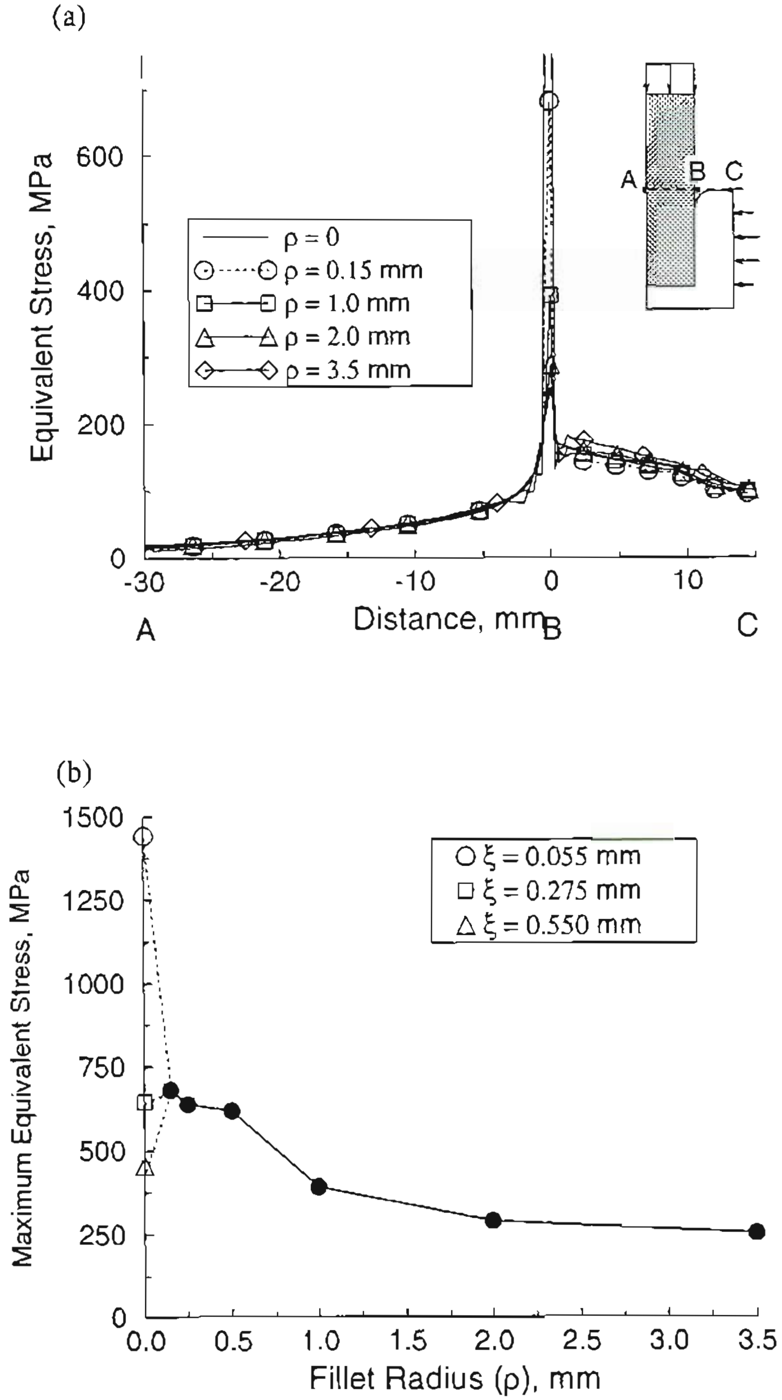

Figure 4.3 : Von-Mises equivalent stress from axisymmetric perfect interface model: (a) Along path ABC, and (b) At point B as a function of fillet radius (ρ).

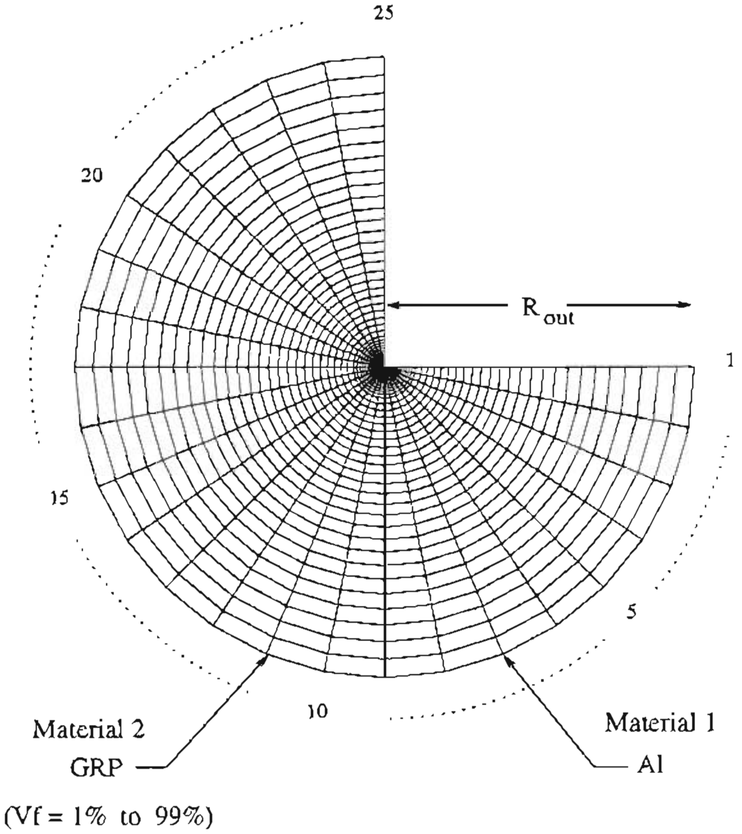

Figure 4.4 : FEIM mesh of GRP-Al bimaterial interface corner.

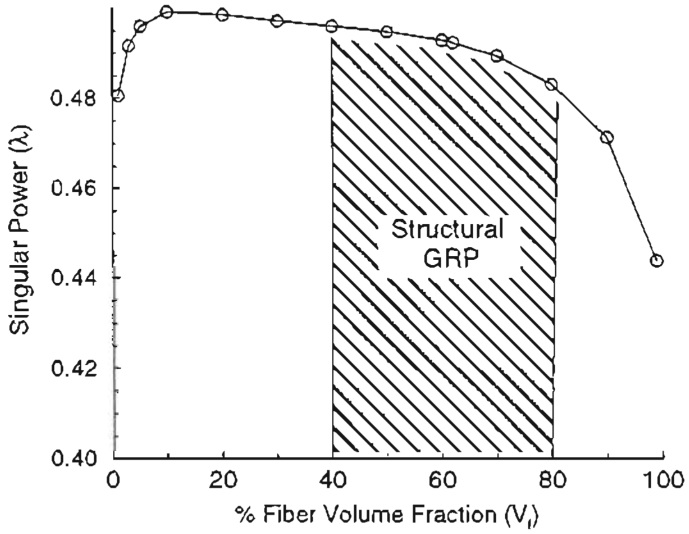

Figure 4.5 : Singular power (λ) versus volume fraction of E-glass fibers in GRP composite.

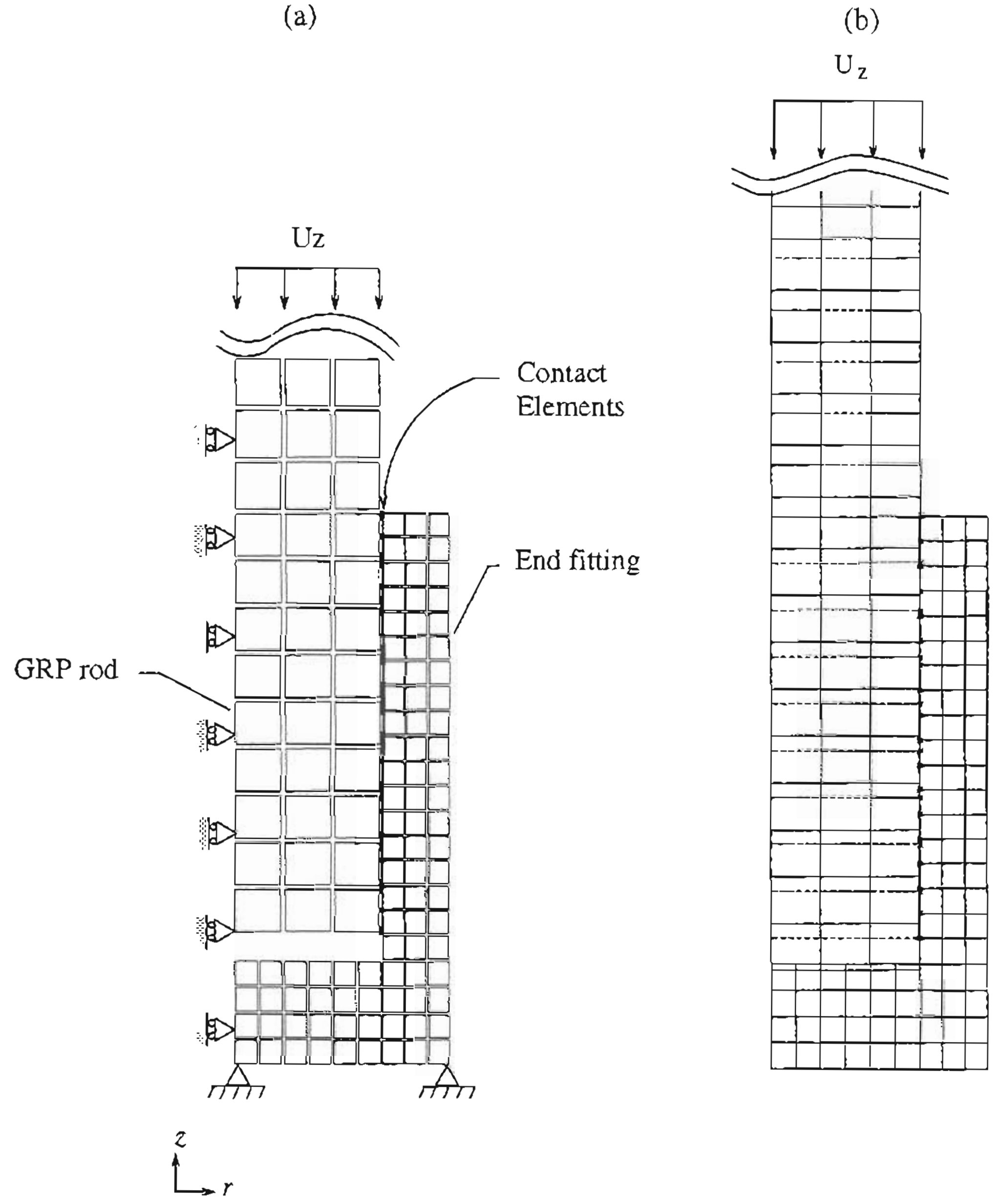

Figure 4.6 : Axisymmetric model with imperfect interface; (a) Finite element mesh, and (b) Deformed mesh superimposed with original mesh (Uz = -8 mm, $\mu = 0.3$).

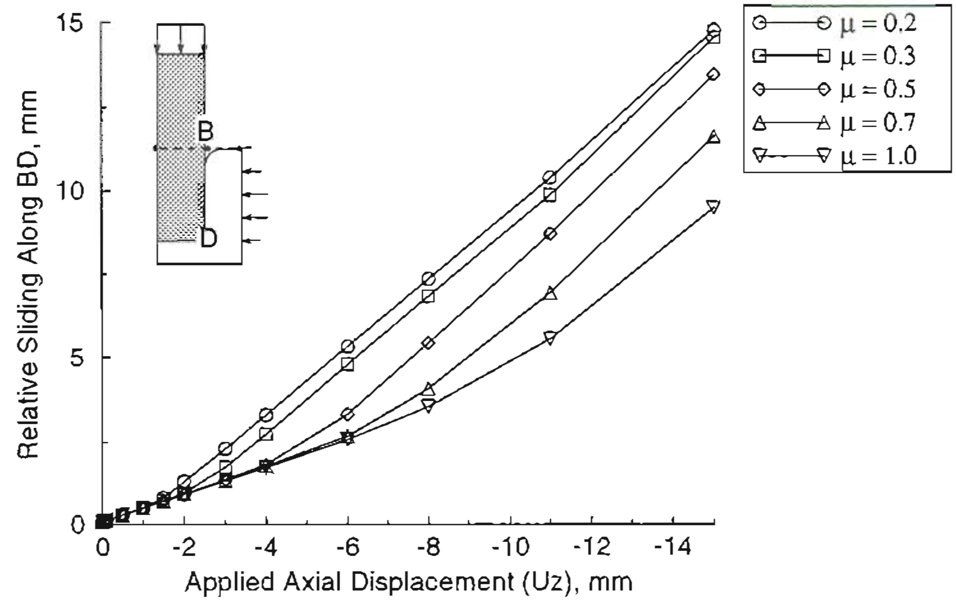

Figure 4.7 : Relative sliding along interface (BD) as a function of applied axial displacement (Uz).

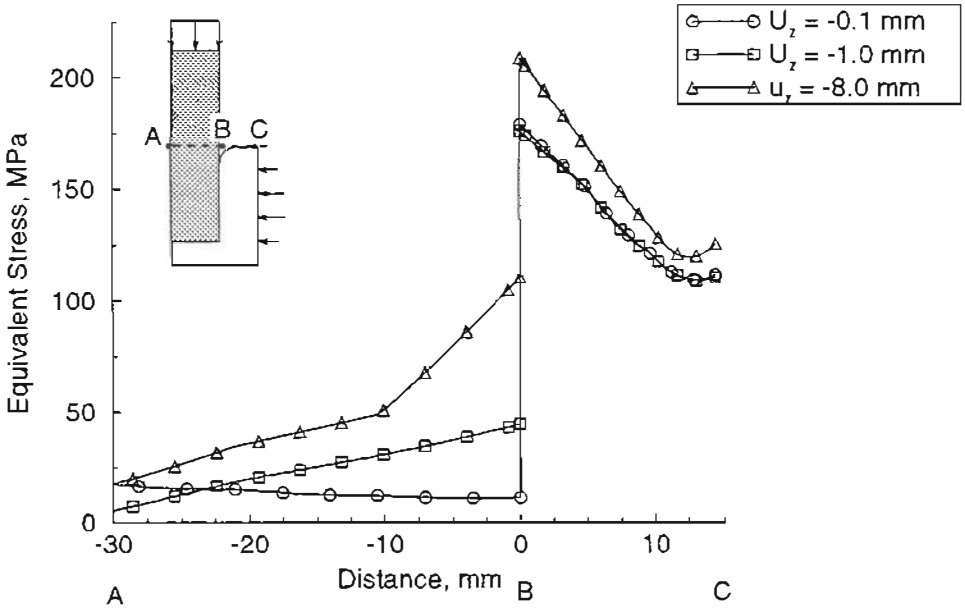

Figure 4.8 : Equivalent stress across interface (ABC) for different Uz ($\mu = 0.3$).

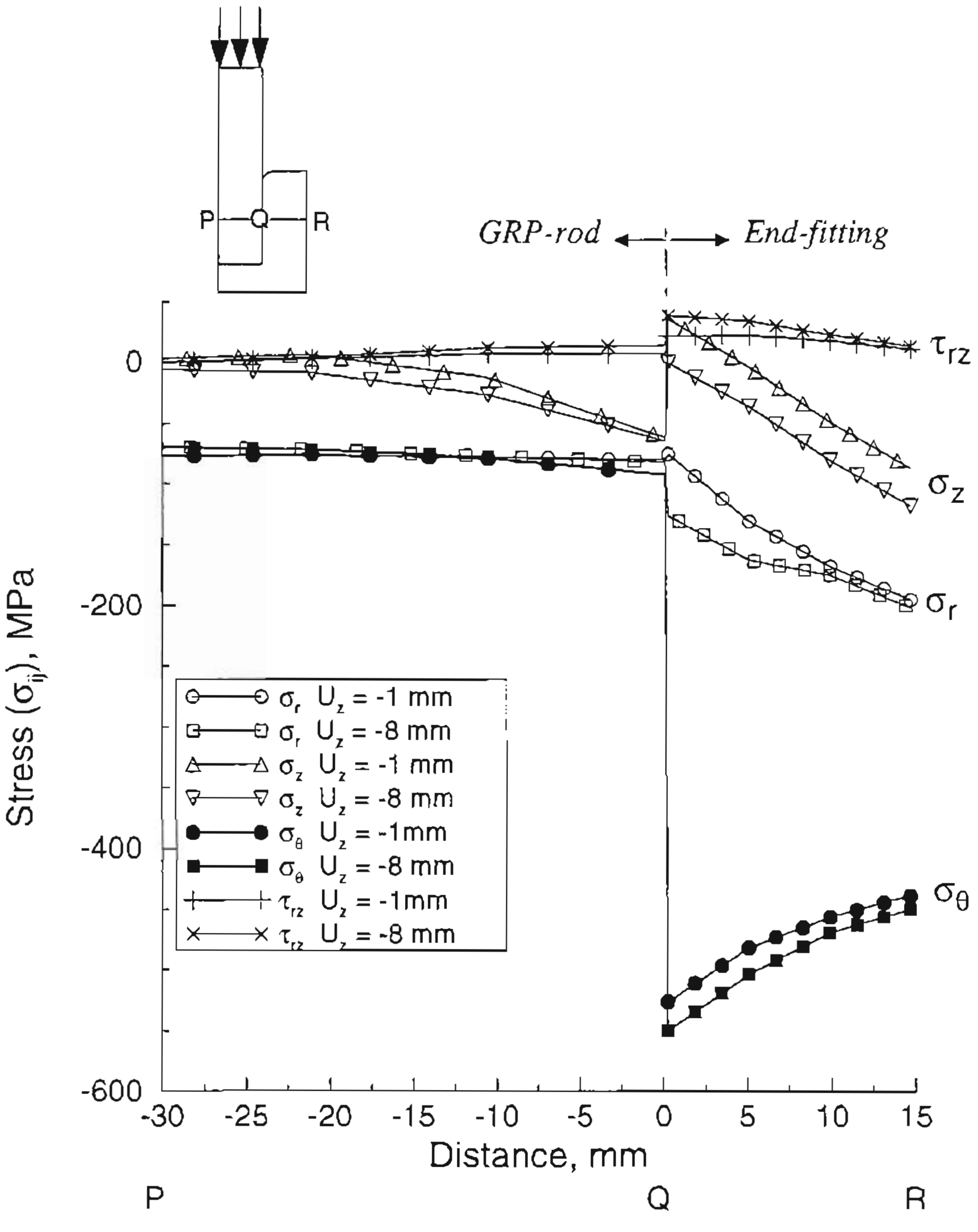

Figure 4.9 : Stress distribution (axisymmetric) along plane PQR (μ = 0.3).

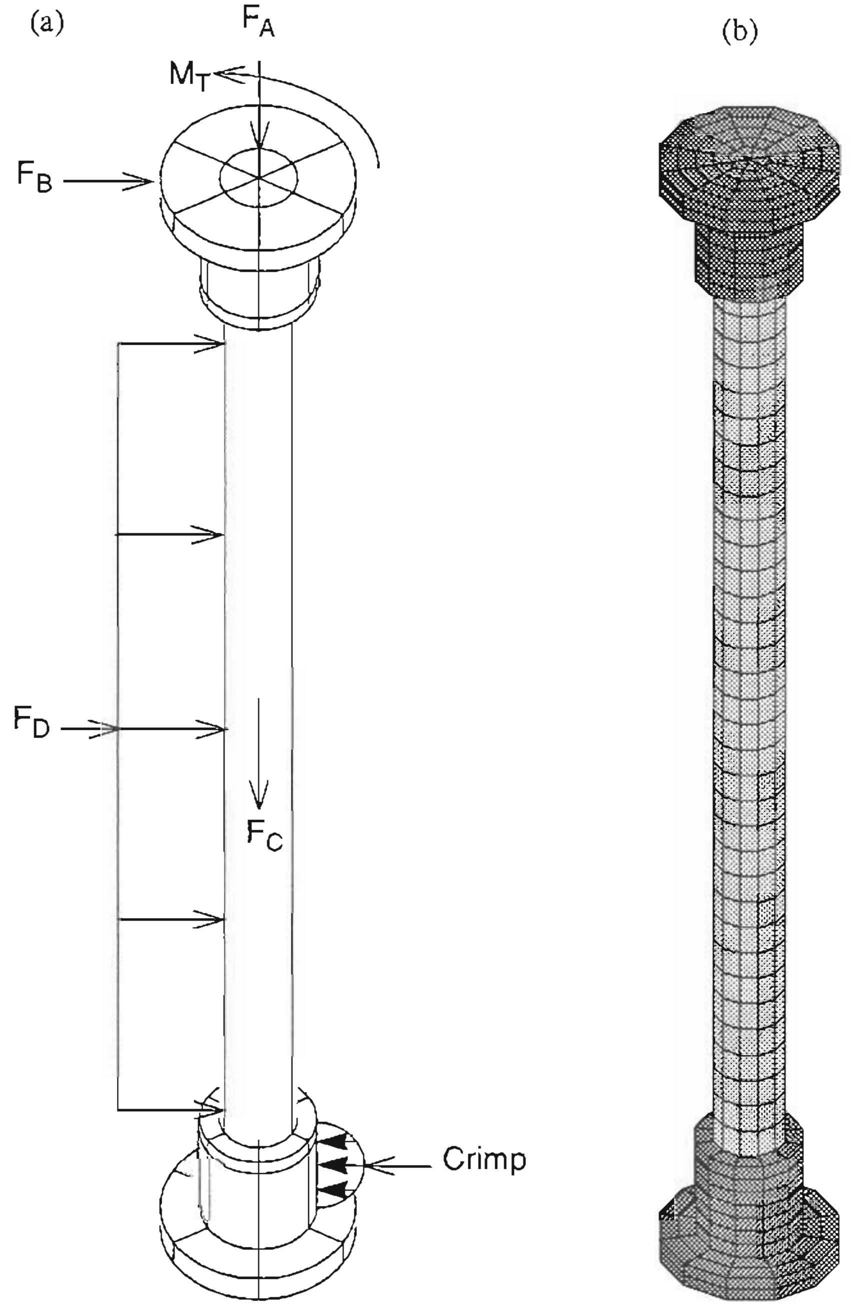

Figure 4.10 : 3-D Global insulator model; (a) Schematic of loads applied, and (b) Finite element mesh.

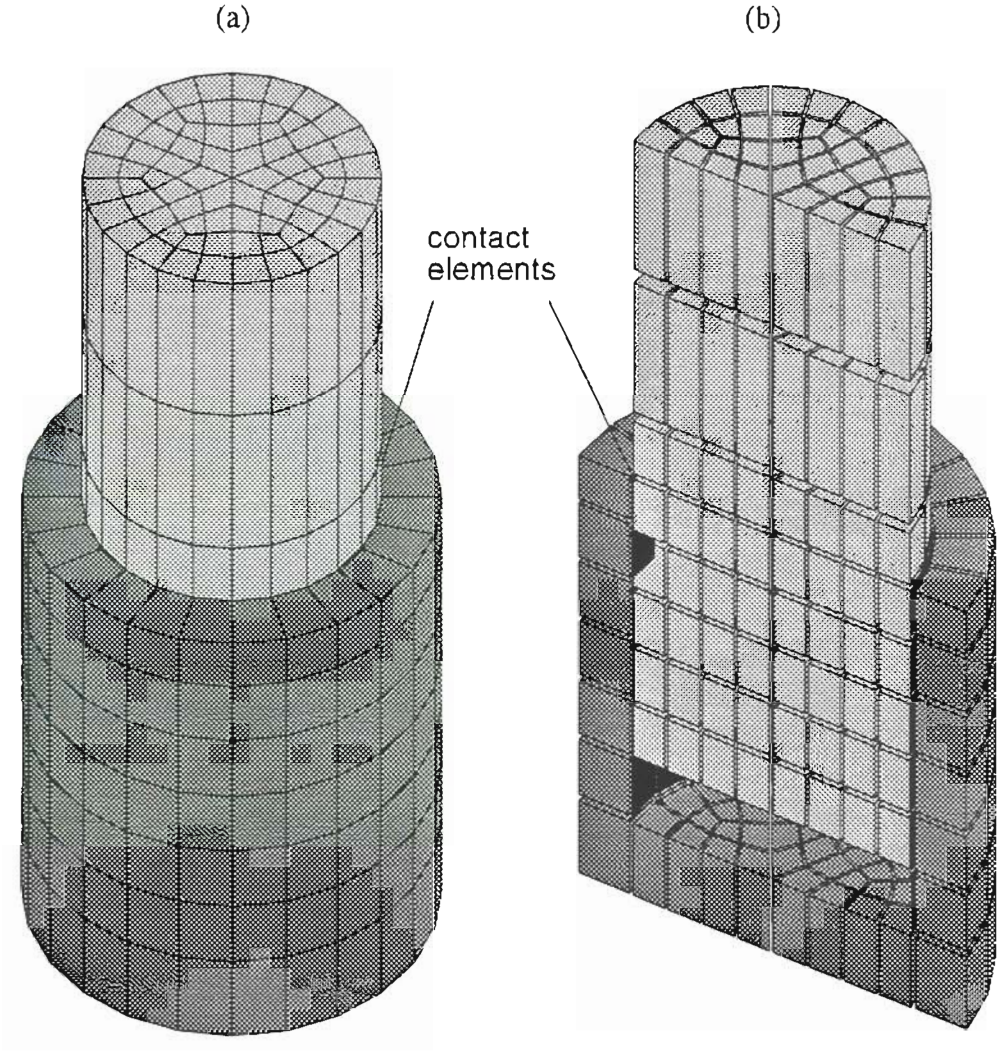

Figure 4.11 : 3-D sub-model with imperfect interface;
(a) Full sub-model, and (b) Cross-sectional view.

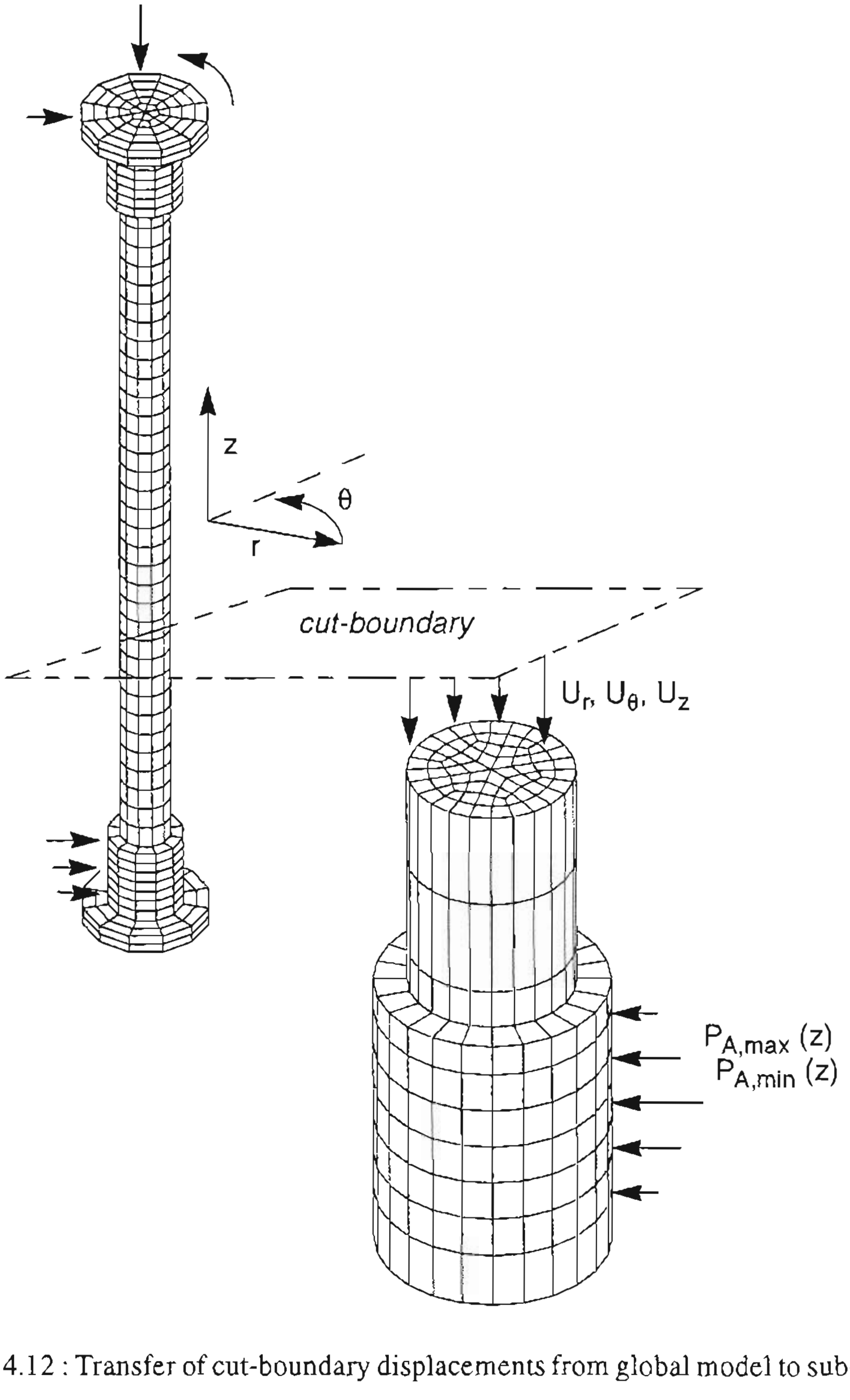

Figure 4.12 : Transfer of cut-boundary displacements from global model to sub-model.

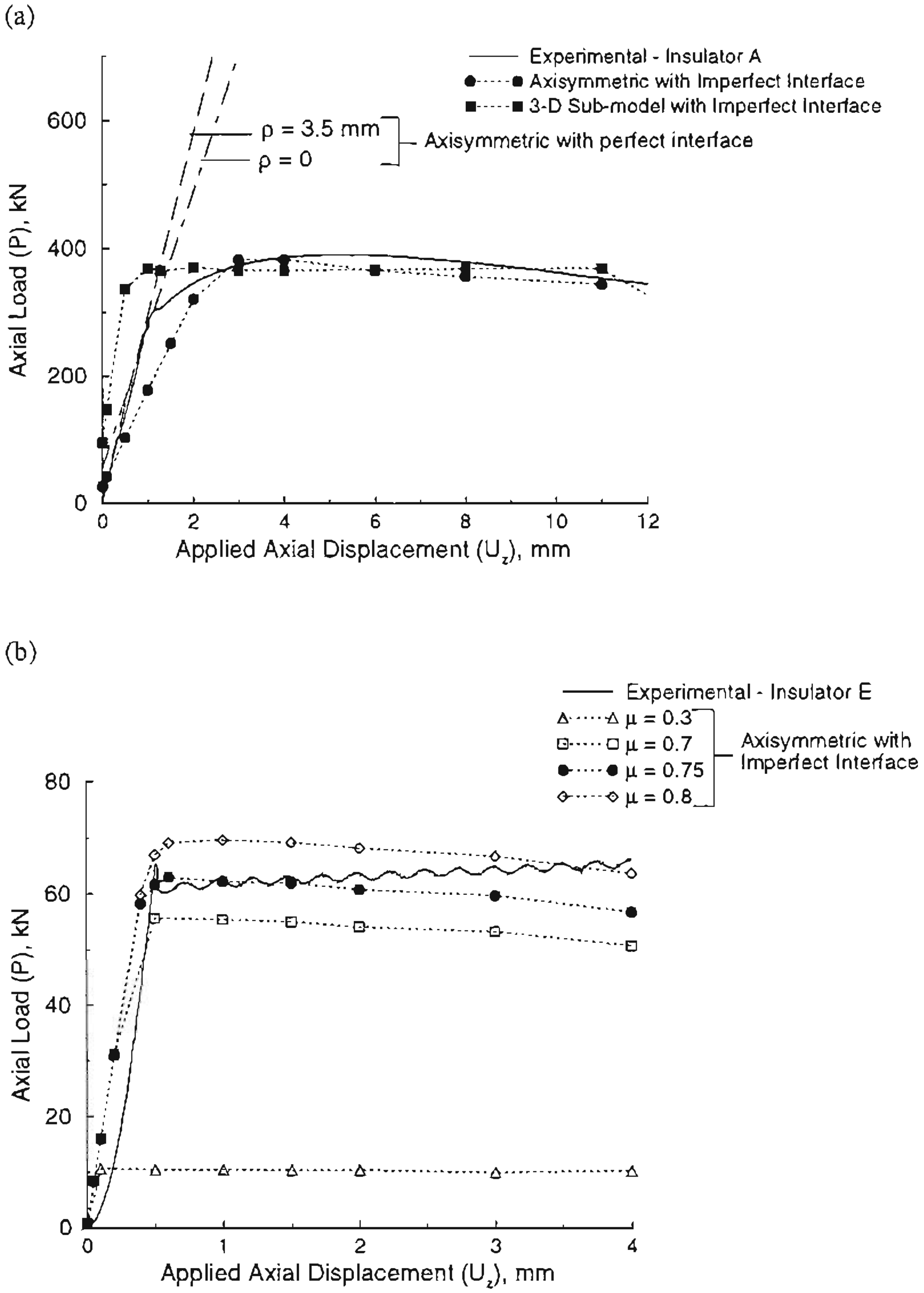

Figure 4.13 : Comparison of experimental and computed axial load versus displacement response; (a) Insulator A ($\mu = 0.3$, $M = M_A$), and (b) Insulator E ($\mu = 0.75$, $M = M_E$).

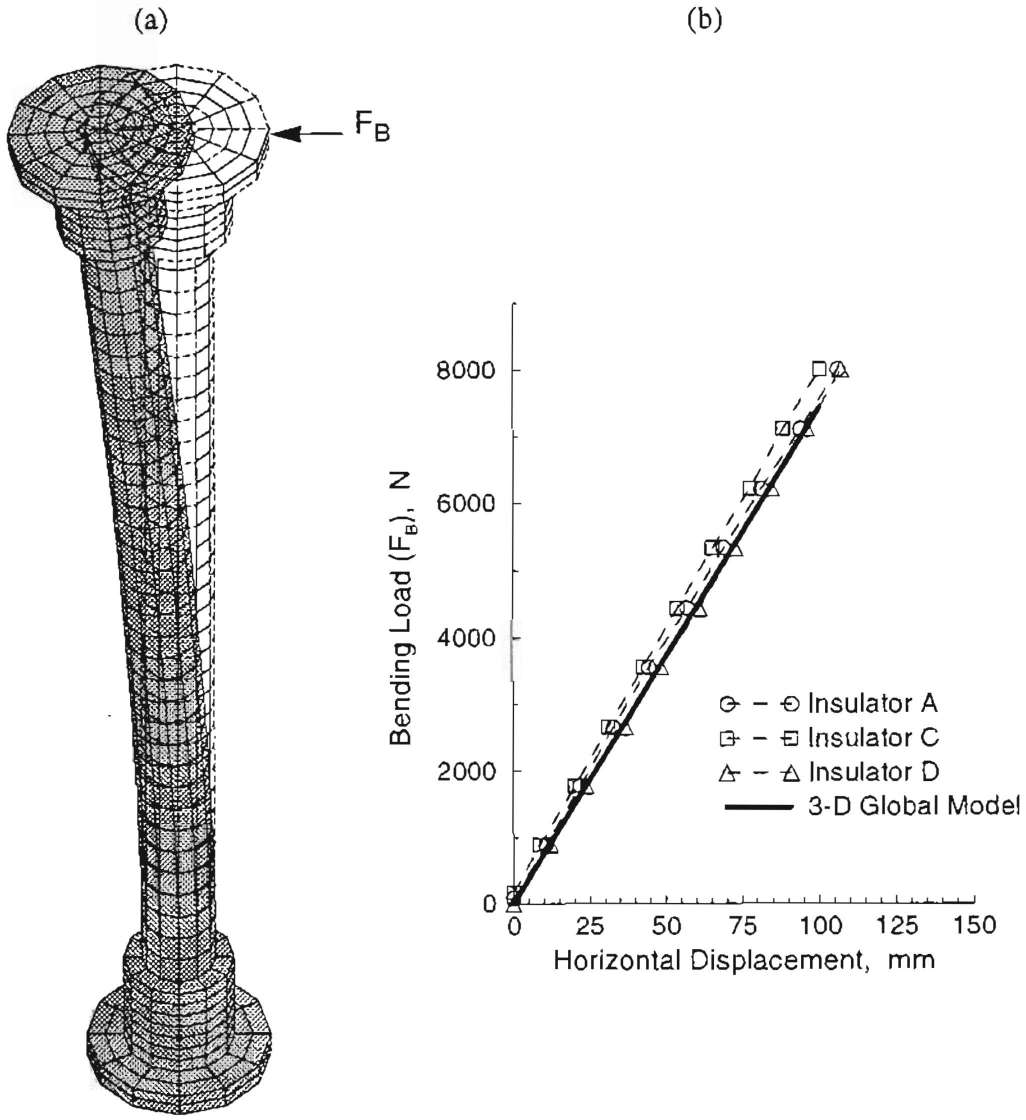

Figure 4.14 : Global insulator model under pure bending load;
(a) Deformed FE mesh, and (b) Comparison with experimental results.

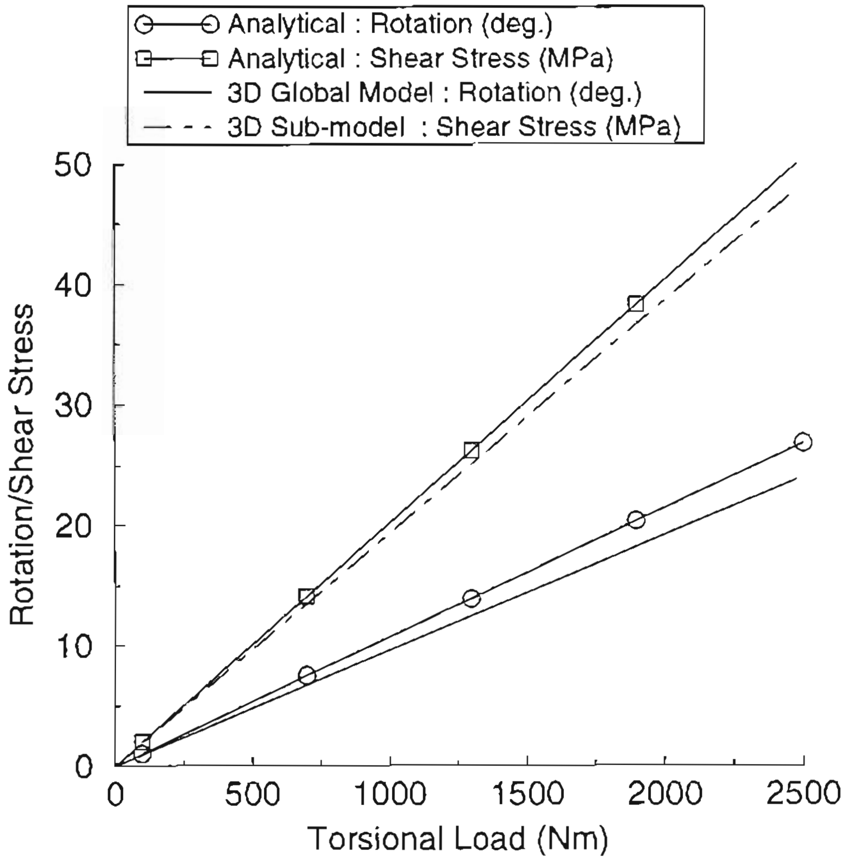

Figure 4.15 : Comparison of analytical solution for torsion of isotropic rod with results computed from 3-D global and sub-models.

(a)

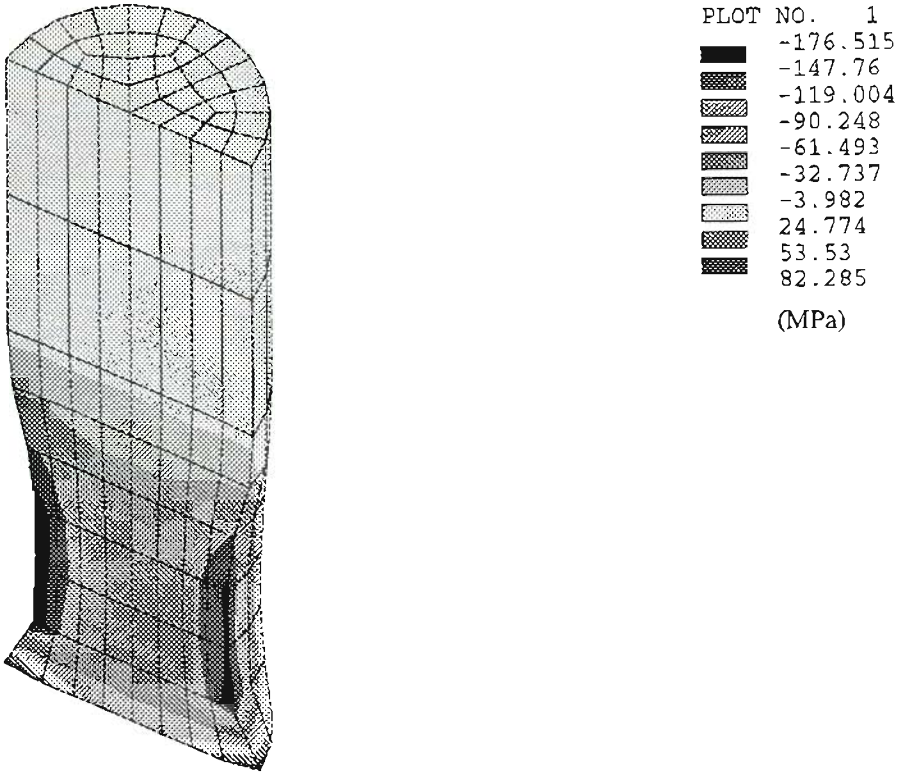
PLOT NO. 1
-176.515
-147.76
-119.004
-90.248
-61.493
-32.737
-3.982
24.774
53.53
82.285
(MPa)

(b)

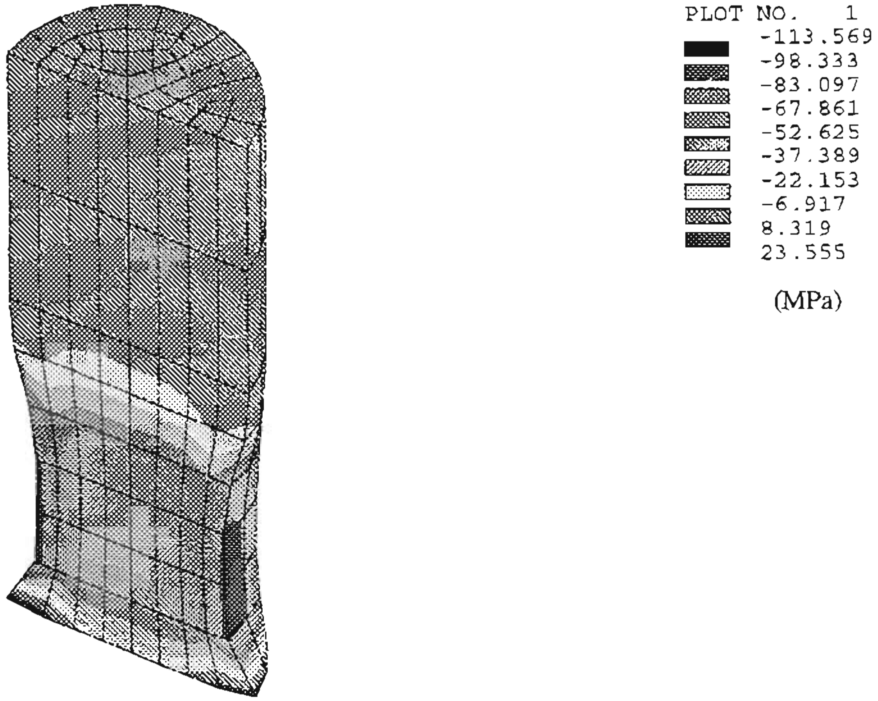
PLOT NO. 1
-113.569
-98.333
-83.097
-67.861
-52.625
-37.389
-22.153
-6.917
8.319
23.555
(MPa)

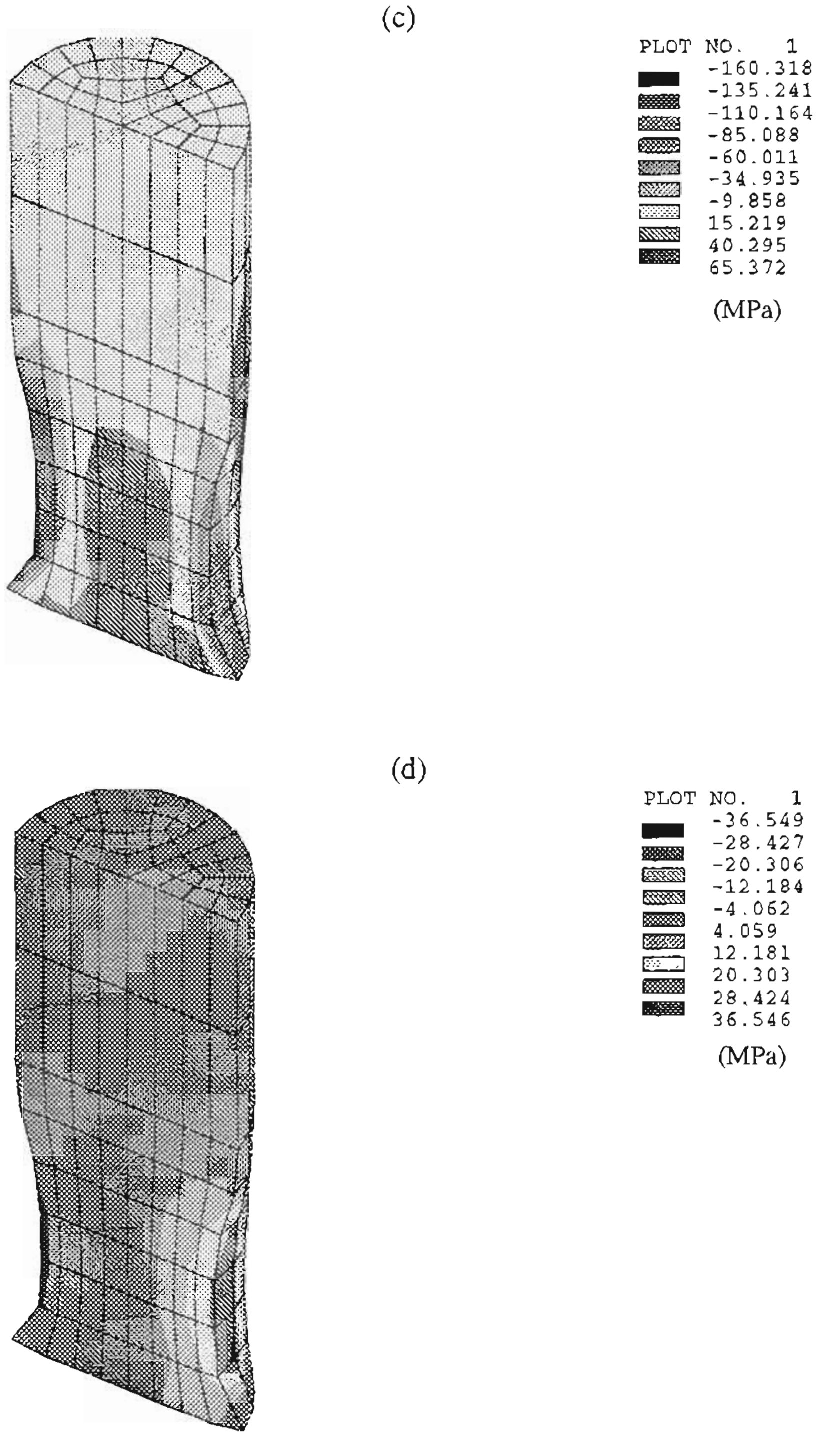

Figure 4.16 : Stresses in GRP rod due to crimping of insulator A; (a) Radial stress (σ_r), (b) Tangential stress (σ_θ), (c) Axial stress (σ_z), and (d) Shear stress ($\tau_{r\theta}$).

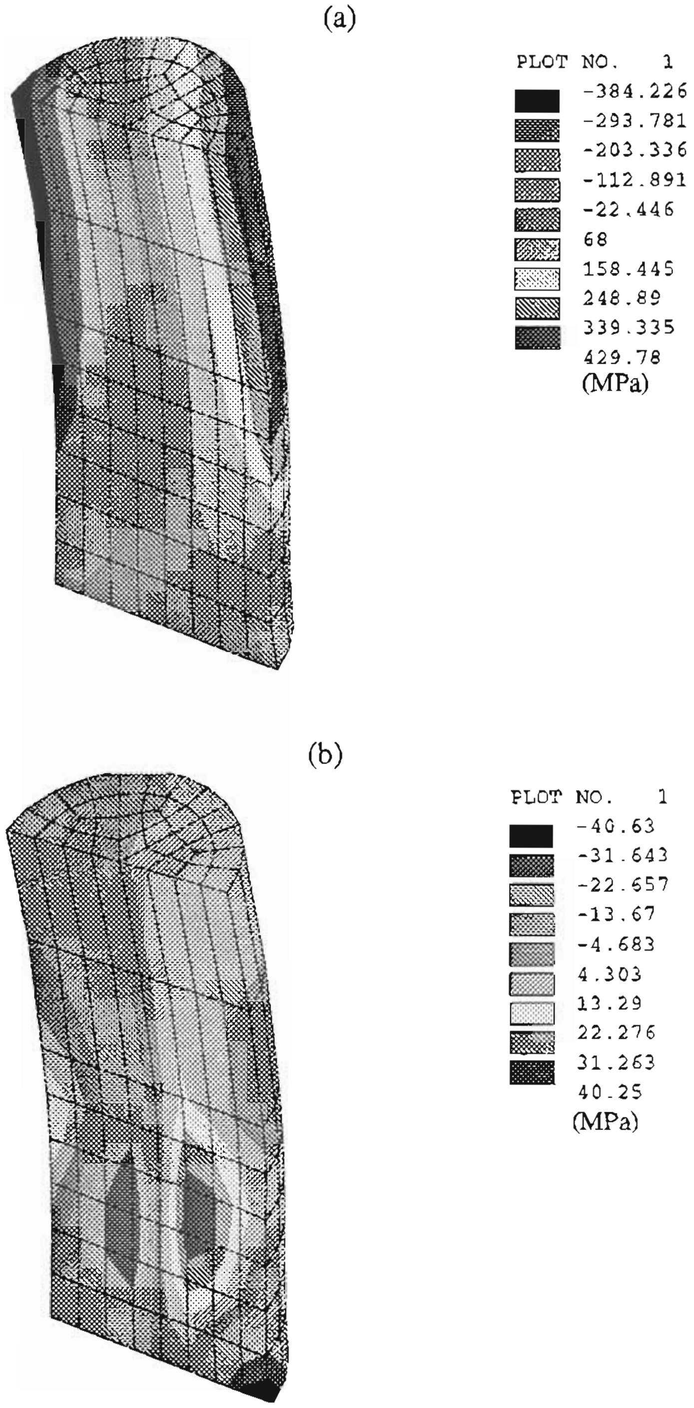

Figure 4.17 : Stresses in GRP rod of insulator A due to extreme fault current forces; (a) Axial stress (σ_z), and (b) Shear stress (τ_{rz}).

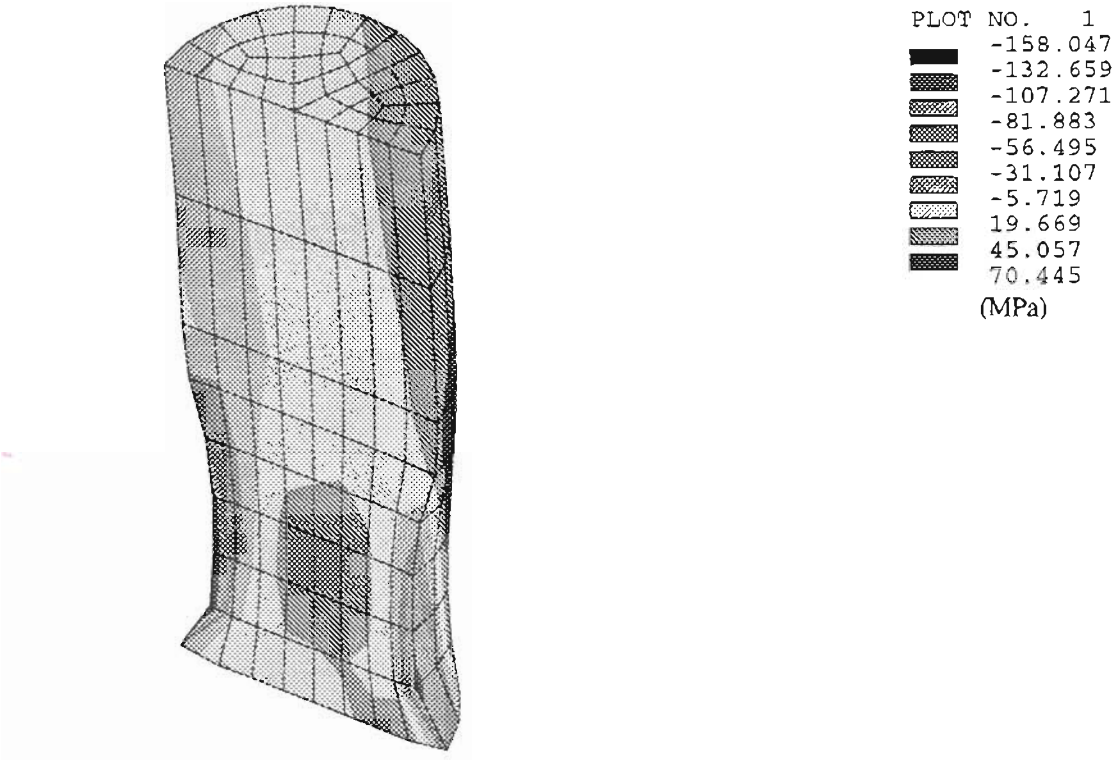

Figure 4.18 : Axial stress (σ_z) in GRP rod of insulator A due to wind with glaze ice.

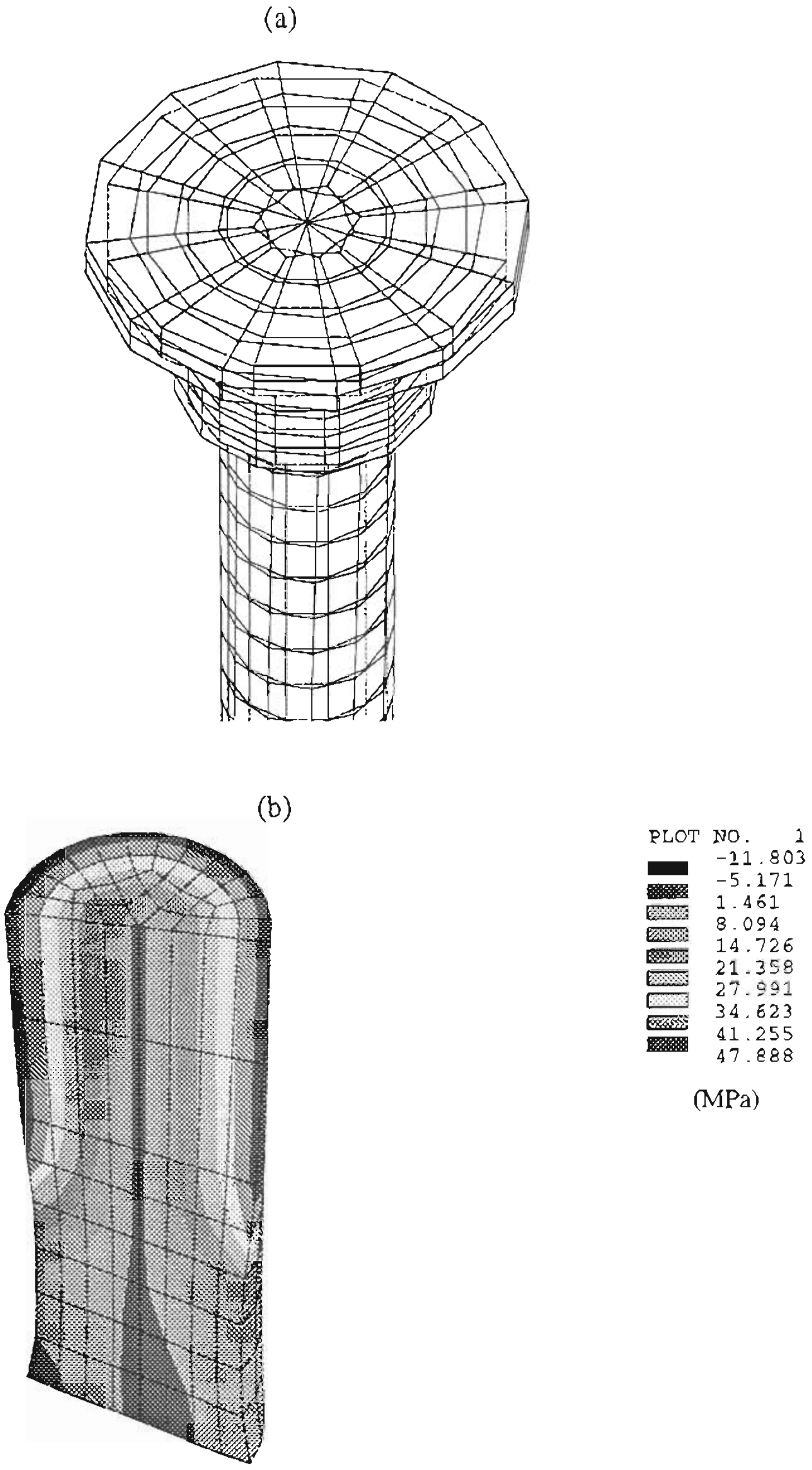

Figure 4.19 : Insulator A subjected to switch torsional forces;
(a) Deformed mesh, and (b) Shear stress ($\tau_{\theta z}$).

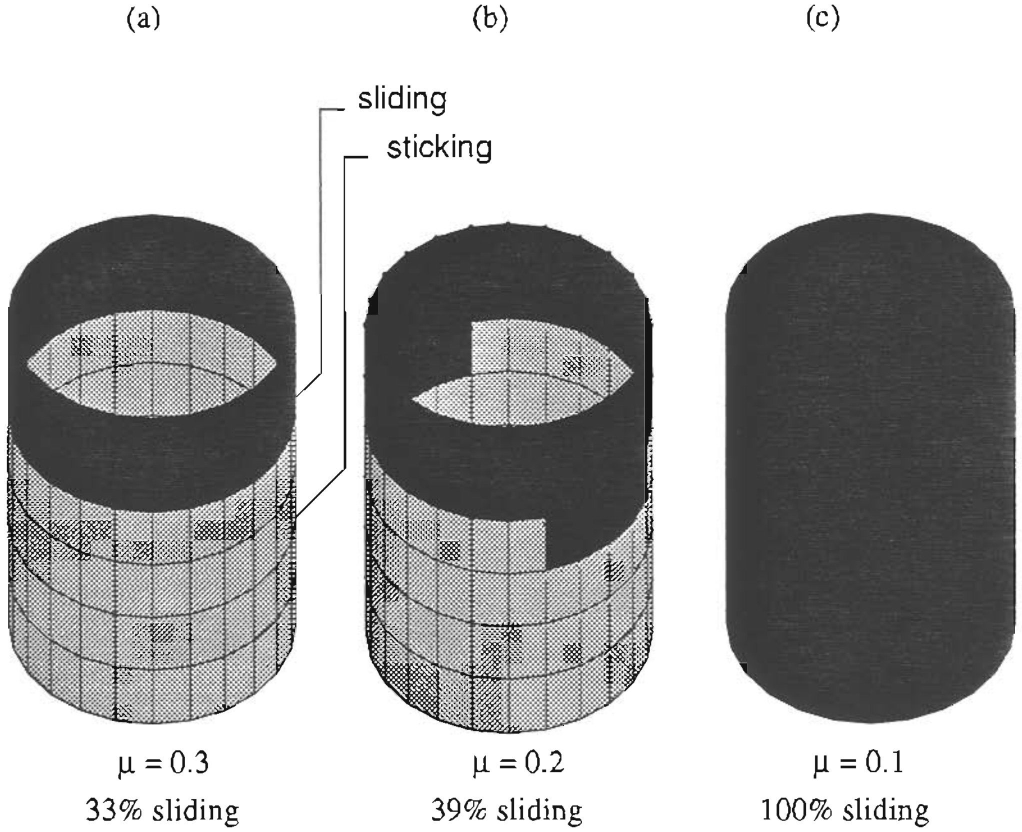

Figure 4.20 : Internal sliding of GRP rod of insulator E subjected to switch torsional forces; (a) $\mu = 0.3$, (b) $\mu = 0.2$, and (c) $\mu = 0.1$.

Chapter 5

Intralaminar Strength of GRP Composite

5.1. INTRODUCTION

The glass/epoxy or glass/polyester rods of composite insulators are subjected to multi-axial loads during service. In chapter 4, detailed three-dimensional finite element analyses of several load cases showed that the GRP rod is subjected to a complex state of multi-axial stresses during service. Due to the crimping process, the part of the GRP rod within the end-fittings is subjected to large biaxial compressive stresses irrespective of the external loading conditions. When external bending loads are active, one edge of the rod (opposite to the loading direction) is subjected to large axial tensile stresses (σ_z), while the other edge (towards the loading direction) is subjected to axial compressive stresses. The center of the rod experiences large shear stresses (τ_{rz} and $\tau_{\theta z}$). This implies that approximately one half of the cross-section of the rod experiences some combination of intralaminar shear and tension, while the other half experiences shear and compression. This situation is further complicated by the inherent anisotropy and heterogeneous nature of unidirectional polymer-matrix composites. In these materials, the tensile strength of the composite parallel to the fibers (σ_{11}^{f}) is significantly greater than the intralaminar shear strength in the 1–2 plane (τ_{12}^{f}), which in turn is greater than the transverse tensile strength (σ_{22}^{f}).[17] Clearly, in order to define the criticality of external loads, and consequently the critical internal stresses required to initiate damage in the GRP rod, the intralaminar strength of the unidirectional composite must be characterized under uniaxial, as well as biaxial loading conditions (*i.e.*, combined shear and tension, or combined shear and compression). In addition, the dominant failure mechanisms for unidirectional composites, and the appropriate failure criteria must be determined under combined loads.

In addition to the *"strength of materials"* approach, one can apply the principles of linear elastic fracture mechanics (LEFM) to determine the criticality of flaws in the composite. In chapter 3 (section 3.6), circumferential micro-cracks were observed in the GRP rod of insulator A. These flaws were detected inside the end-fitting, and were therefore subjected to biaxial compressive stresses. On the other hand if internal cracks are generated under bending loads, they will be located outside the end-fitting and will be subjected to either shear and tensile stresses (mixed-modes I and II), or shear and compressive stresses (mode II with contact and friction between crack faces). If intralaminar cracks are generated under torsional loads, they will most likely be located on the surface of the rod and will be subjected to pure mode II type loads. Therefore, there is a recognized need to determine the intralaminar fracture toughness (K_c or G_c) of the composite under the three fundamental modes of loading (I, II, and III), as well as the complete range of mixed-mode loading conditions. This information, in conjunction with field data of the size and location of internal cracks, can be used to minimize the occurrence of brittle fractures in composite insulators.

In this chapter, the biaxial Iosipescu test method [25, 27, 56, 124] has been used to determine the biaxial failure strength of unidirectional composite materials, and an attempt has been made to extend the approach for determining the mixed-mode fracture toughness of the materials. While most of these studies have been performed on a unidirectional carbon/epoxy composite system, the test results and conclusions are also applicable to the glass/epoxy, glass/polyester, or glass/vinyl-ester composite materials used in insulators. This is because the intralaminar strength, and the mixed-mode fracture properties of these composites (used in insulators) are very similar to the properties of the unidirectional carbon/epoxy composite material selected for these tests. The first phase of this study involves application of the biaxial Iosipescu method for determining the biaxial failure strength of the composites, and the next phase involves the extension of the Iosipescu test for evaluating the mixed-mode fracture properties. A detailed description of the biaxial Iosipescu test (BIT) fixture was given in chapter 2 (section 2.2.1). Additional details of the numerical and experimental techniques are given in the author's recent publications.[56, 60, 124]

5.2. BIAXIAL IOSIPESCU TESTS OF UNIDIRECTIONAL COMPOSITES

The biaxial Iosipescu test (BIT) fixture was first used by Broughton [25] for testing (isotropic) polycarbonate and unidirectional carbon/epoxy and carbon/PEEK specimens under various loading angles (α).

5.2.1. Experimental Work

The materials tested in this study were; (*a*) unidirectional XAS 914 carbon/epoxy composite (from Ciba-Geigy), and (*b*) teak wood. Teak was selected as a test material because it is cheap, easily available, and is known to be among the stiffest variety of woods with unidirectional continuous fibers. The mechanical behavior of teak is very similar to that of a synthetic unidirectional composite material.

The teak specimens were machined to a length (l) of 80mm and a width (h) of 20mm (refer figure 2.5). The fibers were oriented either parallel to the long axis of the specimen (henceforth referred to as orientation A), or parallel to the notch-root axis (referred to as orientation B). Two v-shaped notches were cut to a depth of 4 mm (*i.e.* 20% of specimen width) at opposite edges of the specimen mid-length using a scalpel edged blade such that minimal damage was introduced at the notch tips. The notch angle was 90^o and the notch-root radius (ρ) was measured to be approximately $40 \mu m$. The teak specimens with fiber orientation B had a thickness (t) of 5 mm. In teak specimens with fiber orientation A, the thickness was doubled to 10 mm in order to minimize the effects of localized transverse crushing at the loading points. The XAS 914 carbon/epoxy specimens were machined to the same length and width, with fiber orientations A and B. These specimens had a thickness (t) of 5.2 mm in the "as-received" condition.

The biaxial Iosipescu test fixture was mounted on an Instron (1230-20) universal testing machine with a load capacity of 89 kN (20,000 lb) by securing the base of the fixture to the lower cross-head via an intermediate platform. The teak and carbon/epoxy Iosipescu specimens were mounted in the fixture at a loading angle of $\alpha=0^o$ (pure shear). After ensuring proper centering of the notch-root axis with respect to the four loading plates, the specimen was rotated to the requisite angle for the biaxial tests. Counter-clockwise rotation of the specimen ($\alpha > 0^o$) was used for generating combined shear and compressive stresses along the notch-root axis, and clockwise rotation ($\alpha < 0^0$) was used for generating combined shear and tensile stresses. A monotonic compressive load (P_α) was applied at a cross-head displacement rate of 1.52 mm/minute.

The type of failure in the Iosipescu specimens was found to be highly dependent on the fiber orientation and completely independent of the loading angle (α). Furthermore, the failure modes for both the teak and carbon/epoxy specimens were identical for the same fiber orientation.

(i) *Orientation A*

Figure 5.1 (a) shows the typical load versus displacement response of teak specimens with fiber orientation A. The load-displacement curve of these specimens was initially linear. The onset of non-linearity occurred at approximately 1 kN, and was probably caused by plastic deformation and localized crushing at the loading points. The non-linearity was less pronounced in carbon/epoxy specimens with fiber orientation A. In both the carbon/epoxy and teak specimens, failure under all loading angles (α) occurred due to the initiation of axial splits at the notch tips. This type of failure has previously been reported in orientation A specimens subjected to the traditional Iosipescu shear test ($\alpha = 0^o$).[27,41] The initiation of the axial splits was manifested by two successive drops on the load-displacement curve (see figure 5.1 a). The splits formed parallel to the fibers and propagated away from the nearest loading point. The lengths of the axial splits in teak specimens were measured using a traveling optical microscope. It was found that the splits were longer in specimens loaded in shear and tension, and shorter in specimens loaded in shear and compression. The relationship between the average lengths of the splits and the loading angle (α) was almost linear.[56]

(ii) *Orientation B*

Teak and carbon/epoxy specimens (with fiber orientation B) failed catastrophically in a mode which is characteristic of the shear test.[27,44] For all loading angles, cracks originated at either of the two notch tips and propagated in an unstable manner parallel to the fibers. However, in some specimens, the crack initiation was away from the notch root and farther from the nearest loading point. This offset in the path of failure has been reported earlier in shear-test specimens with fiber orientation B. [41,44] The load displacement curves of both teak and carbon/epoxy specimens were linear up to failure (see figure 5.1 b).

The loads at failure as a function of the loading angle for teak specimens with orientations A and B are presented in figures 5.2 (a) and (b) respectively. Figures 5.3 (a) and (b) show the loads at failure for carbon/epoxy specimens with fiber orientations A and B. It is important to observe that irrespective of the fiber orientation, the failure load was in general found to be maximum under pure shear (*i.e.*, $\alpha=0^o$), and seemed to decrease progressively as the loading angle α was increased in either direction. This observation is in agreement with results obtained by Broughton [25] for isotropic (polycarbonate) and unidirectional carbon/epoxy composite specimens.

The experimental results presented thus far have raised several questions pertaining to the stress distribution in the vicinity of a round notch tip of the Iosipescu specimen under biaxial loads. For instance, it is not clear why the loads at failure under positive loading angles ($\alpha>0^0$, applied shear and compression) were lower than the pure shear case ($\alpha=0^0$). In addition, the influence of the notch-root radius (ρ) on the stress concentration needs to be understood. Since a reliable analytical expression to predict the stress field in the biaxially loaded orthotropic Iosipescu specimens is not presently available, finite element methods were used to study this problem.

5.2.2. Finite Element Analysis

The finite element code ANSYS [119] (version 4.4A) was employed in this study. A linear-elastic analysis was performed to determine the stress distribution in unidirectional carbon/epoxy Iosipescu specimens resulting from the biaxial loading conditions. The analysis was performed only for fiber orientation A by assuming a homogeneous orthotropic material (*i.e.*, $E_{11} = E_x > E_{22} = E_y$). Eight noded isoparametric quadrilateral and collapsed triangular elements with isotropic as well as orthotropic elastic properties were used. Figure 5.4 shows the finite element mesh consisting of 4112 elements and 9699 nodes with the appropriate boundary conditions. The mesh assumes 90^o notches penetrating to a depth of 20% of the specimen width (h). The notch-root radius (ρ) and the notch-root element size (ξ) were variable parameters in the mesh. For each loading angle, two counteracting force-couples P_1 and P_2 were applied to the finite element model in accordance with the force-equilibrium relationships given in chapter 2 (section 2.2.1). The elastic properties used in the model are given in table 5.1.

Iosipescu specimens with perfectly sharp notches have previously been subject to extensive numerical analysis. [27,39,55,59] However, perfectly sharp notches ($\rho = 0$) are practically unfeasible by conventional machining techniques. Therefore, the present study considered notch-root radii (ρ) of 40 μm and 1.7 mm, with loading angles (α) of 0^o, $+30^o$, and -30^o. In order to evaluate the shear stress concentrations at the notch-roots, all stresses were normalized with respect to the average shear stress along the notch-root axis under pure shear loading ($\bar{\tau}_{xy} = P_\alpha / wt$).

The normalized stress distribution along the notch-root axis ($x = 0$) is presented in figure 5.5 for carbon/epoxy specimens with $\rho = 40\,\mu m$. It is evident that the shear stresses (τ_{xy}) are not significantly affected by the loading angle (α). The notch-root radius, however, significantly alters the shear stress concentration at the notch-tips (see table 5.2). For $\rho = 40\,\mu m$ specimens, the shear stresses are highly concentrated at the notch-tip, while for $\rho = 1.7\,mm$ specimens the shear stresses were found to be uniform along the axis, and approached zero at the free surface.[56] The normalized longitudinal stresses

(σ_{xx}) can be regarded as insignificant at the specimen center, and are highly concentrated at the notch tips for both ρ considered (see figure 5.5 and table 5.2). As would be expected, σ_{xx} are tensile under negative loading angles ($\alpha < 0^0$) and compressive under positive loading angles ($\alpha > 0^0$). The transverse stresses (σ_{yy}) exhibit a similar trend.

Further understanding of the stress state in the vicinity of the notch tips can be obtained from figure 5.6, where the distributions of τ_{xy} and σ_{yy} are plotted along the path of the axial splits ($y = w/2$). It can be seen that for all loading angles, σ_{yy} are tensile in the region away from the nearest loading zone (OA), and compressive in the region towards the nearest loading zone (OB).

5.2.3. Discussion

The stress distributions obtained from the finite element analysis can be used to explain some of the experimental results obtained in section 5.2.1. Examination of the stress distribution (see figure 5.5) reveals shear stress concentrations in the vicinity of the notch tip, which are mainly responsible for the onset of failure. The transverse normal stresses (σ_{yy}) are tensile along the path of the crack (along OA in figure 5.6), and therefore contribute to crack growth in this direction. It is interesting to note that σ_{yy}, are tensile in this region even under positive loading angles ($\alpha > 0^o$). This explains the experimentally observed drop in failure loads for 0^o carbon/epoxy and teak specimens when loaded in shear and compression ($\alpha > 0^o$, see figures 5.2 b and 5.3 b). Clearly, the failure mode for specimens loaded at $\alpha > 0^o$ is essentially the same as when loaded in shear and tension ($\alpha < 0^0$). It can therefore be concluded that for unidirectional composite specimens with fiber orientation A, an actual intralaminar damage initiation and propagation under combined shear and transverse compressive stresses cannot be achieved in the biaxially loaded Iosipescu specimen. Figure 5.6 also shows that both σ_{yy} and τ_{xy} approach zero at a point along the path of the crack, thereby arresting it. The point of crack arrest is expected to be farther for specimens loaded at $\alpha = +30^o$ than for specimens loaded at $\alpha = -30^o$. This explains the variations in the lengths of axial splits observed in section 5.2.1 for teak specimens.

Both teak and carbon/epoxy specimens, with fiber orientation B, failed along the notch-root axis in a mode characteristic of the pure shear test.[41] The loads at failure for these specimens were significantly lower than the failure loads of orientation A specimens. This has also been previously observed in the pure shear test.[25, 41] Since the in-plane shear strength should theoretically be identical for specimens with fiber orientations A and B, extensive finite element analysis have been performed in the literature to explain the discrepancy. Barnes et al.[44] showed that Iosipescu specimens with fiber orientation B, loaded at $\alpha = 0^o$, experience a significant contribution of transverse tensile stresses (σ_{xx}) along the notch-root axis. These specimens therefore encounter premature failures, and are not suitable for measuring the shear or biaxial strength of the composite.

Experimental failure loads obtained from the teak and carbon/epoxy specimens, with fiber orientation A, can be used to obtain biaxial failure envelopes for the composites in a wide range of shear and transverse tensile stresses. However, in the absence of a reliable analytical method, an accurate determination of the stress state at the notch tips remains a problem. The finite element analysis performed in section 5.2.2 for carbon/epoxy specimens was used in conjunction with the experimentally obtained failure loads, to determine the notch-tip stresses at the onset of failure.[56] It was found that failure stresses obtained from the numerical analysis were very significantly larger than the failure stresses reported in the literature.[25] Furthermore, the magnitude of the notch-tip stresses was found to increase with a decrease in the notch radius (ρ) and the size of finite elements used at the roots of the notches (ξ).[56] Clearly, this was because our finite element model assumed a linear-elastic material behavior. It is a well documented fact that in linear-elastic media, the stresses at the tip of a notch are either singular (for perfectly sharp notches), [53, 55] or severely concentrated (for round notches). However, from an engineering standpoint, most materials tend to relieve singular (or concentrated) stresses by undergoing localized damage or yielding. Therefore, the only way of accurately predicting the notch-tip stresses at the onset of failure would be a finite element model which accounts for material non-linearities.

In the original study conducted by Broughton, [25] a highly simplistic analytical approach was used to resolve the stress state at the notch tips. This approach assumed a uniform state of stress along the notch-root axis, such that from simple force-equilibrium relationships

$$\sigma_{xx}^{f} = \frac{P_{\alpha} \sin \alpha}{w\,t} \quad \text{and} \quad \tau_{xy}^{f} = \frac{P_{\alpha} \cos \alpha}{w\,t} \tag{5-1}$$

Clearly, this approach does not take into account obvious parameters like the orthotropy ratio, the fiber orientation, the notch geometry, and the non-linearities in the material behavior. However, the biaxial failure envelope obtained from this approach has been found to be in excellent agreement with the Tsai-Hill criterion for biaxial failure of unidirectional composites (refer section 2.1.2). Furthermore, Broughton and co-workers [27] found that the shear strengths of carbon/epoxy and glass/polyester Iosipescu specimens, obtained by using equations (5-1), are in excellent agreement with corresponding data obtained from the torsion tests of hoop-wound tubes. Owing to the fact that stress concentrations are non-existent in tubes, it can be concluded that the shear stress concentration factor (K_t) at the notch-roots of the Iosipescu specimens approach unity at the onset of axial splitting. This was recently verified by Ho and co-workers, [52] who performed a non-linear finite element analysis of carbon/epoxy Iosipescu specimens loaded at $\alpha = 0^o$. They found that at loads large enough to initiate failure, the stress concentrations at the notch-tips get relaxed, while the strains remain concentrated.

Using equations (5-1), figures 5.7 (a,b) show the biaxial failure envelopes obtained for unidirectional carbon/epoxy and teak specimens, respectively. It is evident that the experimental data is in good agreement with the Tsai-Hill criterion. [21] A major limitation of the biaxial Iosipescu fixture is its inability to obtain the transverse tensile strength. Therefore, transverse tensile tests were performed to determine σ^f_{yy}. As explained earlier, the failure envelopes for both carbon/epoxy and teak are approximately symmetric about the $\alpha = 0^o$ axis, since specimens loaded in both ($\alpha > 0^o$) and ($\alpha < 0^o$) fail under the influence of shear and transverse tensile stresses.

Subsequent to this study, the same approach was adopted by Balakrishnan[125] for characterizing the biaxial failure properties of a Ti/SiC metal-matrix composite and an E-glass/epoxy polymer composite. The E-glass/epoxy composite specimens were extracted from the GRP rod of insulator A. Figure 5.8 shows the biaxial failure envelope of the GRP material. Comparing figures 5.7 (a) and 5.8, it is evident that the biaxial properties of the E-glass/epoxy composite are very similar to the properties of the XAS 914 carbon/epoxy composite. More recently, Balakrishnan et al.[126] have demonstrated that the biaxial Iosipescu fixture can be used to obtain the transverse tensile strength of unidirectional composites. This is possible by testing unidirectional composite specimens at $\alpha = 0^o$ with fibers aligned at 45^o with respect to the notch-root axis.

5.3. APPLICATION TO MIXED-MODE FRACTURE

The GRP rod of composite insulators is susceptible to intralaminar cracking either during assembly or in service. Wu [66] has shown that in unidirectional composites, the critical fracture parameters K_{Ic}, K_{IIc}, and K_{IIIc}, associated with the three fundamental modes of loading, are material constants. Therefore, an appropriate test methodology which simulates various mixed mode fracture conditions in unidirectional composites can be used to measure K_{Ic} and K_{IIc}, and to investigate the interaction between K_I and K_{II} under mixed-mode conditions. In the past, researchers have characterized mixed-mode fracture properties by performing biaxial tests on cracked off-axis tension tests, [72,92] edge-cracked Arcan tests, [93] compact tension-shear (CTS) tests, [36,85] and tension/torsion tests of circumferentially cracked hoop-wound thin tubular specimens. [127-131]

In this section, an attempt has been made use the biaxial Iosipescu test for determining the mixed-mode intralaminar fracture properties of unidirectional polymer-matrix composites. Once again, the tests have been performed on the unidirectional XAS 914 carbon/epoxy composite, whose biaxial failure and mixed-mode fracture properties are very similar to the E-glass/polymer composites used in insulators. The analysis considers a center crack (CC) specimen geometry, wherein a crack is placed at the center of the Iosipescu specimen along the notch-root axis, with fiber orientation B to ensure self-similar crack extension (see figure 5.9 a). The finite element method was used to extract the fracture parameters ($K_{I,II}$). These parameters have been correlated with experimentally measured fracture loads in order to obtain the critical fracture parameters $K_{Ic,IIc}$, and the interaction between K_{Ic} and K_{IIc} under combined symmetric and skew-symmetric loads.

5.3.1. Finite Element Analysis

A two-dimensional (plane stress) linear elastic analysis was performed for the carbon/epoxy CC-specimens (fiber orientation B). Figure 5.9 (b) shows the finite element mesh which consists of 2320 eight-noded isoparametric quadrilateral and collapsed triangular elements. Four different crack lengths ($2a$) of 4mm, 6mm, 8mm, and 10mm were considered. The maximum separation between the crack faces was assumed to be 1% of the half crack length (a). A fan-shaped mesh of 12 extremely fine triangular elements (element size $L = 0.05$ mm) was constructed around the crack tip. Depending on the type of numerical scheme being employed, both conventional non-singular and quarter-point elements [74, 75] were used at the crack tips. The total externally applied compressive load (P_α) was assumed to be 1 kN. For the four crack lengths considered, the two counteracting force-couples (P_1 and P_2) were applied at angles of $\alpha = 0^o$ (pure shear), and -10^o, -20^o, -30^o, and -40^o (shear and tension). The case of counter-clockwise specimen rotations ($\alpha > 0^o$) leading to combined shear and transverse compression along the plane of the crack would involve crack-face contact and frictional effects. This case has not been analyzed in this section.

Four different numerical schemes were used to extract the stress intensity factors (SIFs) at the tips of the central crack, namely; the displacement correlation method, the displacement extrapolation method, and the virtual crack closure (VCC) -1c and -2c methods. A detailed description of these schemes was presented in chapter 2 (section 2.3.1.3).

Prior to the application of the four numerical schemes to our CC-specimens, the algorithms had to be verified and numerical experimentation was required to identify the appropriate crack-tip element size. The analytical solution of Kaya and Erdogan. [132] for an edge-cracked boron/epoxy strip under uniaxial tension, was used as a simple benchmark for validation of the VCC-schemes. The analysis was carried out using crack-tip element sizes (L) which were 10% and 1% of the original crack length (a). Results presented in appendix A demonstrate that the use of a crack-tip element size of 1% of the actual crack length generated accurate *SIF* values. In particular, the VCC-2c scheme was found to yield errors within ≈2%. It was now considered safe to implement the numerical schemes for the more complicated CC-specimen geometry.

The crack-tip energy release rates ($G_{I,II}$) obtained from the four numerical schemes are listed in table 5.3. Clearly, all four numerical methods were in good agreement and indicated similar variations in $G_{I,II}$ values as a function of the loading angle (α) and crack length (a). It can be observed from that for a fixed crack length (a), the mode I energy component (G_I) is negligible at $\alpha = 0^o$ and progressively increases as the angle α is increased in a clockwise sense, whereas the value of G_{II} progressively decreases. In addition, if the loading angle (α) is fixed, both mode partitions G_I and G_{II} increase with the crack length. These trends are graphically illustrated in figures 5.10 (a,b). The results clearly demonstrate that the biaxial Iosipescu method, employing CC-specimens, is theoretically capable of generating a wide range of mixed-mode loading conditions (ranging from pure mode II to mixed-modes I and II). It therefore appears to be a suitable method for characterizing the mixed-mode fracture toughness of unidirectional composites. The fact that for any loading angle the total energy release rate ($G_{total} = G_I + G_{II}$) increases monotonically with the length of the crack, predicts that intralaminar crack growth in the carbon/epoxy specimens will be unstable in nature. Furthermore, the ratio G_{II}/G_I (see table 5.3) indicates that the that carbon/epoxy composite specimens with longer cracks provide a wider range of mixed mode conditions at the crack tip. However, cracks longer than 10mm may not be advisable since the size of the ligament remaining between the crack- and notch-tips will become too small.

5.3.2. Fracture Experiments

Unidirectional carbon/epoxy Iosipescu specimens with fiber orientation B were machined to the standard dimensions shown in figure 2.5. Various machining techniques were tried (*e.g.* CO_2 lasers, focussed water-jets, abrasive diamond wires, electrical discharge) in order to create a central crack in the composite specimens. However, all these techniques were unsuccessful in producing a through thickness central slot of the desired geometry. A series of holes were therefore drilled mechanically, using carbide drills of 0.5 mm diameter. These holes were drilled adjacent to each other such that the net result looked like a through-thickness elliptical slot 0.5 mm wide and 6 mm long. The two ends of the elliptical slot were further extended by 1 mm each using a sharp scalpel blade (see figure 5.11 a).

The biaxial Iosipescu tests were performed at a fixed displacement rate of 0.76 mm/min. A total of 15 specimens with a central precrack, and 9 specimens without any precrack, were tested under loading angles of $\alpha = 0^0$, -10^0, -20^0, -30^0, and -40^0. In order to monitor the onset of crack-growth or debondings, acoustic emission (AE) from the specimen was monitored during the test using the AET 5500 system. [120] Due to limited access to the specimen surface, a 100 mm long aluminum wave-guide was adhesively bonded to the specimen surface (3M DP-100 epoxy adhesive) approximately 5mm from the crack plane. The peizo-electric transducer was connected to the system main-frame via a preamplifier with a fixed gain of 60dB. Total gain of the system was 94dB. A schematic of the complete experimental setup is presented in figure 5.11 (b).

All specimens fractured catastrophically along the plane of the pre-crack. However, prior to ultimate fracture, the AE signals did indicated some stable damage accumulation which was most likely due to interfacial debondings at the tips of the precrack. The final burst AE event corresponded with ultimate unstable fracture, and corresponded with a sharp drop in the load sustained by the specimen. Similar to the test results of uncracked carbon/epoxy specimens (section 5.2.1), the CC-specimens tested at $\alpha = 0^o$ sustained highest loads. As the loading angle increased, the loads at fracture dropped.

5.3.3. Discussion

The finite element model considered a perfectly sharp central crack (figure 5.9 b). However, due to practical difficulties, the actual specimens used for fracture experiments had an elliptical central slot (figure 5.11 a). Since it is a well documented fact that *SIF* and *G*-values are highly sensitive to the crack geometry, the finite element model described in section 5.3.1 had to be modified to simulate the actual crack geometry. Figure 5.12 shows the modified mesh consisting of a 6 mm long elliptical slot, with two 1 mm long splits originating from the ends. A single crack length was analyzed for different loading angles (α), and the VCC-2c procedure was used to compute crack tip *SIF* and and *G* values. Results obtained from the analysis are presented in table 5.4. The trends of the computed $G_{I,II}$ and $K_{I,II}$ values are identical to the perfectly sharp crack geometry modeled earlier, only the absolute values are different.

The numerically extracted $K_{I,II}$ values, in conjunction with experimentally measured fracture loads (P_f), could now be used to determine K_{IIc} in pure shear ($\alpha = 0^0$), and the interaction between K_I and K_{II} at the onset of intralaminar fracture in mixed modes ($-40^0 \leq \alpha < 0^0$). The FE model assumed a net applied load of P = 1000 N and a specimen thickness of 1mm (plane stress), whereas the actual specimens were 5 mm thick. Therefore, the numerical K-values were appropriately scaled to arrive at $K_{I,II}$ values which correspond to the catastrophic fracture of unidirectional carbon/epoxy specimens (see table 5.4). Figure 5.13 shows the mixed-mode fracture envelope obtained from this approach. Two edge-cracked carbon/epoxy plates, with the geometry described in appendix A, were tested in tension to obtain the value of K_{Ic}. The average values of K_{Ic} and K_{IIc} were found to be $1.09 MPa\sqrt{m}$ (from the edge-cracked tension test) and $2.81 MPa\sqrt{m}$ (from the Iosipescu test at $\alpha = 0^0$) respectively. The corresponding values of G_{Ic} and G_{IIc} were 93.7 J/m^2 and 165.1 J/m^2 respectively. Based on these K_{Ic} and K_{IIc} values, the mixed-mode fracture criteria (chapter 2, equations 2-19 to 2-21) are also plotted in figure 5.13.

In spite of the obvious scatter in the data, the mixed-mode fracture envelope seems to agree well with the fracture criteria. However, for highly orthotropic materials like carbon/epoxy (E_{11}/E_{22}=14.2), it is expected that the value of G_{IIc} will be at least one order of magnitude higher than G_{Ic}. For the intralaminar fracture of unidirectional carbon/epoxy composites, G_{Ic} values quoted in the literature range from 79 to 190 J/m^2, [93, 96] whereas G_{IIc} values span a much wider range of 570 to 8,690 J/m^2. [96, 127] The G_{Ic} value of 93.7 J/m^2 obtained from the edge-cracked tension test seems to agree well with the literature, however, the G_{IIc} value of 165.1 J/m^2 obtained from the Iosipescu specimen clearly needs to be verified by another independent mode II test. Therefore, mode II double cantilever beam (DCB) tests were performed in this study (see Appendix B). In conjunction with the modified beam theory solutions, the value of G_{IIc} from this test was found to be 6670.3 ± 618 J/m^2. Since the mode II DCB test is a well established procedure, and since for a highly anisotropic material it is reasonable to expect $G_{IIc} >> G_{Ic}$, it is concluded that the K_{IIc} value (at $\alpha=0^0$) and $K_{I,II}$ values (at $-40^0 \leq \alpha < 0^0$) presented in table 5.4 and figure 5.13 are erroneous. The failure process in the CC-specimens clearly requires further examination.

Thus far, we have assumed that the instantaneous failure of the carbon/epoxy CC-specimens occurred as a result of unstable extension of the central crack. Sukumar and Kumosa [53] have demonstrated that the stresses are non-singular at the tip of a perfectly sharp 90^o notch under mode II loading, whereas, the tip of a sharp crack exhibits the classical square-root singularity. It therefore seems reasonable to expect intralaminar fracture to initiate from the tip of the central precrack. However, the instantaneous nature of the fracture process makes it impossible to visually determine the mode of failure. Our only recourse, therefore, is to compare the nominal stresses required to initiate failure in the CC-specimens, and the ordinary uncracked specimens wherein biaxial failure always initiates at the tips of the v-notches. This can be done by employing the simple formulae employed by Broughton (equation 5-1), where the net width of the gauge section (w) is 12 mm for uncracked specimens, and 4 mm for cracked specimens. Results plotted in figure 5.14 show that the nominal failure stresses for cracked specimens were in good agreement with the uncracked specimens and the Tsai-Hill criterion [21] for *biaxial failure*[+] from the tips of the v-notches. Moreover, considering $G_{Ic} = 93.7\ J/m^2$ and $G_{IIc} = 6670.3\ J/m^2$, the nominal stresses ($\sigma_{f,req}$ and $\tau_{f,req}$) required to initiate *mixed−mode fracture*[++] from the crack tip were calculated such that the fracture criterion (equation 2-20) was satisfied.

[+] "biaxial failure" refers to shear-dominated failure of resin and interfaces when the stresses locally exceed their strength values (*i.e.* $\sigma_{xx} \geq (\sigma_{xx})_f$ and $\tau_{xy} \geq (\tau_{xy})_f$).

[++] "mixed-mode fracture" refers to instantaneous failure caused by extension of a pre-existing crack when fracture parameters exceed critical values (*i.e.* $f(G_I, G_{II}) \geq G_c$).

It is evident that the nominal stresses required to initiate mixed-mode fracture from the tip of an 8 mm long elliptical central precrack are significantly higher than the stresses required to initiate biaxial failure from the notch-tips. Therefore, although numerical results were encouraging, the CC-specimens tested in this study encountered premature failure due to applied stresses exceeding the biaxial failure strength of the material. In order to ensure intralaminar failure due to mixed-mode fracture, a double edge-crack (DEC) specimen geometry is proposed for future study. This geometry will consist of orientation B composite Iosipescu specimens, with two identical edge-cracks of length (a) emanating from the roots of the notches (see figure 5.15 a).

Figure 5.15 (b) shows a two-dimensional finite element mesh of the DEC-specimens. The modified virtual crack closure (VCC-1c) method is being used to compute the crack-tip SIFs. The crack-faces are meshed with surface-to-surface contact elements in order to extend the analysis to shear and compression loadings ($+40^o \geq \alpha \geq 0^o$), wherein crack-face contact and friction will be involved. It is important to note that while the problem is structurally non-linear (due to contact and friction), the principles of linear elastic fracture mechanics (LEFM) will be applicable if the material is assumed to be linear elastic. However, the computed stress intensity factors may not be linearly extrapolated to any magnitude of the external load (P). In the past, such solutions have been sought for the analysis of mode II end-notched flexure (ENF) specimens.[73, 86, 133, 134] Preliminary numerical results indicate that the range of mixed-mode loading conditions provided by the DEC-geometry is wider than that of the CC-geometry. Pure mode II fracture can be obtained from long cracks (a = 4 mm) loaded at $\alpha = 0^o$, while almost pure mode I fracture can be obtained from short cracks (a = 0.5 to 1 mm) loaded at $\alpha = -40^o$. Under shear and compression loadings, the cracks are subjected to pure mode II conditions, with the value of G_{II} decreasing with an increase in the friction coefficient (μ) and the loading angle (α). Experimental fracture testing of DEC specimens is proposed for future study.

Table 5.1 : Elastic properties for XAS 914 carbon/epoxy used in finite element analyses.

E_{11} (GPa)	E_{22} (GPa)	$\left[\frac{E_{11}}{E_{22}}\right]$	G_{12} (GPa)	ν_{12}
137.9	9.7	14.2	4.2	0.25

Table 5.2 : Normalized stresses at the notch-tips and specimen center for carbon/epoxy Iosipescu specimens (orientation A).

Loading Angle		Notch-Root Radius	
		ρ = 40 μm	ρ = 1.7 mm
$\alpha = 0°$	σ_{xx}	0.05^c -0.20^r	0.02^c 0.56^r
	σ_{yy}	-0.34^c -0.04^r	-0.29^c 0.01^r
	τ_{xy}	0.83^c 2.30^r	0.90^c 0.33^r
$\alpha = +30°$	σ_{xx}	-0.13^c -8.58^r	-0.17^c -4.32^r
	σ_{yy}	-0.39^c -0.72^r	-0.34^c -0.04^r
	τ_{xy}	0.70^c 2.06^r	0.77^c 0.29^r
$\alpha = -30°$	σ_{xx}	0.14^c 10.06^r	0.12^c 6.36^r
	σ_{yy}	-0.22^c 0.81^r	-0.17^c 0.06^r
	τ_{xy}	0.73^c 1.91^r	0.79^c 0.28^r

^{c} At specimen center, ^{r} At notch-tip

Table 5.3 : Mode partitions G_I and G_{II} in CC carbon/epoxy specimens.

α	a	Displacement - Correlation		Displacement - Extrapolation		VCC - 1c		VCC - 2c	
(deg.)	(mm)	G_I (kJ/m^2)	G_{II} (kJ/m^2)	G_I (kJ/m^2)	G_{II} (kJ/m^2)	G_I (kJ/m^2)	G_{II} (kJ/m^2)	G_I (kJ/m^2)	G_{II} (kJ/m^2)
0^0	2	0.0013	1.1287	0.0159	1.2478	0.0002	1.3629	0.0002	1.3809
	3	0.0022	1.8920	0.0218	2.1480	0.0002	2.2826	0.0002	2.3079
	4	0.0034	3.1427	0.0282	3.5927	0.0002	3.8191	0.0002	3.8735
	5	0.0066	6.2872	0.0582	7.0404	0.0002	7.6147	0.0001	7.7924
-10^0	2	0.0407	1.1093	0.0643	1.2269	0.0387	1.3400	0.0394	1.3575
	3	0.0792	1.8532	0.1088	2.1046	0.0755	2.2362	0.0769	2.2607
	4	0.1626	3.0656	0.1974	3.5051	0.1556	3.7258	0.1587	3.7785
	5	0.4172	6.1097	0.4793	6.8419	0.3987	7.3993	0.4114	7.5713
-20^0	2	0.1534	1.0278	0.1885	1.1371	0.1488	1.2417	0.1514	1.2579
	3	0.3004	1.7096	0.3412	1.9416	0.2917	2.0628	0.2969	2.0851
	4	0.6213	2.8135	0.6646	3.2162	0.6033	3.4184	0.6153	3.4663
	5	1.6021	5.5802	1.6634	6.2465	1.5486	6.7538	1.5980	6.9100
-30^0	2	0.2913	0.8967	0.3442	0.9925	0.2833	1.0835	0.2885	1.0975
	3	0.5859	1.4820	0.6438	1.6830	0.5705	1.7878	0.5811	1.8065
	4	1.2522	2.4198	1.3069	2.7647	1.2183	2.9381	1.2437	2.9786
	5	3.3313	4.7644	3.3875	5.3283	3.2248	5.7587	3.3301	5.8909
-40^0	2	0.3301	0.7423	0.4291	0.8229	0.3206	0.8980	0.3273	0.9093
	3	0.7293	1.2101	0.8352	1.3754	0.7091	1.4605	0.7242	1.4750
	4	1.7352	1.9433	1.8342	2.2198	1.6859	2.3586	1.7254	2.3899
	5	5.0871	3.7669	5.1663	4.2075	4.9181	4.5440	5.0905	4.6465

Table 5.4 : Mixed-mode fracture parameters for carbon/epoxy specimens with an elliptical central crack.

α (deg.)	$(P_f)_{req}$ (N)	At the predicted load $(P_f)_{req}$			
		Normal Stress $(\sigma_f)_{req}$ (MPa)	Shear Stress $(\tau_f)_{req}$ (MPa)	$\left[\frac{G_I}{G_{Ic}}\right]$	$\left[\frac{G_{II}}{G_{IIc}}\right]$
0^0	8838.8	0.00	424.94	0.0083	0.9917
-10^0	3560.2	29.72	168.56	0.8427	0.1573
-20^0	1927.9	31.70	87.10	0.9576	0.0424
-30^0	1376.2	33.08	57.30	0.9814	0.0186
-40^0	1182.1	36.53	43.54	0.9889	0.0111

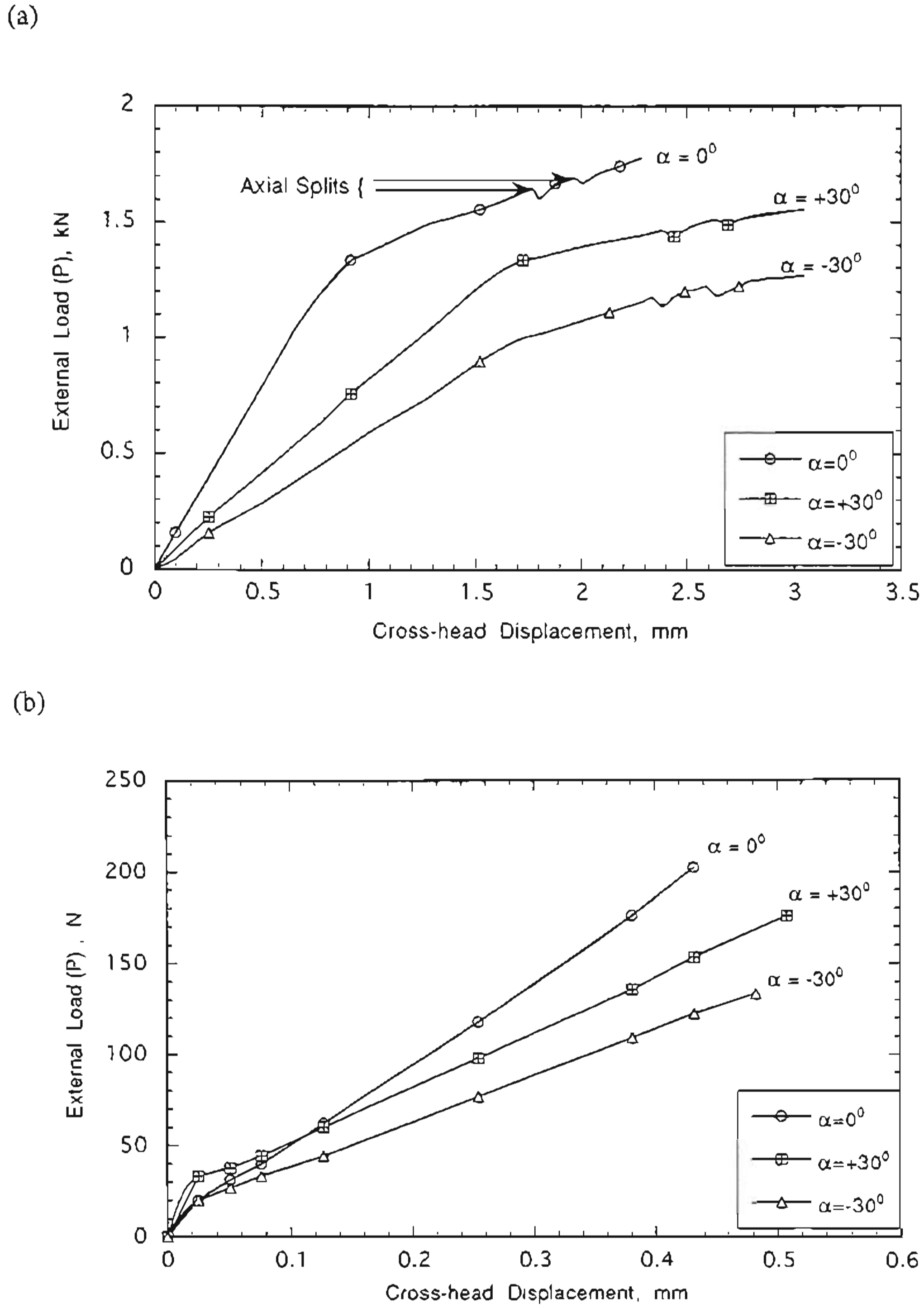

Figure 5.1 : Load versus displacement curves for teak specimens;
(a) Orientation A, and (b) Orientation B.

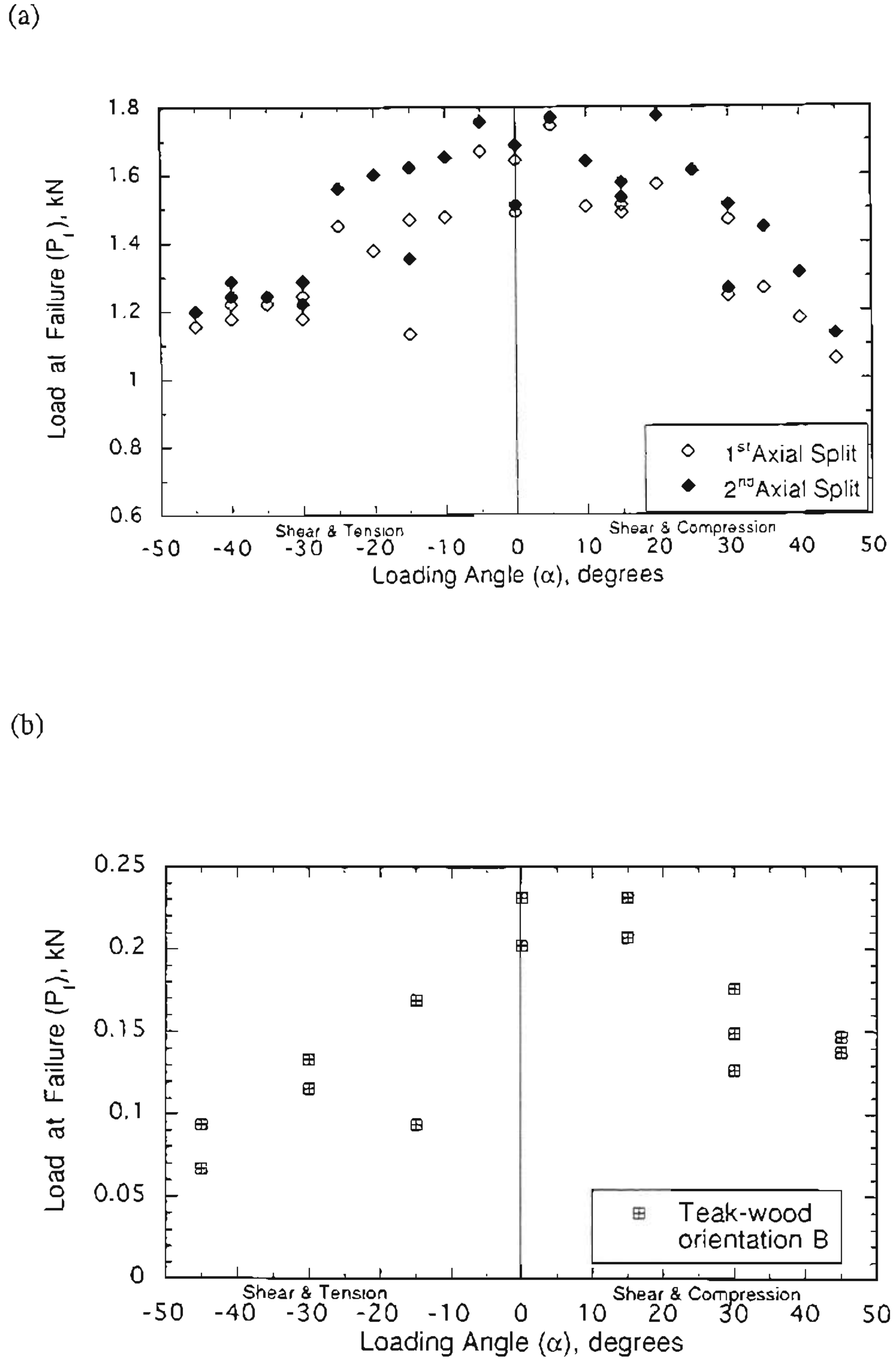

Figure 5.2 : Failure loads as a function of loading angle for teak specimens; (a) Orientation A, and (b) Orientation B.

(a)

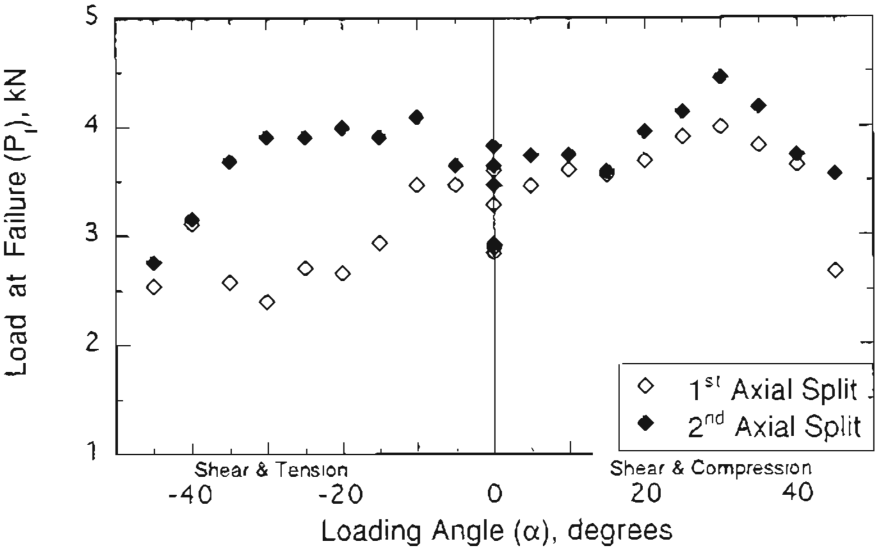

(b)

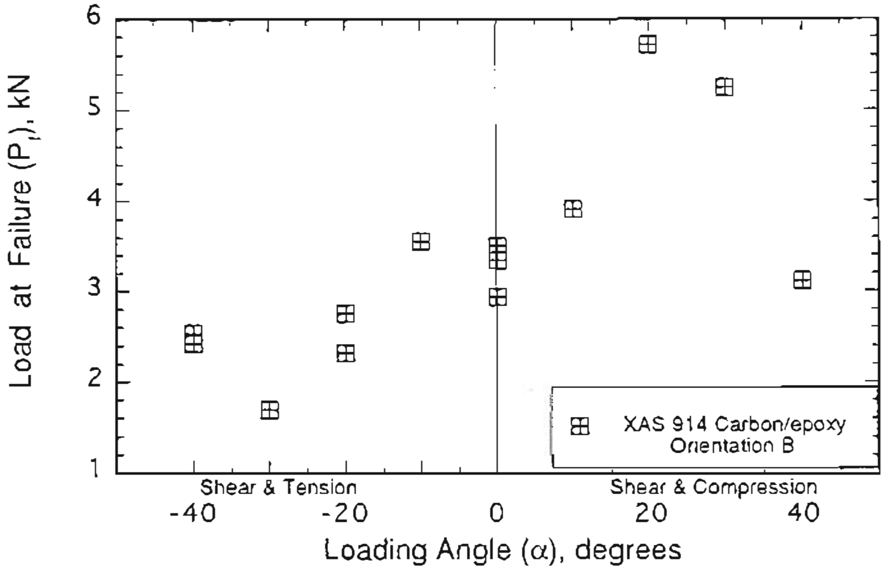

Figure 5.3 : Failure loads as a function of loading angle for carbon/epoxy specimens; (a) Orientation A, and (b) Orientation B.

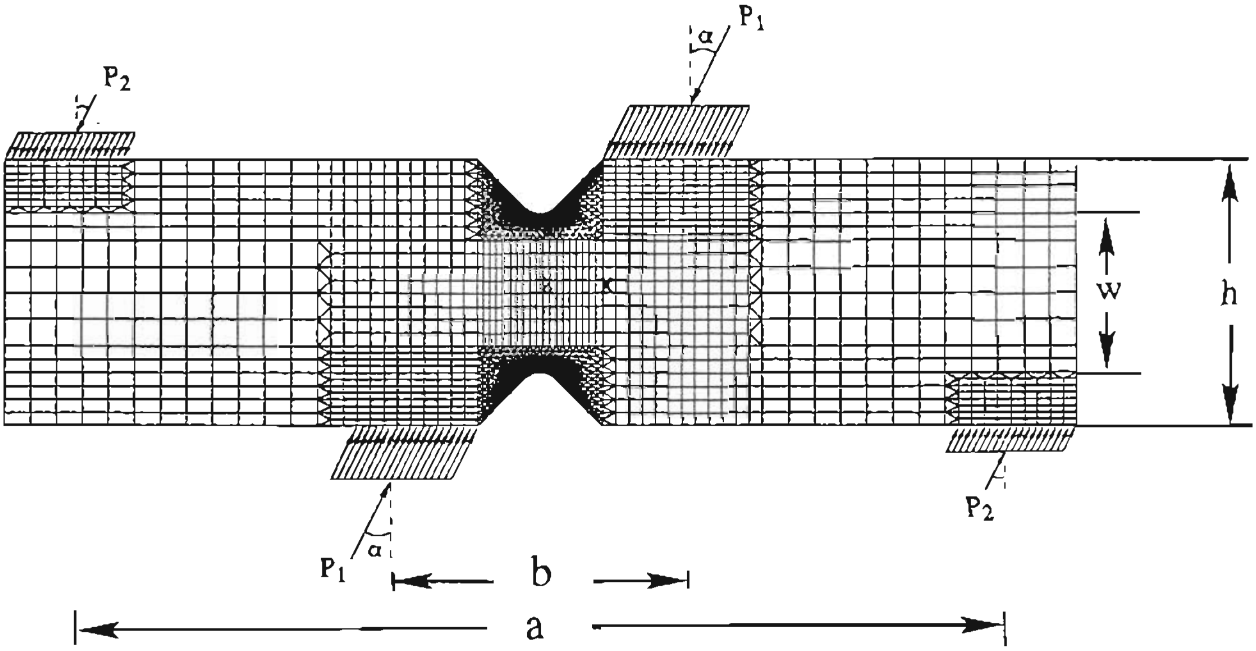

Figure 5.4 : Finite element mesh of the Iosipescu specimen with a finite notch-root radius (ρ = 1.7 mm).

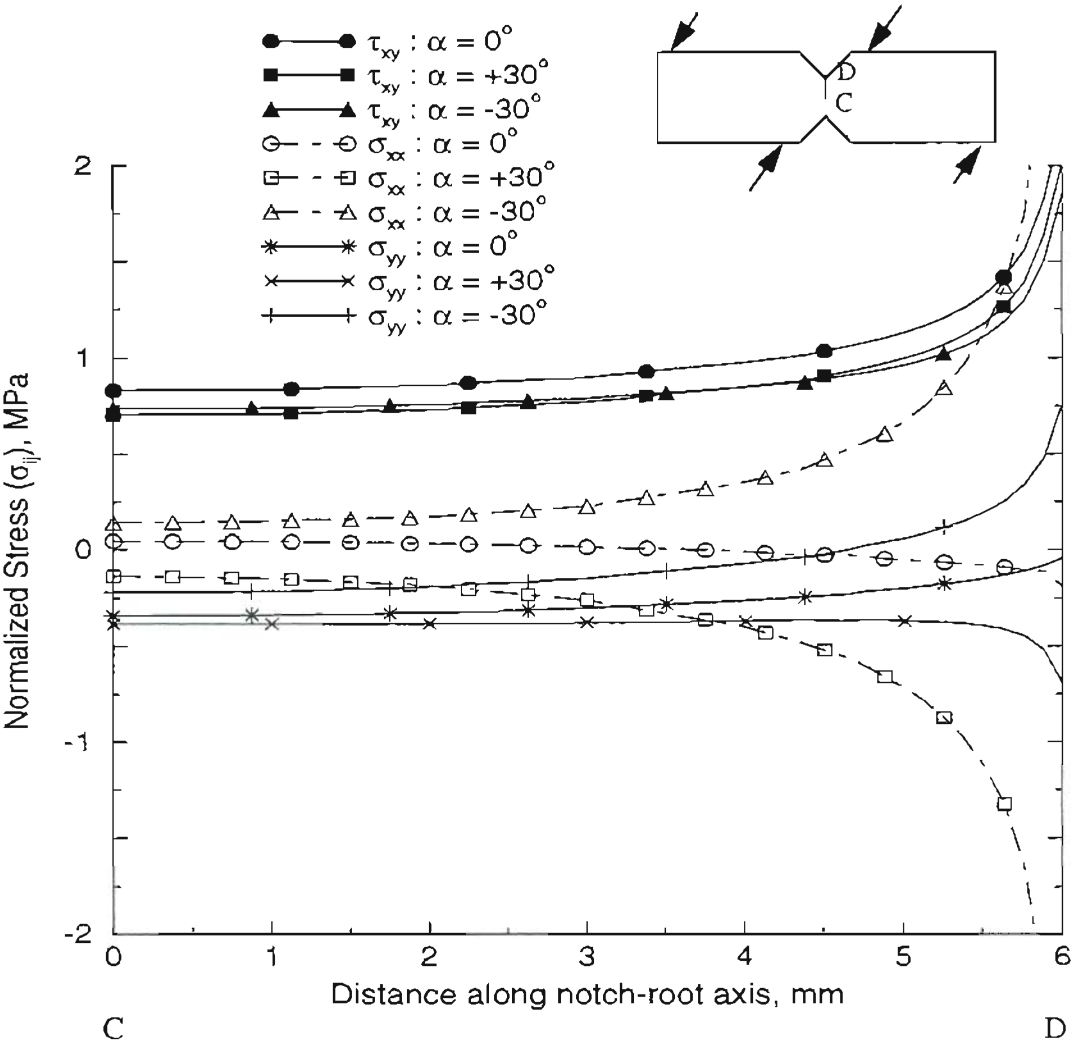

Figure 5.5 : Normalized stresses along the notch-root axis in carbon/epoxy specimens (orientation A, ρ = 40 μm).

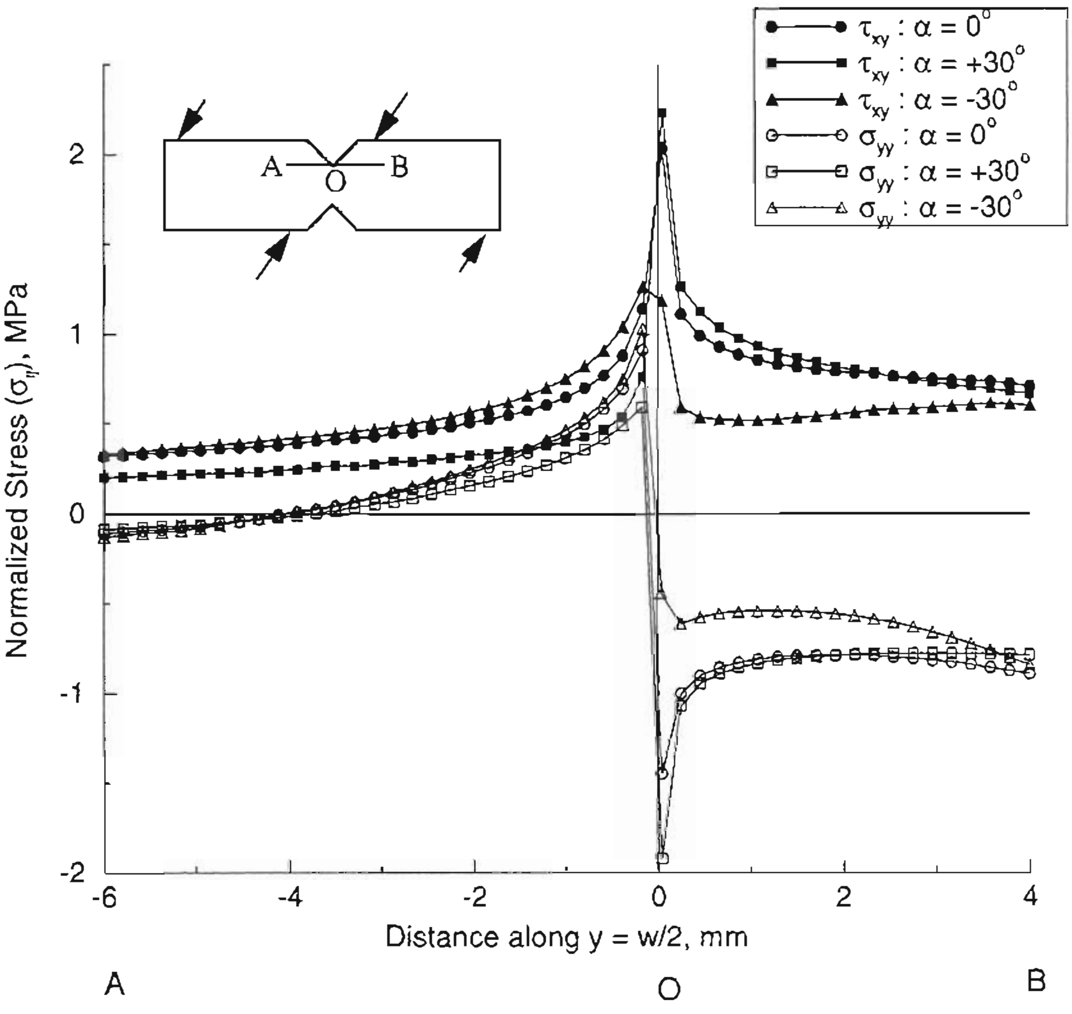

Figure 5.6 : Normalized stresses along $y = w/2$ in carbon/epoxy specimens (orientation A, $\rho = 40$ μm).

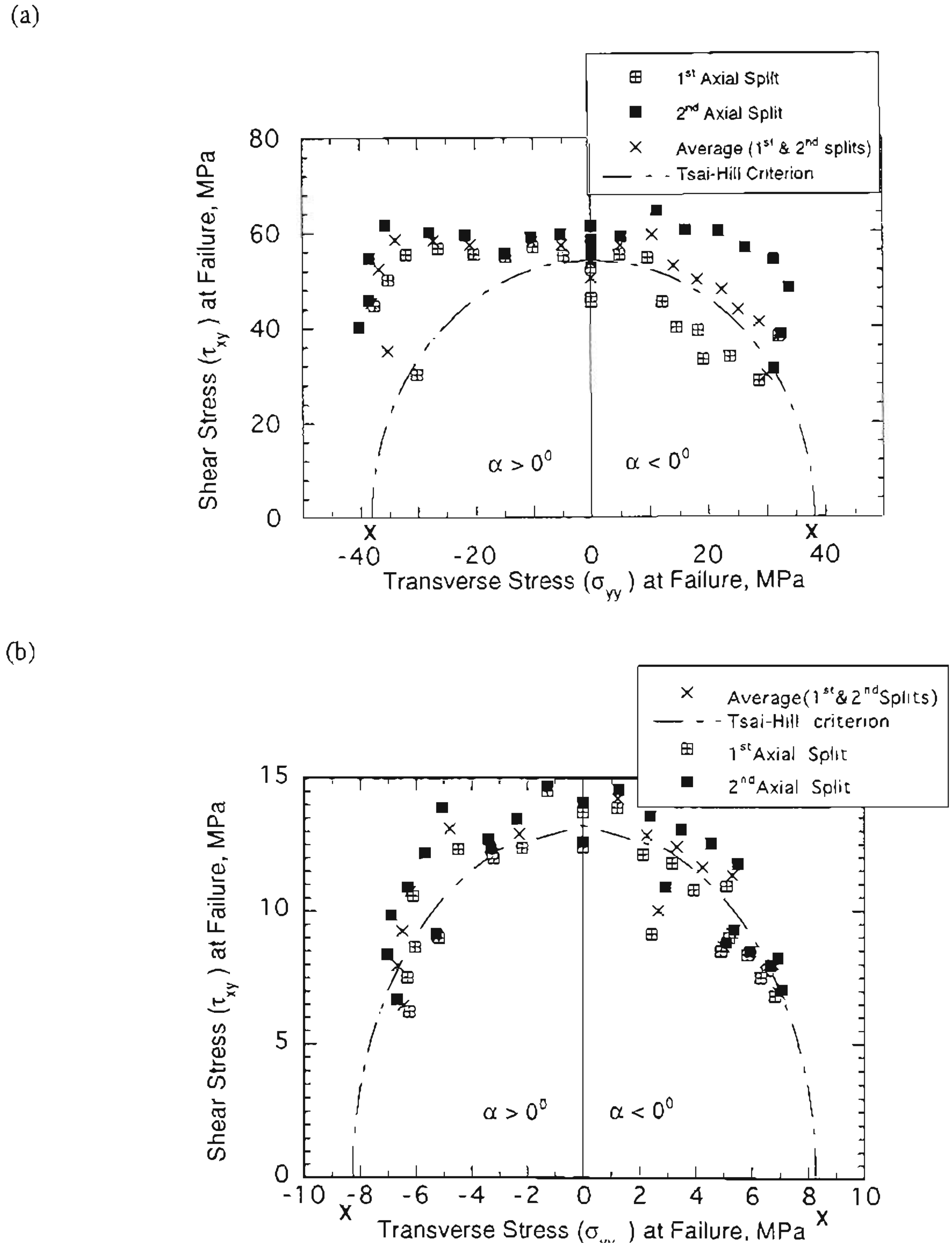

Figure 5.7 : Biaxial failure envelopes obtained from orientation A specimens; (a) XAS 914 carbon/epoxy, and (b) Teak.

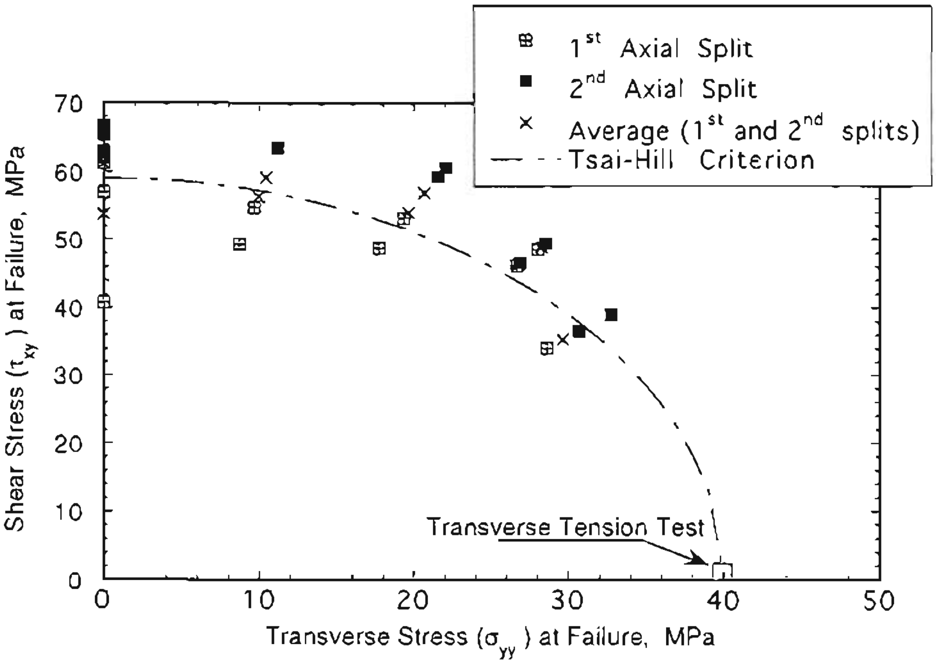

Figure 5.8 : Biaxial failure envelope of E-glass/epoxy composite used in insulator A.

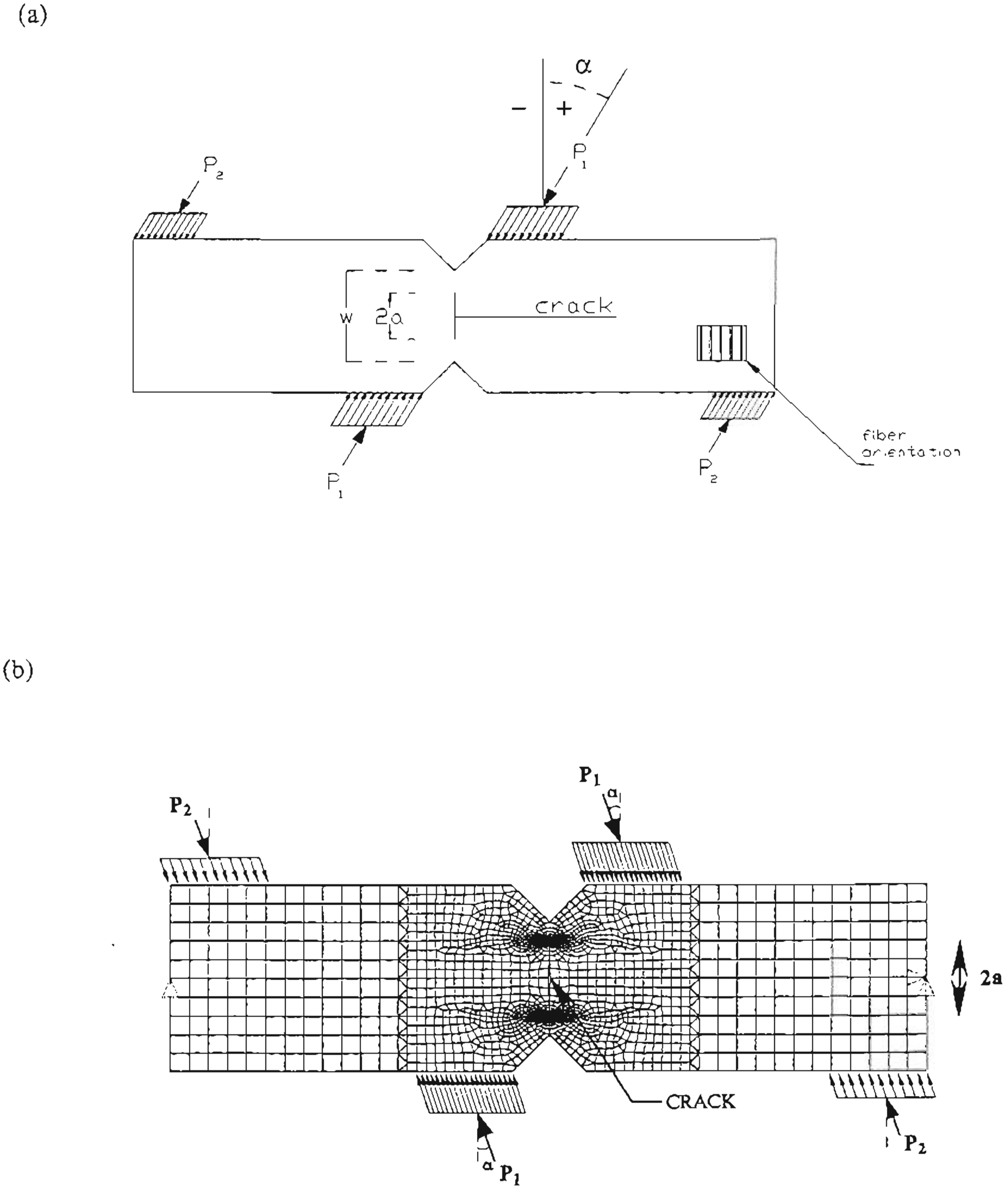

Figure 5.9 : Center cracked (CC) Iosipescu specimens; (a) Geometry and loading, and (b) Finite element mesh.

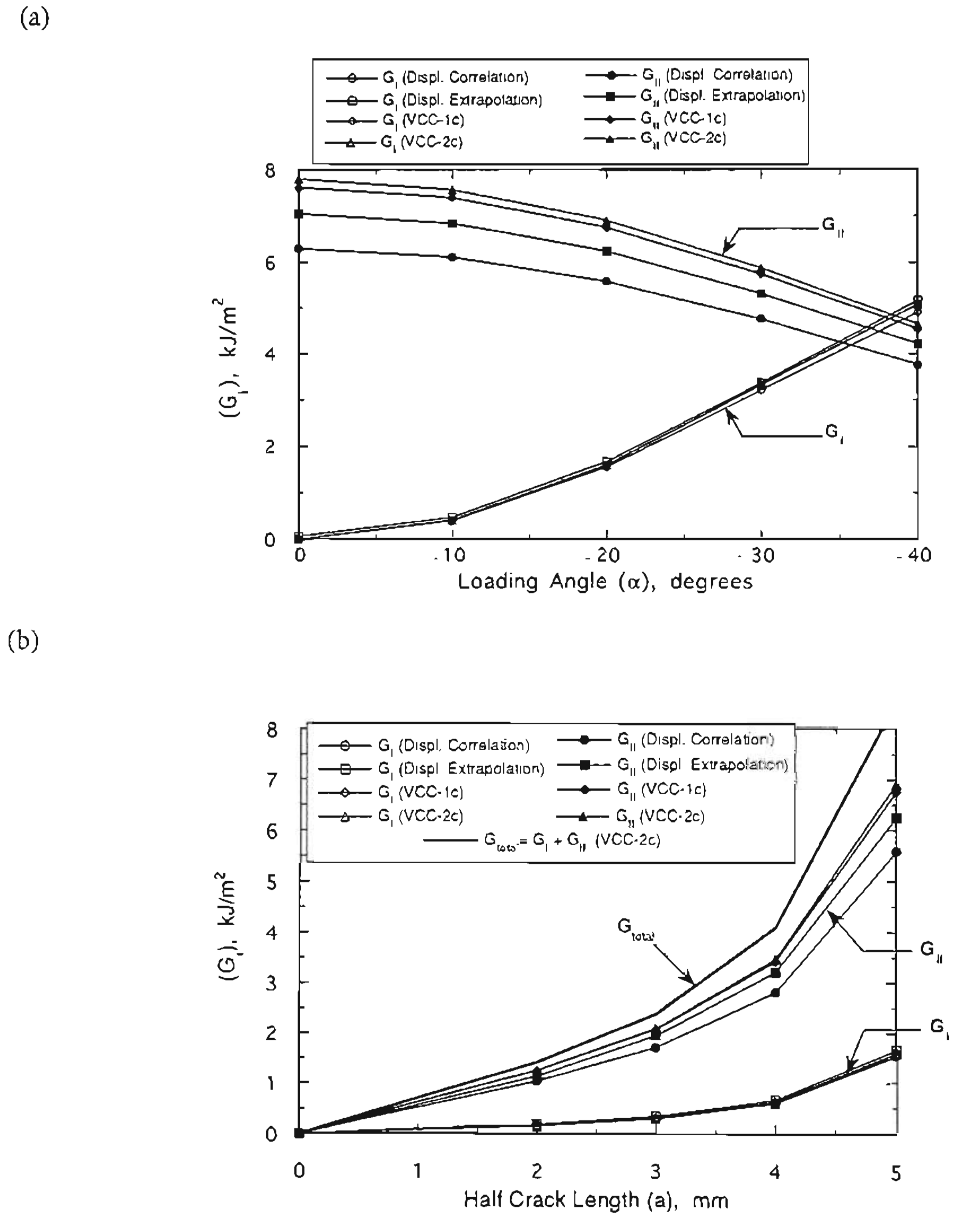

Figure 5.10 : Variation of G_I, G_{II} in carbon/epoxy CC-specimens;
(a) As a function of loading angle, at $2a = 10$ mm, and
(b) As a function of half crack-length, at $\alpha = -20^\circ$.

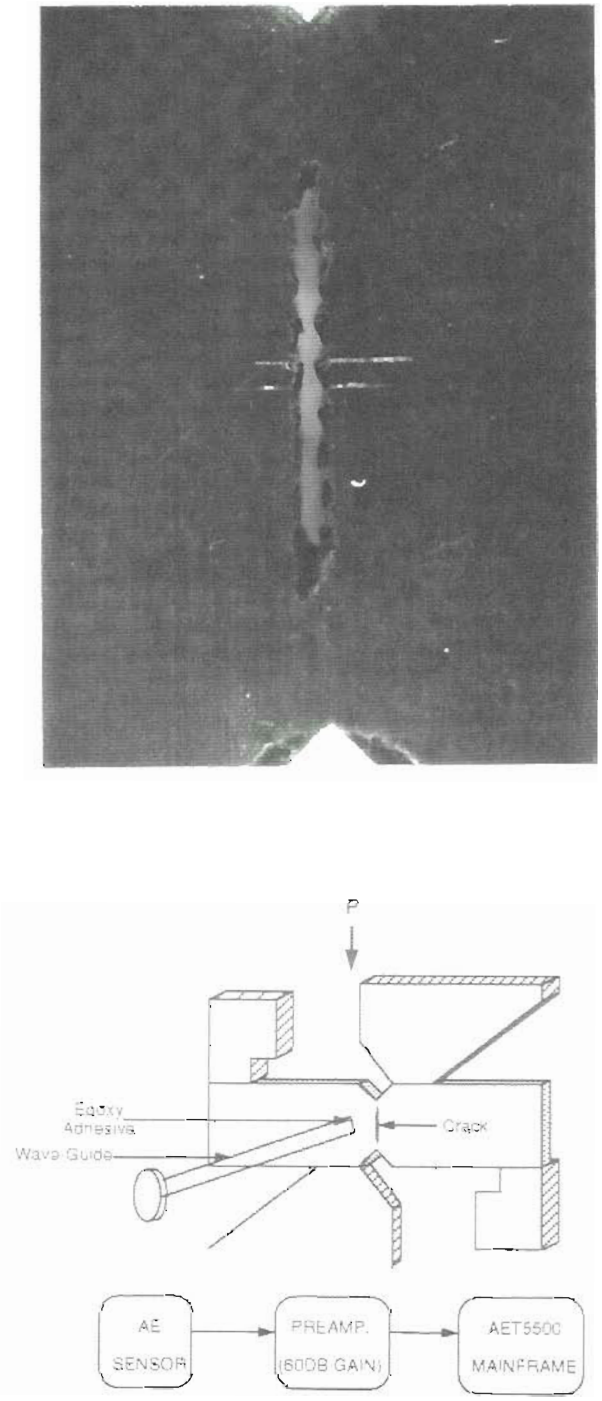

Figure 5.11 : Fracture tests of CC-specimens: (a) An elliptical central slot in a carbon/epoxy specimen, and (b) Schematic of experimental set up.

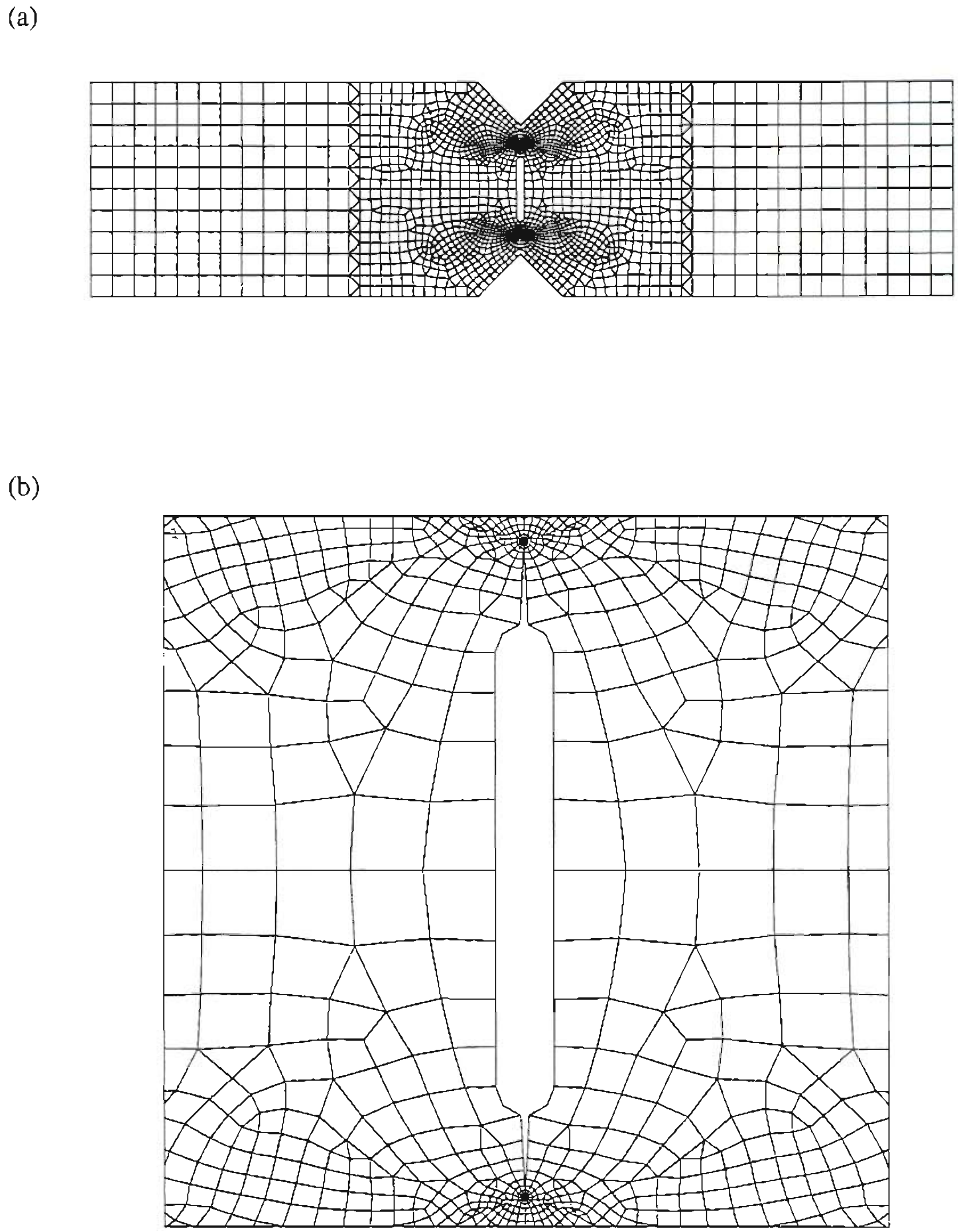

Figure 5.12 : Modified finite element mesh of the elliptical crack geometry.

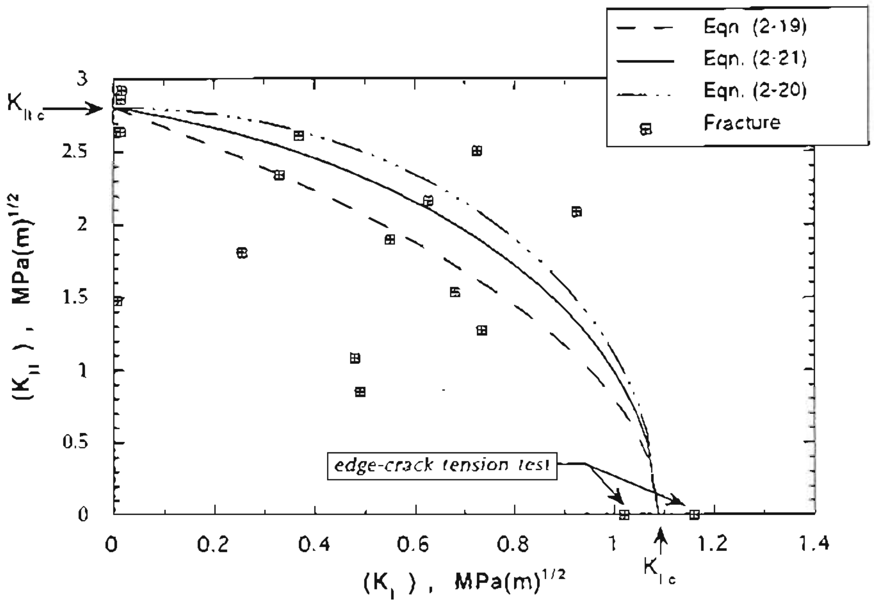

Figure 5.13 : Apparent mixed-mode fracture envelope from CC carbon/epoxy specimens.

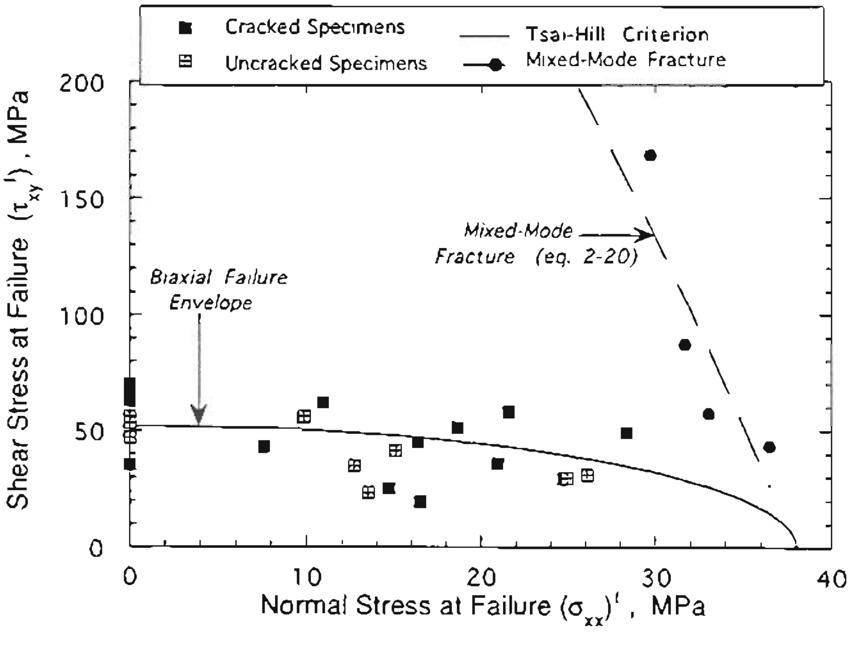

Figure 5.14 : Nominal failure stresses for cracked and uncracked CC-specimens compared with Tsai-Hill criterion, and mixed-mode fracture criterion.

(a)

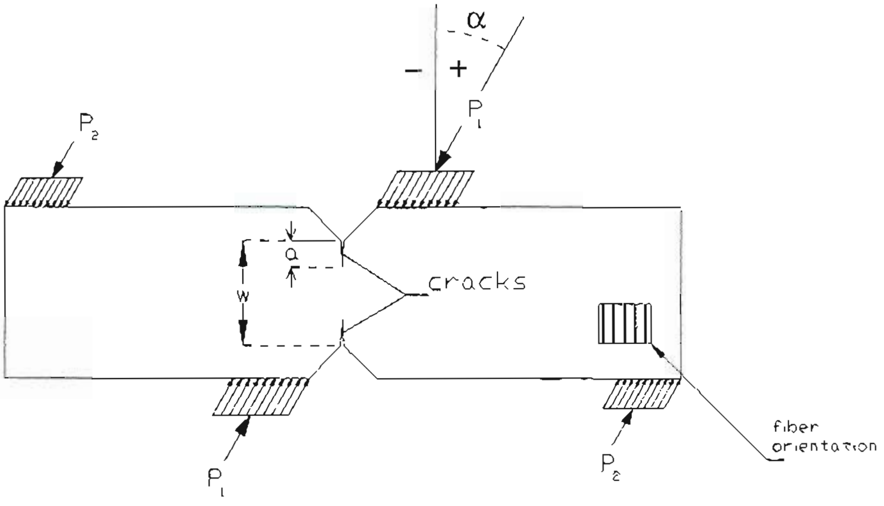

(b)

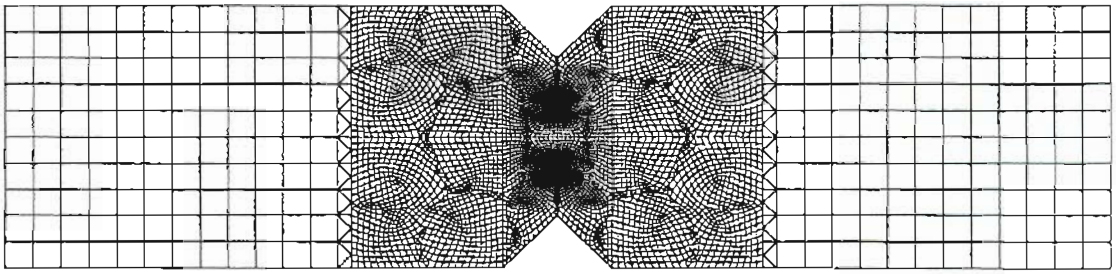

Figure 5.15 : Double edge-cracked (DEC) Iosipescu specimens;
(a) Geometry and loading, and (b) Finite element mesh.

Chapter 6

Discussions

This chapter presents a broad discussion of the experimental and numerical results obtained in the previous chapters. In addition, a parametric study has been performed to evaluate the design of composite insulators with crimped end-fittings.

In chapter 3, the mechanical behavior of five 115 kV substation insulators was characterized by performing both destructive and non-destructive tests. A new ultrasonic pulse-echo technique was used to determine the radial compression profiles of the five substation insulators due to the crimping process. This simple and highly cost-effective non-destructive technique can determine the three-dimensional radial deformation profile of the GRP rod within ± 0.1 mm, and also the presence of internal voids at the GRP-metal interface. In an earlier study, De Tourreil and co-workers [5] attempted to measure the radial compression in suspension insulators by sectioning them through the axis of the rod, and measuring the variation in the diameter of the rod in the axial direction. This method is clearly less sophisticated since it can measure the radial compression profile only along a single plane in the axial direction. The ultrasonic technique employed in this study has demonstrated that the radial compression can vary significantly in the tangential direction. Furthermore, the method employed by De Tourreil et. al. [5] is destructive in nature, and sectioning the end-fitting will significantly relax the tangential stresses and therefore the internal deformation of the GRP rod.

Using the ultrasonic method, the results obtained from insulators A to E appear to be accurate and reproducible. From figures 3.3 (a to e), it is evident that the radial compression profiles of insulators A and C were highly non-uniform, with a wave-like profile in the tangential direction. From the number of maxima (or minima) of the wave-like profile, it appears that a hexagonal radial compression die was used for the crimping of insulator A, and a square die may have been used for insulator C. In contrast, the radial compression profile of insulator E was highly uniform, and much lower in magnitude along the entire surface of the end-fitting. It can therefore be concluded that the shape and magnitude of radial compression applied to the GRP rod of composite insulators, with the same dimensions and mechanical ratings, is strongly dependent upon the manufacturing technique.

From the rod push-out tests performed on the five substation insulators, it is evident that under excessive axial compression, the insulators encounter failure due to internal sliding of the GRP rod within the metal end-fittings. Similar to the radial compression profiles, the maximum loads at the onset of internal sliding (P_f) were found to be significantly different for the five substation insulators. Insulator A had a large average magnitude of radial compression (M) which resulted in a very large value of P_f, while insulator E had the lowest average magnitude of radial compression and therefore the lowest strength under axial compression. Based upon the expected multi-axial loading conditions of substation insulators during service (given in chapter 4), it can be concluded that the axial loads at the onset of sliding (P_f) of all five substation insulators were significantly larger than the maximum axial compressive load (F_A = 1.34 kN under wind with glaze-ice forces) expected during service. Furthermore, based upon the expected axial compressive strength of the GRP composite ($\sigma^f_{11,c}$ in Table C.2), it can be concluded that the axial sliding loads for all five substation insulators were significantly lower than the axial compressive load required to initiate intralaminar failure of the GRP rod.

Similar to the axial compressive strength, the torsional strength of insulators seems to be affected by the average magnitude of radial compression applied during crimping. The relatively large values of M in insulators A, B, and C resulted in torsional failure due to the initiation of intralaminar splits in the GRP rod of these insulators, with the torsional strengths being very similar ($\approx$ 3000 to 3700 Nm). [122] In contrast, the significantly lower value of M in insulator E seems to have caused torsional failure due to internal sliding of the GRP rod within the end-fittings, at a load as low as 903 Nm. It is therefore clear that the average magnitude of radial compression applied to an insulator during the crimping process, and the frictional properties of the GRP-metal interface, can have a very pronounced influence on the axial and torsional strengths of the insulators.

The test results obtained from insulators A, C, and D, subjected to bending, were very similar in terms of the maximum displacements and the bending load at failure ($\approx$ 18 kN). [122] The flexibility of composite insulators, in comparison with their porcelain counterparts, is evident from the fact that the GRP rod can undergo a horizontal displacement of approximately 0.3 meters prior to intralaminar failure. Although the bending test results are not presently available for insulator E, it is expected that its mode of failure, strength, and overall displacement, will be very similar to the other insulators. This is because the walls of the end-fittings will constrain the GRP rod against internal sliding, thus making the value of M (applied during crimping) an insignificant parameter.

In chapter 4, axisymmetric and three-dimensional finite element models were developed for composite insulators. In both cases, the interface between the GRP rod and the end-fittings was assumed to be either perfectly bonded (*i.e.*, no relative sliding and continuous displacements across the interface) or imperfectly bonded (*i.e.*, with frictional sliding and discontinuous stresses/displacements across the interface). The axisymmetric models were used to simulate externally applied axial compression, in conjunction with the residual (axially non-uniform) radial compression applied during crimping. It was found that the assumption of a perfect interface between the GRP rod and the end-fittings resulted in large stress concentrations in the vicinity of the bimaterial interface corner, with the magnitude of the stress concentrations rapidly decreasing with increasing fillet radii (ρ). However, by using the Finite Element Iterative Method (FEIM), it was demonstrated that the actual stresses in the vicinity of a perfectly bonded GRP-Al interface corner will be singular in nature. This lead to the conclusion that the apparent stress concentrations obtained from a perfect interface model will be misleading. Furthermore, the structural response computed from a perfect interface model was linear, whereas from the rod push-out tests results it was evident that as a result of internal sliding of the rod under axial compression, the true response of composite insulators was non-linear. This difficulty was overcome by using the axisymmetric imperfect interface model, with general surface-to-surface contact elements at the GRP-Al interface. In this model, the stresses computed in the vicinity of the interface corner were bounded, and the structural non-linearity caused by internal sliding of the rod could be simulated. Furthermore, it was found that the axisymmetric imperfect interface model could accurately predict the loads at the onset of internal sliding (P_f) for insulators A and E, provided that the coefficient of friction (μ), and the average magnitude of radial compression (M) assumed in the model were accurate.

Since the actual in-service loads applied to composite substation insulators are multi-axial in nature, a global three-dimensional perfect interface model was used to determine the overall displacements of a substation insulator under the seven load cases described in chapter 4. Since this model could not be used to evaluate the internal stresses near the lower end-fitting (due to the reasons explained above), and since a global imperfect interface model would be computationally very expensive, a three-dimensional sub-model was developed with an imperfect interface between the GRP rod and end-fitting. Using this sub-model, the internal stresses were computed, and the partial sliding of the GRP rod could be simulated under several multi-axial loading conditions.

The finite element models developed in chapter 4 were verified under three different modes of uniaxial loading. Under axial compression (F_A), the load-displacement curves computed from the axisymmetric imperfect interface model and the three-dimensional sub-model were found to be in good agreement with the push-out test results of insulator A (employing $\mu = 0.3$ and $M = M_A$), and insulator E (employing $\mu = 0.75$ and $M = M_E$). Under bending loads (F_B), the linear load-displacement response computed from the global perfect interface model was found to be in excellent agreement with bending test results obtained from insulators A, C, and D, up to a load of approximately 8 kN.[122] Under torsional loads (M_T), the maximum angular rotation of insulator A computed from the global perfect interface model, and the maximum shear stress on the surface of the GRP rod, were found to be in good agreement with the predictions of the closed-form linear elastic solution for an isotropic rod subjected to pure torsional loads, and also with the experimental torque versus rotation curves obtained from insulators A, B, C, and D.[122] Based upon the intralaminar shear strength (τ_{12}^f) of 60 MPa determined from the Iosipescu shear test, the finite element analysis predicted intralaminar failure at a nominal torque (M_T) of 3113 Nm, while the closed-form analytical formulae (equations 4-5) predict failure at 2974 Nm. Experimentally, torsional failure of insulators A, B, C, and D was observed at 3672 Nm, 3050 Nm, 3615 Nm, and 3559 Nm respectively.[122] It should be mentioned that although the analytical solution does not consider the effects of end-fittings attached to the ends of the rod, it was expected to be approximately applicable to composite insulators since the GRP rod of insulators is transversely isotropic (in the r–θ plane). Certainly, the analytical solution would not apply in the non-linear case of a GRP rod encountering internal sliding due to excessive torsion. This situation was experimentally observed during torsion tests of insulator E. and was numerically predicted by the imperfect interface analysis of insulator E subjected to torsion. Based upon these comparisons, it can be concluded that the global perfect interface model can be used to accurately predict the overall displacements, and the three-dimensional imperfect interface sub-model can be used to determine the internal stresses in the GRP rods of insulators under the seven multi-axial load cases described in chapter 4.

From the three-dimensional analysis of the crimping stresses in insulator A (section 4.5.1), it was seen that the residual biaxial compressive stresses (σ_r and σ_θ) were quite large in the GRP rod within the end-fitting. While the magnitude of the compressive radial stress (σ_r = -176 MPa) was larger than the expected uniaxial transverse compressive strength of the E-glass/epoxy composite material ($\sigma^f_{22,C}$ = -140 MPa), it was not clear if these stresses were sufficient to generate internal damage in the GRP rod. This is because the transverse compressive strength of the composite material under a state of *biaxial compression* is expected to be larger than the strength under *uniaxial compression*. At present, the biaxial compressive strength of the GRP composite is not known. Indeed, in chapter 3 (section 3.6), optical microscopy of the GRP rod of insulator A showed circumferential microcracks near the GRP-Al interface. However, these cracks were observed after the insulator end had been subjected to the push-out test (section 3.3). It is therefore quite possible that the circumferential micro-cracks were, in fact, generated during the push-out test. In order to investigate this possibility, the three-dimensional imperfect interface sub-model was used to compute the magnification of the biaxial compressive stresses (σ_r and σ_θ) during the push-out test. Figure 6.1 shows the values of σ_r and σ_θ, along one quarter of the circumference of the rod, as a function of the applied axial displacement (U_z). These stresses are plotted along the center of the end-fitting (between z_1 and z_2) where the circumferential cracks were found. Clearly, the radial stress (σ_r) increases by only 5 % during the push-out test, while the tangential stress (σ_θ) increases by 25 %. It can therefore be concluded that even if the circumferential micro-cracks observed in insulator A were generated during the push-out test, the fact that the magnification in the biaxial compressive stresses during this test is not very significant, indicates that the magnitude of residual radial compression applied during crimping of insulator A was, in fact, very close to the critical value required to generate internal cracks in the GRP rod. Some isolated damage was also found in insulators C and D. The damage in insulator D was certainly caused by the highly irregular internal surface of the end-fitting. On the other hand, insulator E showed no signs of internal damage. This was most likely due to the low average magnitude of radial compression (M), which would result in lower biaxial compressive stresses in the GRP rod of this insulator.

6.1. PARAMETRIC DESIGN ANALYSIS

The finite element models presented thus far in this study have been applied to only 115 kV substation insulators such as the insulators A, B, C, D, and E. Since the results computed from both the axisymmetric and the three-dimensional sub-model with an imperfect interface have agreed with the experimental results under axial compression, we may now modify the models to evaluate the influence of some design variables on the performance of composite insulators subjected to externally applied axial loads, in conjunction with the residual radial compression applied during crimping. This section considers the effects of design variables such as the radius of the GRP rod (r), the type of axial load applied (*i.e.*, tension or compression), the coefficient of friction (μ) between the GRP rod and end-fitting, the average magnitude (M) of radial compression, and the shape of the radial compression profiles in both the axial (z) and tangential (θ) directions.

The axisymmetric imperfect interface model has been used to compute axial load versus displacement curves (multiple load-step analysis), while the internal stresses in the GRP rod have been computed from the three-dimensional sub-model (single load-step analysis $U_z = 0$, with axially and tangentially non-uniform radial compression). Radial compression in the axisymmetric models was simulated by using the fifth-order polynomial (equation 3-3a), while the radial compression in the three-dimensional models was simulated by the sinusoidal wave-function (equation 3-5). Figures 6.2 show the three-dimensional finite element meshes with two different rod radii (r).

While the analyses are fairly generic in nature and can be applied to either substation or suspension insulators, some of the variables have been selected to represent the current design of specific insulators. For instance, the cases of a rod radii (r) equal to 30 mm and 31.6 mm, loaded in axial compression, will represent 115 kV substation insulators (*e.g.*, insulators A, B, C, D, and E). The case of $r = 8$ mm, loaded in axial tension, will represent the present design of suspension insulators with an SML rating of 40 to 60 kN, while the case of $r = 15$ mm, loaded in axial tension, will represent suspension insulators with an SML rating of 60 to 111 kN. The length of the GRP rod has not been considered as a variable since it will not have a significant effect on the axial strength and internal stresses of an insulator. The length influences only the electrical leakage distance, and consequently the applicable voltage of an insulator on overhead transmission lines (69 to 735 kV).

6.1.1. Effect of Radius of GRP Rod

Figure 6.3 shows the axial load versus displacement curves obtained from the axisymmetric analysis of insulators with rod radii (r) of 10 mm, 15 mm, 20 mm, and 30 mm loaded in axial compression; and 8 mm and 15 mm loaded in axial tension. In all cases, the average magnitude of radial compression was assumed to be equal to that of insulator A (M_A = 0.176318 mm), and the coefficient of friction (μ) was assumed to be 0.3. It can be seen that the slope, and consequently the stiffness of the GRP rod in the axial direction, decreases with a decrease in the rod radius. This is expected because the axial stress increases when the same axial force is applied to a rod of smaller radius. Since the Youngs modulus remains the same, larger strains will be generated in rods with a smaller radius. Figure 6.3 also shows that under axial compressive loads, the load at the onset of sliding (P_f) increases with a reduction in the rod radius. However, this trend is reversed under axial tension. It is believed that the value of P_f, according to Coulomb's law of friction, should depend linearly on the compressive radial stress acting at the GRP-Al interface. In addition, the value of P_f should also depend on the total contact area between the GRP rod and end-fitting. Clearly, if the rod radius is decreased, the compressive radial stress at the GRP-metal interface increases, while the total surface area of contact decreases. It appears that in axial compression, the effect of larger radial compressive stresses is dominant, leading to larger P_f. However, in axial tension, the influence of a reduced surface area of contact plays the dominant role.

Another interesting observation is that for the same insulator, the value of P_f is found to be significantly lower under axial tension than under axial compression (see r = 15 mm in figure 6.3). This is expected because the radial compression due to crimping causes the radius of the GRP rod within the end-fitting (r_{in}) to be smaller than the radius outside the end-fitting (r_{out}). Therefore, under axial compressive loads, additional elastic strain energy is required to push the rod into the end-fitting.

Figures 6.4 (a, b) show the effect of the rod radius on the radial and tangential stress distributions along the circumference of the rod at the midlength of the end-fitting (*i.e.*, between z_1 and z_2). These results were obtained by considering six peaks (n = 6) in the sinusoidal wave-function, with the value of M once again equal to that of insulator A. Clearly, the resulting biaxial compressive stresses also have six maxima and six minima along the circumference of the rod, and the peak stresses increase significantly if the rod radius is decreased from 30 mm to 8 mm. As discussed earlier for insulator A, we expect that the biaxial compressive stress state given by σ_r equal to -176 MPa, and σ_θ equal to -113 MPa would represent a stress state which is very close to the critical values required to generate compressive damage in the rods. These values have therefore been used to indicate the expected regions of damage in figures 6.4 (a, b). The results demonstrate that insulators with smaller rod radii should not be crimped to the same extent as insulators with a rod radius of 30 mm.

6.1.2. Effect of Friction

Figure 6.5 (a) shows the axial load versus displacement curves computed from insulators with different friction coefficients (μ) at the GRP-Al interface. The substation insulators (r = 31.6 mm, $M = M_A$, loaded in compression) have friction coefficients of 0.2, 0.3, and

0.5; while the suspension insulators (r = 15 mm, M = M_A, loaded in tension) have μ values of 0.3, 0.5, and 0.7. It is evident that the load at the onset of sliding can be significantly increased by increasing the friction coefficient at the GRP-metal interface. Figure 6.5 (b) shows the von-Mises equivalent stress along the path ABC for the substation insulators. The internal stresses are clearly independent of the friction coefficient at the interface. This implies that a large coefficient of friction can be used to significantly improve the strength of crimped joints without increasing the internal stresses in the rod.

6.1.3. Effect of Magnitude of Radial Compression

As described in chapter 3, for the axisymmetric models, the average magnitude of radial compression M could be changed in the axial direction such that the overall shape of the radial compression function remained the same. Figure 6.6 shows the computed load-displacement curves of substation insulators (r = 31.6mm, μ = 0.3, compression loading) and suspension insulators (r = 8mm, μ = 0.3, tension loading), by considering the values of M equal to that of insulator A (M_A = 0.176318 mm), twice of M_A, and half of M_A. In the three-dimensional analysis, the value of M was varied by changing the amplitude of radial compression (A) in the sinusoidal wave-function, while keeping the number of peaks (n) equal to six. As would be expected, the load at the onset of interfacial sliding can be significantly increased by applying larger magnitudes of radial compression during crimping. However, figures 6.7 (a,b) show that unlike the effect of friction, the internal stresses will also increase, thereby increasing the risk of compressive intralaminar damage in the GRP rod.

6.1.4. Effect of Non-uniform Radial Compression

In chapter 3, it was seen that the radial compression profiles of insulators A and C were non-uniform in both the axial (z) and tangential (θ) directions, while the profile of insulator E was highly uniform. In the tangential direction, the profile of insulator A had six peaks of maxima and minima ($n = 6$), while the profile of insulator C had four peaks ($n = 4$). In this section, the non-uniform shapes of the radial compression profiles were individually simulated in the axial and tangential directions, while keeping the average magnitude of radial compression (M) constant.

6.1.4.1. Axially Non-uniform Compression

The axisymmetric imperfect interface model was used to study the effects of different shapes of radial compression in the axial direction. According to equations (3-4), the polynomials $P_2(z)$ at $a = 0.25$, $P_3(z)$ at $a = 0$, and $P_4(z)$ at $a = -1$ were applied. Figures 6.8 (a, b) show the load-displacement curves and the internal von-Mises equivalent stress distribution for substation insulators ($r = 31.6$ mm, $\mu = 0.3$, loaded in compression). It can be concluded that the load at the onset of sliding is independent of the shape of the radial compression profile, provided that the average magnitude (M) of radial compression remains the same. However, the equivalent stress distribution is affected quite significantly by the shape of the compression profile in the axial direction.

6.1.4.2. Tangentially Non-uniform Compression

For the three dimensional analysis, the shape of the radial compression profile was changed in the tangential (θ) direction by keeping the same values of M and A, while considering the number of peaks (n) equal to 3, 4, and 6. These computations assumed a rod radius of 30 mm, and a friction coefficient of 0.3. Figures 6.9 (a, b) show that the radial and tangential stress distributions along the circumference of the GRP rod are quite significantly affected by the number of peaks. The location of the maximum stresses are different for the three cases, and the number of segments subjected to the maximum stresses are equal to n. It is however interesting to note that the maximum and minimum values of σ_r and σ_θ are not very different. This indicates that the amplitude (A) of radial compression influences the magnitude of the maximum and minimum stresses in the rod, while the number of peaks (n) determine the location and the number of peak-stress segments on the surface of the rod within the end-fitting.

6.1.5. Semi-Empirical Relationships

In chapter 4 (section 4.4.1), the axisymmetric imperfect interface model was used, in conjunction with the rod push-out test results, to establish the values of the coefficients of friction (μ) at the GRP-Al interface as 0.3 and 0.75 for insulators A and E, respectively. These values appeared to be reasonable since optical microscopic examinations, performed in chapter 3 (section 3.6), revealed that the internal surface of the end-fitting was smooth for insulator A, and grooved in insulator E. Since the internal surface of end-fittings of insulators B and C were also found to be smooth, it seems reasonable to assume that the coefficients of friction in these insulators will also be 0.3. Furthermore, since the end-fitting surface of insulator D had large u-shaped grooves, we can assume that the value of μ at the GRP-Al interface will be approximately 0.8. Table 6.1 lists the estimated coefficients of friction, the average magnitude of radial compression (M), and the axial load at the onset of sliding (P_f) in the five 115 kV substation insulators examined in this study. In the previous sections, it was numerically demonstrated that insulators with a large value of μ or M will require a larger load to initiate internal sliding. A close examination of table 6.1 indicates a similar trend. In this section, simple empirical relationships are presented which may be used to predict the loads (P_f) as a function of the coefficient of friction at the GRP-Al interface, and the average magnitude of radial compression applied to an insulator during crimping.

The general contact algorithm, employed in the imperfect interface models, makes use of Coulomb's law of friction on a node-to-node basis. According to equation (2-33), the externally applied axial force (f_s) must exceed ($\mu.f_n$) in order to initiate sliding. On a global scale, one may consider the average magnitude of radial compression (M) as a parameter which influences the normal contact force, and the externally applied axial load as a parameter representative of the tangential force. Figure 6.10 shows the values of P_f computed from the axisymmetric imperfect interface model, by considering several values of μ ranging from 0.2 to 0.7, and the values of M equal to M_A, half of M_A, and twice of M_A. In addition, four different shapes of the axially non-uniform radial compression function were considered, while the radius of the GRP rod (r) was kept constant at 31.6 mm. The results clearly indicate that P_f varies linearly with the product of μ and M. The following semi-empirical equation was obtained by a linear regression analysis.

$$P_f = 9093.936\,(\mu M) - 66.54092 \qquad (6\text{-}1)$$

where, the value of P_f is given in kN, and M is in mm. From figure 6.10, it is evident that the rod push-out test results of insulators A, C, and E are in agreement with equation (6-1), while the results of insulators B and D disagree. This disagreement most likely stemmed from the fact that the ultrasonic radial compression data obtained from insulators B and D were inaccurate (as already discussed in section 3.2.1). Using equation (6-

1), the maximum axial loading capacity of substation insulators can be determined from the coefficient of friction, and the average magnitude of radial compression applied during the crimping process. It is important to note that this equation is applicable only to insulators with a GRP rod radius (r) in the range of 30 to 31.6 mm, subjected to axial compressive loads (*i.e.,* 115 kV substation insulators). It has already been seen that the value of P_f will be significantly different in insulators with rod-radii smaller than 30 mm, or insulators subjected to axial tension instead of axial compression. Furthermore, the length of the end-fitting could be a significant parameter affecting the value of P_f, since it affects the total surface area of contact between the GRP rod and end-fitting. However, the numerical data presently available is insufficient to determine a generalized semi-empirical relationship which will include all of these design variables to predict the axial loading capacity of any insulator.

In addition to the axial load at sliding (P_f), it is important to evaluate the maximum radial and tangential stresses in the GRP rod as a function of the design variables. In the previous sections, it was seen that the maximum radial and tangential stresses will increase if the radius of the GRP rod (r) is decreased, or the amplitude of radial compression (A) is increased. Furthermore, it was shown that the magnitude of the applied axial load, the coefficient of friction at the GRP-Al interface (μ), and the number of peaks (n) of the sinusoidal wave-like compression profile will not have a significant effect on the maximum radial stress ($\sigma_{r,max}$) and the maximum tangential stress ($\sigma_{\theta,\max}$) in the GRP rod. Using the three-dimensional imperfect interface model with rod radii (r) of 15 mm, 20 mm, and 30 mm, figures 6.11 (a, b) show the variations of $\sigma_{r,max}$ and $\sigma_{\theta,\max}$ in the GRP rod as a function of the applied amplitude of radial compression (A). Clearly, the maximum biaxial compressive stresses are almost linearly dependent on the amplitude of radial compression applied during crimping. By performing a linear regression analysis, the following semi-empirical equations were obtained:

$$For\ r = 15\ mm, \quad \sigma_{r,max} = -699.1172\,(A) + 9.567293 \tag{6-2a}$$

$$\sigma_{\theta,max} = -654.7625\,(A) + 12.99094 \tag{6-2b}$$

$$For\ r = 20\ mm, \quad \sigma_{r,max} = -589.5175\,(A) - 0.1514219 \tag{6-3a}$$

$$\sigma_{\theta,max} = -539.8505\,(A) + 15.84203 \tag{6-3b}$$

$$\text{and}\ \ For\ r = 30\ mm, \quad \sigma_{r,max} = -497.7695\,(A) - 0.3285568 \tag{6-4a}$$

$$\sigma_{\theta,max} = -386.61\,(A) + 8.130695 \tag{6-4b}$$

where, $\sigma_{r,max}$ and $\sigma_{\theta,\mathrm{max}}$ are expressed in MPa, and A is in mm. Once again, these equations will hold good only for the specified rod-radii (r). The coefficient of friction (μ), the number of radial compression peaks (n), and the axial loading conditions should not have any significant effect on these predictions.

Having established the empirical relationships, it should be possible to determine the critical amplitude of radial compression (A_{crit}) that will generate damage in the GRP rod. Since the biaxial compressive strength of the GRP rod in the $r-\theta$ plane is not presently available, based upon the computed internal stresses (section 4.5.1) and the observation of internal circumferential cracks in the rod of insulator A, we can consider $\sigma_{r,max}$ equal to -176 MPa and $\sigma_{\theta,\mathrm{max}}$ equal to -113 MPa as the critical biaxial stress state. Solving equations (6-2 to 6-4), the critical amplitudes of radial compression (A_{crit}) required to initiate damage in the GRP rods are found to be 0.192 mm for r = 15 mm, 0.239 mm for r = 20 mm, and 0.313 mm for r = 30 mm.

The parametric analysis shows that the axial load bearing capacity of the crimped joint can be increased by;

(a) increasing the average magnitude of radial compression (*M*), and consequently the amplitude of radial compression (*A*) applied during crimping,

(b) increasing the coefficient of friction (μ) at the GRP-metal interface, and

(c) decreasing the radius of the GRP rod (*r*) for insulators loaded under axial compression, and increasing the radius for insulators loaded under axial tension.

In addition, it is shown that the shape of the radial compression profile does not influence the axial load at the onset of sliding, provided that the average magnitude of radial compression remains the same. An increase in the values of *M* or *A*, or a reduction of the radius (*r*), will increase the maximum radial and tangential stresses in the GRP rod, thereby increasing the risk of compressive intralaminar damage in the rod. However, an increase in the value of μ will not have any effect on the biaxial compressive stresses in the rod. Clearly, a high coefficient of friction at the interface between the rod and end-fitting should be recommended. From the results presented in chapters 3 and 4, it is evident that insulators A, B, and C were designed to have large radial compression while the value of μ was relatively low. On the other hand, in insulator E, the grooved internal surface of the end-fitting provided a high frictional resistance, while the average magnitude of radial compression was very low.

6.2. POSSIBLE FAILURE MODES

From the rod push-out test results, it was seen that under excessive axial loads, the crimped insulator end-fittings encounter failure due to internal sliding of the GRP rod. However, these loads were significantly larger than the maximum expected axial compressive load that will be applied to a substation insulator during service. In this study, rod pull-out tests have not been performed on suspension insulators under axial tension. However, even in the suspension insulators, if the value of M is not sufficiently large, sliding failures can occur resulting in separation of the GRP rod from the end-fittings.

The three-dimensional analysis of the crimping stresses indicated that a large magnitude of radial compression will result in higher biaxial compressive stresses in the GRP rod. This can generate internal damage in the GRP rod, which is expected to occur in the form of multiple microscopic cracks and debondings near the GRP-metal interface. These micro-cracks may be mechanically stable since they will be located within the compressive stress field of the end-fitting ($K_I = 0$). However, under long-term multi-axial loads, especially if cyclic loads are involved, the damage accumulated inside the end-fittings will eventually reduce the stiffness of the GRP composite, and consequently the mechanical bond between the rod and end-fitting will become weak. This may significantly reduce the resistance of the GRP rod to internal sliding under axial loads. Furthermore, Fujimoto et. al. [15] have performed electric field calculations by using the finite element method. They showed that if axially aligned cracks are present within the end-fittings of suspension insulators, the field intensity is severely concentrated at the tips of the crack. This will cause internal partial discharge and subsequent degradation of the GRP rod. Clearly, the value of M is a parameter which needs to be carefully optimized in order to have a sufficiently large resistance to internal sliding (P_f), while maintaining the internal compressive stresses below their critical limit. A high coefficient of friction at the GRP-metal interface is recommended, since it can increase P_f without increasing internal stresses in the rod.

The three-dimensional stress analysis of the seven multi-axial load cases indicated that the residual biaxial compressive stresses in the GRP rod, near the lower end-fitting, were not affected by most of the external loading conditions. While most of the multiaxial load cases are safe, the cases of extreme fault current forces and switch-torsional forces can be identified as the ones which are closest to the ultimate strength of the insulator. Under extreme fault current forces, the center of the GRP rod inside the lower end-fitting experiences shear stresses which are close to the critical shear stress ($\tau_{12}^{f} = 60$ MPa) required to initiate intralaminar splits in the GRP rod. This mode of failure will be very similar to the failure of Iosipescu specimens presented in chapter 5, with fiber orientation A. The splits in both cases will initiate under shear stress concentrations. If the splits initiate outside the end-fitting, then they will propagate under mixed-modes (I and II). However, if the splits remain within the end-fittings, they may be stable due to the biaxial compressive stress field.

Under switch torsional forces, there can be two independent modes of failure depending upon the total magnitude of radial compression applied during crimping, and the frictional properties of the GRP-metal interface.

(a) If the magnitude of radial compression is large (as in insulator A), the surface of the GRP rod will develop shear stresses of ≈ 48 MPa, which are close to the critical shear stress required to initiate intralaminar splits. These splits, generated on the surface of the rod, will be located outside the end-fittings. If external bending loads are also active, then the splits can propagate under mixed-modes (I and II). Once again, this failure mode is similar to the failure of unidirectional composite Iosipescu specimens with fiber orientation A.

(b) In insulators where the magnitude of radial compression is low (as in insulator E), the surface shear stresses will be relaxed. However, the GRP-rod might encounter partial sliding within the end-fittings if the coefficient of friction is not very large at the GRP-metal interface.

It can therefore be concluded that torsional loads as large as 2480 Nm should be avoided on the 115 kV substation insulators examined in this study.

In order to enhance the frictional resistance, the internal surface of the end-fittings in insulators D and E was grooved. While these grooves will successfully increase the value of (μ), they might lead to some problems. Firstly, a very coarse grooved surface (as in insulator D) has large peaks which can get embedded in the GRP rod during crimping. This may lead to surface damage in the form of broken fibers and crushing of the resin matrix. In addition, the valleys of a coarse grooved surface will result in internal voids along the GRP-metal interface. These voids will effectively reduce the total surface area of contact between the rod and end-fitting, and therefore the ultimate strength of the crimped joint. Furthermore, circumferentially aligned grooves (as in both insulators D and E), can enhance the friction coefficient only in the axial direction. In the tangential direction, the value of μ may still be similar to that of a smooth end-fitting surface.

6.3. FUTURE WORK

This study addressed the possibility of short-term mechanical failures of composite insulators. Comprehensive three-dimensional finite element analyses were performed to evaluate the internal stresses and overall deformations of substation insulators subjected to a wide variety of multi-axial loads. In addition, destructive and non-destructive mechanical tests were performed to characterize the insulators and to complement the finite element simulations. The recently developed biaxial Iosipescu method was studied both experimentally and numerically, and the biaxial failure properties (under shear and transverse tension) were determined for unidirectional composites. In addition, an attempt was made to extend the biaxial Iosipescu fixture for evaluating the mixed-mode fracture properties of composites. The design of composite insulators is still in an evolutionary stage. In this study, a parametric analysis was conducted in order to evaluate the effects of several design variables on the axial load bearing capacity of insulators, and the internal compressive stresses in the GRP rod.

Since composite insulators are required to be in service for a period of up to fifty years, future work in this area should be focussed on their structural integrity under long-term multi-axial loads. Dynamic effects such as fatigue loading, seismic activity, and aeolian vibrations should also be taken into account. The biaxial Iosipescu test, used in this study, was found to be inappropriate for determining the transverse compressive strength of unidirectional composites. Due to the internal stresses generated during the crimping process, a biaxial compressive test method is required for characterizing the transverse compressive strength of the GRP composite used in insulators. In addition, an appropriate failure criterion is required in order to predict the onset of damage in the GRP rods under biaxial compressive stress fields. Instead of complete structural failure, the failure criterion should define the onset of damage as the initiation of microscopic matrix cracks and debondings at the fiber-matrix interfaces. Furthermore, there is a definite need for generic closed-form analytical solutions which can describe the mechanical behavior of composite insulators by taking into account several design variables such as the radius of the GRP rod, the elastic properties of the rod and end-fitting, the magnitude and shape of the radial compression profile, the length of the end-fitting, and the coefficient of friction at the GRP-metal interface. Composite insulators are frequently subjected to torsional and bending loads during their installation. Since the performance of these insulators can be significantly affected by occasional overloading, detailed guidelines should be set forth to prevent the mishandling of insulators during installation and line maintenance.

Table6.1 : Estimated coefficients of friction at GRP-metal interface, average magnitudes of radial compression, and axial loads at onset of sliding for the five 115 kV substation insulators.

INSULATOR	μ	M (mm)	P_f (kN)
A	0.30	0.176318	310.0
B	≃ 0.3	0.234103 †	145.0
C	≃ 0.3	0.107347	277.0
D	≃ 0.8	0.005609 †	112.0
E	0.75	0.030533	64.5

†Incorrect value

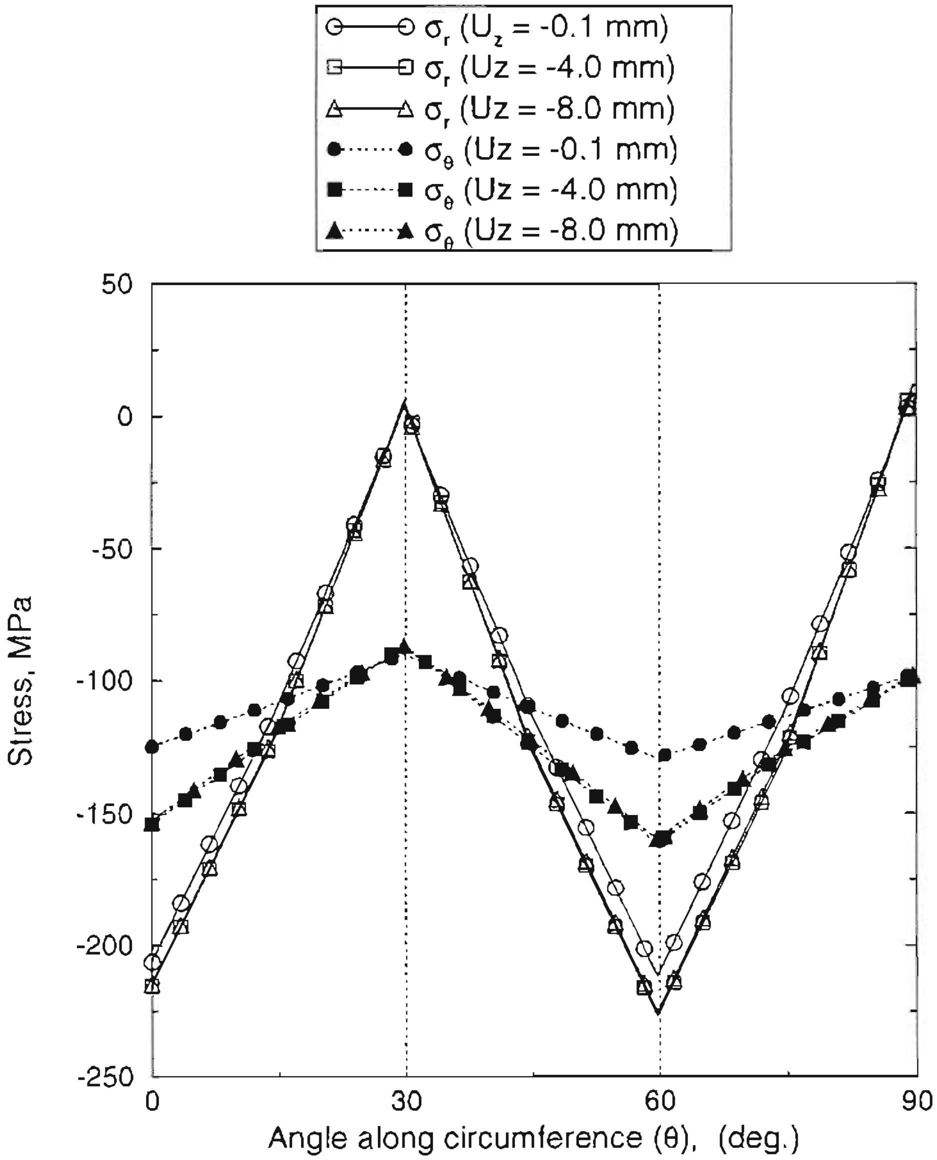

Figure 6.1 : Radial and tangential stresses along circumference of GRP rod as a function of applied axial displacement (U_z) during push-out tests.

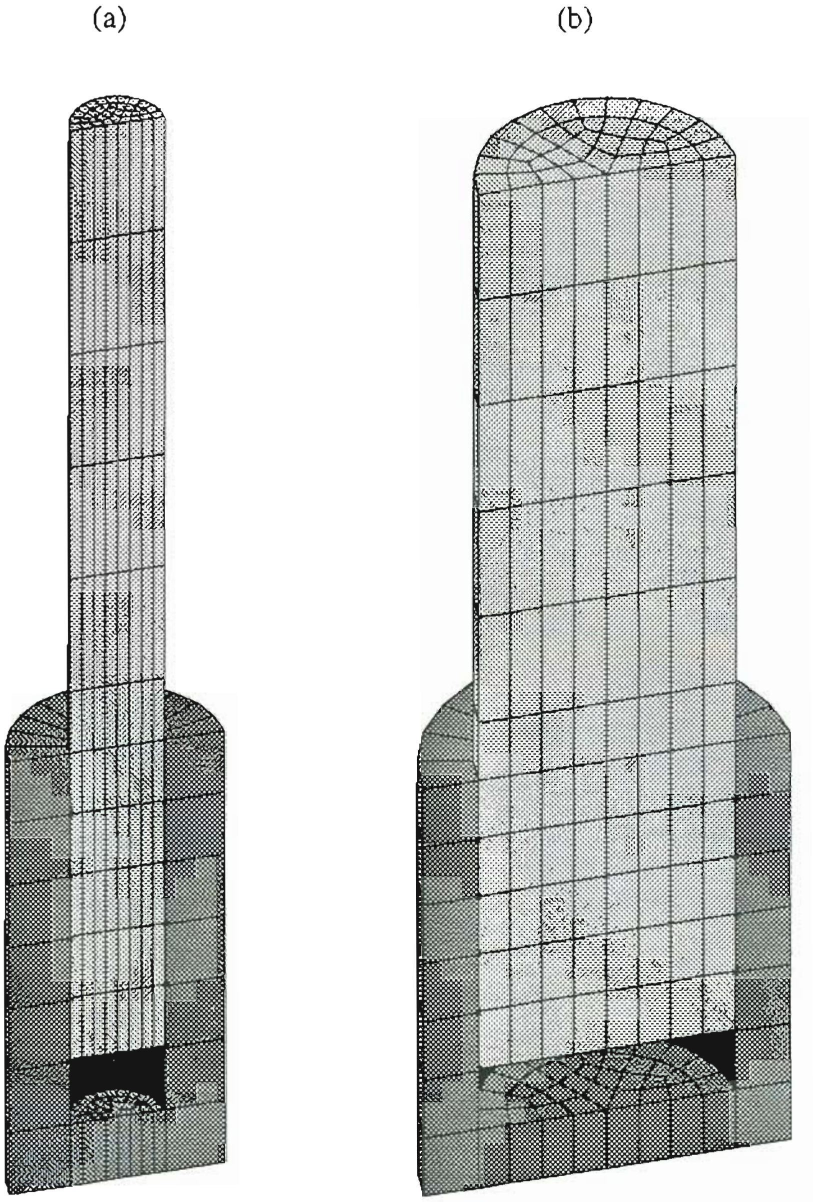

Figure 6.2 : Cross-sectional view of three-dimensional finite element mesh with imperfect interface; (a) $r = 10$ mm, and (b) $r = 30$ mm.

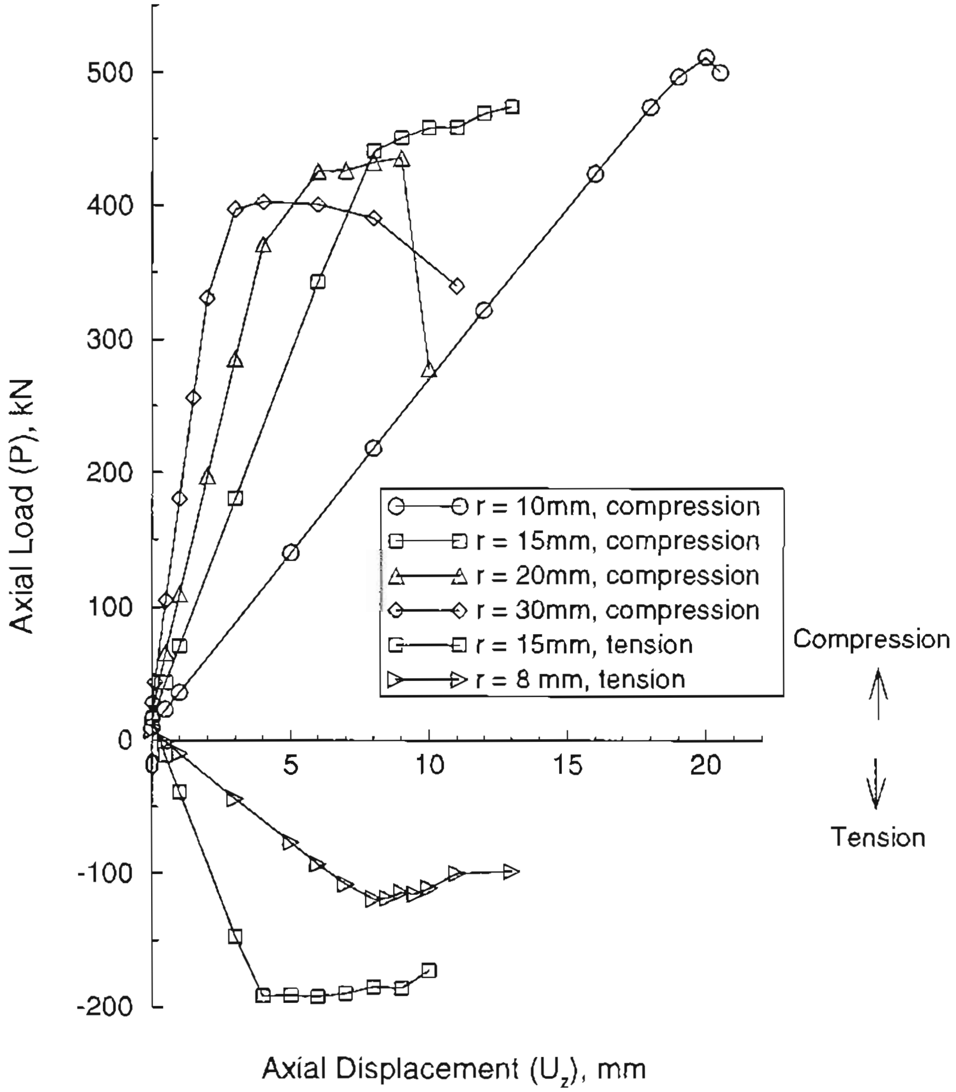

Figure 6.3 : Axial load versus displacement curves computed for insulators with different rod-radii (r) ($\mu = 0.3$, $M = M_A$).

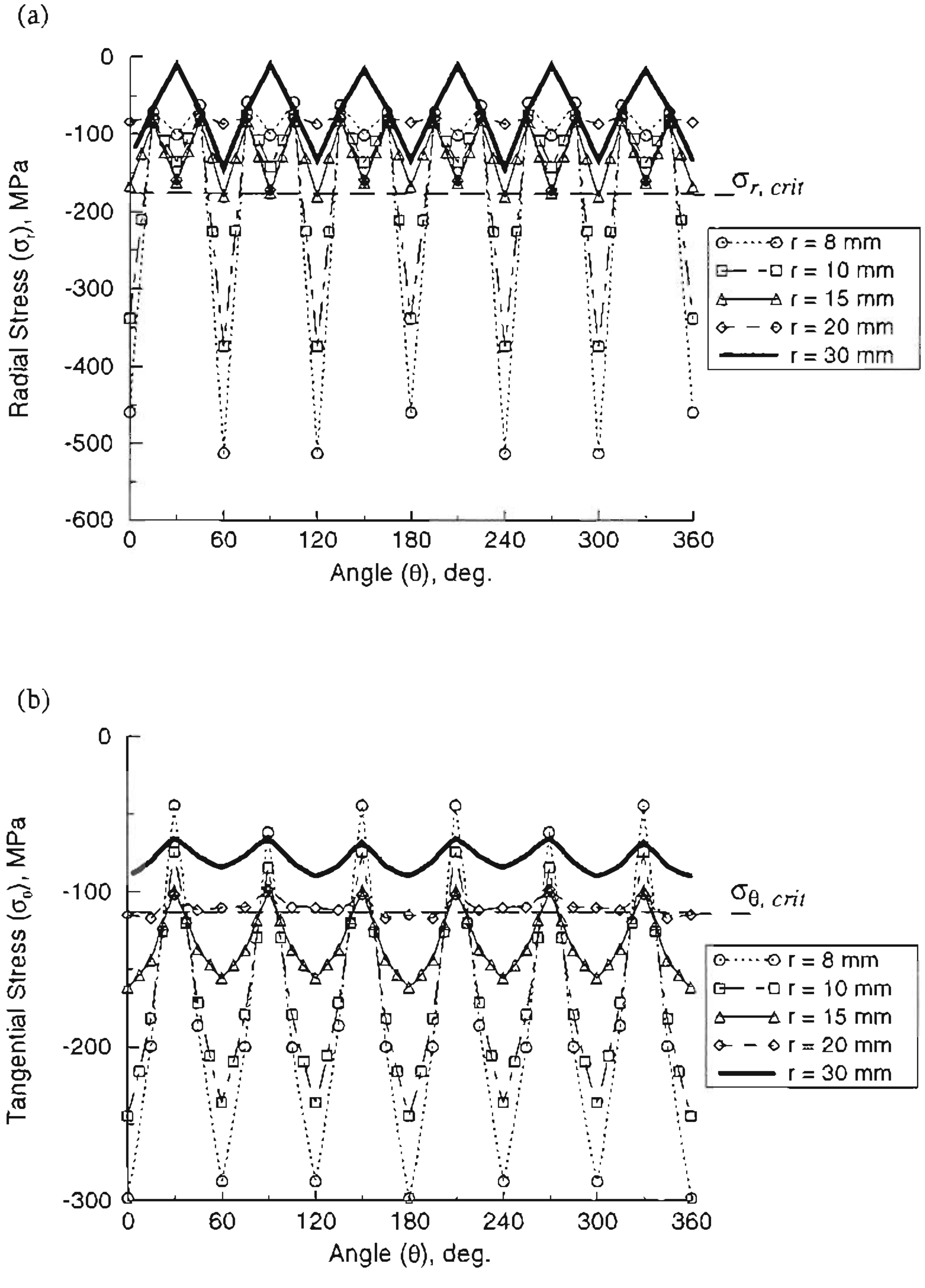

Figure 6.4 : Stress distribution along circumference of GRP rod for insulators with different rod-radii ($\mu = 0.3$, $M = M_A$, $n = 6$) ; (a) Radial stress, and (b) Tangential stress.

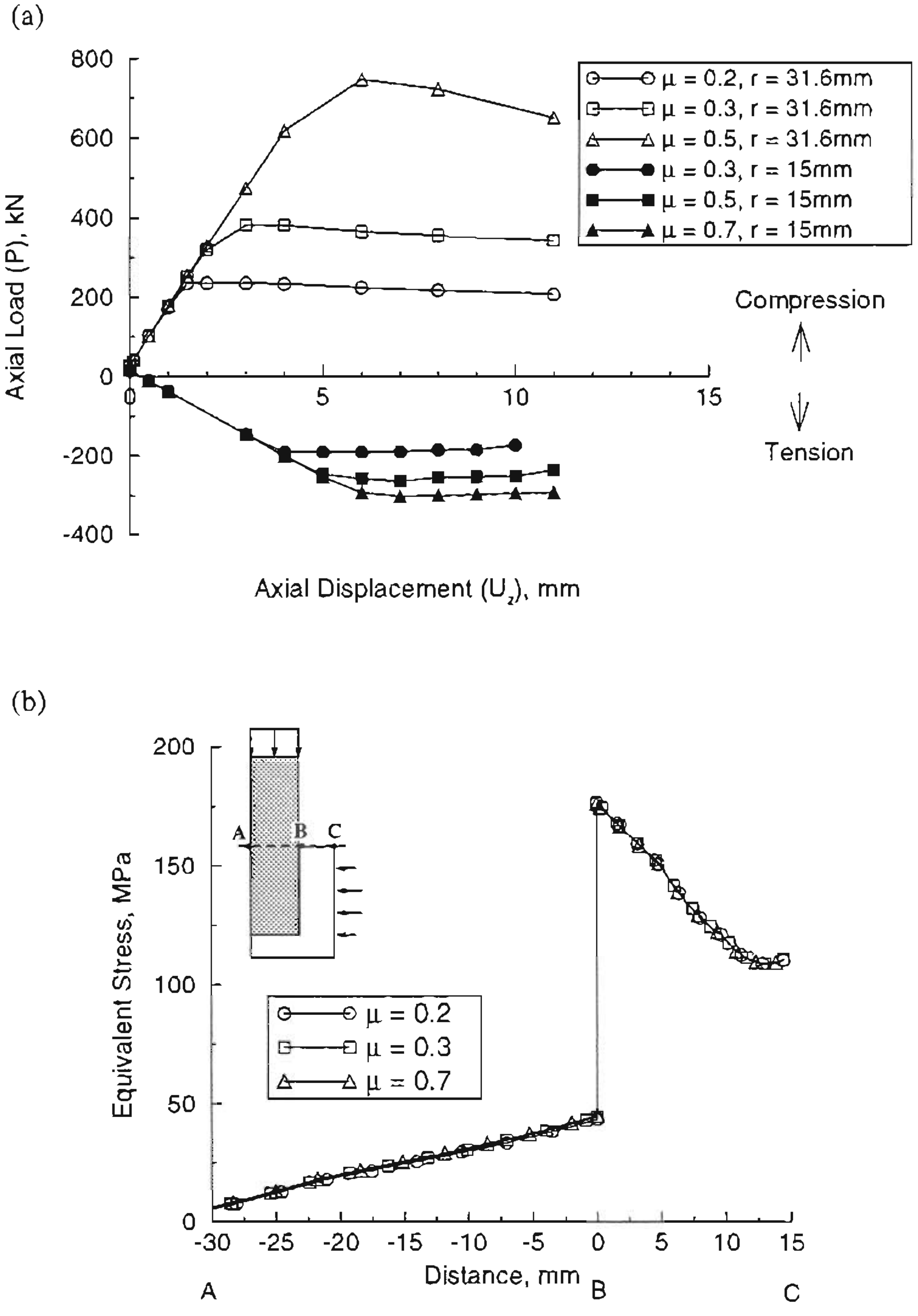

Figure 6.5 : Effect of friction at the GRP-Metal interface;
(a) On the axial load-displacement curves (r = 15 mm and 31.6 mm, $M = M_A$), and (b) On the equivalent stress across the interface (r = 31.6 mm, $M = M_A$).

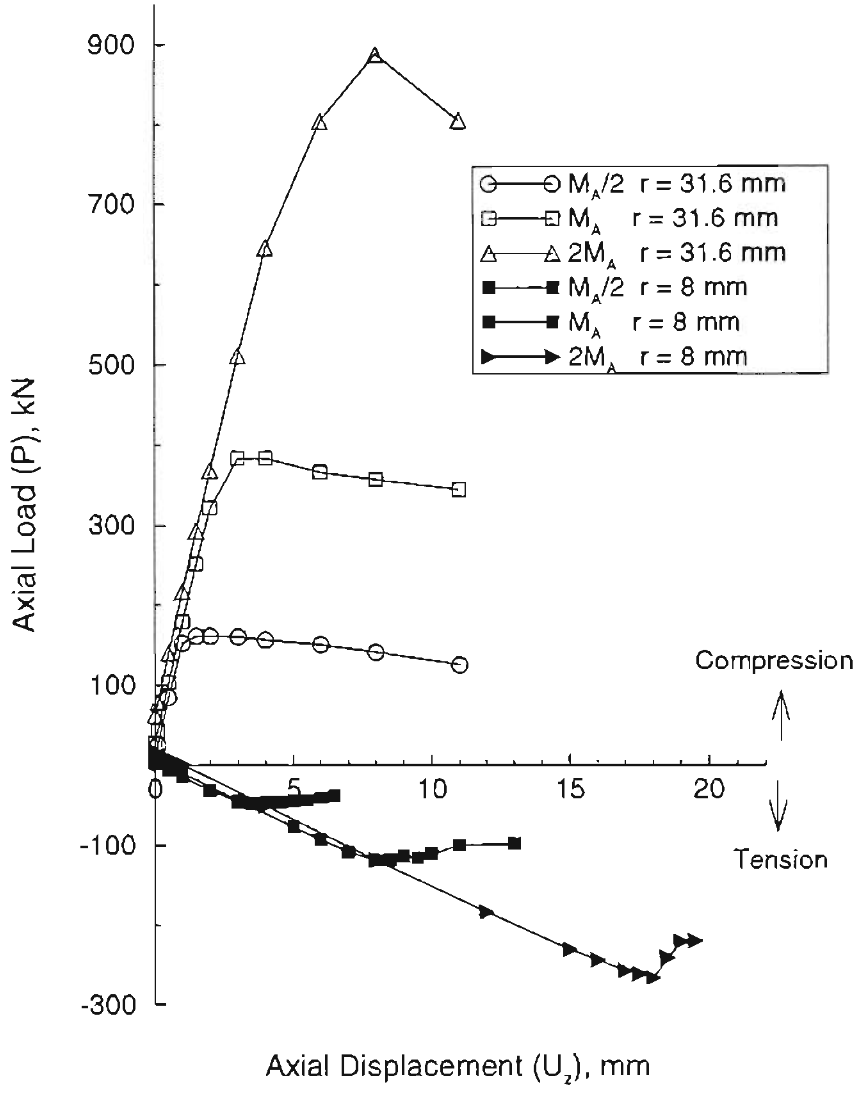

Figure 6.6 : Axial load versus displacement curves computed for insulators with different magnitudes of radial compression (μ = 0.3).

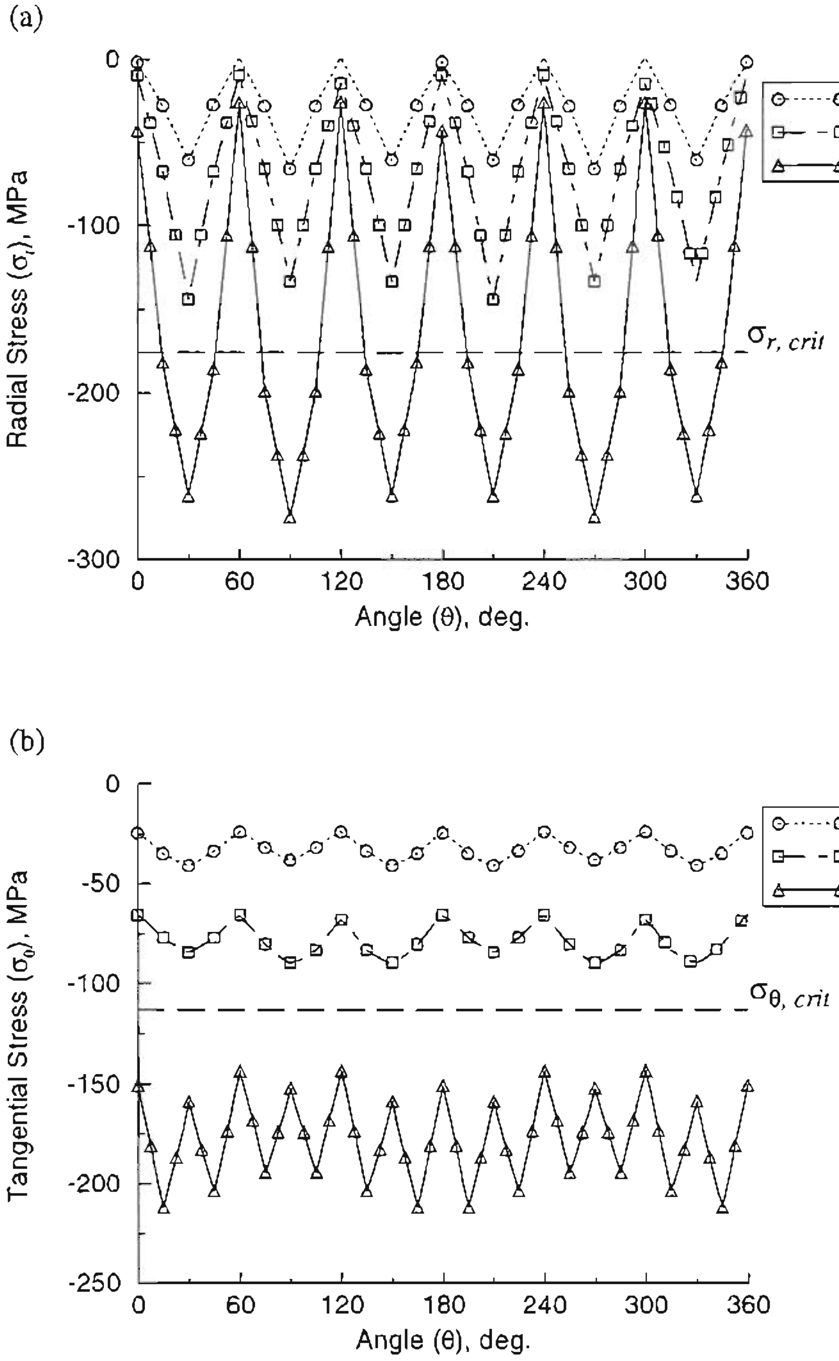

Figure 6.7 : Stress distribution along circumference of GRP rod for insulators with different magnitudes of radial compression ($\mu = 0.3$, $r = 30$ mm, $n = 6$) ; (a) Radial stress, and (b) Tangential stress.

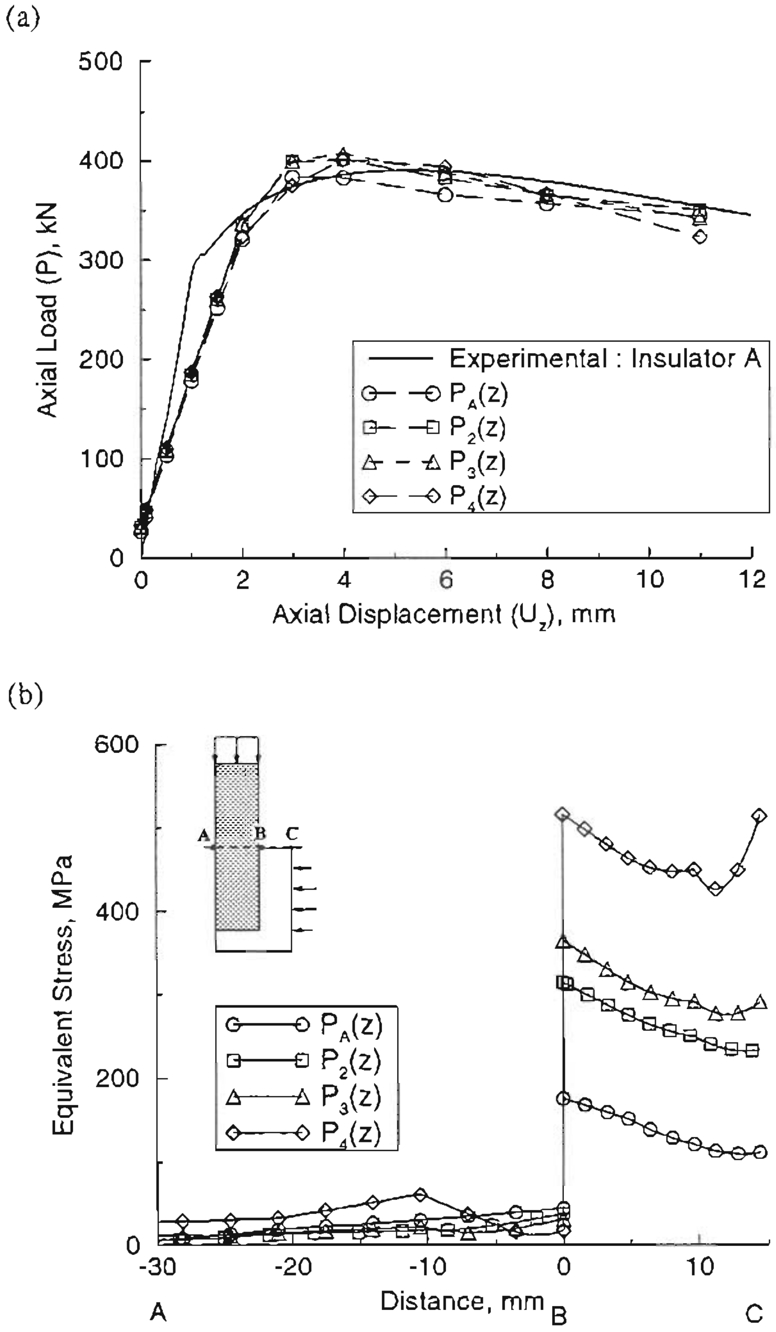

Figure 6.8 : Effect of axially non-uniform radial compression on;
(a) Axial load-displacement curves of insulators, and
(b) Equivalent stress across interface ($r = 31.6$ mm, $\mu = 0.3$, $M = M_A$).

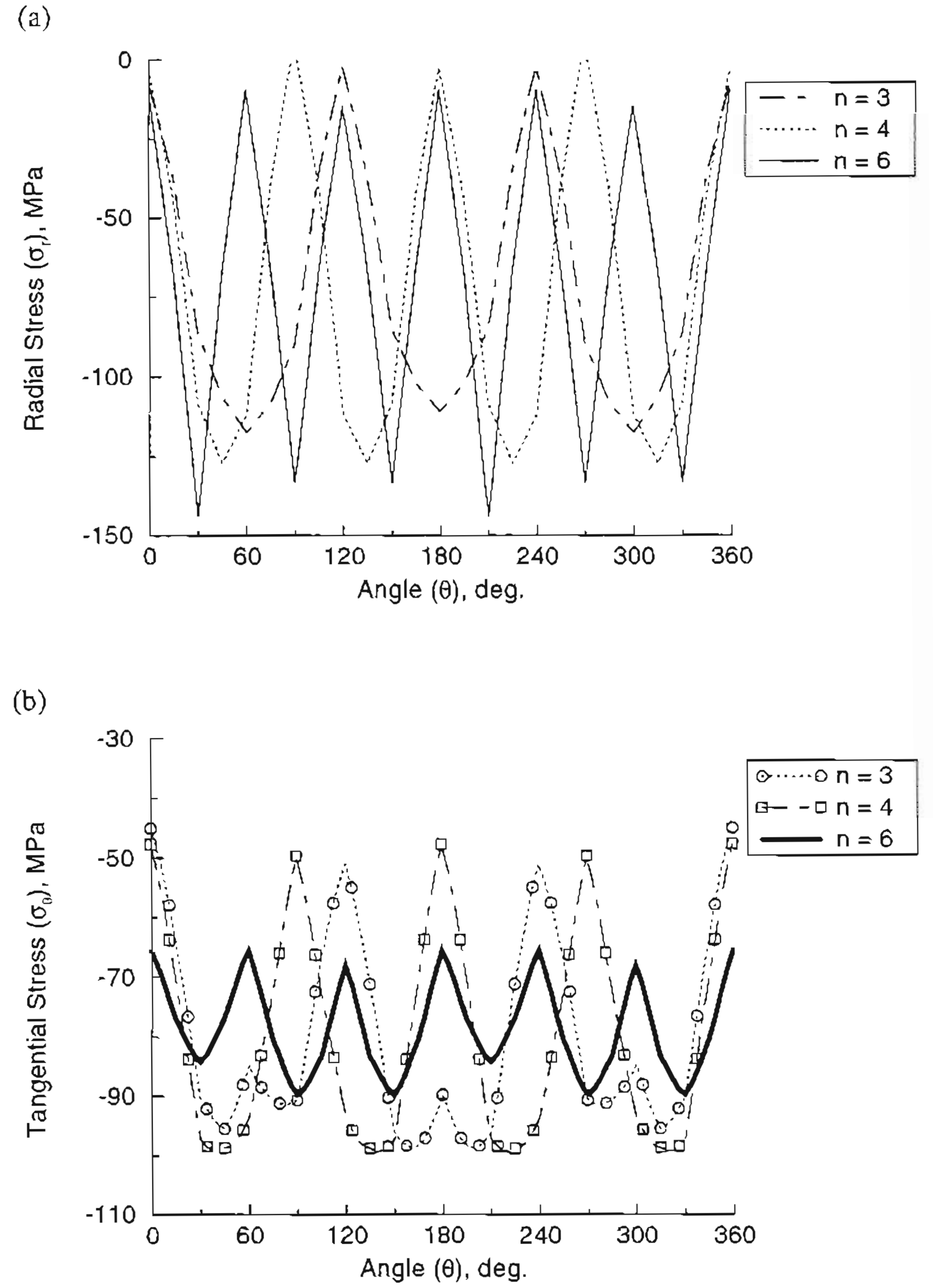

Figure 6.9 : Effect of tangentially non-uniform radial compression on stress distribution along circumference of the GRP rod: (a) Radial stress, and (b) Tangential stress ($r = 31.6$ mm, $\mu = 0.3$, $M = M_A$).

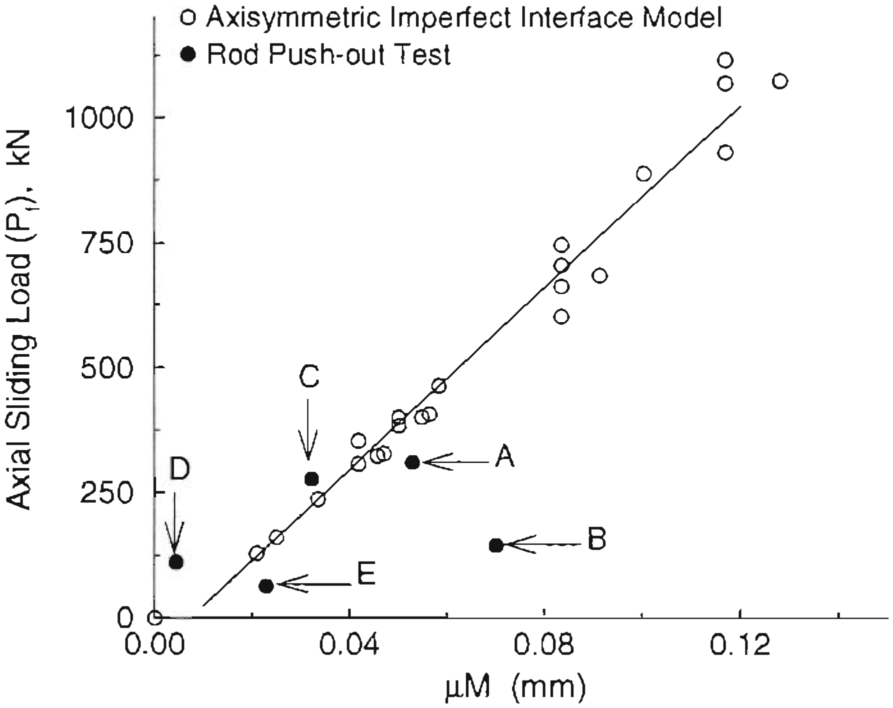

Figure 6.10 : Relationship between axial load at onset of sliding (P_f) and product of μ and M (r = 31.6 mm).

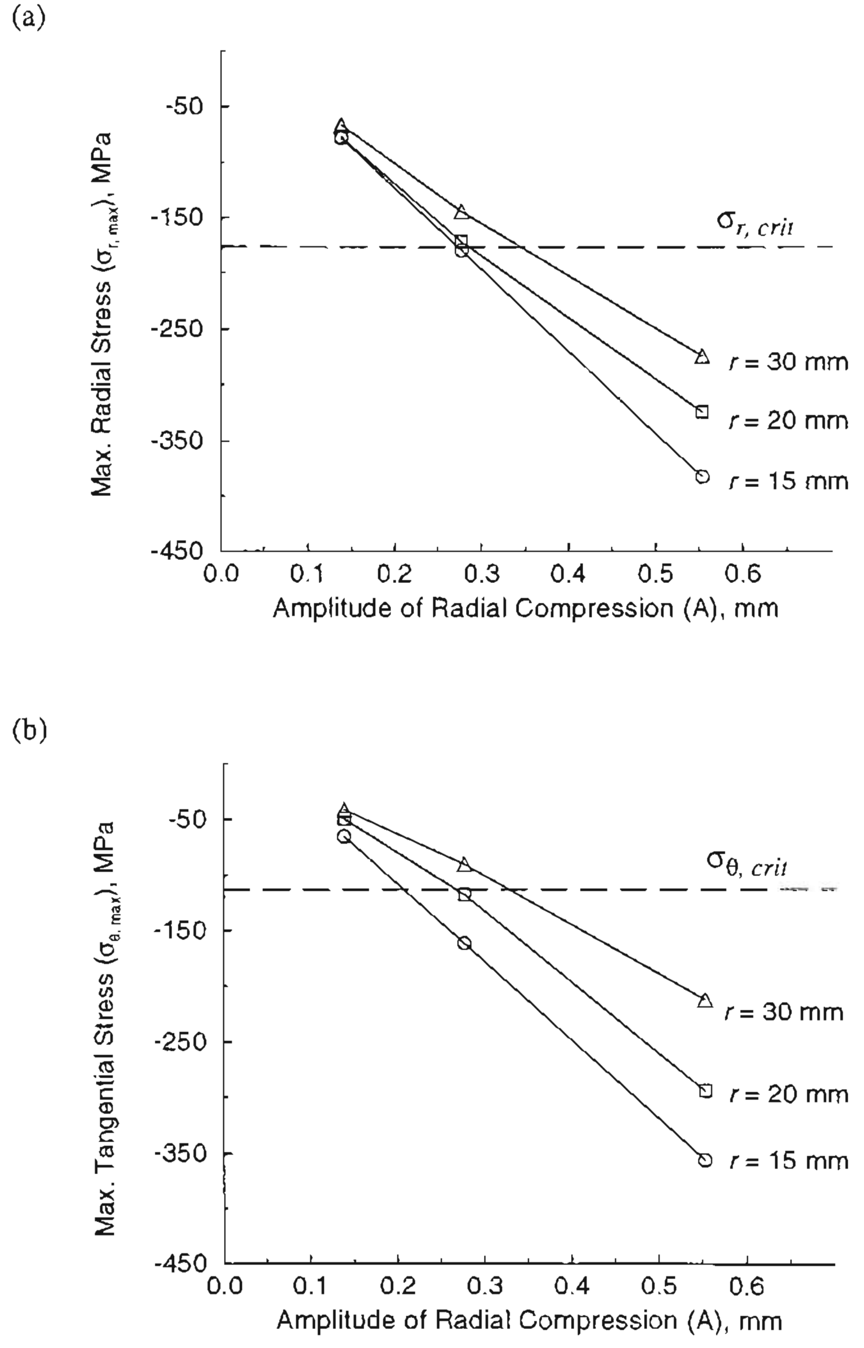

Figure 6.11 : Relationship between applied amplitude of radial compression and maximum stresses on the surface of the GRP rod; (a) Maximum radial stress, and (b) Maximum tangential stress ($\mu = 0.3$, $n = 6$).

Chapter 7

Conclusions

The following conclusions can be drawn from the results presented in this study:

(1) The non-destructive ultrasonic pulse-echo method is a reliable and cost-effective technique for determining the three-dimensional radial compression profiles of the GRP-rod in composite insulators with crimped end-fittings.

(2) The shape and magnitude of the radial compression profile of the GRP rod is highly dependent on the crimping technique employed during assembly of insulators, and can vary significantly among insulators with the same dimensions and mechanical rating.

(3) Under excessive axial compression, substation insulators (with a rod radius of 31.6 mm) will encounter failure due to internal sliding of the GRP rod within the end-fittings. The same mode of failure is expected to occur in suspension insulators subjected to excessive axial tensile loads. These loads, at the onset of internal sliding, can be significantly different among insulators with the same dimensions and mechanical rating.

(4) From rod push-out test results of the five substation insulators, it is concluded that the axial loads at the onset of internal sliding are significantly larger than the maximum axial compressive load which is expected to be applied to a 115 kV substation insulator during service.

(5) The axisymmetric perfect interface model is inappropriate for computing the structural response and maximum stresses of composite insulators, since the true response of insulators is non-linear due to internal sliding, and the stresses at the GRP-metal interface corner are theoretically singular in nature.

(6) The axisymmetric and three-dimensional imperfect interface models can accurately predict the structural non-linearity of composite insulators and the maximum stresses at the GRP-metal interface. Using these models, in conjunction with accurate values for the average magnitude of radial compression applied during crimping and the coefficient of friction at the GRP-metal interface, the axial load at the onset of sliding can be accurately determined.

(7) Since the actual loads applied to insulators during service are multi-axial in nature, three-dimensional models are required to evaluate these cases. The global perfect interface model, developed in this study, can accurately predict the overall deformations of substation insulators under various multi-axial loading conditions. The three-dimensional sub-model with an imperfect interface can accurately predict the maximum internal stresses developed in the GRP rod, and the onset of internal sliding under multi-axial loading conditions.

(8) The biaxial Iosipescu test, employing specimens with fiber orientation A, is very suitable for characterizing the biaxial failure properties of unidirectional composites under combined shear and transverse tension loading conditions. Since composite insulators are subjected to combined loads during service, this test is strongly recommended for determining the biaxial failure strengths of GRP composites for insulator applications. At present the biaxial Iosipescu test can not be used for

characterizing biaxial failure properties under combined shear and transverse compressive stresses.

(9) The centrally cracked Iosipescu specimens, with fiber orientation B, are not suitable for characterizing mixed-mode fracture properties of unidirectional polymeric composites. These specimens encountered biaxial failure from the roots of the notches prior to mixed-mode fracture from the tips of the central crack.

(10) The three-dimensional finite element analysis demonstrated that the crimping stresses generated in the GRP rod of insulator A are close to the critical biaxial compressive stresses required to develop internal damage in the rod. In conjunction with optical microscopic examinations of the internal damage, it is concluded that a biaxial compressive stress state given by $\sigma_r = -176$ MPa and $\sigma_\theta = -113$ MPa is close to the critical limit.

(11) The three-dimensional stress analyses of the seven multi-axial load cases, expected on substation insulators during service, demonstrated that five load cases are safe. The cases of extreme fault current forces and switch-torsional forces can be identified as the ones which are close to the ultimate shear strength of the insulator.

(12) Under extreme fault current forces, the center of the GRP rod inside the lower end-fitting experiences shear stresses which are close to the intralaminar shear strength of the GRP composite. This can result in the initiation of intralaminar splits in the rod. If these splits are formed, they will be located inside the end-fittings, and may not propagate due to the influence of biaxial compressive stress field of the end-fitting.

(13) Under switch torsional forces, there can be two different modes of failure depending upon the total magnitude of radial compression applied during crimping, and the frictional properties of the GRP-metal interface. If the magnitude of radial compression is large, the surface of the GRP rod will develop shear stresses which are close to the critical shear stress required to initiate intralaminar splits. The splits will be located outside the end-fittings, and they may propagate to cause brittle fracture of the insulator. In insulators where the magnitude of radial compression is low, and the coefficient of friction is not very large in the tangential direction, the GRP-rod can encounter partial sliding within the end-fittings. Torsional loads as large as 2480 Nm should therefore be avoided on all 115 kV substation insulators.

(14) The parametric design analysis showed that the axial loads at the onset of sliding can be increased by

- decreasing the radius of the GRP rod for insulators loaded under axial compression, and increasing the radius for insulators loaded under axial tension,
- increasing the average magnitude of radial compression (*M*), and consequently the amplitude of radial compression (*A*) applied during crimping, and
- increasing the coefficient of friction (μ) at the GRP-metal interface.

(15) The biaxial compressive stresses in the GRP rod will be increased by a decrease in the radius of the GRP rod, and an increase in the average magnitude (and amplitude) of radial compression. This will enhance the risk of compressive intralaminar damage in the rod during crimping.

(16) An increase in the coefficient of friction at the GRP-metal interface will have no influence on the stress state in the rod. Since friction will increase the resistance to

the crimped joint to internal sliding without increasing the internal stresses, it is strongly recommended as an alternative to large magnitudes of radial compression.

(17) A grooved internal surface of the end-fitting can be used to increase the coefficient of friction. However, groove geometries should be carefully optimized. If the grooves are too coarse, they will lead to voids at the rod-metal interface. In addition, circumferentially aligned grooves can increase the resistance to sliding only in the axial direction.

(18) The shape of the radial compression profile will not affect the axial load at the onset of sliding, provided that the average magnitude of radial compression remains the same.

(19) The shape of the radial compression profile can significantly affect the stress distribution in the GRP rod. However, if the amplitude of radial compression applied during crimping remains constant, the maximum values of the biaxial compressive stresses in the rod will not be significantly affected. This applies to both axially and tangentially non-uniform compression profiles.

References

1. J. F. Hall, R. S. Gorur, S. Grzybowski, and T. Orbeck, ''History and Bibliography of Polymer Insulators for Outdoor Applications,'' Report of the IEEE Nonceramic History/Bibliography Task Force, IEEE Transmission and Distribution Committee, (1991).

2. E. A. Cherney, ''State-of-the-Art Review on Polymer Insulator Technology for Transmission,'' Report No. ST - 275, Canadian Electrical Association R & D, Montreal, Canada, (Sept. 1987).

3. J. Lanteigne and C. De Tourreil, ''The mechanical performance of GRP used in electrical suspension insulators,'' *Computers and Mathematics with Applications*, vol. 11, no. 10, pp. 1007-1021, (1985).

4. D. Dumora and S. Wright, ''Structural Aspects of Composite Insulators for Transmission Systems,'' Report No. 9820, Sediver Inc. (R & D), Saint Yorre, France.

5. C. De. Tourreil, P. Bourdon, J. Lanteigne, and P. Nguyen-Duy, ''Mechanical evaluation of non-ceramic insulators,'' Report No. CEA 122 T356, Canadian Electrical Association, Montreal, Canada, (Sept. 1988).

6. R. Mier-Maza, J. Lanteigne, and C. De Tourreil, ''Failure analysis of synthetic insulators with fiberglass rod submitted to mechanical loads,'' *IEEE Trans. Power Apparatus and Systems*, vol. PAS-102, pp. 3123-3129, (1983).

7. L. Paris, L. Pargamin, D. Dumora, and R. Parraud, ''Rating of composite suspension insulators related to the long term mechanical strength of rods,'' in *Proceedings of the 1994 IEEE/PES Winter Power Meeting*, pp. 21-27, New York, NY, (Feb.

1994).

8. E. Bennett, in *Short course on non-ceramic insulators (lecture notes)*, Oregon Graduate Institute of Science and Technology, Portland, OR, (July 1995).
9. American National Standard for Composite Suspension Insulators for Overhead Transmission Lines - Tests, American National Standards Institute, Inc., ANSI C29.11-1989, USA, (Aug. 1989).
10. Composite insulators for a.c. overhead lines with a nominal voltage greater than 1000 V, International Electrotechnical Commission, IEC 1109, Geneva, Switzerland, (1992).
11. D. De Decker and C. Lumb, ''Mechanical strength of composite suspension insulators,'' in *Proceedings of the SEE International Workshop on Non-Ceramic Outdoor Insulation,*, pp. 7-15, Paris, France, (April 1993).
12. M. Kumosa, Q. Qiu, M. Ziomek-Moroz, A. Moroz, and J. M. Braun, ''Microfracture mechanisms in glass/polymer insulator materials under combined effects of electrical, mechanical, environmental stresses,'' Report to Bonneville Power Administration, Contract No. DE-AC79-92BP61873, Portland, OR, (June 1994).
13. M. Kumosa, Q. Qiu, E. Bennett, C. Ek, T. S. McQuarrie, and J. M. Braun, ''Brittle fracture of non-ceramic insulators,'' in *Proceedings of Fracture Mechanics for Hydroelectric Power Systems Symposium*, pp. 235-254, CSFM and Powertech Labs, Vancouver, Canada, (Sept. 1994).
14. S. P. Timoshenko and J. N. Goodier, *Theory of Elasticity, 3rd Edition*, McGraw-Hill, (1970).
15. N. Fujimoto, J. M. Braun, M. Kumosa, and C. Ek, ''Critical fields in composite

insulators effect of voids and contaminants,'' *9th International Symposium on High Voltage Engineering*, Austria, (Aug. 1995).

16. E. A. Cherney, ''Partial discharge - part V : PD in polymer-type line insulators,'' *IEEE Electrical Insulation Magazine*, vol. 7, no. 2, pp. 28-32, (1991).
17. D. Hull, *An Introduction to Composite Materials*, Cambridge University Press, Cambridge, U.K., (1981).
18. M. Schwartz, *Composite Materials Handbook (Second Edition),* McGraw-Hill, Inc., (1992).
19. S. I. Krishnamachari, *Applied Stress Analysis of Plastics*, Van Nostrand Reinhold Publishers, (1986).
20. R. M. Jones, *Mechanics of Composite Materials*, McGraw-Hill Book Company, (1982).
21. V. D. Azzi and S. W. Tsai, ''Anisotropic strength of composites,'' *Experimental Mechanics*, vol. 5, pp. 283-288, (1965).
22. S. W. Tsai and E. M. Wu, ''A general theory of strength for anisotropic materials,'' *Journal of Composite Materials*, vol. 5, pp. 58-80, (1971).
23. M. J. Owen and J. R. Griffiths, ''Evaluation of biaxial stress failure surfaces for a glass fabric reinforced polyester resin under static and fatigue loading,'' *Journal of Materials Science*, vol. 13, pp. 1521-1537, (1978).
24. M. S. Found, ''A review of the multiaxial fatigue testing of fiber reinforced plastics,'' in *Multiaxial Fatigue*, ed. M. W. Brown, pp. 381-395, American Society for Testing and Materials STP 853, Philadelphia, PA, (1985).

25. W. R. Broughton, ''Shear properties of unidirectional carbon fiber composites,'' Ph.D. thesis, University of Cambridge, U.K., (1989).

26. N. J. Pagano and J. M. Whitney, ''Geometric design of composite cylindrical characterization specimens,'' *Journal of Composite Materials*, vol. 4, pp. 538-548, (1970).

27. W. R. Broughton, M. Kumosa, and D. Hull, ''Analysis of the Iosipescu shear test as applied to unidirectional carbon-fiber reinforced composites,'' *Composites Science and Technology*, vol. 38, pp. 299-325, (1990).

28. M. J. Pindera and C. T. Herakovich, ''Shear Characterization of Unidirectional Composites with the Off-Axis Tension Test,'' *Experimental Mechanics*, vol. 26, no. 1, pp. 103-112, (1986).

29. N. Iosipescu, ''New accurate procedure for single shear testing of metals,'' *Journal of Materials*, vol. 2, no. 1, pp. 537-566, (1967).

30. R. Garcia, T. W. Weisshaar, and R. R. McWithey, ''An experimental and analytical investigation of the rail shear-test method as applied to composite materials,'' *Experimental Mechanics*, vol. 20, no. 8, pp. 273-279, (1980).

31. S. Lee and M. Munro, ''Evaluation of in-plane shear test methods for advanced composite materials by the decision analysis technique,'' *Composites*, vol. 17, no. 1, pp. 11-22, (1986).

32. M. J. Pindera, G. Choski, J. S. Hidde, and C. T. Herakovich, ''A methodology for accurate shear characterization of unidirectional composites,'' *Journal of Composite Materials*, vol. 21, pp. 1164-1184, (1978).

33. M. Arcan, Z. Hashin, and A. Voloshin, ''A method to produce plane-stress states

with applications to fiber-reinforced materials,'' *Experimental Mechanics*, vol. 13, no. 3, pp. 141-146, (1978).

34. A. Voloshin and M. Arcan, ''Failure of unidirectional fiber-reinforced materials - new methodology and results,'' *Experimental Mechanics*, vol. 20, no. 8, pp. 280-284, (1980).
35. R. H. Marloff, ''Finite element analysis of biaxial stress test specimen for graphite/epoxy and glass fabric/epoxy composites,'' in *Composite Materials : Testing and Design (6th Conference)*, ed. I. M. Daniel, pp. 34-39, American Society for Testing and Materials STP 787, Philadelphia, PA, (1982).
36. H. A. Richard and K. Benitz, ''A Loading Device for the Creation of Mixed Mode in Fracture Mechanics,'' *International Journal of Fracture*, vol. 22, no. 2, pp. R55-R58, (1983).
37. D. F. Adams and D. E. Walrath, ''Iosipescu shear properties of SMC composite materials,'' in *Composite Materials : Testing and Design (6th Conference)*, ed. I. M. Daniel, pp. 19-33, American Society for Testing and Materials STP 787, Philadelphia, PA, (1982).
38. D. E. Walrath and D. F. Adams, ''The Iosipescu shear test as applied to composite materials,'' *Experimental Mechanics*, vol. 23, no. 1, pp. 105-110, (1983).
39. D. E. Walrath and D. F. Adams, ''An analysis of the stress state in an Iosipescu shear test specimen,'' Report UWME-DR-301-102-1, Department of Mechanical Engineering, University of Wyoming, Wyoming, (June 1983).
40. D. E. Walrath and D. F. Adams, ''Verification and application of the Iosipescu shear test method,'' Report UWME-DR-401-103-1, Department of Mechanical

Engineering, University of Wyoming, Wyoming, (June 1984).

41. D. F. Adams and D. E. Walrath, "Further development of the Iosipescu shear test method," *Experimental Mechanics*, vol. 27, no. 2, pp. 113-119, (1987).

42. J. L. Sullivan, B. G. Kao, and H. V. Oene, "Shear properties and stress analysis obtained from vinyl-ester Iosipescu specimens," *Experimental Mechanics*, vol. 24, no. 3, pp. 223-232, (1984).

43. B. S. Spigel, R. Prabhakaran, and J. W. Sawyer, "An investigation of the Iosipescu and asymmetrical four-point bend tests," *Experimental Mechanics*, vol. 27, no. 1, pp. 57-63, (1987).

44. J. A. Barnes, M. Kumosa, and D. Hull, "Theoretical and experimental evaluation of the Iosipescu shear test," *Composites Science and Technology*, vol. 28, pp. 251-268, (1987).

45. J. L. Sullivan, "The use of Iosipescu specimens (Discussion)," *Experimental Mechanics*, vol. 28, no. 3, pp. 326-328, (1988).

46. M. G. Abdallah and H. E. Gascoigne, "The influence of test fixture design on the Iosipescu shear test for fiber composite materials," in *Test Methods and Design Allowables for Fibrous Composites* , ed. C. C. Chamis, vol. 2, pp. 231-260, American Society for Testing and Methods STP 1003, Philadelphia, PA, (1989).

47. M. J. Pindera, P. Ifju, and D. Post, "Iosipescu shear characterization of polymeric and metal matrix composites," *Experimental Mechanics*, vol. 30, pp. 101-108, (1990).

48. S. Lee and M. Munro, "Evaluation of testing techniques for the Iosipescu shear test for advanced composite materials," *Journal of Composite Materials*, vol. 24, pp.

419-440, (1990).

49. H. Ho, M. Y. Tsai, J. Morton, and G. L. Farley, "An experimental investigation of Iosipescu specimen for composite materials," *Experimental Mechanics*, vol. 31, no. 4, pp. 328-336, (1991).

50. J. Morton, H. Ho, M. Y. Tsai, and G. L. Farley, "An evaluation of the Iosipescu specimen for composite materials shear property measurement," *Journal of Composite Materials*, vol. 26, no. 5, pp. 708-750, (1992).

51. H. Ho, M. Y. Tsai, J. Morton, and G. L. Farley, "Numerical analysis of the Iosipescu specimen for composite materials," *Composites Science and Technology*, vol. 46, pp. 115-128, (1993).

52. H. Ho, J. Morton, and G. L. Farley, "Non-linear numerical analysis of the Iosipescu specimen for composite materials," *Composites Science and Technology*, vol. 50, pp. 355-365, (1994).

53. N. Sukumar and M. Kumosa, "Application of the finite element iterative method to cracks and sharp notches in orthotropic media," *International Journal of Fracture*, vol. 58, pp. 177-192, (1992).

54. N. Sukumar and M. Kumosa, "Stress Singularities at Sharp Notches: Interpolation Formulas," *International Journal of Fracture*, vol. 58, pp. R45-R49, (1992).

55. N. Sukumar, "Finite element analysis of mixed mode fracture and failure in Iosipescu specimens," M.S. Thesis, Oregon Graduate Institute of Science & Technology, Portland, Oregon, (1992).

56. A. Bansal and M. Kumosa, "Experimental and analytical studies of failure modes in Iosipescu specimens under biaxial loadings," *Journal of Composite Materials*,

vol. 29, no. 3, pp. 334-358, (1995).

57. P. G. Ifju, *The shear gauge : for reliable shear modulus measurements of composite materials*, Micro-Measurements Group, Inc. (Catalog), (1994).
58. J. M. Slepetz, T.F. Zageski, and R. Novello, ''In-Plane Shear Test for Composite Materials,'' Rep. AMMRC TR 78-30, Army Materials and Mechanics Research Center, Watertown, MA, (July 1978).
59. M. Kumosa and D. Hull, ''Mixed-mode fracture of composites using the Iosipescu shear test,'' *International Journal of Fracture*, vol. 35, pp. 83-102, (1987).
60. A. Bansal and M. Kumosa, ''Application of the Biaxial Iosipescu Method to Mixed-Mode Fracture of Unidirectional Composites,'' *International Journal of Fracture*, vol. 71, no. 2, pp. 131-150, (1995).
61. N. Sukumar and M. Kumosa, ''Finite element analysis of axial splits in composite Iosipescu specimens,'' *International Journal of Fracture*, vol. 62, no. 1, pp. 55-85, (1993).
62. J. R. Rice, ''A path independent integral and the approximate analysis of strain concentration by notches and cracks,'' *Journal of Applied Mechanics*, vol. 35, pp. 379-386, (1968).
63. M. L. Williams, ''On the stress distribution at the base of a stationary crack,'' *Journal of Applied Mechanics*, vol. 24, pp. 109-114, (1957).
64. G. C. Sih, P. C. Paris, and G. R. Irwin, ''On cracks in rectilinearly anisotropic bodies,'' *International Journal of Fracture*, vol. 1, pp. 189-203, (1965).
65. S. Parhizgar, L. W. Zachary, and C. T. Sun, ''Application of the principles of linear fracture mechanics to the composite materials,'' *International Journal of*

Fracture, vol. 20, pp. 247-256, (1982).

66. E. M. Wu, "Application of fracture mechanics to anisotropic plates," *Journal of Applied Mechanics*, vol. 34, no. 4, pp. 967-974, (1967).

67. J. G. Williams, "Large displacement effects in the DCB test for interlaminar fracture in modes I and II," *6th International Conference on Composite Materials*, vol. 3, pp. 233-242, Elsevier Science Publishers Ltd., U.K., (1987).

68. J. G. Williams, "On the calculation of energy release rates for cracked laminates," *International Journal of Fracture*, vol. 36, pp. 101-119, (1988).

69. J. G. Williams, "End corrections for orthotropic DCB specimens," *Composites Science and Technology*, vol. 35, pp. 367-376, (1989).

70. J. W. Gillespie, L. A. Carlsson, and R. B. Pipes, "Finite element analysis of end-notched flexure specimen for measuring mode II fracture toughness," *Composites Science and Technology*, vol. 27, pp. 177-197, (1986).

71. J. M. Slepetz and L. Carlson, "Fracture of composite compact tension specimens," in *Fracture Mechanics of Composites*, pp. 143-162, American Society for Testing and Materials STP 593, Philadelphia, PA, (1975).

72. J. G. Williams and M. W. Birch, "Mixed-mode fracture in anisotropic media," in *Cracks and Fracture*, pp. 125-137, American Society for Testing and Materials STP 601, Philadelphia, PA, (1976).

73. S. A. Salpekar, I. S. Raju, and T. K. O'Brien, "Strain energy release rate analysis of the end-notched flexure specimen using the finite element method," NASA Technical Memorandum 100494, NASA Langley Research Center and AVSCOM, (Nov. 1987).

74. R. S. Barsoum, ''On the use of isoparametric finite elements in linear fracture mechanics,'' *International Journal for Numerical Methods in Engineering*, vol. 10, pp. 25-37, (1976).

75. R. D. Henshell and K. G. Shaw, ''Crack tip finite elements are unnecessary,'' *International Journal for Numerical Methods in Engineering*, vol. 9, pp. 495-507, (1975).

76. S. K. Chan, I. S. Tuba, and W. K. Wilson, ''On the finite element method in linear fracture mechanics,'' *Engineering Fracture Mechanics*, vol. 2, pp. 1-17, (1970).

77. D. M. Parks, ''A stiffness derivative finite element technique for determination of elastic crack tip stress intensity factors,'' *International Journal of Fracture*, vol. 10, pp. 487-502, (1974).

78. D. M. Parks, ''The virtual crack extension method for nonlinear material behavior,'' *Computer Methods in Applied Mechanics and Engineering*, vol. 12, pp. 353-364, (1977).

79. T. K. Hellen, ''On the method of virtual crack extensions,'' *International Journal for Numerical Methods in Engineering*, vol. 9, pp. 187-207, (1975).

80. E. F. Rybicki and M. F. Kanninen, ''A finite element calculation of stress intensity factors by a modified crack closure integral,'' *Engineering Fracture Mechanics*, vol. 9, pp. 931-938, (1977).

81. F. G. Buchholz and M. F. Kanninen, ''Fracture analysis by the improved and generalized modified crack closure integral,'' *Paper presented at 1st World Congress on Computational Mechanics*, pp. 931-938, Austin, Texas, (1986).

82. I. S. Raju, ''Calculation of strain energy release rates with higher order and singular

finite elements,'' *Engineering Fracture Mechanics*, vol. 28, pp. 251-274, (1987).

83. C. F. Shih, H. G. deLorenzi, and M. D. German, ''Crack extension modeling with singular quadratic isoparametric elements,'' *International Journal of Fracture*, vol. 12, no. 4, pp. 647-651, (1976).

84. E. R. Rybicki, D. W. Schmuesser, and J. Fox, ''An energy release rate approach for stable crack growth in the free-edge delamination problem,'' *Journal of Composite Materials*, vol. 11, pp. 470-487, (1977).

85. F. G. Buchholz, P. J. M. Pirro, H. A. Richard, and K. H. Dreyer, ''Numerical and experimental mixed-mode analysis of a compact tension-shear specimen,'' in *Proceedings of Fourth International Conference on Numerical Methods in Fracture Mechanics*, pp. 641-656, San Antonio, Texas, (1987).

86. H. Wang, S. Ding, F. G. Buchholz, and R. Rikards, ''Delamination analysis for 2D- and 3D-models of a cross-ply laminated three-point bending specimen,'' *Localized Damage III: Computer Aided Assessment and Control*, pp. 251-258, Udine, Italy, (June 1994).

87. V. E. Saouma and E. S. Sikiotis, ''Stress intensity factors in anisotropic bodies using singular isoparametric elements,'' *Engineering Fracture Mechanics*, vol. 25, no. 1, pp. 115-121, (1986).

88. T. J. Boone, P. A. Wawrzynek, and A. R. Ingraffea, ''Finite element modeling of fracture propagation in orthotropic materials,'' *Engineering Fracture Mechanics*, vol. 26, no. 2, pp. 185-201, (1987).

89. R. Sethuraman and S. K. Maiti, ''Finite element based computation of strain energy release rate by modified crack closure integral,'' *Engineering Fracture Mechanics*,

vol. 30, no. 2, pp. 227-231, (1988).

90. K. Badrinarayana, B. Dattaguru, T. S. Ramamurthy, and K. Vijayakumar, ''Modified crack closure integral using six-noded isoparametric quadrilateral singular elements,'' *Engineering Fracture Mechanics*, vol. 36, pp. 945-955, (1990).

91. T. K. O'Brien, ''Characterization of delamination onset and growth in a composite laminate,'' in *Damage in Composite Materials*, ed. K. L. Reifsnider, pp. 140-167, American Society for Testing and Materials STP 775, Philadelphia, PA, (1982).

92. J. M. McKinney, ''Mixed-mode fracture of unidirectional graphite/epoxy composites,'' *Journal of Composite Materials*, vol. 6, pp. 164-166, (1972).

93. R. A. Jurf and R. B. Pipes, ''Interlaminar fracture of composite materials,'' *Journal of Composite Materials*, vol. 16, pp. 386-394, (1982).

94. A. J. Russell and K. N. Street, *Moisture and temperature effects on the mixed-mode delamination fracture of unidirectional graphite/epoxy,* pp. 349-370, American Society for Testing and Materials STP 976, Philadelphia, PA, (1985).

95. H. T. Hahn, ''A mixed-mode fracture criterion for composite materials,'' *Composites Technology Review*, vol. 5, no. 1, pp. 26-29, (1983).

96. C. Corleto, W. Bradley, and M. Henriksen, ''Correspondence between stress fields and damage zones ahead of crack-tip of composites under mode I and mode II delamination,'' *6th International Conference on Composite Materials,*, vol. 3, pp. 378-387, Elsevier Science Publishers Ltd., U.K., (1987).

97. M. L. Williams, ''Stress singularities resulting from various boundary conditions in angular corners of plates in extension,'' *Journal of Applied Mechanics*, vol. 19, pp. 526-528, (1952).

98. D. B. Bogy, ''Edge-bonded dissimilar orthogonal elastic wedges under normal and shear loading,'' *Journal of Applied Mechanics*, vol. 35, pp. 460-466, (Sept. 1968).

99. D. B. Bogy and K. C. Wang, ''Stress singularities at interface corners in bonded dissimilar isotropic elastic materials,'' *International Journal of Solids and Structures*, vol. 7, pp. 993-1005, (1971).

100. V. L. Hein and F. Erdogan, ''Stress singularities in a two-material wedge,'' *International Journal of Fracture Mechanics*, vol. 7, no. 3, pp. 317-330, (1971).

101. S. Ding and M. Kumosa, ''Singular stress behavior at an adhesive interface corner,'' *Engineering Fracture Mechanics*, vol. 47, no. 4, pp. 503-519, (1994).

102. S. Ding, L. Meekisho, and M. Kumosa, ''Analysis of stress singular fields at a bimaterial wedge corner,'' *Engineering Fracture Mechanics*, vol. 49, no. 4, pp. 569-585, (1994).

103. I. S. Raju and J. H. Crews, Jr., ''Interlaminar stress singularities at a straight free edge in composite laminates,'' *Computers and Structures*, vol. 14, no. 1-2, pp. 21-28, (1981).

104. R. S. Barsoum, ''Cracks in anisotropic materials - an iterative solution of the eigenvalue problem,'' *International Journal of Fracture*, vol. 32, pp. 59-67, (1986).

105. R. S. Barsoum, ''Theoretical basis of the finite element iterative method for the eigenvalue problem in stationary cracks,'' *International Journal for Numerical Methods in Engineering*, vol. 26, pp. 531-539, (1988).

106. R. S. Barsoum, ''Application of the finite element iterative method to the eigenvalue problem of a crack between dissimilar media,'' *International Journal for Numerical Methods in Engineering*, vol. 26, pp. 541-554, (1988).

107. R. S. Barsoum, ''Asymptotic fields at interfaces using the finite element iterative method,'' *Computers and Structures*, vol. 35, no. 4, pp. 285-292, (1990).

108. R. S. Barsoum and T. K. Chen, ''Three-dimensional surface singularity of an interface crack,'' *International Journal of Fracture*, vol. 50, pp. 221-237, (1991).

109. K. L. Johnson, *Contact Mechanics*, Cambridge University Press, Cambridge, U.K., (1985).

110. A. E. Love, *A treatise on the mathematical theory of elasticity (Fourth edition)*, Dover Publications, New York, USA, (1944).

111. E. A. Wilson and B. Parsons, ''Finite element analysis of elastic contact problems using differential displacements,'' *International Journal for Numerical Methods in Engineering*, vol. 2, pp. 387-395, (1970).

112. S. K. Chan and I. S. Tuba, ''A finite element method for contact problems of solid bodies - part I. theory and validation,'' *International Journal of Mechanical Science*, vol. 13, pp. 615-625, (1971).

113. S. K. Chan and I. S. Tuba, ''A finite element method for contact problems of solid bodies - part II. application to turbine blade fastenings,'' *International Journal of Mechanical Science*, vol. 13, pp. 627-639, (1971).

114. A. Francavilla and O. C. Zienkiewicz, ''A note on numerical computation of elastic contact problems,'' *International Journal for Numerical Methods in Engineering*, vol. 9, pp. 913-924, (1975).

115. N. Okamoto and M. Nakazawa, ''Finite element incremental contact analysis with various frictional conditions,'' *International Journal for Numerical Methods in Engineering*, vol. 14, pp. 337-357, (1979).

116. K. J. Bathe and A. Chaudhary, ''A solution method for planar and axisymmetric contact problems,'' *International Journal for Numerical Methods in Engineeringg*, vol. 21, pp. 65-88, (1985).

117. W. H. Chen and T. C. Chen, ''Boundary element analysis for contact problems with friction,'' *Computers and Structures*, vol. 45, no. 3, pp. 431-438, (1992).

118. J. A. Garrido, A. Foces, and F. Paris, ''An incremental procedure for three-dimensional contact problems with friction,'' *Computers and Structures*, vol. 50, no. 2, pp. 201-215, (1994).

119. in *ANSYS User's Manual, vol. 4 (Theory)*, ed. P. Kohnke, Swanson Analysis Systems Inc., Houston, PA, (1992).

120. in *Acoustic emission monitoring system AET 5500 (Operating Instructions)*, Hartford Steam Boiler Inspection Technologies, Software Version D07, Sacramento, CA, (Nov. 1990).

121. M. Kumosa, A. Bansal, A. Schubert, and M. V. Balakrishnan, ''Experimental and analytical studies of substation NCIs,'' Final Report, Contract no. 94 AC 08103, Bonneville Power Administration, Portland, OR, (1994).

122. C. W. Ek, ''Substation non-ceramic insulator torsion tests,'' Report no. TTL(M) 95-61, Bonneville Power Administration, Vancouver, WA, (May. 1995).

123. A. Bansal, A. Schubert, M. V. Balakrishnan, and M. Kumosa, ''Finite Element Analysis of Composite Substation Insulators,'' *Composites Science and Technology*, (1995). in press

124. A. Bansal and M. Kumosa, ''Mixed-mode failure of unidirectional composite materials for electrical applications,'' in *Proceedings of Fracture Mechanics for*

Hydroelectric Power Systems Symposium, pp. 255-267, CSFM and Powertech Labs, Vancouver, Canada, (Sept. 1994).

125. M. V. Balakrishnan, ''Application of the biaxial Iosipescu test fixture for the mechanical characterization of unidirectional composites,'' M.S. Thesis, Oregon Graduate Institute of Science & Technology, Portland, OR, (Sept., 1995).
126. M. V. Balakrishnan, A. Bansal, M. Kumosa, and Biaxial testing of unidirectional carbon/epoxy composite using biaxial Iosipescu test fixture, *Journal of Composite Materials*, (July 1995). Submitted for publication
127. G. S. Giare, A. Herold, V. Edwards, and R. R. Newcomb, ''Fracture toughness of unidirectional graphite fiber reinforced/epoxy composite in mode II (forward shear), using a thin tubular specimen,'' *Engineering Fracture Mechanics*, vol. 30, no. 4, pp. 531-545, (1988).
128. M. Kumosa and D. Hull, ''Finite element analysis of a circumferentially cracked cylindrical shell under uniform tensile loading,'' *Engineering Fracture Mechanics*, vol. 31, no. 5, pp. 817-826, (1988).
129. M. Kumosa and D. Hull, ''Finite element analysis of a circumferentially cracked cylindrical shell loaded in torsion,'' *Engineering Fracture Mechanics*, vol. 32, no. 1, pp. 123-136, (1989).
130. M. Kumosa, ''Bulging effects in circumferentially cracked orthotropic cylindrical shells,'' *Engineering Fracture Mechanics*, vol. 38, no. 4/5, pp. 255-262, (1991).
131. X. N. Huang, ''Mode I and mode II intralaminar fracture of unidirectional composites,'' Ph.D. Thesis, University of Cambridge, U.K., (1990).
132. A. C. Kaya and F. Erdogan, ''Stress intensity factors and COD in an orthotropic

strip,'' *International Journal of Fracture*, vol. 16, no. 2, pp. 171-190, (1980).

133. S. Mall and N. K. Kochhar, ''Finite element analysis of end-notched flexure specimens,'' *Journal of Composites Technology and Research*, vol. 8, no. 2, pp. 54-57, (1986).

134. F. G. Buchholz, H. Wang, S. Ding, and R. Rikards, ''Delamination analysis for cross-ply laminates under bending with consideration of crack face contact and friction,'' in *Proc. of 10th Intl. Conference on Composite Materials*, pp. 605-610, Whistler, B.C., Canada, (Aug. 1995).

Appendix A

Benchmark Test For VCC Method

This appendix presents the numerical results obtained from the energy based virtual crack closure (VCC -1c and -2c) methods described in chapter 2. The analytical solutions of Kaya and Erdogan, [132] for on edge-cracked orthotropic boron/epoxy strip under transverse tension, were used for the benchmark test.

Due to the symmetric boundary conditions, only one half of the strip was analyzed. The analyses were carried out for crack-length to width (a/w) ratios ranging from 0.1 to 0.8. Moreover, in order to examine an adequate mesh density which yields sufficiently accurate results, element sizes (L) of 10% and 1% of the total crack length (a) were used at the crack tip.

Figure A.1 shows a half-symmetry mesh of the orthotropic plate with $a/w = 0.4$ and the crack-tip element size $L = 0.1a$. Also indicated in figure A.1 are the material properties used in the analyses. Table A.1 compares the numerically determined K_I values with the analytical solutions of Kaya and Erdogan. [132]

Table A.1 : Comparison of numerical and reference solutions [132]

for an edge-cracked orthotropic strip in tension.

Crack-Length	Reference Solution	$L = 0.1a$				$L = 0.01a$			
		VCC-1c Method		VCC-2c Method		VCC-1c Method		VCC-2c Method	
a/w	$K_I/\sigma_0\sqrt{\pi a}$	$K_I/\sigma_0\sqrt{\pi a}$	% Error	$K_I/\sigma_0\sqrt{\pi a}$	% Error	$K_I/\sigma_0\sqrt{\pi a}$	% Error	$K_I/\sigma_0\sqrt{\pi a}$	% Error
0.1	1.1284	1.1180	0.86	1.1539	2.30	1.1218	0.58	1.1253	0.27
0.2	1.3172	1.3039	0.96	1.3614	3.40	1.3097	0.57	1.3153	0.15
0.3	1.6069	1.5884	1.12	1.6849	4.89	1.5977	0.57	1.6070	0.01
0.4	2.0421	2.0136	1.39	2.1813	6.80	2.0295	0.62	2.0453	0.16
0.5	2.7199	2.6724	1.71	2.9826	9.67	2.7017	0.67	2.7298	0.36
0.6	3.8590	3.7701	2.27	4.4069	14.22	3.8305	0.74	3.8857	0.69
0.7	6.0350	5.8342	3.33	7.4218	23.00	5.9845	0.84	6.1105	1.25
0.8	11.274	10.584	6.04	-	-	11.1481	1.12	11.5346	2.31

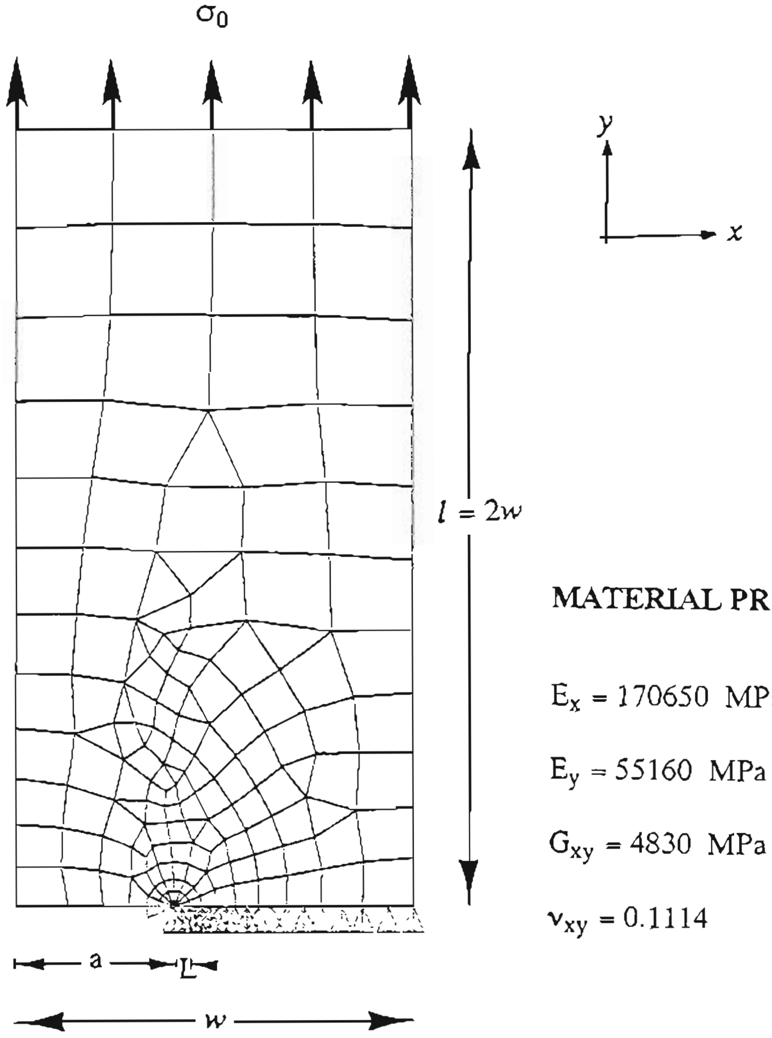

MATERIAL PROPERTIES

$E_x = 170650$ MPa

$E_y = 55160$ MPa

$G_{xy} = 4830$ MPa

$\nu_{xy} = 0.1114$

Figure A.1 : Finite element mesh of an edge-cracked orthotropic strip in tension.

Appendix B

Mode II DCB Test

This appendix presents the mode II double cantilever beam (DCB) tests performed on XAS 914 carbon/epoxy specimens to determine the value of G_{IIc}.

Figure B.1 shows the loading arrangement and dimensions of the mode II DCB specimens. The critical energy release rate G_{IIc} is related to the specimen compliance C by

$$G_{IIc} = \frac{P_f^2}{2\,t}\left[\frac{dC}{da}\right] \tag{B-1}$$

where P_f is the critical load at the onset of fracture, t is the specimen thickness and a is the length of the precrack. Four specimens with normalized precrack lengths (a/L) ranging between 0.35 and 0.60 were tested under displacement control at a rate of 6 mm/min. The load-displacement curve exhibited significant nonlinearity due to large deflection of the DCB arms. Fracture was catastrophic from the tip of the pre-crack to the constrained end of the specimen.

Assuming small deflection of the DCB arms, the following expression has been derived by Williams[67, 68] for the mode-II DCB configuration;

$$G_{IIc} = \frac{9\,P_f^2\,a^2}{4\,E_{11}\,t^2\,h^3} \tag{B-2}$$

The effect of elastic foundation of the beam-root (section AB) has subsequently been accounted for by an extra crack length (χh), [69]

$$a_{eff} = a + \chi h \tag{B-3}$$

$$where \quad \chi = \left[\frac{1}{18K} \frac{a_{66}}{a_{11}} \right]^{1/2} \left[3 - 2 \left[\frac{\Gamma}{1+\Gamma} \right]^2 \right]^{1/2} \tag{B-4}$$

$$\Gamma = \frac{1}{K} \frac{a_{66}}{\sqrt{a_{11}\, a_{22}}} \tag{B-5}$$

and

$$K = \frac{10\,(1 + \nu_{12})}{12 + 11\nu_{12}} \tag{B-6}$$

a_{ij} and ν_{12} represent the material elastic compliance coefficients and poissons ratio respectively. For the present unidirectional graphite/epoxy composite, $K = 0.847$, $\Gamma = 10.275$, and $\chi = 1.6977$.

In addition to the ligament elastic foundation, the effects of bending, and bending induced shear deformation have been included. The following expression for the analytical specimen compliance has been determined by a modified beam analysis method [131]

$$C = \frac{1}{4E_{11}th^3} \left[6(a + \chi h)^3 + 2(L + \chi h)^3 + \frac{3E_{11}h^2}{5\,G_{12}} (a + 4L + 5\chi) \right] \tag{B-7}$$

Results presented in table B.1 show the G_{IIc} values computed from the ordinary beam analysis (equation B-2) and the modified beam analysis (equations B-1 and B-7) methods. Values of $G_{IIc,ob}$ are about 65% lower than $G_{IIc,mb}$ due to large deflections observed in the specimens.

Table B.1 : G_{IIc} values from mode II DCB tests of unidirectional carbon/epoxy specimens.

Crack - Length (a/L)	Fracture Load, P_f (N)	$G_{IIc,ob}$ † (J/m^2)	$G_{IIc,mb}$ ‡ (J/m^2)
0.37	2846.9	1884.4	6286.97
0.37	3158.2	2319.2	7737.46
0.48	2241.9	2494.5	6385.25
0.60	2135.1	2787.4	6271.58

† Ordinary Beam Analysis, ‡ Modified Beam Analysis

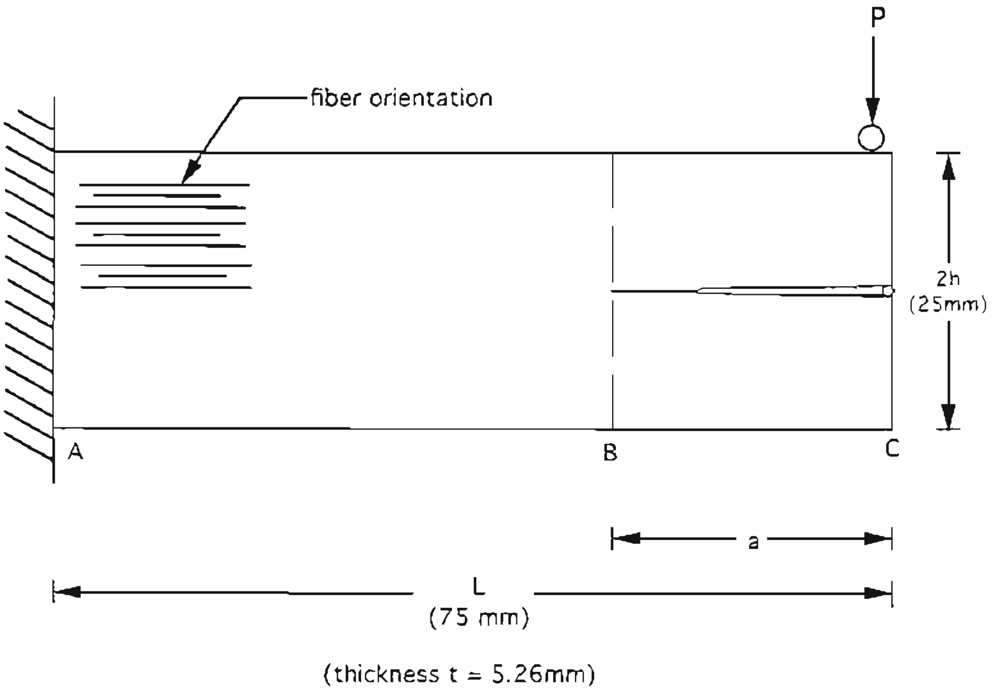

Figure B.1 : Geometry and loading of mode II DCB specimens.

Appendix C

Elastic Properties of E-glass/epoxy Composite

In this appendix, the elastic properties of the E-glass/epoxy (GRP) composite, used as the core material of insulators, have been estimated from analytical micromechanics based methods. In addition, the elastic properties determined experimentally from the GRP rod of insulator A are given.

Assuming an E-glass fiber volume fraction (V_f) of 62 %, the rule of mixtures (equation 2-5) was used to evaluate E_{11} and ν_{12} from the constituent properties given in table C.1. The modified Halpin-Tsai equations (equations 2-6) were used to estimate the values for E_{22}, G_{12}, and ν_{23}. Assuming a parallel hexagonal packing of fibers ($V_{f,max}$ = 0.907^{19}), the value of ψ was found to be 1.07 from equation (2-6c).

The main difficulty in using the modified Halpin-Tsai equations is the selection of an appropriate value for the empirical parameter ξ. For the present case, we used ψ = 1.07, ξ = 2, and η = 0.867 for the estimation of E_{22}. For estimating G_{12}, the values of η = 0.907 and ξ = 1.336 were obtained from equations (2-6b) and (2-6d) respectively. For estimating ν_{23}, we used ξ = 2 and η = -0.1939. Since the 1–2 and 1–3 planes are identical, and since the composite is transversely isotropic in the 2–3 plane, the shear modulus in the 2–3 plane was determined by

$$G_{23} = \left[\frac{E_{22}}{2(1+\nu_{23})} \right] \qquad \text{(C-1)}$$

The constituent elastic moduli, and the calculated composite moduli are presented in table C.1.

Since the analytical estimation of elastic properties is dependent on the value of empirical parameters ξ, ψ, and $V_{f,max}$, experimental determination of some of the elastic properties and strengths was essential. Therefore, the true elastic and strength properties were measured by extracting GRP specimens from the rod of insulator A. [121] Table C.2 shows the comparison of elastic properties determined experimentally and analytically.

Table C.1 : Elastic properties for constituents and GRP composite estimated from analytical equations.

E-Glass Fiber	Epoxy Resin	GRP-Composite (62% V_f)
$E_f = 72.00$ GPa	$E_m = 3.50$ GPa	$E_{11} = 45.97$ GPa $E_{22} = 17.10$ GPa $E_{33} = 17.10$ GPa
$G_f = 30.00$ GPa	$G_m = 1.26$ GPa	$G_{12} = 5.54$ GPa $G_{13} = 5.54$ GPa $G_{23} = 6.77$ GPa
$\nu_f = 0.20$	$\nu_m = 0.39$	$\nu_{12} = 0.270$ $\nu_{13} = 0.270$ $\nu_{23} = 0.262$

Table C.2 : Analytical and experimental properties of GRP composite used in insulator A.

Material Property	Analytical	Experimental	Used in FE-model
E_{11} (GPa)	45.97	38.857	38.857
E_{22} (GPa)	17.10	10.085	10.085
G_{12} (GPa)	5.54	3.819	3.819
G_{23} (GPa)	6.77	-	3.897
ν_{12}	0.270	0.294	0.294
ν_{23}	0.262	-	0.294
$\sigma^f_{11,T}$ (MPa)	-	849.6	-
$\sigma^f_{11,C}$ (MPa)	-	480-690 †	-
$\sigma^f_{22,T}$ (MPa)	-	40.0 ‡	-
$\sigma^f_{22,C}$ (MPa)	-	−140.0 ‡	-
τ^f_{12} (MPa)	-	60.0	-

†Obtained from reference 5 ‡ from reference 17

Vita

The author was born on February 10, 1970, in Bahar-dar, Ethiopia. Being the son of professors in Mathematics and English, he was raised in a highly academic environment. He completed most of his primary education in Ethiopia, and his secondary education in Nigeria. The author earned his Bachelor's degree in Metallurgical Engineering from the Institute of Technology, Banaras Hindu University, India, in 1991.

In September 1991, the author joined the Oregon Graduate Institute of Science and Technology (OGI) to pursue a Ph.D. degree in Materials Science and Engineering. During the course of his study at OGI, he has co-authored the following technical papers:

(1) A. Bansal and M. Kumosa, "Experimental and analytical studies of failure modes in Iosipescu specimens under biaxial loadings", *Journal of Composite Materials*, vol. 29, no. 3, (1995), pp. 334-358.

(2) A. Bansal and M. Kumosa, "Application of the biaxial Iosipescu method to mixed-mode fracture of unidirectional composites", *International Journal of Fracture*, vol. 71, no. 2, (1995), pp. 131-150.

(3) A. Bansal and M. Kumosa, "Mixed-mode failure of unidirectional composite materials for electrical applications", *Proc. of Fracture Mechanics for Hydroelectric Power Systems Symposium*, CSFM and Powertech Labs, Vancouver, Canada, (Sept. 1994), pp. 255-267.

(4) A. Bansal, A. Schubert, M. V. Balakrishnan, and M. Kumosa, "Finite element analysis of composite substation insulators", *Composites Science and Technology*, (1995), in press.

(5) M. V. Balakrishnan, A. Bansal, and M. Kumosa, "Biaxial testing of unidirectional carbon/epoxy composite using biaxial Iosipescu test fixture", *Journal of Composite Materials*, (July 1995), submitted.

(6) A. Bansal and M. Kumosa, "Finite element simulation of composite insulators with crimped end-fittings", in preparation.

The author also gave a presentation entitled "Experimental and analytical studies of substation NCIs" at the Fracture Mechanics for Hydroelectric Power Systems Symposium held in Vancouver, Canada, in September, 1994.